BEILSTEIN JOURNAL OF NANOTECHNOLOGY

Molecular materials – towards quantum properties

Edited by Mario Ruben

Imprint

Beilstein Journal of Nanotechnology
www.bjnano.org
ISSN 2190-4286
Email: journals-support@beilstein-institut.de

The *Beilstein Journal of Nanotechnology* is published by the Beilstein-Institut zur Förderung der Chemischen Wissenschaften.

Beilstein-Institut zur Förderung der Chemischen Wissenschaften
Trakehner Straße 7–9
60487 Frankfurt am Main
Germany
www.beilstein-institut.de

BEILSTEIN JOURNAL OF NANOTECHNOLOGY

Molecular materials – towards quantum properties

Mario Ruben[1,2]

Editorial

Open Access

Address:
[1]Institute of Nanotechnology, Karlsruhe Institute of Technology, D-76344 Eggenstein-Leopoldshafen, Germany and [2]Institut de Physique et Chimie des Matériaux, Université de Strasbourg, 23 Rue du Loess, F-67200 Strasbourg, France

Email:
Mario Ruben - mario.ruben@kit.edu

Beilstein J. Nanotechnol. **2015,** *6,* 1485–1486.
doi:10.3762/bjnano.6.153

Received: 15 June 2015
Accepted: 28 June 2015
Published: 08 July 2015

This article is part of the Thematic Series "Molecular materials – towards quantum properties".

Editor-in-Chief: T. Schimmel

Molecular materials are promising candidates for the expression of quantum properties, mainly due to the inherent monodispersity of their building blocks and the unique possibility to tailor the local environments of (natural) atoms.

Both artificial as well as natural atoms have been proposed as quantum objects in the realisation of quantum information schemes. As a result of their confinement, electrons in both natural atoms and in quantum dots, so-called artificial atoms, are characterized by the formation of discrete energy levels. Similarly, in the case of a Josephson junction, Cooper pairs are confined in the potential well of the Josephson coupling energy leading to a discrete distribution of energy levels. Hence, the junction can be considered as a superconducting artificial atom. With regard to magnetism, single spins of impurities in semiconductors as well as molecular nanomagnets have been proposed as solid-state candidates for quantum bits (qubits). The used quantum correlations (e.g., entanglement, coherence) are usually observed only on the nanometer scale and have long been recognized as an information resource for quantum communication and processing. In particular, there is a considerable motivation to produce quantum computers, and a great deal of interest from scientists working in materials science, chemistry, physics, and nanofabrication technologies has been attracted. For example, the company D-wave has demonstrated a quantum annealer that performs certain calculations sufficiently rapidly to have a consortium, which involves Google and NASA, investing staggering sums of money in one such device [1].

The main advantage of the use of the molecular approach here is that molecules are quantum objects that can be produced by synthetic tools in a large number of atomically precise copies – a requirement for the scalable exploitation of the quantum properties. Devices based on single, or small numbers of, molecules, could speed up information treatment or allow for processing schemes that have not been possible to date. In a series of recent publications, it could be shown that magnetic molecules, in particular lanthanide complexes can be considered to be spin-qubits [2] or spin qugates [3]. Moreover, it was shown that molecule-based nuclear spins are extremely well insulated from environmental perturbations, rendering them less prone to decoherence. By means of synthetic engineering the central fine-tuning of the delicate trade-off between decoupling of the quantum object for low decoherence and connecting it for the electrical read-out could be achieved [2].

Quantum computing, the manipulation of data encoded in qubits instead of bits of information such as spin states of electrons or of an atomic nucleus, has been a long standing goal of scientists. In principle, if the qubits can maintain their coherence, without being perturbed by the noise of the surrounding environments (e.g., neighbouring atoms), quantum computers could be powered to find the best solutions far more quickly than current conventional computers. In some of the proposed device materials, quantum information is carried by the spin and the orbital degree of freedom of the electron. The challenge consists in circumventing the strong coupling of the latter one with the environment in order to achieve the needed long coherence times to carry out quantum operations.

In this context, molecular quantum materials offer the additional advantage that the active quantum processing elements comprise an atomic core of one to a few open-spin ions surrounded by a shell of organic material. At low temperatures, the behavior of such molecular spin objects can be well described by simple few-level systems. Moreover, their spin degree of freedom can be sufficiently decoupled from environmental perturbations to attain long coherence times, thus making them the ideal candidates for the implementation of qubits. The organic shell can be used to fine-tune the coupling between molecular qubits as required by scalability for logical quantum gate operations.

We have gathered in the Thematic Series contributions dealing with the magnetic properties of molecules, partially under use of lanthanide metal ions und their coordination under surface confinement. By the same token, the needed surface attachment and positioning of molecular materials by self-assembly techniques is addressed – an important prerequisite for the electrical addressing of molecules by lateral graphene electrodes or vertical scanning tunnelling microscopy set-ups or e-beam lithographed gold or Prussian blue nano-arrays. Complementary, quantum chemical calculations have addressed lanthanide complexes and metal-organic frameworks.

This Thematic Series is part of a subsession of the same title, which took place at the E-MRS spring meeting in May 2014 in Lille, France. I would like to kindly thank Prof. G. Aromi (Barcelona) and Prof. A. Bousseksou (Toulouse) for co-chairing this event.

Mario Ruben

Karlsruhe, June 2015

References

1. Johnson, M. W.; Amin, H. M. S.; Gildert, S.; Lanting, T.; Hamze, F.; Dickson, N.; Harris, R.; Berkley, A. J.; Johansson, J.; Bunyk, P.; Chapple, E. M.; Enderud, C.; Hilton, J. P.; Karimi, K.; Ladizinsky, E.; Ladizinsky, N.; Oh, T.; Perminov, I.; Rich, C.; Thom, M. C.; Tolkacheva, E.; Truncik, C. J. S.; Uchaikin, S.; Wang, J.; Wilson, B.; Rose, G. *Nature* **2011,** *473,* 194–198. doi:10.1038/nature10012
2. Thiele, S.; Balestro, F.; Ballou, R.; Klyatskaja, S.; Ruben, M.; Wernsdorfer, W. *Science* **2014,** *344,* 1135–1138. doi:10.1126/science.1249802
3. Aromí, G.; Aguilà, D.; Gamez, P.; Luis, F.; Roubeau, O. *Chem. Soc. Rev.* **2012,** *41,* 537–546. doi:10.1039/C1CS15115K

License and Terms

BEILSTEIN JOURNAL OF NANOTECHNOLOGY

Quasi-1D physics in metal-organic frameworks: MIL-47(V) from first principles

Danny E. P. Vanpoucke*, Jan W. Jaeken, Stijn De Baerdemacker, Kurt Lejaeghere and Veronique Van Speybroeck

Full Research Paper

Open Access

Address:
Center for Molecular Modeling, Ghent University, Technologiepark 903, Zwijnaarde 9052, Belgium

Email:
Danny E. P. Vanpoucke* - Danny.Vanpoucke@Ugent.be

* Corresponding author

Keywords:
band structure; density functional theory (DFT); low-dimensional electronics; metal-organic frameworks (MOFs); MIL-47

Beilstein J. Nanotechnol. **2014,** *5,* 1738–1748.
doi:10.3762/bjnano.5.184

Received: 02 July 2014
Accepted: 22 September 2014
Published: 09 October 2014

This article is part of the Thematic Series "Molecular materials – towards quantum properties".

Guest Editor: M. Ruben

Abstract

The geometric and electronic structure of the MIL-47(V) metal-organic framework (MOF) is investigated by using ab initio density functional theory (DFT) calculations. Special focus is placed on the relation between the spin configuration and the properties of the MOF. The ground state is found to be antiferromagnetic, with an equilibrium volume of 1554.70 $Å^3$. The transition pressure of the pressure-induced large-pore-to-narrow-pore phase transition is calculated to be 82 MPa and 124 MPa for systems with ferromagnetic and antiferromagnetic chains, respectively. For a mixed system, the transition pressure is found to be a weighted average of the ferromagnetic and antiferromagnetic transition pressures. Mapping DFT energies onto a simple-spin Hamiltonian shows both the intra- and inter-chain coupling to be antiferromagnetic, with the latter coupling constant being two orders of magnitude smaller than the former, suggesting the MIL-47(V) to present quasi-1D behavior. The electronic structure of the different spin configurations is investigated and it shows that the band gap position varies strongly with the spin configuration. The valence and conduction bands show a clear V d-character. In addition, these bands are flat in directions orthogonal to VO_6 chains, while showing dispersion along the the direction of the VO_6 chains, similar as for other quasi-1D materials.

Introduction

Metal-organic frameworks (MOFs) present a class of materials located at the conceptual interface between molecules and solids. They consist of inorganic metal or metal-oxide clusters (i.e., nodes) connected through organic molecules (i.e., linkers), giving rise to porous, highly tunable frameworks. Their porous nature, with internal surface areas of 1000 m^2g^{-1} or more, and

chemical tunability, through the choice of nodes and linkers, makes them versatile materials that are receiving an exponentially growing interest with a special focus on industrial, chemically oriented processes, such as catalysis, sensing, gas separation and gas storage [1-22].

In addition to providing large internal surface areas, the framework topology also allows to organize metal sites in a well-defined, ordered fashion, creating zero-, one- and two-dimensional metal(-oxide) structures. Such structures provide interesting systems to observe and study exotic and low-dimensional physics [23-37]. Transition-metal oxides, on the other hand, have proven to be a rich source of multiferroic materials [38-41]. Such materials, which combine at least two magnetic and/or electronic ordering phenomena, are of great interest for technological applications. MOFs containing transition-metal oxides as nodes are therefore expected to show physically interesting behavior. For example Canepa et al. [36] investigated the MOF-74 frameworks with Fe, Ni and Co at their metal centers, and found quasi-1D ferromagnetic behavior with quenched antiferromagnetic inter-chain interactions. Stroppa et al. [40] and Wang et al. [41] investigated Cu-based MOFs with an ABX_3 perovskite architecture and found these to exhibit quasi-1D multiferroic behavior. In both cases, Jahn–Teller distortions of the Cu-ion environment were shown to play a crucial role in the 1D nature of the magnetic behavior. Chen et al. [37] reported on the observation of spin canting in a 2D Mn-based MOF with a transition temperature of 40 K and Sibille et al. [42] investigated the magnetism of the $Co^{II}_4(OH)_2(C_{10}H_{16}O_4)_3$ MOF. In each of these cases, a fundamental understanding of the electronic and magnetic properties was obtained by means of high-quality ab initio methods.

In this work, we present an ab initio investigation of the MIL-47(V) MOF [1] (cf. Figure 1a). The were three reasons to chose this particular MOF: (1) The topology of MIL-47(V) provides access to 1D metal-oxide chains. (2) The V version provides one unpaired electron per metal site, which is of interest for magnetic properties. (3) MIL-47 belongs to the family of so-called breathing MOFs [4,11,43-49], leading to interesting opportunities with regard to sensing applications. In this family, MIL-47(V) has a somewhat special status, because, unlike most breathing MOFs MIL-47(V^{IV}) does not show breathing under thermal stimuli or after the adsorption of gases or liquids [5,44,50], but only under significant mechanical pressure [45]. In contrast, MIL-47(V^{III}), also referred to as MIL-53(V), shows breathing behavior induced by temperature or by gas adsorption [44]. For the MIL-53(V) MOF, the presence of small amounts of V^{IV} has a detrimental effect on its flexibility, which indicates that the metal center plays an important role [44].

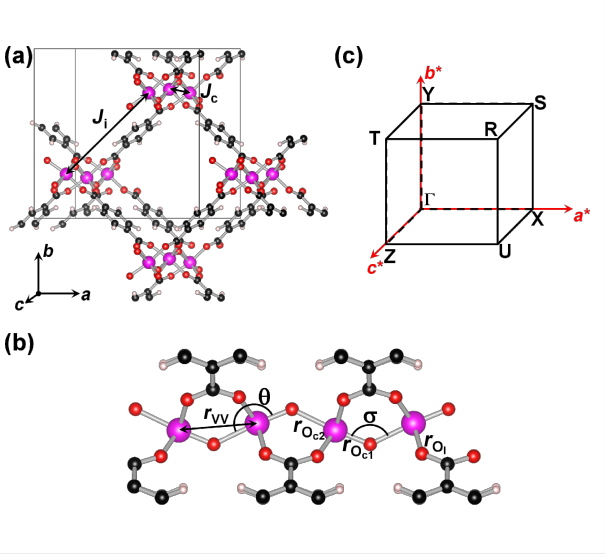

Figure 1: (a) Ball-and-stick representation of the MIL-47(V) MOF. Pink, red, black, and white spheres indicate V, O, C and H positions, respectively. The grey box indicates the unit cell used. The intra- and inter-chain couplings J_c and J_i (cf. section "Stability and magnetic coupling") are indicated. (b) Representation of the Brillouin zone of the unit cell, showing the high symmetry *k*-points. (c) Ball-and-stick representation of a single vanadium oxide chain, indicating the superexchange angle σ, the octahedral backbone angle θ, the inter-V-distance r_{VV}, and the V–O bond lengths $r_{O_{c1}}$ and $r_{O_{c2}}$ along the chain, and r_{O_l} to the linker.

Because of the rigid nature of MIL-47(V^{IV}) under standard breathing conditions it is often used as a material for comparison in studies of breathing (due to sorption) of other MOFs [3,7,10,13,51,52]. In addition, the 1D pores of MIL-47(V) make this material well-suited for gas storage and separation. As a result, much of the work since its first synthesis focuses on these topics. The adsorption and diffusion behavior of different molecules, ranging from hydrogen and carbon dioxide to methane and xylene isomers, has been studied both experimentally and theoretically [3,5-7,10,12,13,18-22,50,51]. The size of the MIL-47 system, however, limits the computational possibilities. As a result, most theoretical work in the above studies is limited to force-field based simulations [7,10,12,13,18-20,22,51]. In these, DFT calculations are often used to provide partial charges. Due to their computational cost (the work presented in this paper amounts to 25 years of CPU time), DFT calculations for other purposes tend to be limited to fixed geometries [50] or small *k*-point sets [53], with some exceptions [22].

In this paper, the influence of the spin configuration on the geometric and electronic structure is investigated: equilibrium structure, energy, bulk modulus and band structure. Also the transition pressure for the large-pore-to-narrow-pore phase transition is estimated, and inter- and intra-chain coupling constants are calculated.

Computational details

Density functional theory calculations

Density functional theory (DFT) calculations are performed within the projector augmented wave (PAW) method as implemented in the "Vienna ab initio Simulation Package" (VASP) while using the generalized gradient approximation (GGA) functional as constructed by Perdew, Burke and Ernzerhof (PBE) [54-58]. The plane wave kinetic energy cutoff is set to 500 eV. Due to the large difference in lattice vector lengths for the structures (cf. Figure 1) a Monkhorst–Pack special *k*-point grid of 2 × 2 × 6 *k*-points is used to sample the Brillouin zone [59,60]. Dispersive interactions, which play an important role in the flexibility of the crystal structure of MOFs [61], are included through the DFT-D3 method as formulated by Grimme et al. [62,63], including Becke–Johnson damping [64].

Due to the presence of Pulay stresses [65], MIL-47(V) tends to collapse during geometry optimization [60]. To prevent such collapse, the volume is optimized through fitting constant-volume optimized structures to the Rose–Vinet equation of state [60,66]. The constant-volume optimizations are performed by using a conjugate gradient method, allowing simultaneous optimization of atomic positions and cell shape. The convergence criterion is set to a difference in energy of less than 1.0×10^{-7} eV between subsequent ionic steps. After full relaxation, the forces on the ions are then found to be below 1.2 meV/Å.

The density of states (DOS) was obtained by using a denser *k*-point grid of 3 × 3 × 9 *k*-points, and the band structure was calculated along the edges of the first Brillouin zone (cf. Figure 1b).

The atomic charges in the systems are calculated by using the Hirshfeld-I approach [67,68] as implemented in our in-house-developed code HIVE [69-71]. The atom-centered spherical integrations [72] are done by using Lebedev–Laikov grids [73] of 1202 grid points per shell, and a logarithmic radial grid. The iterative scheme is considered to be converged when the largest difference in charge of a system atom is less than $1.0 \times 10^{-5}e$ between two consecutive iterations.

Structure of MIL-47(V)

The periodic cell used in this work contains 4 formula units or 72 atoms, and is shown in Figure 1a. This cell contains 2 vanadium oxide chains with 2 vanadium atoms per chain. Each V atom contains one unpaired d-electron, since the V atoms have a formal charge of +IV in the MIL-47(V) topology. This leads to 2^4 possible spin configurations of which five are inequivalent (cf. Figure 2): (FM) ferromagnetic for both inter- and intra-chain spin alignment; (SFM) semi-ferromagnetic, containing one ferromagnetic and one antiferromagnetic chain; (AF1) although globally antiferromagnetic, this system contains ferromagnetic chains in an antiferromagnetic configuration; (AF2 and AF3) systems containing antiferromagnetic chains in either a ferromagnetic (AF2) or antiferromagnetic (AF3) configuration.

Results and Discussion

Structure and elastic behavior

The optimized parameters of the Rose–Vinet equation of state [66] are presented in Table 1. The equilibrium volumes for the five different spin configurations are within a range of 2 $Å^3$, while the lattice parameters are within a range of 0.4, 0.2, and 0.03 Å for the *a*-, *b*-, and *c*-axis, respectively. A comparison to

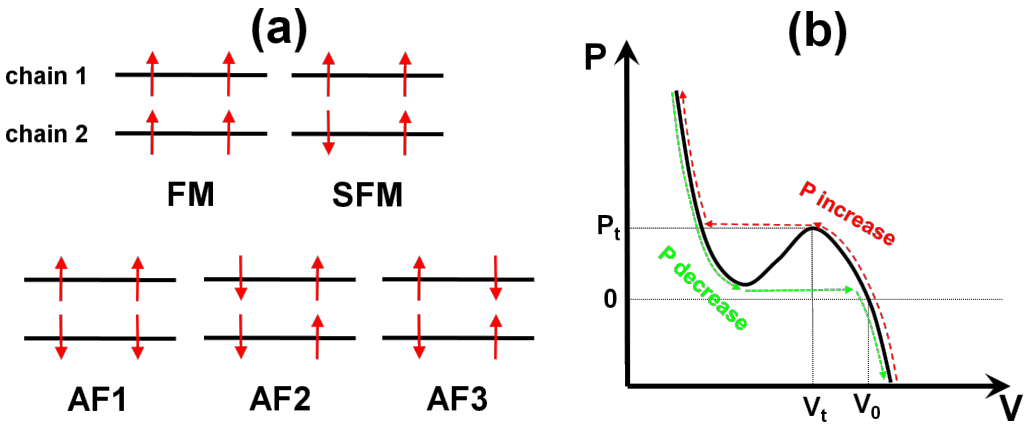

Figure 2: (a) Schematic representation of the five inequivalent magnetic configurations investigated in this work: ferromagnetic (FM), semi-ferromagnetic (SFM) with one ferromagnetic and one antiferromagnetic chain, and three different antiferromagnetic (AF) configurations. (b) Schematic representation of the P(V) relation of the MIL-47(V) MOF. The extrema of the s-shaped curve represent the points at which a pressure-induced phase transition occurs. The red dashed and green dotted curves indicate the path followed for increasing and decreasing pressure, respectively.

Table 1: Equilibrium structure parameters obtained from a 9-point fit to the Rose–Vinet equation of state with volumes ranging over ±4% with regard to the equilibrium volume: the ground state energy of the magnetic configuration relative to the ferromagnetic configuration (E_0), the equilibrium volume (V_0), the bulk modulus (B_0) and its pressure derivative (B_0'). The root-mean-square deviation (rmsd) for each of the five fits is less than 0.8 meV. In addition, also the transition pressure P_t and volume V_t for which a large-pore MIL-47(V) is expected to transform into a narrow-pore structure is given.

	E_0 [meV]	V_0 [Å^3]	B_0 [GPa]	B_0' [–]	P_t [MPa]	V_t [Å^3]
FM	0	1553.38	5.95	−53.2	83	1495.30
SFM	−144	1555.02	7.17	−52.2	102	1495.46
AF1	−16	1554.45	6.14	−55.6	82	1498.50
AF2	−279	1554.71	8.13	−48.5	124	1490.70
AF3	−278	1554.70	8.12	−48.5	124	1490.70

the experimentally measured lattice parameters and volumes shows that the calculated values are generally slightly larger [1,6,22,44] (cf. Table 2), as it is expected from the underbinding nature of the PBE functional [74-77]. The calculated equilibrium volume of about 1555 Å^3 is 1.3 and 1.7% larger than the experimental value measured by Barthelet et al. [1] and Leclerc et al. [44], respectively. Table 2 shows that the largest contribution to this deviation originates from the long *a*-axis (up to 1.6%), while the *b*-and the *c*-axis show a deviation from experiment of 1% or less. An interesting global aspect to note regarding the MIL-47(V) structure is the symmetry breaking in the V-chain. Whereas for the as-synthesized version all V atoms are positioned on a straight line, the V atoms exhibit a zig-zag configuration in the *b*–*c*-plane of the calculated structure. Although the separation in the *b*-direction (b_{VV}) is rather small in absolute value (cf. Table 2), the resulting improvement in energy due to this symmetry breaking is about 300 meV for the 72-atom unit cell used. A more detailed investigation of the crystal geometry, presented in Table 2, shows that the vanadium–oxygen chains present almost identical bond lengths and angles, all in excellent agreement with the experimental values for such chains [1,6,78]. As a result, the different spin configurations give rise to nearly indistinguishable crystal structures. It is, however, important to note that these very small differences in the crystal structure do give rise to small variations in the system energy, in addition to the variations due to the different spin configurations. These small geometry contributions are not negligible, and lead to significant variations in the calculated

Table 2: Structural parameters of the equilibrium volume-optimized structures. *a*, *b*, and *c*: lattice parameters; $r_{O_{c1}}$, $r_{O_{c2}}$, r_{O_I}: vanadium oxide bond length; r_{VV}: intra-chain vanadium distance; σ: superexchange angle and θ octahedral backbone angle; b_{VV}: component along the *b*-direction of r_{VV}. Experimental data are given in comparison.

	a [Å]	*b* [Å]	*c* [Å]	$r_{O_{c1}}$ [Å]	$r_{O_{c2}}$ [Å]	r_{O_I} [Å]	r_{VV} [Å]	σ [°]	θ [°]	b_{VV} [Å]
FM	16.408	13.836	6.842	1.657	2.085	2.007	3.435	132.95	175.31	0.311
SFM	16.311	13.914	6.851	1.654	2.095	1.991	3.439	132.70	175.81	0.309/0.302[a]
AF1	16.397	13.844	6.847	1.656	2.087	2.005	3.437	133.00	175.36	0.311
AF2	16.237	13.969	6.855	1.654	2.097	1.991	3.441	132.69	175.88	0.302
AF3	16.231	13.975	6.854	1.654	2.097	1.975	3.440	132.69	175.87	0.301
MIL-47 experimentally derived structure										
exp. [1]	16.143	13.939	6.818	1.672	2.108	1.970	3.422	129.4	176.10	0.302
exp.[b] [1]	17.519	12.168	6.875	1.947	1.947	1.995	3.438	123.98	180.00	0.000
exp.[c] [6]	16.062	13.991	6.808	1.671	2.108	1.968	3.418	129.17	176.10	0.303
exp. [44]	16.070	13.960	6.818	–	–	–	–	–	–	–
exp. [22]	17.434	13.433	6.620	–	–	–	–	–	–	–
vanadyl acetate										
exp. [78]	14.065	6.877	6.926	1.684	2.131	2.002	3.480	131.2	174.6	–

[a]ferromagnetic/anti-ferromagnetic chain.
[b]MIL-47(V) as-synthesized.
[c]MIL-47(V) loaded with *meta*-xylene.

coupling constants as will be shown in the following section (cf. section "Stability and magnetic coupling" and Table 3).

Table 2 shows that the VO_6 octahedra are asymmetrically distorted. The double bond at one apex ($r_{O_{c1}}$ = 1.65 Å) lies in the center of the range of lengths of normal V=O bonds (1.55–1.75 Å), while the V···O *trans* bond ($r_{O_{c2}}$) is at the lower end of the length range of such bonds (2.1–2.6 Å) [78]. The four bonds forming the plane of the octahedron (r_{O_l}) are about 0.1 Å shorter than the $r_{O_{c2}}$ bond, which are typical single V–O bond lengths. A further distortion of the octahedral configuration is found in the O=V···O angle (the octahedral backbone angle θ), which is about 5° smaller than the expected 180°, showing the octahedra to bend toward the central axis of the chain. The alternating bridge position of the organic linkers leads to the undulate nature of the chains, giving rise to a superexchange angle σ of about 133° (cf. section "Atomic charges and magnetization"). These two angles show how the competition between the linker bridges and the V=O···V bridges affects the orientation of the VO_6 octahedra in the chains; longer bond lengths (or weaker bonds) in the linker bridges will give rise to larger superexchange angles, changing the preference from antiferromagnetic to ferromagnetic interactions according to Goodenough rules [79].

Focusing on the local environment of the vanadyl chain in the MIL-47(V) MOF, one may wonder how strongly the nature of the linker influences the chain geometry. Removing the central four C atoms from the benzene ring, and protonating the dangling bonds of the remaining two C atoms, presents a system of vanadyl acetate chains, which are known to form in solvothermal reactions [78]. X-ray powder diffraction (XRPD) experiments (cf. Table 2) show these chains to have the exact same structure, suggesting that only the bridging part of the linker is of importance for the chain geometry.

In contrast to the structure parameters, the bulk modulus B_0 displays a clear variation with the spin configurations (cf. Table 1), starting at about 6 GPa for structures presenting ferromagnetic chains (FM and AF1) up to 8 GPa for structures containing antiferromagnetic chains (AF2 and AF3). These values are in agreement with the elastic parameters calculated by Ortiz et al. [80,81] for MIL-47, and of the same order of magnitude found for other MOFs [82,83]. The pressure derivative B_0' shows the same trend, i.e., it becomes larger (less negative) going from the ferromagnetic to the antiferromagnetic chains. Since the bulk modulus of a material is a measure for its resistance to deformation under an external pressure, and a negative pressure derivative (cf. B_0' in Table 1) indicates a breakdown of this resistance under an applied pressure, a qualitative picture emerges in which the MIL-47(V) is expected to collapse or show a structural phase transition under sufficiently large external pressure. As with other MOFs of this topology, which are known as breathing MOFs, these results suggest that the MIL-47(V) MOF should show breathing behavior. However, in this case the breathing is due to the application of an external pressure. This qualitative picture is in good agreement with recent experimental observations by Yot et al. [45]

Based on the experimental observation of hysteresis in the $P(V)$-behavior of the MIL-47(V) MOF [45], we know that the $P(V)$ relation should present an s-shape with a maximum at the large-pore-to-narrow-pore phase transition, and a minimum at the narrow-pore-to-large-pore phase transition (cf. Figure 2). By using the Rose–Vinet equation of state to generate the $P(V)$ relation of the large-pore MIL-47(V) MOF, the large-pore-to-narrow-pore transition pressure P_t and transition volume V_t are calculated for each of the five spin configurations (cf. Table 1). Note that for the narrow-pore-to-large-pore transition, an equation of states fit to narrow-pore structures would be required, which is beyond the scope of this work. Relating P_t to the spin configurations yields two interesting features: (i) ferromagnetic chains (FM and AF1) give rise to a significantly lower transition pressure than antiferromagnetic chains (AF2 and AF3), (ii) the transition pressure for a system containing both types of chains (SFM) is a (weighted) average of the transition pressures of the antiferromagnetic and ferromagnetic systems. This provides interesting opportunities for sensor applications, e.g., combined with guest-induced magnetic transitions [35].

The calculated transition pressures are in good agreement with previous force-field based molecular dynamics simulations, which found P_t = 137 MPa [45]. In contrast to these simulations, experimental Hg-intrusion measurements did not give a transition at one specific pressure. Instead, the transition spanned a broader range of pressures: P_t = 85–125 MPa [45]. This is in perfect agreement with our calculations and suggests the sample consists of grains with varying mixtures of ferromagnetic and antiferromagnetic chains: Systems that only contain ferromagnetic chains show a phase-transition from large pores to narrow pores already at 82 MPa, while mixed systems with ever larger fractions of antiferromagnetic chains show increasingly higher transition pressures, until the systems contain only antiferromagnetic chains, which have the highest transition pressure of 124 MPa. Alternately, in XRPD experiments at room temperature while using a diamond anvil cell the transition pressure range was found to begin at 178.1 MPa [45]. At that pressure, the XRPD experiments discerned two phases of which the large-pore phase had a unit cell volume of 1506.6 $Å^3$, which is in good agreement with the large-pore-form volumes V_t calculated in Table 1.

The differences in experimentally measured transition pressures were assigned to differences between the samples and the experimental conditions. In addition, it was suggested, based on XRPD, that different grain sizes may have different transition pressures, leading to a gradual transition of the entire sample [45].

In conclusion, the dependency of P_t on the spin configuration may provide insight in the relation between the ground state and the grain size. It is well-known that defects in a solid, such as grain boundaries, promote the presence of non-ground-state (sub)structures. When grains are, therefore, considered to consist of an internal bulk region surrounded by a surface shell region, it is natural for the MIL-47(V) MOF to assume that the internal region should (at low temperature) contain mainly antiferromagnetic chains (i.e., the ground state configuration). In contrast, ferromagnetic chains may dominate the surface region. In such case, smaller grains may have a larger ferromagnetic contribution, while large grains have a larger antiferromagnetic contribution. This might explain the experimentally observed range of P_t. However, additional theoretical and experimental studies are required to formulate a definite conclusion in this regard.

Stability and magnetic coupling

The spin configuration plays an important role in the stability of the system as is shown in Table 1. As is expected from magnetic measurements on MIL-47(V) [1] and magnetic susceptibility measurements on vanadyl acetate chains [78], an antiferromagnetic ground state is found, which is 70 meV per V atom more stable than the ferromagnetic state. Also note that the antiferromagnetic coupling of ferromagnetic chains (AF1) leads to a small improvement of the stability by 4 meV per V atom, showing that in addition to the intra-chain coupling of the V spin, an (albeit much weaker) inter-chain coupling is present as well.

To calculate the coupling interactions we have mapped the DFT energies onto a 1D Ising model:

$$H_s = -\sum_{i,j} J_{i,j} S_i S_j \ , \qquad (1)$$

with S_i being the spin operator projected along the z-direction and $J_{i,j}$ being the coupling interactions. Two coupling interactions are taken into account: the intra-chain coupling J_c, and the inter-chain coupling J_i (cf. Figure 1a). The V magnetic moment in the current systems can be obtained by projection of the electron density onto atomic orbitals. However, in such an approach the magnitude of the obtained moment will strongly depend on the projection operation. As such, we will take a pragmatic stance and use spin 1/2 based on the presence of a single unpaired electron for each of the V ions, and the observed spin 1/2 for vanadyl acetate chains [78].

Each of the five spin configurations gives rise to a slightly different eigenvalue of the spin-Hamiltonian H_s. By solving the overdetermined system of five equations (one for each configuration) using a least-squares fit, the coupling constants J_c and J_i are calculated. Table 3 shows both couplings to be antiferromagnetic in nature, with the inter-chain coupling being two orders of magnitude smaller than the intra-chain coupling. As a result, one expects the MIL-47(V) system to present (quasi-)1D behavior at low temperatures. The ratio of the coupling constants is much larger than those found for other MOFs (a factor of 5 was found for Cu-based perovskite MOFs [40], a factor of about 20 was found for MOF-74(X) with X = Co, Fe, Ni [36]). Our findings corroborate the suggestion of Barthelet et al. [1] that the antiferromagnetic behavior of the MIL-47(V) system stems from antiferromagnetic chains and not from antiferromagnetically ordered ferromagnetic chains. As a result, this also shows that the calculated superexchange angle of 133° is below the blank angle.

Table 3: Calculated coupling constants (in meV) based on the DFT-D3 energies by using the fully optimized geometries (DFT-D3), the pure DFT energies without D3 correction (DFT), and the DFT energies obtained by using the fixed AF3 ground-state atomic structure (DFT fix).

	DFT-D3	DFT	DFT fix
J_c	−135.28	−131.81	−144.57
J_i	−1.85	−1.59	−2.30

The coupling constants shown in Table 3 are rather large ($|J_c/k_B| \approx 1530$–1678 K), in contrast to the values suggested from experiments: $|J_c/k_B| = 275$ K for vanadyl acetate chains [78], and $|J_c/k_B| \approx 186$ K for MIL-47(V) [1]. This difference may have several reasons: (1) the experimental coupling constant is obtained from fitting a Curie–Weiss law to the linear high-temperature part of reciprocal magnetic susceptibility; (2) the choice of the DFT functional, e.g., based on LDA energies, not shown, the coupling constants are almost a factor of two larger. Also, Wang et al. [41] showed that the choice of the Hubbard U, in DFT+U calculations, significantly modifies the coupling constants.); (3) finite size effects (the calculated systems represent perfect infinite-size systems, while it was shown, for example, for vanadyl acetate chains that finite size contributions to the magnetization curve are significant [78]), and (4) the actual atomic structure used: Table 3 shows that the J_c coupling constant is about 10% smaller for geometries that are optimized while including the spin configuration. This

effect is even more pronounced for smaller coupling constants. This last point may also be important for other systems in which energy differences can be even smaller, which is often the case for quasi-1D spin configurations in MOFs.

Atomic charges and magnetization

Hirshfeld-I (HI) atoms-in-molecules (AIM) charges [67,69-71] have been calculated to provide a better understanding of the superexchange mechanism in the vanadium oxide chains and the influence of the spin configuration on the electron distribution. For all spin configurations, the calculated V charge is found to be 2.44*e* and 2.43*e* for antiferromagnetic and ferromagnetic chains, respectively. This shows that the same oxidation state is present in both cases. Comparison to V charges in MIL-47(V) MOFs with functionalized linkers shows exactly the same charge, indicative of a +IV oxidation state [22]. Note that, as is to be expected from Hirshfeld-I charges, these charges are significantly larger than Mulliken (1.207*e*) [51] or CHELPG (1.68*e*) [12] charges. Similarly, the O atoms in the ferromagnetic chains have a slightly larger negative charge (−1.01*e*) than their counterparts in the antiferromagnetic chains (−1.00*e*). In contrast, the O atoms in the plane of the VO_6 octahedra have an atomic charge of $-(0.73 \pm 0.01)e$ in line with their different bonding to the V atoms (cf. section "Structure and elastic behavior"). The same trends are also present in the calculated magnetization. For the V sites the magnetization is found to be slightly larger in ferromagnetic chains (≈0.9 μ_B) than in the antiferromagnetic chains (≈0.8 μ_B). However, both are indicative of a V^{4+} oxidation state. Interestingly, all O atoms in the vanadyl chains also show a small magnetization (0.06 and 0.08 μ_B in the antiferromagnetic and ferromagnetic chain, respectively) with a sign opposite to that of the magnetization of the nearest V atom (cf. Figure 3). Furthermore, also the in-plane O atoms present an even smaller opposing magnetization to the nearby V atom. From Figure 3 it is clear that the magnetization is localized (almost) entirely on the metal-oxide chains, in agreement with the relatively small inter-chain coupling. The induced magnetization supports the suggested presence of a superexchange mechanism. The larger charge and magnetization on the vanadyl O atoms presents a magnetic interaction pathway directly along the chain. Furthermore, the tilted nature of the magnetic orbitals increases their overlap, strengthening the antiferromagnetic interactions.

Electronic structure

The MIL-47(V) systems show a very rich band structure around the band gap due to the interaction of the unpaired V d-electrons. The high-symmetry lines of the first Brillouin zone of the orthorhombic MIL-47(V) cell used are shown in Figure 1b. For the configurations for which the total magnetization is non-zero (FM and SFM), majority and minority spin components have a different band gap, making them of interest for spintronic applications (cf. Table 4 and Figure 4a) [84]. In general, each of the configurations leads to at least one direct band gap, which is located at a different point of high symmetry (cf. Table 4). The electronic structures for the FM and AF3 configurations are shown as examples in Figure 4.

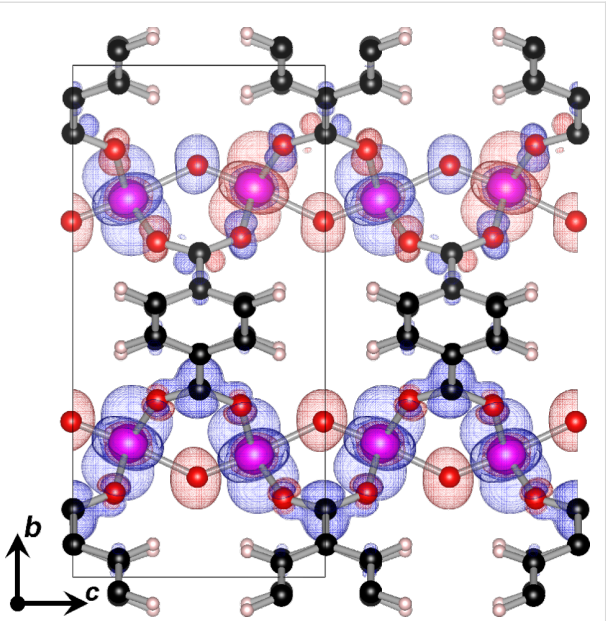

Figure 3: The spin density distribution of the SFM system. The upper chain has an antiferromagnetic spin configuration, while the lower chain has a ferromagnetic spin configuration. The iso-surface is taken at 0.00125, with majority spin shown in blue, and minority in red. The black rectangle indicates a single unit cell.

Table 4: Band structure features: the band gap size and the location of the direct band gap. Values for the minority spin component are given in brackets if they differ from the value for the majority spin component.

	band gap size [eV]	band gap location
FM	0.48	Γ
	(2.50)	(Γ)
SFM	0.50	Γ–X–Y plane
	(0.87)	(X and Y)
AF1	0.46	X and Y
AF2	0.92	Z
AF3	0.94	T

The valence and conduction bands (in the range [−1, +3] eV of the Fermi level) mainly have a V d-character, combined with a smaller fraction of O p-character, clearly showing these bands to originate from the VO_6 chains of the MOF. For the valence band the band character is, more specifically, $d_{x^2-y^2}$ combined with a small fraction of p_x and p_y character of the O atoms in

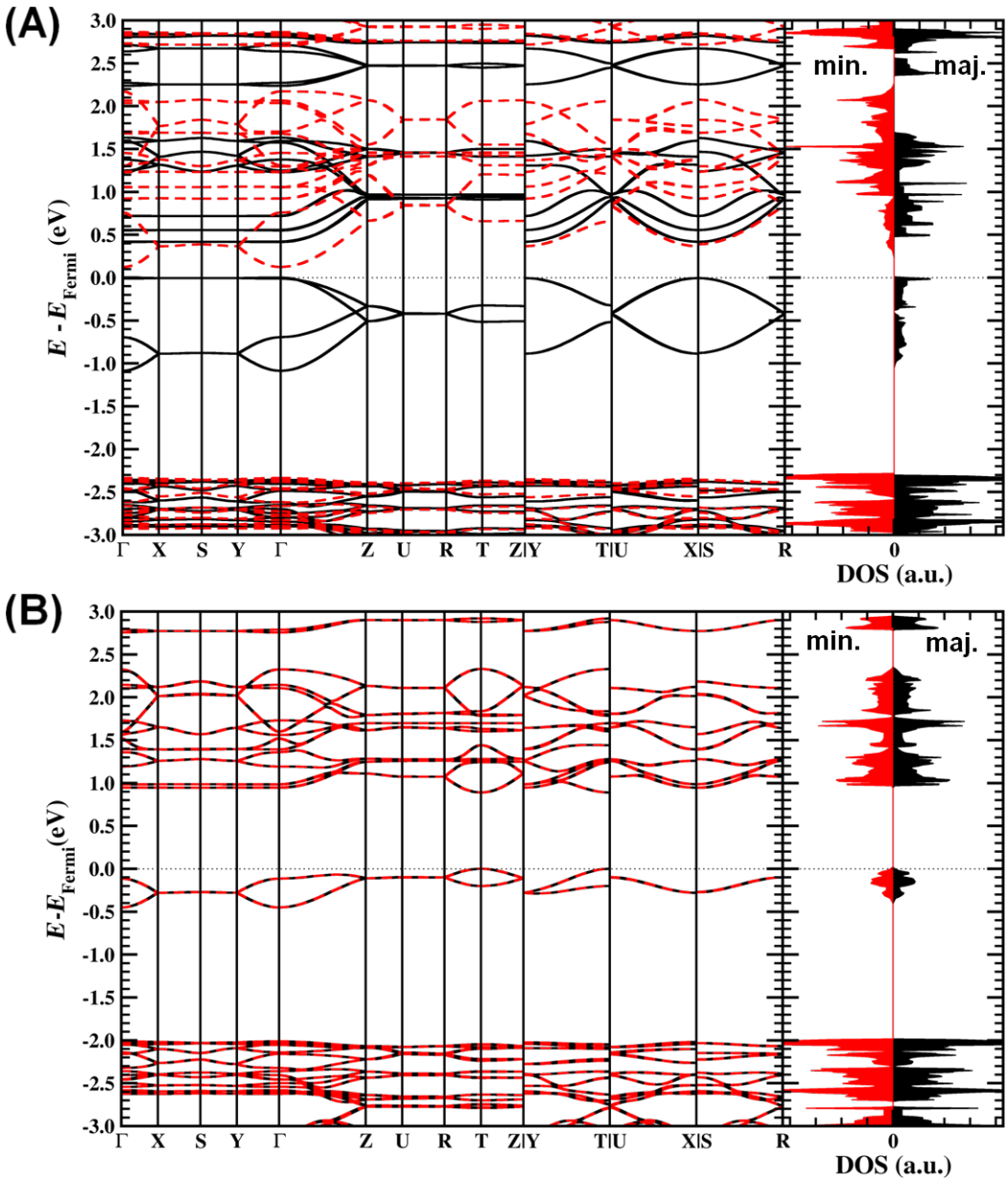

Figure 4: Band structure and density of states (DOS) near the Fermi level for the FM (A) and AF3 (B) spin configurations. Solid black/dashed red curves indicate the bands for the majority/minority spin components, respectively.

the planes of the octahedra. The lowest conduction bands, on the other hand, show complex combinations of different d-band characters combined with p-character of the O atoms. For the AF configurations the lowest conduction band at the band gap position always shows the same character makeup as the valence band. On the other hand, the second conduction band at these points is a mixture of d_{z^2}, d_{xy}, d_{xz}, and d_{yz} combined with p_x and p_y character of the O atoms in the vanadyl chains.

For all configurations, the valence and conduction bands along the high-symmetry lines split into two main groups: (1) For the high-symmetry lines parallel to the VO_6 chains the bands show a clear dispersion. For the antiferromagnetic chains this dispersion is much smaller than for the ferromagnetic chains showing the repulsion between parallel unpaired V d-electrons in the $d_{x^2-y^2}$ orbitals (cf. Figure 3). (2) The bands along the high-symmetry lines orthogonal to the VO_6 chain direction, on the other hand, are extremely flat (with some exceptions, see below). As a result, the majority spin band gap for the FM configuration consists of two flat parallel bands covering the entire Γ–X–Y plane of the Brillouin zone. Upon closer examination, there is, however, a very small band splitting at the Γ-point for

both the valence and the conduction band (about 20 meV in total) resulting in a direct band gap that is just marginally smaller than the band gap of the Γ–X–Y plane. This picture of dispersive bands parallel to a specific direction, and flat bands orthogonal to this direction is also found for other quasi-1D systems, such as atomic-scale nanowires [85]. This is another example of 1D behavior of the VO_6 chains in MIL-47(V). Of the second group of high-symmetry lines, the Γ–Y and Z–T lines are also interesting to consider, since the zigzag of the vanadyl chain is located in this plane. Only for the antiferromagnetic chains, the valence and the conduction band show a finite dispersion, while flat bands are present for the ferromagnetic chains.

Combined, this shows that in the MIL-47(V) system, conductivity is expected to be directed almost entirely along the VO_6 chains with the unpaired V d-electrons providing the current. The position of the direct band gap, depending on the spin configuration, makes this an interesting feature for experimental characterization, and validation of these results.

Conclusion

In this work, the geometric and electronic structure of MIL-47(V) is investigated by using first principles calculations. An antiferromagnetic ground state is found, consisting of antiferromagnetic chains with an antiferromagnetic inter-chain coupling. This supports the experimental assumption of such a ground state favored over an antiferromagnetic ordering of ferromagnetic chains [1]. The derived coupling constants point toward an antiferromagnetic coupling between the chains, albeit two orders of magnitude weaker than the intra-chain coupling. The atomic structure of the different spin configurations is found to be nearly indistinguishable. However, the resulting small geometry based contribution to the system energy results in significant variations in the derived coupling constants.

The electronic band structure and the spin density distribution further confirm the quasi-1D nature of the VO_6 chains in the MIL-47(V) MOF, with the conduction channel clearly located along the chain direction. Conduction and valence bands are found to exhibit almost perfectly flat bands along the high-symmetry lines orthogonal to the chains, which indicative of heavy-fermion behavior and reminiscent of the band structure of 1D systems.

The calculated bulk modulus and its pressure derivative show a clear relation between the spin configuration and the flexibility of the MIL-47(V) MOF, with antiferromagnetic chains increasing the bulk modulus significantly. By using the bulk modulus and its pressure derivative, the transition pressure for the large-pore-to-narrow-pore phase transition is derived and found to be in perfect agreement with experiments. The presence of 1D magnetic and electronic properties and the mechanic properties of the MIL-47(V) may provide interesting opportunities for sensing applications.

Supporting Information

Supporting information contains the spin-dependent optimized MIL-47(V) structures. These structures have also been deposited in the Cambridge Crystalographic Data Center database CCDC 1021380–1021384.

Supporting Information File 1

MIL-47(V) structure in the FM spin configuration.
[http://www.beilstein-journals.org/bjnano/content/supplementary/2190-4286-5-184-S1.cif]

Supporting Information File 2

MIL-47(V) structure in the SFM spin configuration.
[http://www.beilstein-journals.org/bjnano/content/supplementary/2190-4286-5-184-S2.cif]

Supporting Information File 3

MIL-47(V) structure in the AF1 spin configuration.
[http://www.beilstein-journals.org/bjnano/content/supplementary/2190-4286-5-184-S3.cif]

Supporting Information File 4

MIL-47(V) structure in the AF2 spin configuration.
[http://www.beilstein-journals.org/bjnano/content/supplementary/2190-4286-5-184-S4.cif]

Supporting Information File 5

MIL-47(V) structure in the AF3 spin configuration.
[http://www.beilstein-journals.org/bjnano/content/supplementary/2190-4286-5-184-S5.cif]

Acknowledgements

The authors acknowledge financial the support from the European Research Council for funding through the European Community's Seventh Framework Programme (FP7(2007-2013) ERC Grant Agreement 240483). D.E.P.V. is a postdoctoral researcher funded by the Foundation of Scientific Research-Flanders (FWO) (project no. 12S3415N). We also acknowledge the Research Board of Ghent University. The computational resources (Stevin Supercomputer Infrastructure) and services used in this work were provided by the VSC (Flemish Supercomputer Center), funded by Ghent University, the Hercules Foundation and the Flemish Government - department EWI.

References

1. Barthelet, K.; Marrot, J.; Riou, D.; Férey, G. *Angew. Chem., Int. Ed.* **2002,** *41,* 281–284. doi:10.1002/1521-3773(20020118)41:2<281::AID-ANIE281>3.0.CO;2-Y
2. Rosseinsky, M. *Microporous Mesoporous Mater.* **2004,** *73,* 15–30. doi:10.1016/j.micromeso.2003.05.001
3. Bourrelly, S.; Llewellyn, P. L.; Serre, C.; Millange, F.; Loiseau, T.; Férey, G. *J. Am. Chem. Soc.* **2005,** *127,* 13519–13521. doi:10.1021/ja054668v
4. Llewellyn, P. L.; Bourrelly, S.; Serre, C.; Filinchuk, Y.; Férey, G. *Angew. Chem., Int. Ed.* **2006,** *45,* 7751–7754. doi:10.1002/anie.200602278
5. Wang, X.; Liu, L.; Jacobson, A. J. *Angew. Chem., Int. Ed.* **2006,** *45,* 6499–6503. doi:10.1002/anie.200602556
6. Alaerts, L.; Kirschhock, C. E. A.; Maes, M.; van der Veen, M. A.; Finsy, V.; Depla, A.; Martens, J. A.; Baron, G. V.; Jacobs, P. A.; Denayer, J. F. M.; De Vos, D. E. *Angew. Chem., Int. Ed.* **2007,** *46,* 4293–4297. doi:10.1002/anie.200700056
7. Rosenbach, N.; Jobic, H.; Ghoufi, A.; Salles, F.; Maurin, G.; Bourrelly, S.; Llewellyn, P. L.; Devic, T.; Serre, C.; Férey, G. *Angew. Chem., Int. Ed.* **2008,** *47,* 6611–6615. doi:10.1002/anie.200801748
8. Murray, L. J.; Dincă, M.; Long, J. R. *Chem. Soc. Rev.* **2009,** *38,* 1294–1314. doi:10.1039/B802256A
9. Allendorf, M. D.; Bauer, C. A.; Bhakta, R. K.; Houk, R. J. T. *Chem. Soc. Rev.* **2009,** *38,* 1330–1352. doi:10.1039/B802352M
10. Yazaydın, A. O.; Snurr, R. Q.; Park, T.-H.; Koh, K.; Liu, J.; LeVan, M. D.; Benin, A. I.; Jakubczak, P.; Lanuza, M.; Galloway, D. B.; Low, J. J.; Willis, R. R. *J. Am. Chem. Soc.* **2009,** *131,* 18198–18199. doi:10.1021/ja9057234
11. Finsy, V.; Kirschhock, C. E. A.; Vedts, G.; Maes, M.; Alaerts, L.; De Vos, D. E.; Baron, G. V.; Denayer, J. F. M. *Chem. – Eur. J.* **2009,** *15,* 7724–7731. doi:10.1002/chem.200802672
12. Finsy, V.; Calero, S.; García-Pérez, E.; Merkling, P. J.; Vedts, G.; De Vos, D. E.; Baron, G. V.; Denayer, J. F. M. *Phys. Chem. Chem. Phys.* **2009,** *11,* 3515–3521. doi:10.1039/B822247A
13. Bueno-Pérez, R.; García-Pérez, E.; Gutiérrez-Sevillano, J. J.; Merkling, P. J.; Calero, S. *Adsorpt. Sci. Technol.* **2010,** *28,* 823–835. doi:10.1260/0263-6174.28.8-9.823
14. Gascon, J.; Kapteijn, F. *Angew. Chem., Int. Ed.* **2010,** *49,* 1530–1532. doi:10.1002/anie.200906491
15. Li, J.-R.; Sculley, J.; Zhou, H.-C. *Chem. Rev.* **2012,** *112,* 869–932. doi:10.1021/cr200190s
16. Khoshaman, A. H.; Bahreyni, B. *Sens. Actuators, B* **2012,** *162,* 114–119. doi:10.1016/j.snb.2011.12.046
17. Yoon, M.; Srirambalaji, R.; Kim, K. *Chem. Rev.* **2012,** *112,* 1196–1231. doi:10.1021/cr2003147
18. Yu, D.; Ghosh, P.; Snurr, R. Q. *Dalton Trans.* **2012,** *41,* 3962–3973. doi:10.1039/C2DT11908K
19. Kolokolov, D. I.; Jobic, H.; Stepanov, A. G.; Ollivier, J.; Rives, S.; Maurin, G.; Devic, T.; Serre, C.; Férey, G. *J. Phys. Chem. C* **2012,** *116,* 15093–15098. doi:10.1021/jp302995b
20. Sarkisov, L. *J. Phys. Chem. C* **2012,** *116,* 3025–3033. doi:10.1021/jp210633w
21. Llewellyn, P. L.; Bourrelly, S.; Vagner, C.; Heymans, N.; Leclerc, H.; Ghoufi, A.; Bazin, P.; Vimont, A.; Daturi, M.; Devic, T.; Serre, C.; Weireld, G. D.; Maurin, G. *J. Phys. Chem. C* **2013,** *117,* 962–970. doi:10.1021/jp308525k
22. Biswas, S.; Vanpoucke, D. E. P.; Verstraelen, T.; Vandichel, M.; Couck, S.; Leus, K.; Liu, Y.-Y.; Waroquier, M.; Van Speybroeck, V.; Denayer, J. F. M.; Van Der Voort, P. *J. Phys. Chem. C* **2013,** *117,* 22784–22796. doi:10.1021/jp406835n
23. Luttinger, J. M. *J. Math. Phys. (Melville, NY, U. S.)* **1963,** *4,* 1154–1162. doi:10.1063/1.1704046
24. Voit, J. *Rep. Prog. Phys.* **1995,** *58,* 977. doi:10.1088/0034-4885/58/9/002
25. Yeom, H. W.; Takeda, S.; Rotenberg, E.; Matsuda, I.; Horikoshi, K.; Schaefer, J.; Lee, C. M.; Kevan, S. D.; Ohta, T.; Nagao, T.; Hasegawa, S. *Phys. Rev. Lett.* **1999,** *82,* 4898–4901. doi:10.1103/PhysRevLett.82.4898
26. Gambardella, P.; Dallmeyer, A.; Maiti, K.; Malagoli, M. C.; Eberhardt, W.; Kern, K.; Carbone, C. *Nature* **2002,** *416,* 301–304. doi:10.1038/416301a
27. Nilius, N.; Wallis, T. M.; Ho, W. *Science* **2002,** *297,* 1853–1856. doi:10.1126/science.1075242
28. Snijders, P. C.; Rogge, S.; Weitering, H. H. *Phys. Rev. Lett.* **2006,** *96,* 076801. doi:10.1103/PhysRevLett.96.076801
29. Snijders, P. C.; Weitering, H. H. *Rev. Mod. Phys.* **2010,** *82,* 307–329. doi:10.1103/RevModPhys.82.307
30. Thielemann, B.; Rüegg, C.; Rønnow, H. M.; Läuchli, A. M.; Caux, J.-S.; Normand, B.; Biner, D.; Krämer, K. W.; Güdel, H.-U.; Stahn, J.; Habicht, K.; Kiefer, K.; Boehm, M.; McMorrow, D. F.; Mesot, J. *Phys. Rev. Lett.* **2009,** *102,* 107204. doi:10.1103/PhysRevLett.102.107204
31. Blumenstein, C.; Schäfer, J.; Mietke, S.; Meyer, S.; Dollinger, A.; Lochner, M.; Cui, X. Y.; Patthey, L.; Matzdorf, R.; Claessen, R. *Nat. Phys.* **2011,** *7,* 776–780. doi:10.1038/nphys2051
32. Nakatsuji, K.; Komori, F. *Nat. Phys.* **2012,** *8,* 174. doi:10.1038/nphys2240
33. Vanpoucke, D. E. P. *J. Phys.: Condens. Matter* **2014,** *26,* 133001. doi:10.1088/0953-8984/26/13/133001
34. Yeates, R. M.; Murdoch, M. J.; Southon, P. D.; Mclaughlin, A. C.; Howe, R. F.; Bonino, F.; Bordiga, S.; Damin, A. *Dalton Trans.* **2009,** 8025–8032. doi:10.1039/b908099f
35. Park, J.; Kim, H.; Jung, Y. *J. Phys. Chem. Lett.* **2013,** *4,* 2530–2534. doi:10.1021/jz4015103
36. Canepa, P.; Chabal, Y. J.; Thonhauser, T. *Phys. Rev. B* **2013,** *87,* 094407. doi:10.1103/PhysRevB.87.094407
37. Chen, X.; Wang, Y.-Y.; Liu, B.; Yin, B.; Liu, P.; Shi, Q.-Z. *Dalton Trans.* **2013,** *42,* 7092–7100. doi:10.1039/C3DT32556C
38. Eerenstein, W.; Mathur, N. D.; Scott, J. F. *Nature* **2006,** *442,* 759–765. doi:10.1038/nature05023
39. Cheong, S.-W.; Mostovoy, M. *Nat. Mater.* **2007,** *6,* 13–20. doi:10.1038/nmat1804
40. Stroppa, A.; Jain, P.; Barone, P.; Marsman, M.; Perez-Mato, J. M.; Cheetham, A. K.; Kroto, H. W.; Picozzi, S. *Angew. Chem., Int. Ed.* **2011,** *50,* 5847–5850. doi:10.1002/anie.201101405
41. Wang, Z.; Jain, P.; Choi, K.-Y.; van Tol, J.; Cheetham, A. K.; Kroto, H. W.; Koo, H.-J.; Zhou, H.; Hwang, J.; Choi, E. S.; Whangbo, M.-H.; Dalal, N. S. *Phys. Rev. B* **2013,** *87,* 224406. doi:10.1103/PhysRevB.87.224406
42. Sibille, R.; Lhotel, E.; Mazet, T.; Malaman, B.; Ritter, C.; Ban, V.; François, M. *Phys. Rev. B* **2014,** *89,* 104413. doi:10.1103/PhysRevB.89.104413
43. Serre, C.; Bourrelly, S.; Vimont, A.; Ramsahye, N. A.; Maurin, G.; Llewellyn, P. L.; Daturi, M.; Filinchuk, Y.; Leynaud, O.; Barnes, P.; Férey, G. *Adv. Mater.* **2007,** *19,* 2246–2251. doi:10.1002/adma.200602645

44. Leclerc, H.; Devic, T.; Devautour-Vinot, S.; Bazin, P.; Audebrand, N.; Férey, G.; Daturi, M.; Vimont, A.; Clet, G. *J. Phys. Chem. C* **2011,** *115,* 19828–19840. doi:10.1021/jp206655y
45. Yot, P. G.; Ma, Q.; Haines, J.; Yang, Q.; Ghoufi, A.; Devic, T.; Serre, C.; Dmitriev, V.; Férey, G.; Zhong, C.; Maurin, G. *Chem. Sci.* **2012,** *3,* 1100–1104. doi:10.1039/C2SC00745B
46. Coudert, F.-X.; Boutin, A.; Fuchs, A. H.; Neimark, A. V. *J. Phys. Chem. Lett.* **2013,** *4,* 3198–3205. doi:10.1021/jz4013849
47. Murdock, C. R.; Hughes, B. C.; Lu, Z.; Jenkins, D. M. *Coord. Chem. Rev.* **2014,** *258-259,* 119–136. doi:10.1016/j.ccr.2013.09.006
48. Mukherjee, G.; Biradha, K. *Chem. Commun.* **2014,** *50,* 670–672. doi:10.1039/C3CC48020H
49. Alhamami, M.; Doan, H.; Cheng, C.-H. *Materials* **2014,** *7,* 3198–3250. doi:10.3390/ma7043198
50. Wang, X.; Eckert, J.; Liu, L.; Jacobson, A. J. *Inorg. Chem.* **2011,** *50,* 2028–2036. doi:10.1021/ic1025087
51. Ramsahye, N. A.; Maurin, G.; Bourrelly, S.; Llewellyn, P. L.; Devic, T.; Serre, C.; Loiseau, T.; Férey, G. *Adsorption* **2007,** *13,* 461–467. doi:10.1007/s10450-007-9025-5
52. Devautour-Vinot, S.; Maurin, G.; Henn, F.; Serre, C.; Devic, T.; Férey, G. *Chem. Commun.* **2009,** 2733–2735. doi:10.1039/b822834e
53. Kolokolov, D.; Jobic, H.; Stepanov, A.; Plazanet, M.; Zbiri, M.; Ollivier, J.; Guillerm, V.; Devic, T.; Serre, C.; Férey, G. *Eur. Phys. J. Special Topics* **2010,** *189,* 263–271. doi:10.1140/epjst/e2010-01331-y
54. Blöchl, P. E. *Phys. Rev. B* **1994,** *50,* 17953–17979. doi:10.1103/PhysRevB.50.17953
55. Kresse, G.; Joubert, D. *Phys. Rev. B* **1999,** *59,* 1758–1775. doi:10.1103/PhysRevB.59.1758
56. Perdew, J. P.; Burke, K.; Ernzerhof, M. *Phys. Rev. Lett.* **1996,** *77,* 3865–3868. doi:10.1103/PhysRevLett.77.3865
57. Kresse, G.; Hafner, J. *Phys. Rev. B* **1993,** *47,* 558–561. doi:10.1103/PhysRevB.47.558
58. Kresse, G.; Furthmüller, J. *Phys. Rev. B* **1996,** *54,* 11169–11186. doi:10.1103/PhysRevB.54.11169
59. Monkhorst, H. J.; Pack, J. D. *Phys. Rev. B* **1976,** *13,* 5188–5192. doi:10.1103/PhysRevB.13.5188
60. Ghysels, A.; Vanpoucke, D. E. P.; Lejaeghere, K.; Van Speybroeck, V. to be submitted.
61. Walker, A. M.; Civalleri, B.; Slater, B.; Mellot-Draznieks, C.; Corà, F.; Zicovich-Wilson, C. M.; Román-Pérez, G.; Soler, J. M.; Gale, J. D. *Angew. Chem., Int. Ed.* **2010,** *49,* 7501–7503. doi:10.1002/anie.201002413
62. Grimme, S. *J. Comput. Chem.* **2006,** *27,* 1787–1799. doi:10.1002/jcc.20495
63. Grimme, S.; Antony, J.; Ehrlich, S.; Krieg, H. *J. Chem. Phys.* **2010,** *132,* 154104. doi:10.1063/1.3382344
64. Grimme, S.; Ehrlich, S.; Goerigk, L. *J. Comput. Chem.* **2011,** *32,* 1456–1465. doi:10.1002/jcc.21759
65. Dacosta, P. G.; Nielsen, O. H.; Kunc, K. *J. Phys. C: Solid State Phys.* **1986,** *19,* 3163–3172. doi:10.1088/0022-3719/19/17/012
66. Vinet, P.; Smith, J. R.; Ferrante, J.; Rose, J. H. *Phys. Rev. B* **1987,** *35,* 1945–1953. doi:10.1103/PhysRevB.35.1945
67. Bultinck, P. *Faraday Discuss.* **2007,** *135,* 347–365. doi:10.1039/b609640a
68. Bultinck, P.; Van Alsenoy, C.; Ayers, P. W.; Carbó-Dorca, R. *J. Chem. Phys.* **2007,** *126,* 144111. doi:10.1063/1.2715563
69. Vanpoucke, D. E. P. HIVE v2.1. http://dannyvanpoucke.be/ (accessed June 22, 2014).
70. Vanpoucke, D. E. P.; Bultinck, P.; Van Driessche, I. *J. Comput. Chem.* **2013,** *34,* 405–417. doi:10.1002/jcc.23088
71. Vanpoucke, D. E. P.; Van Driessche, I.; Bultinck, P. *J. Comput. Chem.* **2013,** *34,* 422–427. doi:10.1002/jcc.23193
72. Becke, A. D. *J. Chem. Phys.* **1988,** *88,* 2547–2553. doi:10.1063/1.454033
73. Lebedev, V. I.; Laikov, D. *Dokl. Math.* **1999,** *59,* 477–481.
74. Ozoliņš, V.; Körling, M. *Phys. Rev. B* **1993,** *48,* 18304–18307. doi:10.1103/PhysRevB.48.18304
75. Haas, P.; Tran, F.; Blaha, P.; Schwarz, K.; Laskowski, R. *Phys. Rev. B* **2009,** *80,* 195109. doi:10.1103/PhysRevB.80.195109
76. Vanpoucke, D. E. P.; Cottenier, S.; Van Speybroeck, V.; Bultinck, P.; Van Driessche, I. *Appl. Surf. Sci.* **2012,** *260,* 32–35. doi:10.1016/j.apsusc.2012.01.032
77. Lejaeghere, K.; Van Speybroeck, V.; Van Oost, G.; Cottenier, S. *Crit. Rev. Solid State Mater. Sci.* **2014,** *39,* 1–24. doi:10.1080/10408436.2013.772503
78. Weeks, C.; Song, Y.; Suzuki, M.; Chernova, N. A.; Zavalij, P. Y.; Whittingham, M. S. *J. Mater. Chem.* **2003,** *13,* 1420–1423. doi:10.1039/B208100H
79. Goodenough, J. B. *Magnetism, the chemical bond;* Interscience monographs on chemistry: Inorganic chemistry section; Interscience Publishers, 1963.
80. Ortiz, A. U.; Boutin, A.; Fuchs, A. H.; Coudert, F.-X. *Phys. Rev. Lett.* **2012,** *109,* 195502. doi:10.1103/PhysRevLett.109.195502
81. Ortiz, A. U.; Boutin, A.; Fuchs, A. H.; Coudert, F.-X. *J. Chem. Phys.* **2013,** *138,* 174703. doi:10.1063/1.4802770
82. Zhou, W.; Yildirim, T. *Phys. Rev. B* **2006,** *74,* 180301. doi:10.1103/PhysRevB.74.180301
83. Neimark, A. V.; Coudert, F.-X.; Triguero, C.; Boutin, A.; Fuchs, A. H.; Beurroies, I.; Denoyel, R. *Langmuir* **2011,** *27,* 4734–4741. doi:10.1021/la200094x
84. Žutić, I.; Fabian, J.; Das Sarma, S. *Rev. Mod. Phys.* **2004,** *76,* 323–410. doi:10.1103/RevModPhys.76.323
85. Vanpoucke, D. E. P.; Brocks, G. *Phys. Rev. B* **2010,** *81,* 085410. doi:10.1103/PhysRevB.81.085410

License and Terms

BEILSTEIN JOURNAL OF NANOTECHNOLOGY

High speed e-beam lithography for gold nanoarray fabrication and use in nanotechnology

Jorge Trasobares[*1], François Vaurette[*1], Marc François[1], Hans Romijn[2], Jean-Louis Codron[1], Dominique Vuillaume[1], Didier Théron[1] and Nicolas Clément[1]

Full Research Paper

Open Access

Address:
[1]Institut d'Electronique Microélectronique et Nanotechnologie (IEMN) CNRS, Avenue Poincaré, 59652, Villeneuve d'Ascq, France and [2]Vistec Lithography BV, De Dintel 27a, 5684 PS Best, The Netherlands

Email:
Jorge Trasobares[*] - jorge.trasobares@ed.univ-lille1.fr;
François Vaurette[*] - francois.vaurette@iemn.univ-lille1.fr

* Corresponding author

Keywords:
gold nanodot; gold nanoparticle; high-speed e-beam lithography; molecular electronics; nanoarray; self-assembled monolayers; XPS

Beilstein J. Nanotechnol. **2014,** *5,* 1918–1925.
doi:10.3762/bjnano.5.202

Received: 15 July 2014
Accepted: 30 September 2014
Published: 30 October 2014

This article is part of the Thematic Series "Molecular materials – towards quantum properties".

Guest Editor: M. Ruben

Abstract

E-beam lithography has been used for reliable and versatile fabrication of sub-15 nm single-crystal gold nanoarrays and led to convincing applications in nanotechnology. However, so far this technique was either too slow for centimeter to wafer-scale writing or fast enough with the so-called dot on the fly (DOTF) technique but not optimized for sub-15 nm dots dimension. This prevents use of this technology for some applications and characterization techniques. Here, we show that the DOTF technique can be used without degradation in dots dimension. In addition, we propose two other techniques. The first one is an advanced conventional technique that goes five times faster than the conventional one. The second one relies on sequences defined before writing which enable versatility in e-beam patterns compared to the DOTF technique with same writing speed. By comparing the four different techniques, we evidence the limiting parameters for the writing speed. Wafer-scale fabrication of such arrays with 50 nm pitch allowed XPS analysis of a ferrocenylalkyl thiol self-assembled monolayer coated gold nanoarray.

Introduction

Well-ordered arrays of nanoparticles are already showing exciting applications in nanotechnology, including materials science [1-5], electronics [6-10], biology [11-14] and information technology [14,15]. Combined top-down/bottom-up fabrication with versatile and well-controlled fabrication of gold nanoarrays coupled with (bio)molecules self-assembly offer great promises for fundamental research on molecular electronics [4,8] or high-throughput screening based on single-biomolecule arrays [12]. However, the top-down approach using e-beam lithography is actually too slow for fabricating dense gold nanoarrays at cm^2-scale, which precludes use of these technologies for some applications (mainly optics) or for

chemical characterization (such as XPS). Typically, fabrication of 1 cm^2 nanoarray of 10 nm gold NPs with 100 nm pitch requires 4 days of e-beam writing [1]. To overcome this problem, several alternative techniques are proposed [2,16-18]. The diblock-copolymer approach that consists of two chemically different polymer chains (or blocks) joined by a covalent bond is one of the most promising methods for low-cost and high speed fabrication of such gold nanoarrays [18]. However, to keep the versatility, well positioning and reliable nanoarray fabrication offered by e-beam lithography, another way is to notice that high-speed e-beam writing can be specifically developed for such nanoarray fabrication. Such high-speed e-beam technique called "dot-on-the-fly" (DOTF) has been previously developed for 25 nm diameter periodic metal patterns fabrication [19] and more recently for making 14 nm diameter holes for thermoelectricity application [20]. DOTF technique is however restricted to rectangle patterns. Here, we demonstrate that gold nanoarrays of sub-15 nm diameter, 50 nm pitch can be successfully fabricated either by the DOTF technique or by a new technique called "sequence method" allowing us XPS characterization of ferrocene-thiolated gold NPs prior molecular electronics study. We also propose an "advanced" conventional technique and discuss quantitatively the limiting parameter for each technique.

Conventional and fast e-beam fabrication of gold nanoarrays

The usual strategy for making these gold nanoarrays using e-beam lithography is to open nano-holes in a positive resist (see experimental section for details), evaporate gold and remove the resist with lift-off. The gold evaporation step is of great importance because the gold implantation inside the silicon substrate together with the diffusion process allows the formation of perfect gold nanocrystals after annealing (ideal truncated octahedron or cuboctahedron nanoparticles (NPs)) [1,4]. In addition, these NPs have an ohmic contact for the bottom electrode, which is of great importance for molecular electronics applications. For example, in [8], a conducting AFM tip (CAFM) is used as a top electrode and the gold nanocrystals act as bottom electrodes. Within a single CAFM image it is possible to get statistics on thousands of molecular junctions which allowed us, in particular, to evidence the presence of 2 phases of organization on alkyl-thiolated gold nanoparticles. In order to study more functional molecular junction (for example redox molecules), we need few mm-large gold nanoarray for chemical characterization with usual techniques such XPS. This requires high-speed e-beam lithography.

We first describe the relevant e-beam operation mechanisms (Figure 1a) that include specific parameters related to our e-beam writer (Vistec EBPG 5000+ operating at 100 keV, 20 bits). As the beam cannot be deflected over several mm, the layout has to be divided into main fields of up to 512 µm square at maximum. Inside this main field, the beam is deflected thanks to two sets of scanning coils: the main field coils and the subfields coils. Eventually, the efficient use of subfields (4 µm square at maximum) can lead to faster e-beam writing since settling times of subfield and mainfield coils are typically 0.5 µs and 40 µs, respectively. The procedure (path and exposure time) used by the e-beam is generated in real time using a pattern generator. This pattern generator is called for each shape (here we call shape one design to be written). This step, that also consumes time, can be optimized. The stage is moving from one main field to the other one for the complete layout writing. Below, we describe each of the proposed method for nanoarray fabrication (Figure 1b) and discuss their performance in the next section.

In the conventional method, we design a grating of 5 nm by 5 nm nanodots equivalent to the beam step size (BSS) of the machine. Thus, each dot is equivalent to a shape consisting on one pixel and then moved to the next shape again consisting of one pixel. Since each dot is considered as an independent shape, the pattern generator is called for each dot. The e-beam exposes the first dot with the desired dose and then moves to the second dot using the main field deflection. The process is repeated for the other dots. Another method presented, that we call "advanced conventional method", uses the subfield coils instead of the mainfield coils inside one subfield. In this last method, main coils are only used to go from one subfield to another one. Both of the conventional methods call the pattern generator for each dot because one dot is considered as one shape.

To overpass the pattern generator limitation, alternative high speed writing techniques are emerging. Firstly, with the called "dots on the fly" (DOTF) approach [19,20], compatible with the use of sub-fields, the array of dots layout is simplified to a single "big square" so as to generate the pattern only once. The main idea is that each pixel corresponds to the distance between dots. Technically, this can be achieved by increasing the BSS to the exact distance between dots (Figure 1b). This technique works because the beam dimension is around 10 nm whatever the BSS. This "big square" pattern, however, limits the patterns to rectangular array of dots within a single exposure. For example, the triangular structure, of importance to optimize the density of dots, may only be obtained by aligning several layouts.

The last method called "sequence method" that we introduce here for the gold nanodots array fabrication defines shapes as a series of lines and jumps with either beam "on" or "off" (See Supporting Information File 1 for the detailed code). In this way

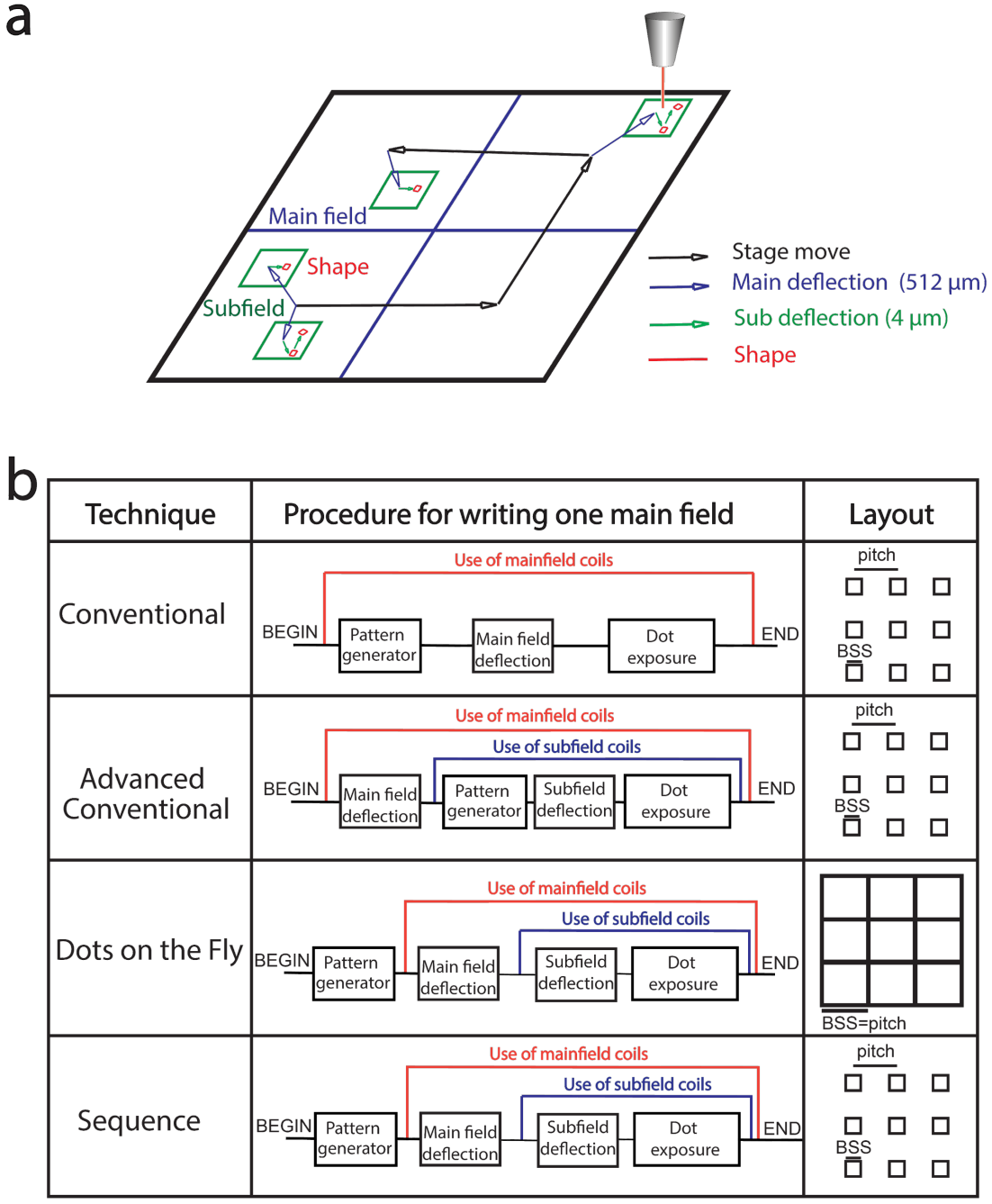

Figure 1: a) Schematic description of the writing strategy in e-beam lithography. The beam is deflected into a main field (≈512 µm) thanks to 2 sets of scanning coils, and to write a complete pattern, the stage moves from one main field to the other one. b) Schematic description of the 4 e-beam lithography techniques compared for their writing sequence inside a main field and their layout (BSS is the beam step size).

it is possible to define many dots as a single shape (ideally its dimension is that of a subfield) which can be repeated. As a consequence this method also reduces drastically the call to the pattern generator but with the additional flexibility to define the geometry of the shape (for example triangular array). Below, we demonstrate its efficiency for nanoarray fabrication.

Results and Discussion

Fabricated dots

Figure 2 shows scanning electron microscope (SEM) images of the gold nanoarray (dots 10–15 nm, pitch = 50 nm) fabricated by the "conventional" (Figure 2a), the "advanced conventional" (Figure 2b), the DOTF (Figure 2c) and the "sequence"

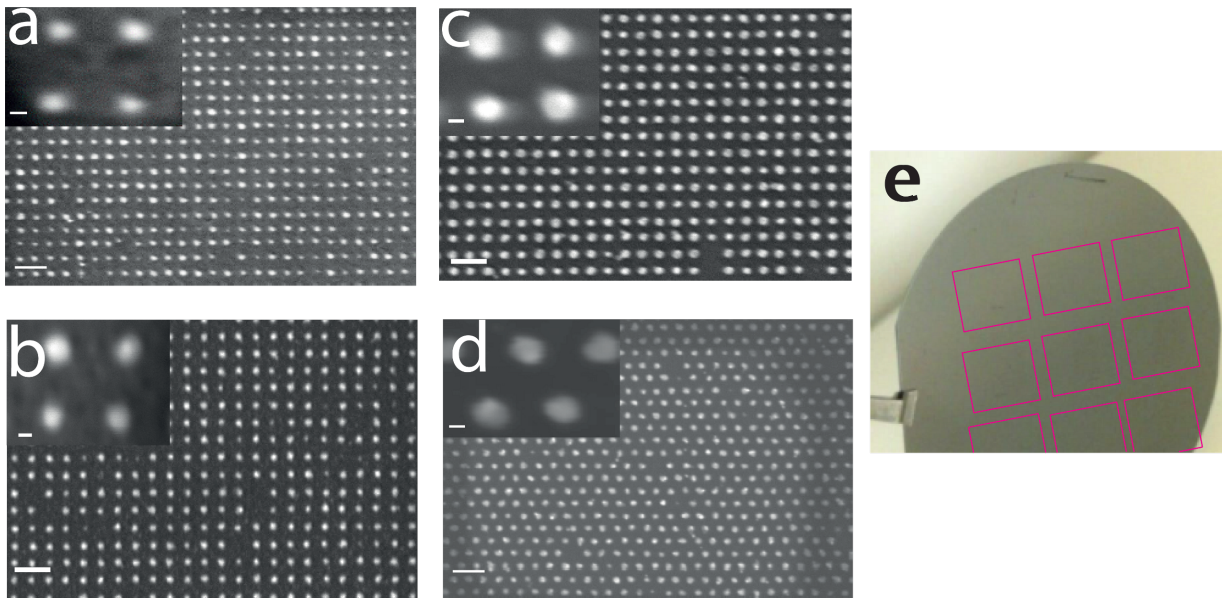

Figure 2: Scanning electron microscope (SEM) images of the gold nanodot arrays fabricated by (a) the "conventional" method with an exposure dose of 16000 μC/cm^2 (4 fC/dot), (b) the "advanced conventional" method with an exposure dose of 16000 μC/cm^2 (4 fC/dot) (c) the DOTF method with an exposure dose of 160 μC/cm^2 (4 fC/dot) (d) the "sequence" method with an exposure dose of 12000 μC/cm^2 (3.5 fC/dot). The beam current is set to 10 nA for the three techniques. The scale bar is 100 nm for the 4 SEM images and 10 nm for zoomed SEM images shown in inset. (e) Picture of a 3 inch wafer where 9 sequences of 1 cm^2 have been written using DOTF and "sequence" methods. Given the small contrast provided by the 8 nm thick gold nanoparticles, these arrays are indicated by pink squares.

(Figure 2d) techniques. We didn't notice significant difference in the fabricated gold nanoarrays. The dose per dot, corresponding to optimized nanodots (meaning less than 5% of missing dots and dots size below 15 nm), is similar for all the studied techniques: 3–4 fC/dot.

Comparison of e-beam writing time for the four methods

The inset of the Figure 3a shows the writing time normalized per dot for the four different techniques at a given e-beam current of 10 nA. We see a gain of two orders of magnitude in writing speed with both DOTF and "sequence" methods when compared to the conventional approach. Experimentally measured writing times for patterned square of width of 500 μm and 1 cm for high-speed lithography (100 nm-pitch) give a perfect match with the time per area (black points in Figure 3a). We can thus extrapolate time as a function of the size for all the techniques. Therefore, we plot in Figure 3a the estimated writing time as a function of nanoarray area for the four techniques. Whereas it would take 7 months for full wafer writing with the conventional method, it can take only ≈2 days with high-speed e-beam lithography. For molecular electronics application, chemical characterization of self-assembled monolayer coated gold nanoparticles is of prime importance, but it could not be achieved in [4,8] because a 1 cm^2 nanoarray is required for comfortable XPS analysis. Whereas it would have required almost one full week of writing, we have written such nanoarray in less than 2 hours. This time can even be reduced to 25 minutes (and to 17 hours for a full 3" wafer) if an e-beam current of 100 nA is selected with the high speed techniques (Figure 3a). A systematic study of the influence of e-beam current on the writing time per dot $t_{exp/dot}$ is shown in Figure 3b for the conventional and high speed techniques. These results can be satisfactorily explained with Equation 1:

$$t_{exp/dot} = \frac{(dose * area)}{current} + t_{overhead} \quad (1)$$

The first term corresponds to the exposure time and the second term to overhead time that includes mainfield, subfield settling times, pattern generator overhead and beam blanker. In the conventional method, the overhead time, mainly due to the mainfield settling (≈40 μs), is the limiting parameter (time per dot is equal to 46.6 μs, 42.3 μs and 41.7 μs for 1 nA, 10 nA and 100 nA, respectively). For the "advanced conventional method", that uses the subfield coils, the time per dot has been reduced down to ≈8 μs. As the settling time of the subfield coils are typically in the order of 500 ns, we attribute this overhead time to the pattern generator. On the opposite, with the DOTF technique, $t_{overhead}$ is negligible and a reasonable agreement with the experimental curve is obtained considering for example an e-beam current of 10 nA, an exposed area of 100 nm

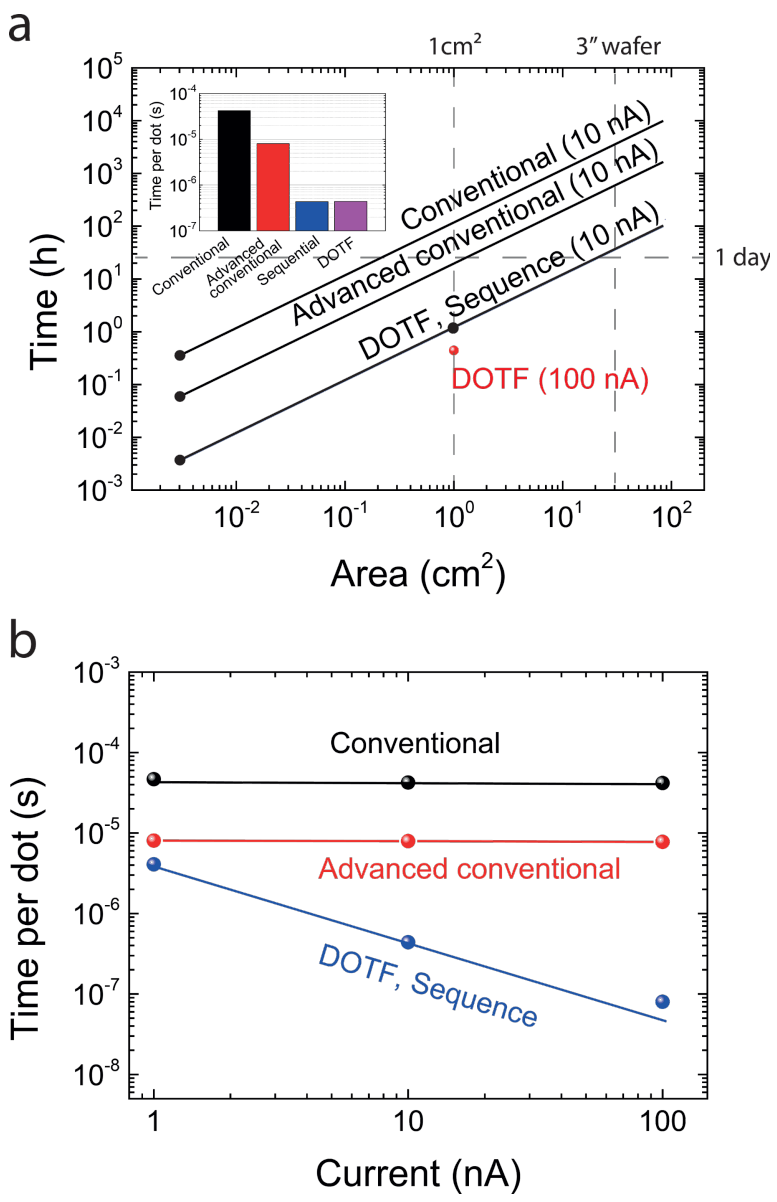

Figure 3: a) Plot of the estimated writing times per gold nanoarray area for each of the four different methods using an e-beam current of 10 nA and a pitch of 100 nm. Black points correspond to measured values. The writing time for DOTF technique with 100 nA is plotted for discussion. Inset: Equivalent writing time per dot for the four techniques. (b) Time per dot plotted as a function of the e-beam current for the four methods: ≈40 µs for the conventional method (limiting factor is the main field deflection) and ≈8 µs for the advanced conventional method (limiting factor is the pattern generator overhead). There is almost no overhead with DOTF and "sequence" methods, so the time is linear with the exposure time (inversely proportional to the current).

× 100 nm (corresponding to the distance between dots as explained previously) and a dose of 40 µC/cm^2 (also equivalent to 4 fC per dot). Interestingly simple linear dependence, proposed in Equation 1, matches relatively nicely because the limitation parameter is the exposure time. With this technique, the pattern generator overhead is not present anymore because only one shape is sent to the pattern generator at the beginning of the writing (see Figure 1b). As we increase the e-beam current to large values (≈100 nA), higher dose should, however, be considered due to an increased spot diameter. We also noticed an increase in dot size to ≈30 nm diameter. For the "sequence" method, the approach is basically the same as with the DOTF technique: define many dots as a single shape which can be repeated. This enables to reduce drastically the overhead for settling times of the beam by reducing the number of shapes. It has the additional flexibility to define the geometry of the shape (e.g., triangular array). The corresponding writing time is therefore exactly the same as for the DOTF technique.

As a consequence the actual limitation of the proposed high-speed writing technique is the resist exposure time. Recently, direct patterning of high density sub-15 nm gold dot array using ultrahigh contrast electron beam lithography process on positive tone resist has been demonstrated [21]. Combination of high contrast resist and high speed writing e-beam lithography may further improve nanoarray fabrication's speed.

XPS measurements

Using high-speed e-beam lithography with the "sequence" method, we have fabricated triangular nanoarrays of 1 cm^2 with 50 nm pitch (Figure 2d) to optimize the area with useful signal (dots) for XPS characterization. Details for XPS measurements can be found in the Experimental section. We have selected the Ferrocene-thiol electroactive molecule, an important model system for the formation of electronic devices based self-assembly and biological sensors. XPS spectra have been well studied for such SAMs on a gold substrate, which allows a direct comparison with the literature. A self-assembled monolayer (SAM) of 11-ferrocenyl-1-undecanethiol (FcC_{11})-coated gold nanoarray was characterized by XPS (Figure 4).

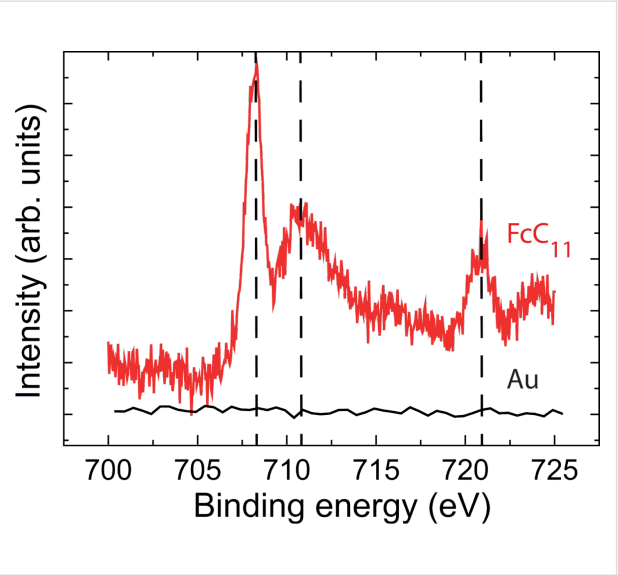

Figure 4: Fe 2p XPS spectra corresponding to the bare Au nanoarray and 11-ferrocenyl-1-undecanethiol (FcC_{11}) SAM from bottom to top.

The bare Au nanoarray shows no Fe 2p XPS signal confirming that the initial conditions prior to SAM formation corresponds to clean Au surface. XPS spectrum corresponding to the SAM with ferrocene (FcC_{11}) show a Fe $2p_{3/2}$ and Fe $2p_{1/2}$ doublet located at 707.8 eV and 720.7 eV. The position of the doublet is in excellent agreement with previously reported values for adsorbed ferrocene [22,23]. Even more interestingly, we see a doublet of the Fe $2p_{3/2}$ peak that corresponds to the signal of Fc at 707.8 eV and Fc in its reduced state given that the signal of the ferricinium cation is expected at 710.6 eV [23,24]. As a consequence, ferrocene and ferricinium species coexist on our gold nanoarray [24]. Among the possible origins of the oxidation of the ferrocene into ferricinium [24], the exposure to light, although minimized, is the most likely in our sample.

Conclusion

Gold nanoarrays with an ohmic contact to an highly doped silicon substrate fabricated by e-beam lithography have been proposed as a novel technique for molecular electronics study [1,4,8]. However, chemical characterization of the grafted molecules on these gold NPs could not be achieved because of the small patterned area limited by the e-beam writing time. Here, we have shown that a gain of 2 orders of magnitude in writing speed could be achieved for 10 nm dots and 3 orders of magnitude for 30 nm dots by optimizing a technique called "dot-on-the fly" and proposing a new "sequence" technique. A simple equation, proposed to explain the various parameters coming into play for e-beam writing, gave good agreement with our experimental datas. Using the "sequence" technique, we could successfully fabricate triangular pattern nanoarrays with dots every 50 nm at cm^2-scale and obtain the XPS spectrum of a ferrocenylalkylthiol-coated nanoarray. We found that ferrocene and ferricinium (oxidized state) coexist after the self-assembly process. The developed technology, which will surely be of great importance for molecular electronics study on such nanoarrays, also promising exciting future works in chemistry and biosensing.

Experimental

Nanoarray fabrication

As described in [1,8], for e-beam lithography, we use an EBPG 5000 Plus from Vistec Lithography. The (100) Si substrate (resistivity = 10^{-3} Ω·cm) is cleaned with UV/ozone and native oxide etched before resist deposition. The e-beam lithography has been optimized by using a 45 nm-thick diluted (3:5 with anisole) PMMA (950 K). For the writing, we use an acceleration voltage of 100 keV, which reduces proximity effects around the dots, compared to lower voltages. We played with different beam currents to expose the nanodots (from 1 nA to 100 nA) as discussed in the paper. Then, the conventional resist development/e-beam Au evaporation (8 nm)/lift-off processes are used. Immediately before evaporation, native oxide is removed with dilute HF solution to allow good electrical contact with the substrate. Single crystal Au nanodots can be obtained after thermal annealing at 260 °C during 2 h under N_2 atmosphere. At the end of the process, these nanodots are covered with a thin layer of SiO_2 that is removed by HF at 1% for 1 mn prior to SAM deposition. Spacing between Au nanodots is flexible and is typically set between 50 nm to 200 nm.

Self-assembled monolayer

As described in [1], for the SAM deposition, we exposed the freshly evaporated gold surfaces and nanodots to 1 mM solution of 11-ferrocenyl-1-undecanethiol (from Aldrich) in 80% ethanol (VLSI grade from Carlo Erba) 20% dichloromethane during 24 h in a glovebox in the darkness. Then, we rinsed the treated substrates with ethanol followed by a cleaning in an ultrasonic bath of chloroform (99% from Carlo Erba) during 1 min.

XPS

As described in [25], X-ray photoemmission spectroscopy (XPS) measurements have been performed using a Physical Electronics 5600 spectrometer. A monochromatic Al Kα X-ray source ($h\nu$ = 1486.6 eV) and an analyzer pass energy of 12 eV. The acceptance angle of the analyzer has been set to 14°, the detection angle was 45°, and the analyzed area was defined by an entrance slit of 400 μm.

Supporting Information

Supporting Information File 1

Detailed code for the "sequence method".
[http://www.beilstein-journals.org/bjnano/content/supplementary/2190-4286-5-202-S1.pdf]

Acknowledgements

The authors would like to thank Xavier Wallart for fruitful discussions on X-ray photoemission spectroscopy. J.T. PhD funding by a Marie curie grant, EU-FP7 Nanomicrowave project and Renatech (the French Network of major Technology Central).

References

1. Clément, N.; Patriarche, G.; Smaali, K.; Vaurette, F.; Nishiguchi, K.; Troadec, D.; Fujiwara, A.; Vuillaume, D. *Small* **2011,** *7,* 2541–2548. doi:10.1002/smll.201190065
2. Lee, S. H.; Jo, G.; Park, W.; Lee, S.; Kim, Y.-S.; Cho, B. K.; Lee, T.; Kim, W. B. *ACS Nano* **2010,** *4,* 1829–1836. doi:10.1021/nn100197u
3. Shin, D. O.; Lee, D. H.; Moon, S.-J.; Jeong, S.-J.; Kim, J. Y.; Mun, J. H.; Cho, H.; Park, S.; Kim, S. O. *Adv. Funct. Mater.* **2011,** *21,* 201–207. doi:10.1002/adfm.201090119
4. Smaali, K.; Desbief, S.; Foti, G.; Frederiksen, T.; Sanchez, D.; Andres, A.; Leclère, P.; Vuillaume, D.; Clément, N. "On the Mechanical and Electronic Properties of Thiolated Gold Nanocrystals". To be submitted for publication.
5. Schaal, P. A.; Simon, U. *Beilstein J. Nanotechnol.* **2013,** *4,* 336–344. doi:10.3762/bjnano.4.39
6. Balcells, L.; Abad, L.; Rojas, H.; Perez del Pino, A.; Estrade, S.; Arbiol, J.; Peiro, F.; Martínez, B. *Small* **2008,** *4,* 365–371. doi:10.1002/smll.200700537
7. Mäder, T.; Höche, T.; Gerlach, J. W.; Perlt, S.; Dorfmüller, J.; Saliba, M.; Vogelgesang, R.; Kern, K.; Rauschenbach, B. *Nano Lett.* **2010,** *10,* 47–51. doi:10.1021/nl903633z
8. Smaali, K.; Clément, N.; Patriarche, G.; Vuillaume, D. *ACS Nano* **2012,** *6,* 4639–4647. doi:10.1021/nn301850g
9. Jett, J. E.; Lederman, D.; Wollenberg, L. A.; Li, D.; Flora, D. R.; Bostick, C. D.; Tracy, T. S.; Gannet, P. M. *J. Am. Chem. Soc.* **2013,** *135,* 3834–3840. doi:10.1021/ja309104g
10. Wang, F.; Clément, N.; Ducatteau, D.; Troadec, D.; Tanbakuchi, H.; Legrand, B.; Dambrine, G.; Théron, D. *Nanotechnology* **2014,** *25,* 405703. doi:10.1088/0957-4484/25/40/405703
11. Liu, P.; Sun, J.; Huang, J.; Peng, R.; Tang, J.; Ding, J. *Nanoscale* **2010,** *2,* 122–127. doi:10.1039/b9nr00124g
12. Palma, M.; Abramson, J. J.; Gorodetsky, A. A.; Penzo, E.; Gonzalez, R. L.; Sheetz, M. P.; Nuckolls, C.; Hone, J.; Wind, S. J. *J. Am. Chem. Soc.* **2011,** *133,* 7656–7659. doi:10.1021/ja201031g
13. Pi, F.; Dillard, P.; Limouzin, L.; Charrier, A.; Sengupta, K. *Nano Lett.* **2013,** *13,* 3372–3378. doi:10.1021/nl401696m
14. Guilles, S.; Winter, S.; Michael, K. E.; Meffert, S. H.; Li, P.; Greben, K.; Simon, U.; Offenhäusser, A.; Mayer, D. *Small* **2012,** *8,* 3357–3367. doi:10.1002/smll.201200465
15. Huang, J.-S.; Callegari, V.; Geisler, P.; Brüning, C.; Kern, K.; Prangsma, J. C.; Wu, X.; Feichtner, T.; Ziegler, J.; Weinmann, P.; Kamp, M.; Forchel, A.; Biagioni, P.; Sennhauser, U.; Hecht, B. *Nat. Commun.* **2010,** *1,* 150. doi:10.1038/ncomms1143
16. Barcelo, S. J.; Lam, S.-T.; Gibson, G. A.; Sheng, X.; Henze, D. *Proc. SPIE* **2012,** *8323,* 83232L. doi:10.1117/12.916600
17. Park, M.; Harrison, C.; Chaikin, P. M.; Register, R. A.; Adamson, D. H. *Science* **1997,** *276,* 1401–1404. doi:10.1126/science.276.5317.1401
18. Pearson, A. C.; Pound, E.; Wooley, A. T.; Linford, M. R.; Harb, J. N.; Davis, R. C. *Nano Lett.* **2011,** *11,* 1981–1987. doi:10.1021/nl200306w
19. Gadegaard, N.; Thoms, S.; Macintyre, D. S.; Mcghee, K.; Gallagher, J.; Casey, B.; Wilkinson, C. D. W. *Microelectron. Eng.* **2003,** *67–68,* 162–168. doi:10.1016/S0167-9317(03)00067-4
20. Lacatena, V.; Haras, M.; Robillard, J.-F.; Monfray, S.; Skotnicki, T.; Dubois, E. *Microelectron. Eng.* **2014,** *121,* 131–134. doi:10.1016/j.mee.2014.04.034
21. Tobing, L. Y. M.; Tjahjana, L.; Zhang, D. H. *Nanotechnology* **2013,** *24,* 075303. doi:10.1088/0957-4484/24/7/075303
22. Woodbridge, C. M.; Pugmire, D. L.; Johnson, R. C.; Boag, N. M.; Langell, M. A. *J. Phys. Chem. B* **2000,** *104,* 3085–3093. doi:10.1021/jp993235+
23. Méndez De Leo, L. P.; de la Llave, E.; Scherlis, D.; Williams, F. J. *J. Chem. Phys.* **2013,** *138,* 114707. doi:10.1063/1.4795575
24. Umaña, M.; Rolison, D. R.; Nowak, R.; Daum, P.; Murray, R. W. *Surf. Sci.* **1980,** *101,* 295–309. doi:10.1016/0039-6028(80)90623-8
25. Clément, N.; Guérin, D.; Pleutin, S.; Godey, S.; Vuillaume, D. *J. Phys. Chem. C* **2012,** *116,* 17753–17763. doi:10.1021/jp3018106

BEILSTEIN JOURNAL OF NANOTECHNOLOGY

Towards bottom-up nanopatterning of Prussian blue analogues

Virgile Trannoy[1], Marco Faustini[2], David Grosso[2], Sandra Mazerat[1], François Brisset[1], Alexandre Dazzi[3] and Anne Bleuzen[*1]

Full Research Paper

Open Access

Address:
[1]Institut de Chimie Moléculaire et des Matériaux d'Orsay,UMR CNRS 8182, Université Paris-Sud, 15 rue Georges Clémenceau, 91405 Orsay Cedex, France, [2]Laboratoire de Chimie de la Matière Condensée de Paris, Université Pierre et Marie Curie-Paris 6 and CNRS Collège de France, 11 place Berthelot 75231 Paris, France and [3]Laboratoire de Chimie Physique, UMR CNRS 8000, Université Paris-Sud, 15 avenue Jen Perrin, 91405 Orsay Cedex, France

Email:
Anne Bleuzen[*] - anne.bleuzen@u-psud.fr

* Corresponding author

Keywords:
nanopatterning; nanoperforated oxide monolayer; Prussian blue analogues

Beilstein J. Nanotechnol. **2014,** *5,* 1933–1943.
doi:10.3762/bjnano.5.204

Received: 30 June 2014
Accepted: 08 October 2014
Published: 31 October 2014

This article is part of the Thematic Series "Molecular materials – towards quantum properties".

Guest Editor: M. Ruben

Abstract

Ordered nanoperforated TiO_2 monolayers fabricated through sol–gel chemistry were used to grow isolated particles of Prussian blue analogues (PBA). The elaboration of the TiO_2/CoFe PBA nanocomposites involves five steps. The samples were characterized by scanning electron microscopy (SEM), atomic force microscopy (AFM), infrared spectroscopy and X-ray photoelectron spectroscopy (XPS) all along the synthesis process. Selected physico-chemical parameters have been varied in order to determine the key steps of the synthesis process and to optimize it. This study is an important step towards the full control of the fabrication process.

Introduction

The development of methods to place nanoparticles into spatially well-defined, ordered arrays is one challenging aspect of nanotechnology. This is usually achieved by using top-down approaches, implementing optical and electron beam lithography. Here, we explore the possibilities of elaborating nanopatterned surfaces by a pure bottom-up approach.

The nanopatterned surfaces are mainly built from molecular precursors in solution through a succession of chemical steps. The advantages of this approach are very low fabrication costs, and easy adaptability of the fabrication process to the industrial scale. Our synthesis process is based on two main chemistries. The positioning of the functional objects and their isolation from each other is realized thanks to the exceptional processing flexibility inherent to sol–gel chemistry combined with organic templating agents. Coordination chemistry allowing for the controlled assembly of a large variety of transition metal building units is preferred to build the functional compound.

Prussian blue analogs (PBAs) are interesting for the design of bistable compounds for two reasons. Firstly, some of them are molecular magnets with an ordering magnetic temperature that can exceed room temperature [1,2]. Secondly, some PBAs exhibit a photomagnetic effect [3,4]. Thus, in some CoFe Prussian blue analogs, an irradiation in the visible range transforms a diamagnetic state into a ferrimagnetic state with a long life time. This photomagnetic effect is interesting for high-density storage since the property of bistability is intrinsically molecular and therefore persists up to molecular scale [5-8]. These coordination polymers are obtained by a reaction between hexacyanometalates and hydrated cations of the transition metal series in aqueous solution. The resulting solid exhibits the well-known face centered cubic structure of Prussian blue [9].

The sol–gel process is a method for producing metal oxides from small molecules via inorganic polymerization reactions in solution. The sol–gel transition allows one to obtain the oxide in any desired shape including films, fibers, monolithes [10]. Furthermore, the addition of self-assembling liquid crystalline templates to the sol can lead to the ordered nanostructuration of the oxide matrix [11]. Thus, nanoperforated thin layers, exhibiting hexagonal arrays of nanoperforations aligned perpendicular to the surface of the film surface have been developed [12,13]. These nanoperforated films are particularly appealing to organize isolated bistable dots on a solid surface [14,15].

The elaboration of the oxide/Prussian blue analogue nanocomposite involves five main steps, which have been described elsewhere for the fabrication of nanometer-scale patterns of photoswitchable PBA [15]. The substrate is first covered with a gold layer through sputtering, which will allow for the chemical differentiation of the surfaces and therefore their selective functionalization in the following. The second step is the deposition through dip-coating of an ethanolic solution of titanium molecular species containing block copolymers to obtain an ordered nanostructured organic–inorganic hybrid layer. The third step is a thermal treatment, which induces the decomposition of the organic part and the crystallization of the titanium dioxide leading to the nanoperforated layer. The fourth step is the selective functionalization of the surfaces to localize the PBA growth within the perforations while avoiding its formation outside. The last step is the PBA growth by a layer-by-layer directed assembly approach inspired from methods already implemented for the synthesis of PBA thin films [16-18].

Here, we study the impact of each step on the structure of the nanocomposite. We show that the first gold layer can undergo some changes in the course of the fabrication process and has to be optimized in order to obtain well-ordered nanoperforated oxide layers. We also show that the density of filled perforations strongly depends on physico-chemical parameters used for the PBA growth step, which turns out to be the trickiest step of the elaboration process.

Experimental

Synthesis of the TiO_2/PBA nanocomposite

The five steps involved in the fabrication of the PBA/TiO_2 nanocomposites are the following [15]: In a first step, the silicon substrate is covered by a gold layer by sputtering under vacuum in a sputter coater (Quorum, Q150T ES) for use in scanning electron microscopy. This gold layer will allow for the chemical differentiation of the surfaces in the following. Layers having thicknesses of 10 nm, 20 nm and 50 nm were deposited under an electric current of 30 mA during calibrated times (30 s, 60 s and 150 s). The three samples resulting from this first step and corresponding to the different thicknesses are called **Au10**, **Au20** and **Au50** in the following (see below in Table 1).

The second step is the deposition by dip-coating of an ethanolic solution of titanium molecular species containing block copolymers micelles that after evaporation are self-assembled to obtain an ordered nanostructured organic–inorganic hybrid layer. The solution for dip-coating was prepared by dissolving 37.5 mg of polybutadiene-*block*-poly(ethylene oxide) (M_w(PB) = 22000 g·mol^{-1}, M_w(PEO) = 15500 g·mol^{-1}) in 9.85 g of EtOH and 0.5 g of H_2O at 70 °C for 2 h. It was added then 0.27 g of an ethanolic solution of $TiCl_4$ (molar ratio 1:5) [12,19]. The deposition of the film was performed under controlled conditions of temperature of the chamber (80 °C), of ascent speed (2 mm/s) and of humidity rate (<2%).

The third step is a thermal treatment under an IR-lamp at 450 °C over 5 min, which results in the decomposition of the organic part and the crystallization of the titanium dioxide leading to the nanoperforated layer (ca. 15 nm) with homogeneous and ordered holes (50 nm in diameter) giving access to the gold layer underneath (Scheme 1) [15]. The three samples resulting from this third step and corresponding to the three different thicknesses of the gold layer are called **Au10NC**, **Au20NC** and **Au50NC** in the following (see below in Table 1).

The fourth step is the selective functionalization of the surfaces. In order to prevent the formation of PBA outside the nanoperforations, the TiO_2 surface was passivated by grafting with hydrophobic groups. The sample was placed in a solution of phenylphosphonic acid ($3\cdot10^{-3}$ M) in an ethanol/water mixture (3:1 EtOH/H_2O) for 12 h. The film was rinsed with EtOH and acetone and allowed to dry at 120 °C for 2 h. Then, an anchoring layer for PBA was grafted onto the gold bottom of the nanoperforations by dipping the substrate in an ethanolic

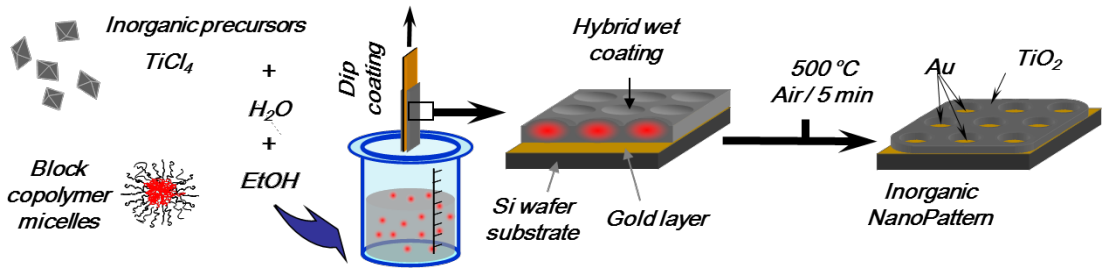

Scheme 1: Fabrication of the nanoperforated TiO_2 layer (steps 2 and 3).

solution of mercaptohexanoic acid ($3{\cdot}10^{-3}$ M), 4-mercaptopyridine ($3{\cdot}10^{-3}$ M) or 4-aminothiophenol ($3{\cdot}10^{-3}$ M) for 12 h. Mercaptohexanoic acid, 4-mercaptopyridine or 4-aminothiophenol are abbreviated as MHA, 4-MPy and 4-ATP, respectively, in the following. The film was rinsed with EtOH and water. Scheme 2 shows the successive functionalization steps of the film in the case of the MHA anchorage [20,21].

The last step is the PBA growth through a layer-by-layer approach consisting of successive immersions of the functionalized substrate in PBA precursor solutions. The substrate was first immersed in a hexaaquacobalt(II) solution for 12 h. Then, it was successively immersed for 2 min in a $3{\cdot}10^{-3}$ M $[Fe(CN)_6]^{3-}$ aqueous solution and in a 10^{-1} M $[Co(H_2O)_6]^{2+}$ aqueous solution. The substrate was carefully rinsed with water after each immersion. The sample was dipped 15 times in both solutions (Scheme 3) [15].

The same protocol was carried out while replacing the water solvent with i) butanol for the Co^{2+} solution and ethanol/water (1:1 EtOH/H_2O) for the $[Fe(CN)_6]^{3-}$ solution and ii) ethanol/water (1:1 EtOH/H_2O) for the Co^{2+} solution and for the $[Fe(CN)_6]^{3-}$ solution. The name and the conditions used for the preparation of the samples resulting from this fifth step are gathered in Table 1 (**NC01**–**NC05**).

Materials characterization

SEM images were obtained by using a field emission gun scanning electron microscope (FEG-SEM Zeiss Sigma HD microscope) equipped with an in-lens detector working at 1 kV and at a short working distance (WD) equal to 3.3 mm for the TiO_2 thin film images and equipped with a secondary electron detector (SE) working at 1 kV and at a short working distance (WD) equal to 3.8 mm for the TiO_2/PBA nanocomposite images. Tapping mode topography and phase imaging was

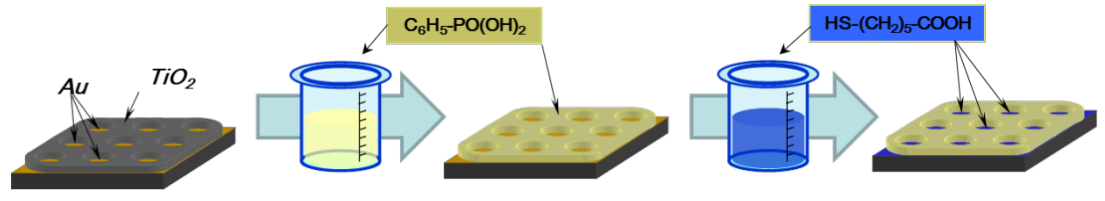

Scheme 2: Selective functionalization of the TiO_2 and gold surfaces (step 4).

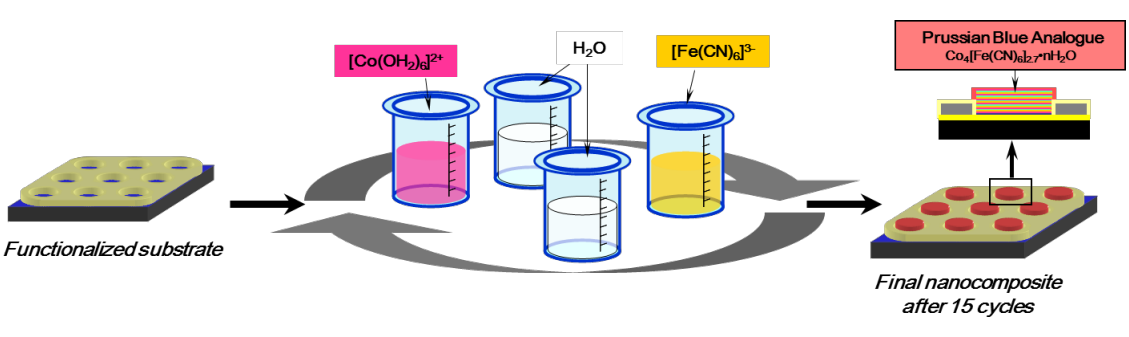

Scheme 3: Layer-by-layer PBA growth (step 5).

Table 1: Conditions used for the preparation of the different samples.

name of the sample	thickness of the gold layer/nm	TiO_2 deposition	gold functionalization	solvent or mixture of solvents for the PBA precursor solution	
				Co^{2+}	$[Fe(CN)_6]^{3-}$
Au10	10	—	—	—	—
Au20	20	—	—	—	—
Au50	50	—	—	—	—
Au10NC	10	×	—	—	—
Au20NC	20	×	—	—	—
Au50NC	50	×	—	—	—
NC01	20	×	MHA	H_2O	H_2O
NC02	20	×	4-ATP	H_2O	H_2O
NC03	20	×	4-MPy	H_2O	H_2O
NC04	20	×	MHA	BuOH	EtOH/H_2O = 1:1
NC05	20	×	MHA	EtOH/H_2O = 1:1	EtOH/H_2O = 1:1

accomplished by using an Innova AFM (Bruker) with NanoDrive v8.02 software. Tapping mode images were acquired by using silicon tips from Nanosensors (PPP NCSTR) with a resonance frequency ranging between 76 and 263 kHz. Images were processed by using WsXM software. Fourier transform-infrared (FTIR) spectra were collected in the attenuated total reflection (ATR) mode by using a Vertex 70 spectrometer with a germanium crystal. XPS spectra were collected on a SPECS (Phoibos MCD 150) X-ray photoelectron spectrometer, by using Mg Kα ($h\nu$ = 1253.6 eV) X-ray source having a 150 W (12 mA, 12.5 kV) electron beam power and a 7 × 20 mm spot size. The emissions of photoelectrons from the sample were analyzed at a takeoff angle of 90° under ultra-high vacuum conditions ($1 \cdot 10^{-8}$ Pa). High resolution spectra were collected at a pass energy of 10 eV for S 2p core XPS levels. No charge compensation was applied during acquisition.

Results and Discussion

The gold layer

The silicon wafer and the samples **Au10**, **Au20** and **Au50** were studied by AFM. Representative AFM images are shown in Figure 1. After gold deposition, whatever the deposition time, the silicon substrate is completely and homogeneously covered by gold nanoparticles (as expected for sputtering deposition). But, the size of the particles depends on the deposition time. The gold layers obtained with 30 s, 60 s and 150 s deposition time are composed of gold nanoparticles of 10 nm, 15 nm and 40 nm in diameter, respectively. The roughness is 0.27 nm for the silicon substrate, 0.44 nm for the 10 nm thick gold layer, 0.48 nm for the 20 nm thick gold layer and 1.01 nm for the 50 nm thick one. After the gold deposition, the surfaces exhibit a small roughness and are therefore of good quality for the nanoperforated oxide layer deposition.

The nanoperforated TiO_2 monolayer

The nanoperforated TiO_2 monolayer deposited on the silicon wafer covered by a 10 nm thick gold layer (sample **Au10**) was studied by AFM and SEM. Representative AFM and SEM images are shown in Figure 2a and Figure 2b. Two different kinds of zones can be observed on the AFM and SEM pictures. Some lighter islands appear on the darker background. The fraction of the light areas can be estimated to be around 40%. The dark spots correspond to nanoperforations aligned perpendicularly to the surface. Their depth has been estimated to be 15 nm and their diameter to be 50 nm (Figure S1 in Supporting Information File 1). The distance between two adjacent nanoperforations is 80 nm. Whatever the area, light or dark, the 2D-hexagonal organization of the perforations is visible. This indicates

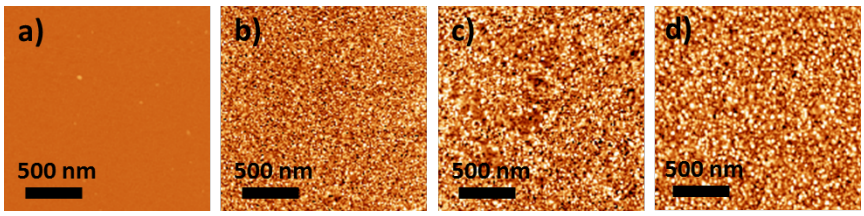

Figure 1: AFM images of a) the Si substrate b) **Au10**, c) **Au20** and d) **Au50**.

that the nanoperforated oxide film covers the whole surface. The two kinds of zones have been assigned to areas with and without gold between the silicon substrate and the perforated oxide layer. Figure 2c and Figure 2d show the depth distribution histogram in the dark and light areas of the AFM image. This AFM study indicates that the bright zones have higher relief (up to 80 nm above the silicon wafer) with a wide height distribution. In contrast, the depth distribution histogram in dark areas shows a narrow distribution centered around 15 nm corresponding to the thickness of the TiO_2 nanoperforated layer. This suggests a dewetting of the gold layer from the silicon surface to form gold droplets between the silicon wafer and the nanoperforated oxide layer corresponding to the light areas. The bottom of the nanoperforations in the dark areas would therefore be made of silicon rather than of gold. This hypothesis has been confirmed by energy dispersive X-ray analysis (EDX) performed in a bright and in a dark area. The results clearly show the presence of gold in the bright area, whereas this element is absent in the dark area (Figure S2 in Supporting Information File 1).

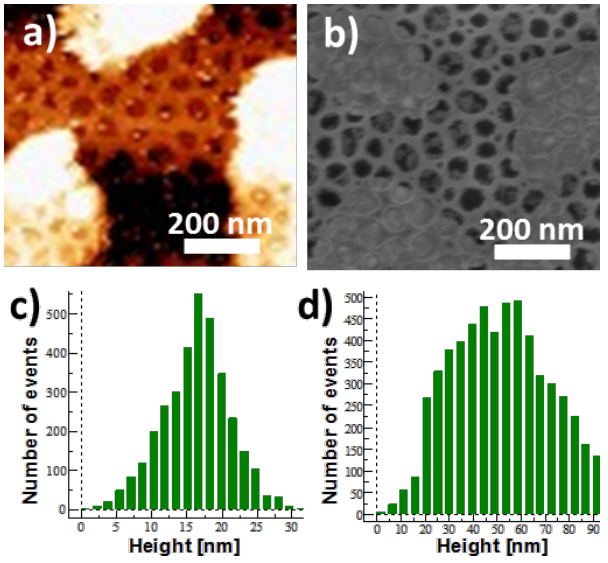

Figure 2: a) AFM and b) SEM images of the sample **Au10NC**. Depth distribution histogram in the c) dark and d) light areas.

Nanoperforated TiO_2 monolayers deposited on 20 nm and 50 nm thick gold layers (samples **Au20NC** and **Au50NC**) were also studied by AFM and SEM. Representative SEM images of **Au20NC** and **Au50NC** at a low magnification are shown in Figure 3, and AFM and SEM images with higher magnification are shown in Figure 4.

The SEM images of **Au20NC** and **Au50NC** show few dark islands of around 1 µm, standing out from the light background.

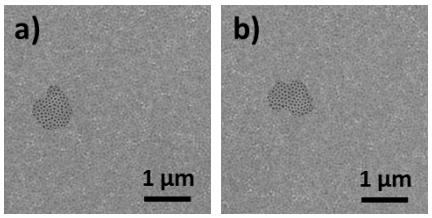

Figure 3: SEM micrographs of a) **Au20NC** and b) **Au50NC**.

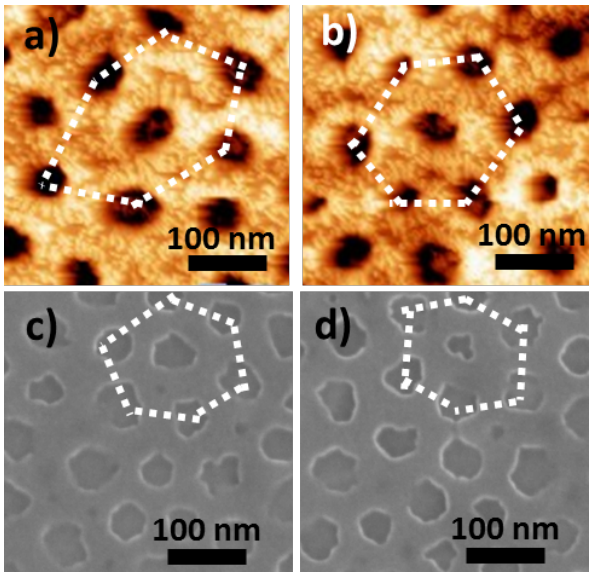

Figure 4: AFM images of a) **Au20NC**, b) **Au50NC** and SEM micrographs of c) **Au20NC** and d) **Au50NC**.

As for the sample **Au10NC**, the 2D organization of the nanoperforations is visible over the whole surface. The minority of dark areas (less than 6% of the whole surface) are assigned to zones where a dewetting of the gold layer from the silicon substrate occurred. In contrast to sample **Au10NC**, the gold layer still covers a great majority of the surface after the formation of the oxide nanoperforated layer.

Figure 4, corresponding to a magnification of the majority of light areas, shows that the AFM and SEM images of the films obtained with the 20 nm and the 50 nm gold layers are comparable. They show dark spots corresponding to nanoperforations of same depth and of same diameter as those obtained with the 10 nm thick gold layer and exhibiting a 2D-hexagonal organization (shown by the dashed lines in Figure 4). Nevertheless, the degree of hexagonal order is lower for these films deposited on gold layers than for films directly deposited on the silicon substrate [19,22-24]. This loss of order is probably due to matter displacement during the thermal treatment, leading to an accumulation of gold in some regions of the sample and to a lack of

gold in others. As a consequence, the TiO_2 nanoperforated layer forms on an undulating gold surface, which results in a certain lowering of the degree of long-range order.

Whatever the sample, the AFM and SEM studies also revealed the presence of some perforations, the bottom of which seems not to be completely cleared of TiO_2. This effect is more visible in areas without gold. A SEM image corresponding to such areas of sample **Au20NC** is shown in Figure 5. A light grey pellicle, indicating the presence of TiO_2, partially covers the bottom of some perforations.

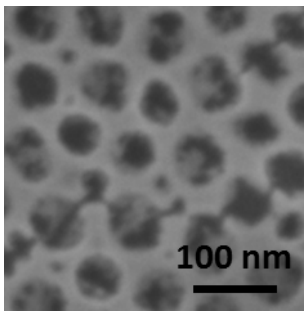

Figure 5: SEM image corresponding to a dark area of the sample **Au20NC**.

The non-homogeneous and non-planar surface exhibiting a different chemical nature of the bottom of the nanoperforations of the films deposited on a 10 nm thick gold layer, such as sample **Au10NC**, can be assigned to a dewetting of the gold layer from the silicon during the thermal treatment at 450 °C. This inhomogeneity of the surface led us to exclude samples with such gold layers for the study. The films synthesized with the 20 nm thick gold layer, such as sample **Au20C**, were used in the following without further optimization. Nevertheless, this study shows an unexpected behavior of the gold layer, which has to be optimized in the future.

Functionalization of the Au and TiO_2 surfaces

To localize the growth of PBA into the nanoperforations, a selective functionalization of the Au and TiO_2 surfaces has been implemented. The oxide surface is rendered hydrophobic in order to prevent the adsorption of PBA precursors. The phosphonate function allows for the selective grafting of the phenyl group on TiO_2 [20,21]. Then, MHA, 4-MPy or 4-ATP are used as coupling agents for anchoring a first layer of Co^{2+} ions at the bottom of the nanoperforations.

To evaluate the efficiency of the TiO_2 functionalization, this step was omitted while the functionalization with MHA and the growth of CoFe PBA in aqueous solution were performed. A representative SEM image of this sample is shown in Figure 6. The whole surface seems bumpy as if a crust constituted by very small PBA particles covered it and under which the nanoperforations are hardly visible. Without hydrophobization of TiO_2, PBA precursors interact with the accessible oxide surface leading to the formation of PBA particles everywhere.

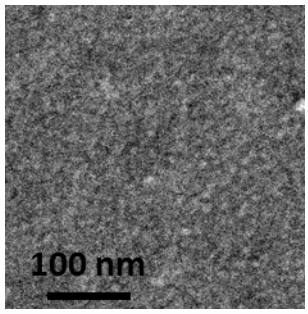

Figure 6: SEM image corresponding to CoFe PBA grown on the nanoperforated films without prior functionalization of TiO_2.

In order to verify the effectiveness of the gold functionalization through the MHA anchoring function at the bottom of the perforations, the presence of sulfur atoms at the surface of the sample was monitored by X-ray photoelectron spectroscopy (XPS) throughout the functionalization step. XPS was carried out right after removing the sample from the MHA solution and after rinsing with EtOH (Figure 7). Before rinsing (Figure 7a), the spectrum exhibit two doublets that can be assigned to a free thiol function and a thiolate species bound to the gold surface [25,26]. After rinsing, the band characteristic of the free function has disappeared (Figure 7b). But, the band corresponding to bound thiolate species still remains. The grafting of the gold surface with MHA therefore was successful.

The effect of the functionalized gold layer at the bottom of the perforations on the growth of PBA is nicely illustrated by a SEM image of the film exhibiting areas with and without gold after PBA growth. PBA particles are concentrated in the areas with gold at the bottom of the nanoperforations, whereas the areas without gold are almost completely free of PBA particles (Figure S3 in Supporting Information File 1).

TiO_2/PBA nanocomposites

Microscopy study

The TiO_2/CoFe PBA nanocomposite **NC01** synthesized by using MHA as anchor and water as the solvent was studied by AFM and SEM. Representative AFM and SEM images of the sample **NC01** are shown in Figure 8a and Figure 8c. The height profile along the green dashed line passing through one hole and three particles on the AFM image is shown in Figure 8b.

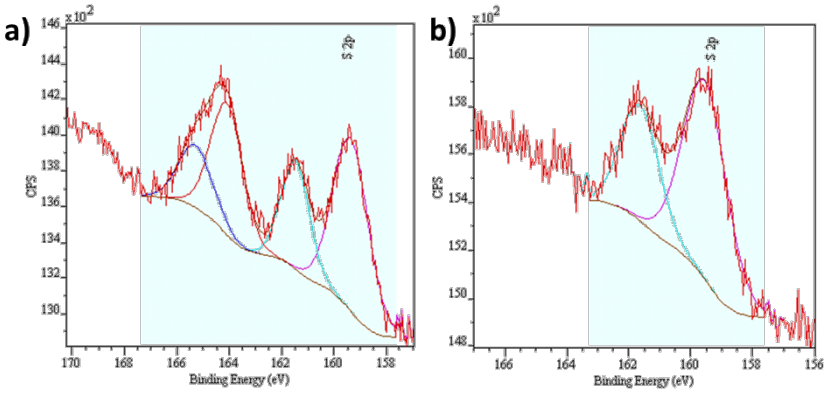

Figure 7: XPS spectra of a film immersed in MHA solution a) before and b) after rinsing with EtOH.

The AFM and SEM images show the 2D-hexagonal arrangement of the nanoperforations and some light objects assigned to PBA particles localized on some of the nanoperforations (Figure 8a and Figure 8c). The shape of the particles is spherical or half-spherical. On the TEM image it is difficult to see if the particles are located in the pores or on the TiO_2 grid. On the contrary, in the AFM image, the particles clearly seem to be located in the nanoperforations. Furthermore, the AFM height profile (Figure 8b) shows three maxima and one minimum corresponding to three particles and one perforation. The distance between these maxima and minimum fairly corresponds to the distance between adjacent nanoperforations of the TiO_2 film before PBA growth (see above), which supports the location of the particles on the nanoperforations. Nevertheless, one cannot conclude whether or not the particles are anchored to the bottom of the perforations.

Each particle seems to be located on one perforation, but not all of the nanoperforations are filled. The average rate of perforations containing one PBA particle is around 15%. The localization of the PBA particles in the perforations indicates that the hydrophobic groups have successfully passivated the oxide surface. The partial loading of the perforations by PBA particles can be due to several reasons listed below:

- the presence of TiO_2 at the bottom of the perforations, which have been rendered hydrophobic when the substrate has been immersed in phenylphosphonic acid, which prevents i) the grafting of the anchoring function for PBA growth and ii) the adsorption of any of the PBA precursors or PBA particles;

- a low yield of the complexation reaction of the Co^{2+} ions by the anchoring functions grafted onto the bottom of the nanoperforations;

- the occurrence of dissolution–recrystallization phenomena during the PBA growth step: during the successive immersions of the functionalized film, the particles or a few of the particles formed during the first cycles can dissolve and the released precursors reform new particles.

The size of the PBA particles ranges from 20 to 100 nm. The size of the smallest particles is of the order of magnitude expected for PBA particles formed by a layer-by-layer ap-

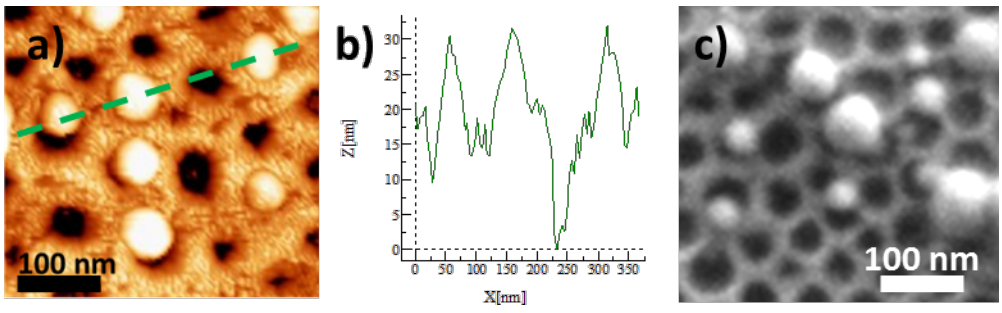

Figure 8: a) AFM image, b) height profile along the green dotted line on the AFM image and c) SEM image of **NC01**.

proach since 15 units of –Fe–CN–Co- (corresponding to 15 cycles) corresponds to approximately 8 nm. Therefore, a growth from Co ions anchored to the bottom of the perforations could result in half-spherical particles of 16 nm in diameter. The formation of particles of bigger size can be explained by the occurrence of dissolution–recrystallization phenomena.

Effect of the chemical nature of the anchoring function for PBA: The TiO_2/CoFe PBA nanocomposites **NC02** synthesized by using 4-MPy (Figure 9a and Figure 9c) and **NC03** synthesized by using 4-ATP (Figure 9b and Figure 9d) as anchoring functions while keeping water as the solvent were studied by AFM and SEM. Representative AFM and SEM images are shown Figure 9.

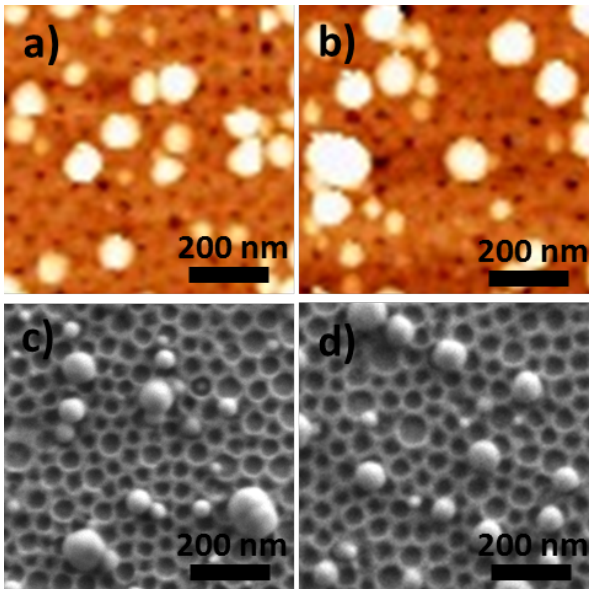

Figure 9: AFM images of a) **NC02**, b) **NC03** and SEM micrographs of c) **NC02**, d) **NC03**.

The AFM and SEM images are very similar to those obtained with MHA. They show the same spherical or half-spherical particles localized on the nanoperforations. The size of these PBA particles ranging from 20 to 80 nm in diameter is comparable to that of the previous sample. As before, around 15% of the nanoperforations are filled with PBA particles. The chemical nature of the complexing agent for the transition metal ion seems to play little or no role in the growth process of the PBA particles.

Effect of the solvent or of the solvent mixture of the PBA precursors solutions: The TiO_2/CoFe PBA nanocomposites synthesized by using alcohol or a water/alcohol mixture for the PBA growth were studied by AFM and SEM. Figure 10a and Figure 10c show representative AFM and SEM images of the TiO_2/CoFe PBA nanocomposite **NC04** synthesized by using a butanolic Co^{2+} solution and $[Fe(CN)_6]^{3-}$ in a 1:1 EtOH/H_2O mixture as PBA precursors solutions. Figure 9b and Figure 9d show representative AFM and SEM images of the TiO_2/CoFe PBA nanocomposite **NC05** synthesized by using solutions of Co^{2+} in a 1:1 EtOH/H_2O mixture and $[Fe(CN)_6]^{3-}$ in 1:1 EtOH/H_2O mixture as PBA precursors solutions. The AFM and SEM images are very different from those of the previous samples (**NC01** to **NC03**). This difference shows the important role of the reaction medium for PBA growth. The images show a great number of faceted particles with a pyramidal shape or a cubic shape with one corner inserted in one perforation.

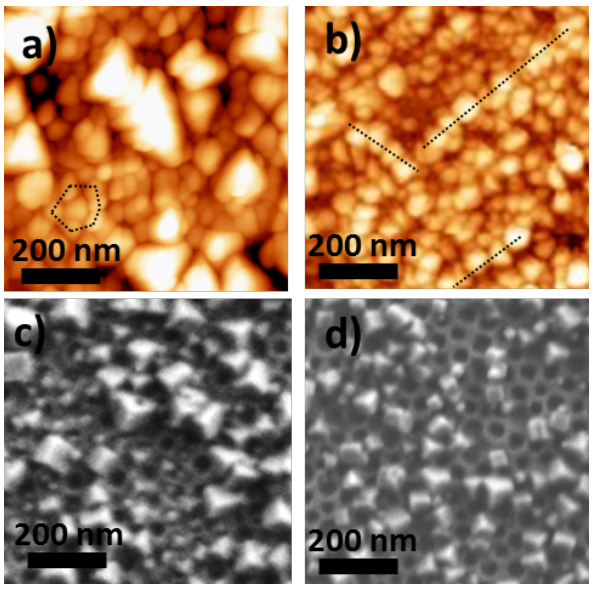

Figure 10: AFM images of a) **NC04**, b) **NC05** and SEM micrographs of c) **NC04**, d) **NC05**.

Except some differences in the particles size range, which seems somewhat larger in the case of **NC04** than in the case of **NC05**, the AFM and SEM images of **NC04** and of **NC05** are very similar. The average density of filled perforations is very high for the two samples, which makes it difficult to see if the particles are localized in the perforations. However, some organization of the particles can be seen in the AFM images (dotted lines in Figure 10a and Figure 10b), which could result from the organization of the perforations. For instance, a hexagonal organization of some particles is visible and the distance between the aligned particles fairly corresponds to the distance between the centers of the perforations. **NC04** and **NC05** exhibit particles with a completely different shape compared to samples **NC01** to **NC03**. Because the particles have the same chemical composition (see IR spectroscopic study below), these different shapes probably reflect different determining factors in the

particles formation. Indeed, different shapes for particles of same chemical composition usually correspond to growth rates limited by different parameters. PBA particles crystallize in the *Fm*−3*m* cubic face centered space group. They are often cubic due to different interface energies for the different crystallographic faces and therefore different growth rates leading to the formation of cubic particles. Nevertheless, under some specific conditions of concentrations, spherical particles can be obtained when the growth reaction rate is limited by the diffusion of the precursors. In the case of the films, the pyramidal or cubic shape is systematically obtained when the reaction medium is BuOH or the 1:1 mixture EtOH/H_2O whereas the half-spherical or spherical shape is obtained in aqueous solutions. PBA particles are less soluble in BuOH and in the EtOH/H_2O mixture than in H_2O and therefore the dissolution–recrystallization rates are different. The diffusion rates of the precursors in the two reaction media are also different. These differences probably accounts for the different shape of the particles.

A pyramidal shape has been predicted by Tricard et al. [27,28] for a layer-by-layer growth process without additional dissolution–recrystallization phenomena. The study of the mechanisms involved in the PBA nanoparticles growth is still in progress and seems to be more complicated than the layer-by-layer process often evoked in the literature to describe the growth of PBA films [16-18].

Infrared spectroscopic investigation

Infrared spectroscopy, and especially the ν(C≡N) vibration band located in the spectral range of 2100–2200 cm^{-1} is usually used to characterize PBA species. Indeed, the cyanide bridge is extremely sensitive to its environment, including the oxidation state and the spin state of the transition metal ions [29].

Because samples **NC01** to **NC03** on the one hand and samples **NC04** and **NC05** on the other hand are very similar, the results are presented for samples **NC01** and **NC04**. The spectra of **NC01** and **NC04** are shown in the range of 1900–2250 cm^{-1} in Figure 11. Both spectra display one narrow and intense band centered at 2106 cm^{-1}. This band is attributed to the CN stretching vibration. The position of the band corresponds neither to a terminal Fe^{III}–CN group (expected around 2118 cm^{-1}) [29] nor to a Fe^{II}–CN group (expected around 2044 cm^{-1}) [29]. The narrowness of this band and its energy position are in line with the formation of a CoFe PBA. The band is located at the same energy (within the experimental resolution) in both spectra. This indicates the formation of PBA of the same chemical composition for all the samples. The position of the band corresponds to CN in Fe^{II}–CN–Co^{II} linkages of the $Co^{II}Fe^{II}$ PBA. Starting from Co^{II} and $[Fe^{III}(CN)_6]^{3-}$ ions as PBA precursors, the energy position of the band indicates the reduction of $[Fe^{III}(CN)_6]^{3-}$ into $[Fe^{II}(CN)_6]^{4-}$ during the formation of PBA. Such a reduction reaction during the synthesis of PBA thin films has already been observed [30]. The strong difference in the intensity of the band from **NC04** to **NC01** reflects different amounts of PBA on the surface of the films. The intensity ratio of the bands of **NC04** and **NC01** is 15% in agreement with the average density of filled perforations determined by microsopy: around 15% for **NC01** and very high, close to 100%, for **NC04**.

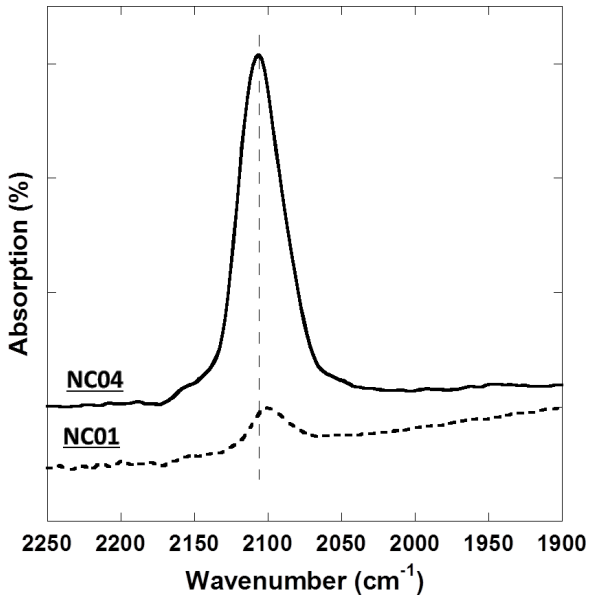

Figure 11: IR spectra of **NC01** and **NC04**.

Conclusion

In conclusion, this first approach to study step-by-step the controlled growth of PBA particles within the perforations of ordered nanoperforated oxide layers allows for pointing out the steps the optimization of which would improve the final composite. Some steps are well-controlled or already optimized and some others are trickier and need to be optimized in order to get perfectly ordered nanoperforated layers with all the perforations filled with PBA particles.

After deposition, the small roughness of the gold layer is suitable for the subsequent deposition of the oxide layer. Nevertheless, the morphology of this layer undergoes important changes during the thermal treatment (step 3). The evolution is spectacular in the case of the 10 nm thick gold layer, but also exists for the layers with higher thicknesses. The unexpected thermal behavior of the gold layer shows that the first step clearly needs to be optimized to avoid any gold displacement modifying the planarity of the layer, which necessarily affects the ordered organization of the nanoperforations.

The deposition (step 2) and the thermal treatment (step 3) of the ordered hybrid organic–inorganic layer have already been extensively studied [12,19]. The smaller the diameters of the perforations are, the higher is the degree of order. Nevertheless, a perfect accessibility of the gold bottom of all the perforations is mandatory in order to fill all of them with PBA particles. Work is in progress to check and to improve this point.

The selective functionalization of the surfaces is a necessary step to localize PBA growth within the nanoperforations. The hydrophobization of the accessible oxide layer efficiently avoids the formation of PBA outside the perforations. The chemical nature of the anchoring function for the PBA growth seems not to be a determining factor in the average density of filled perforations.

The growth of PBA is undoubtedly the trickiest step. The average density of filled perforations and the shape of the particles seem strongly linked to the solubility of the growing particles in the reaction media. Work is in progress in order to fully control this step.

Supporting Information

Supporting Information File 1

Additional experimental data.
[http://www.beilstein-journals.org/bjnano/content/supplementary/2190-4286-5-204-S1.pdf]

Acknowledgements

This research was carried out with the support of C'Nano IdF, the University Paris-Sud and the University Paris 6. Virgile Trannoy thanks Region Ile-de-France C'Nano program for the Ph.D. financial support.

References

1. Entley, W. R.; Girolami, G. S. *Science* **1995,** *268,* 397–400. doi:10.1126/science.268.5209.397
2. Ferlay, S.; Mallah, T.; Ouahes, R.; Veillet, P.; Verdaguer, M. *Nature* **1995,** *378,* 701–703. doi:10.1038/378701a0
3. Sato, O.; Iyoda, T.; Fujishima, A.; Hashimoto, K. *Science* **1996,** *272,* 704–705. doi:10.1126/science.272.5262.704
4. Bleuzen, A.; Lomenech, C.; Escax, V.; Villain, F.; Varret, F.; Cartier dit Moulin, C.; Verdaguer, M. *J. Am. Chem. Soc.* **2000,** *122,* 6648–6652. doi:10.1021/ja000348u
5. Li, D.; Clérac, R.; Roubeau, O.; Harté, E.; Mathonière, C.; Le Bris, R.; Holmes, S. M. *J. Am. Chem. Soc.* **2008,** *130,* 252–258. doi:10.1021/ja0757632
6. Mercurol, J.; Li, Y.; Pardo, E.; Risset, O.; Seuleiman, M.; Rousselière, H.; Lescouëzec, R.; Julve, M. *Chem. Commun.* **2010,** *46,* 8995–8997. doi:10.1039/c0cc02024a
7. Hoshino, N.; Iijima, F.; Newton, G. N.; Yoshida, N.; Shiga, T.; Nojiri, H.; Nakao, A.; Kumai, R.; Murakami, Y.; Oshio, H. *Nat. Chem.* **2012,** *4,* 921–926. doi:10.1038/nchem.1455
8. Cafun, J.-D.; Cartier dit Moulin, C.; Fornasieri, G.; Arrio, M.-A.; Briois, V.; Bleuzen, A. *New J. Chem.* **2011,** *35,* 2074–2080. doi:10.1039/c1nj20180h
9. Ludi, A.; Güdel, H. Structural chemistry of polynuclear transition metal cyanides. *Inorganic Chemistry;* Structure and Bonding, Vol. 14; Springer: Berlin, Germany, 1973; pp 1–21. doi:10.1007/BFb0016869
10. Brinker, C. J.; Scherer, G. W., Eds. *Sol-Gel Science: The Physics and Chemistry of Sol-Gel Processing;* Gulf Professional Publishing, 1990.
11. Kresge, C. T.; Leonowicz, M. E.; Roth, W. J.; Vartuli, J. C.; Beck, J. S. *Nature* **1992,** *359,* 710–712. doi:10.1038/359710a0
12. Fisher, A.; Kuemmel, M.; Järn, M.; Linden, M.; Boissière, C.; Nicole, L.; Sanchez, C.; Grosso, D. *Small* **2006,** *2,* 569–574. doi:10.1002/smll.200500333
13. Schulze, C.; Faustini, M.; Lee, J.; Schletter, H.; Lutz, M. U.; Krone, P.; Gass, M.; Sader, K.; Bleloch, A. L.; Hietschold, M.; Fuger, M.; Suess, D.; Fidler, J.; Wolff, U.; Neu, V.; Grosso, D.; Makarov, D.; Albrecht, M. *Nanotechnology* **2010,** *21,* 495701. doi:10.1088/0957-4484/21/49/495701
14. Allouche, J.; Lantiat, D.; Kuemmel, M.; Faustini, M.; Laberty, C.; Chaneac, C.; Tronc, E.; Boissiere, C.; Nicole, L.; Sanchez, C.; Grosso, D. *J. Sol-Gel Sci. Technol.* **2010,** *53,* 551–554. doi:10.1007/s10971-009-2130-z
15. Lepoutre, S.; Grosso, D.; Sanchez, C.; Fornasieri, G.; Rivière, E.; Bleuzen, A. *Adv. Mater.* **2010,** *22,* 3992–3996. doi:10.1002/adma.200903768
16. Volatron, F.; Heurtaux, D.; Catala, L.; Mathonière, C.; Gloter, A.; Stéphan, O.; Repetto, D.; Clemente-León, M.; Coronado, E.; Mallah, T. *Chem. Commun.* **2011,** *47,* 1985–1987. doi:10.1039/c0cc04940a
17. Pajerowski, D. M.; Gardner, J. E.; Frye, F. A.; Andrus, M. J.; Dumont, M. F.; Knowles, E. S.; Meisel, M. W.; Talham, D. R. *Chem. Mater.* **2011,** *23,* 3045–3053. doi:10.1021/cm2003337
18. Cobo, S.; Molnár, G.; Carcenac, F.; Szilágyi, P. Á.; Salmon, L.; Vieu, C.; Bousseksou, A. *J. Nanosci. Nanotechnol.* **2010,** *10,* 5042–5050. doi:10.1166/jnn.2010.2430
19. Kuemmel, M.; Allouche, J.; Nicole, L.; Boissière, C.; Laberty, C.; Amenitsch, H.; Sanchez, C.; Grosso, D. *Chem. Mater.* **2007,** *19,* 3717–3725. doi:10.1021/cm0706245
20. Mutin, P. H.; Guerrero, G.; Vioux, A. *C. R. Chim.* **2003,** *6,* 1153–1164. doi:10.1016/j.crci.2003.07.006
21. Guerrero, G.; Mutin, P. H.; Vioux, A. *Chem. Mater.* **2001,** *13,* 4367–4373. doi:10.1021/cm001253u
22. Sanchez, C.; Boissière, C.; Grosso, D.; Laberty, C.; Nicole, L. *Chem. Mater.* **2008,** *20,* 682–737. doi:10.1021/cm702100t
23. Faustini, M.; Drisko, G. L.; Boissiere, C.; Grosso, D. *Scr. Mater.* **2014,** *74,* 13–18. doi:10.1016/j.scriptamat.2013.07.029
24. Faustini, M.; Boissière, C.; Nicole, L.; Grosso, D. *Chem. Mater.* **2014,** *26,* 709–723. doi:10.1021/cm402132y
25. Shon, Y.-S.; Gross, S. M.; Dawson, B.; Porter, M.; Murray, R. W. *Langmuir* **2000,** *16,* 6555–6561. doi:10.1021/la000329y
26. Pasquinet, E.; Bouvier, C.; Thery-Merland, F.; Hairault, L.; Lebret, B.; Méthivier, C.; Pradier, C. M. *J. Colloid Interface Sci.* **2004,** *272,* 21–27. doi:10.1016/j.jcis.2003.11.025
27. Tricard, S.; Raza, Y.; Mazerat, S.; Aissou, K.; Baron, T.; Mallah, T. *Dalton Trans.* **2013,** *42,* 8034–8040. doi:10.1039/c3dt50259g
28. Tricard, S.; Fabrice, C.; Mallah, T. *Dalton Trans.* **2013,** *42,* 15835–15845. doi:10.1039/c3dt51636a

29. Nakamoto, K. *Infrared and Raman spectra of inorganic and coordination compounds,* 4th ed.; Wiley-Interscience: New York, NY, USA, 1986.
30. Bonhommeau, S.; Pontius, N.; Cobo, S.; Salmon, L.; de Groot, F. M. F.; Molnár, G.; Bousseksou, A.; Durr, H. A.; Eberhardt, W. *Phys. Chem. Chem. Phys.* **2008,** *10,* 5882–5889. doi:10.1039/b806783j

License and Terms

BEILSTEIN JOURNAL OF NANOTECHNOLOGY

Optical properties and electrical transport of thin films of terbium(III) bis(phthalocyanine) on cobalt

Peter Robaschik[1], Pablo F. Siles[2,3], Daniel Bülz[1], Peter Richter[1], Manuel Monecke[1], Michael Fronk[1], Svetlana Klyatskaya[4], Daniel Grimm[2,3], Oliver G. Schmidt[2,3], Mario Ruben[4,5], Dietrich R. T. Zahn[1] and Georgeta Salvan[*1]

Full Research Paper

Open Access

Address:
[1]Semiconductor Physics, Technische Universität Chemnitz, Reichenhainer Straße 70, 09107 Chemnitz, Germany, [2]Material Systems for Nanoelectronics, Technische Universität Chemnitz, Reichenhainer Straße 70, 09107 Chemnitz, Germany, [3]Institute for Integrative Nanosciences, IFW Dresden, Helmholtzstraße 20, 01069 Dresden, Germany, [4]Institute of Nanotechnology, Karlsruhe Institute of Technology (KIT), 76344 Eggenstein-Leopoldshafen, Germany, and [5]Université de Strasbourg, Institut de Physique et de Chimie des Materiaux de Strasbourg, CNRS UMP 7504, 23 Rue du Loess, 67034 Strasbourg Cedex 2, France

Email:
Georgeta Salvan[*] - salvan@physik.tu-chemnitz.de

* Corresponding author

Keywords:
current sensing AFM; ellipsometry; spintronics; $TbPc_2$; transport properties

Beilstein J. Nanotechnol. **2014,** *5,* 2070–2078.
doi:10.3762/bjnano.5.215

Received: 14 July 2014
Accepted: 15 October 2014
Published: 11 November 2014

This article is part of the Thematic Series "Molecular materials – towards quantum properties".

Associate Editor: P. Ziemann

Abstract

The optical and electrical properties of terbium(III) bis(phthalocyanine) ($TbPc_2$) films on cobalt substrates were studied using variable angle spectroscopic ellipsometry (VASE) and current sensing atomic force microscopy (cs-AFM). Thin films of $TbPc_2$ with a thickness between 18 nm and 87 nm were prepared by organic molecular beam deposition onto a cobalt layer grown by electron beam evaporation. The molecular orientation of the molecules on the metallic film was estimated from the analysis of the spectroscopic ellipsometry data. A detailed analysis of the AFM topography shows that the $TbPc_2$ films consist of islands which increase in size with the thickness of the organic film. Furthermore, the cs-AFM technique allows local variations of the organic film topography to be correlated with electrical transport properties. Local current mapping as well as local I–V spectroscopy shows that despite the granular structure of the films, the electrical transport is uniform through the organic films on the microscale. The AFM-based electrical measurements allow the local charge carrier mobility of the $TbPc_2$ thin films to be quantified with nanoscale resolution.

Introduction

Molecular spintronic devices could bring a new era of information technology, as the materials are inexpensive and have a potentially higher efficiency than conventional electronic devices [1-9]. Therefore, many studies were carried out to identify organic molecules with suitable properties for spintronics over the past few years. Terbium(III) bis(phthalocyanine) ($TbPc_2$) is an excellent candidate to provide all the necessary features for molecular spintronics, as it is both an organic semiconductor and a single molecule magnet (SMM). $TbPc_2$ was previously implemented in an organic field effect transistor (OFET) as a hole transporting layer [10] and recently Urdampilleta et al. reported a supramolecular spin valve made of a carbon nanotube (CNT) covered by only a few $TbPc_2$ molecules [5]. For electronic and spintronic devices it is crucial to know and to control the molecular orientation on the device-related substrates. The $TbPc_2$/Co heterojunction was already proposed to serve as a model system for a SMM semiconducting layer on top of a ferromagnetic electrode for a future spintronic device. The chemical and magnetic properties of this interface were investigated by Klar et al. and it was found that the magnetic moment of the Tb couples antiferromagnetically to the Co substrate [11]. In this work we focus on the study of other device-relevant aspects: the influence of the film thickness, morphology, and molecular orientation on the electrical transport in $TbPc_2$ layers on polycrystalline cobalt films. The $TbPc_2$ molecule and the investigated layer stack are schematically shown in Figure 1, which includes a sketch of the molecular orientation which will be discussed later. The present manuscript reveals the optical and electrical properties of $TbPc_2$ films with different thicknesses on Co substrates as well as the molecular tilt angle and grain size distribution of the samples using spectroscopic ellipsometry, AC atomic force microscopy, and current sensing atomic force microscopy. Topographic and electrical AFM techniques provide a reliable method to investigate and correlate the structural and local electrical properties of $TbPc_2$ thin films. This knowledge is crucial for the implementation and fabrication of $TbPc_2$-based devices.

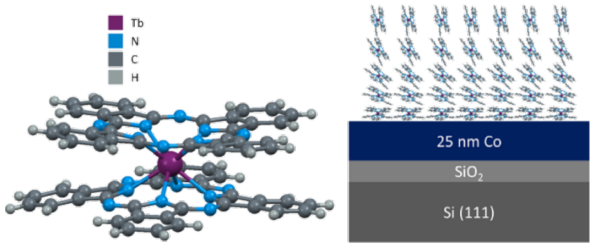

Figure 1: $TbPc_2$ molecule (left). Investigated layer stack: $TbPc_2$ thin films on cobalt grown on SiO_2/Si(111).

Results and Discussion

Spectroscopic ellipsometry

For the ellipsometric analysis, four $TbPc_2$ films with different thicknesses (18 ± 1 nm, 41 ± 1 nm, 58 ± 2 nm, and 87 ± 3 nm) were prepared by organic molecular beam deposition. The underlying 25 nm thick cobalt film was prepared by electron beam evaporation. Both depositions were performed without breaking the vacuum in between to avoid any oxidation of the Co films. Figure 2 shows the dielectric function, $\tilde{\varepsilon} = \varepsilon_1 + i\varepsilon_2$, of Co taken from [12] and a 58 nm $TbPc_2$ film on Co. $TbPc_2$ films exhibit a uniaxial anisotropy of the dielectric function similar to

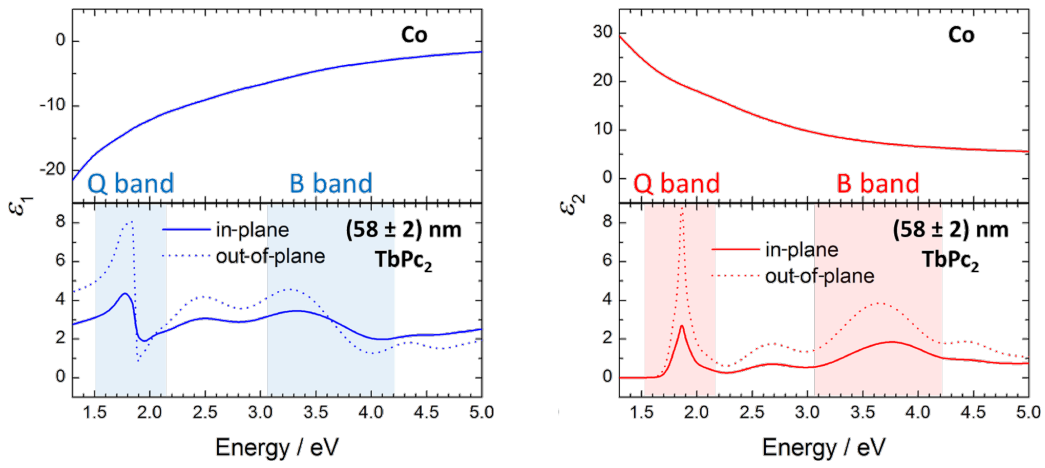

Figure 2: Dielectric function of a $TbPc_2$ film on cobalt. The blue lines and the red lines represent the real part (left) and the imaginary part (right), respectively, of the dielectric function. The top graphs show the dielectric function of Co and bottom graphs are obtained from 58 nm $TbPc_2$ on top of the Co layer.

many planar phthalocyanines, for example, CuPc [13] or H_2Pc [14]. Consequently, the dielectric function parallel (in-plane) and perpendicular (out-of-plane) to the sample surface differs ($\varepsilon_{xx} = \varepsilon_{yy} \neq \varepsilon_{zz}$). For a numerical analysis of the measured spectroscopic ellipsometry data a model employing eleven Gaussian oscillators was used. The energy position and the full width half maximum (FWHM) of the oscillators were fixed for all samples, while their amplitudes were allowed to vary during the Kramers–Kronig consistent fitting procedure (experimental data and model fit for one sample: Supporting Information File 1, Figure S1). From the numerical analysis we can extract the anisotropic dielectric function as well as the thickness of the different layers in the stack.

The most prominent absorption bands, namely the Q and B band, of phthalocyanines are highlighted in Figure 2. They correspond to ligand-related π–π* transitions [15].

For organic semiconductors we can consider the relative magnetic permeability to be $\mu_r \approx 1$. Thus, we can easily determine the optical constants ($\tilde{n} = n + ik$) from the diagonal elements ε_{ii} of the dielectric tensor using Equation 1:

$$n_{ii}^2(\omega) = \mu_r \cdot \varepsilon_{ii}(\omega) \approx \varepsilon_{ii}(\omega), \quad (1)$$

where $i = x, y, z$.

From the anisotropy of the extinction coefficient k in the Q band region (1.6–2.0 eV), it is possible to estimate the molecular orientation [13,14]. According to the model described in [16] we assume that two electronic transition dipole moments in the Q band are parallel to the ligand plane and that all molecules have the same tilt angle α with respect to the substrate, but with a random azimuthal orientation in the substrate plane. It was shown that under these assumptions the average molecular tilt angle α can be written as [16]:

$$\alpha = \arccos\sqrt{\frac{2 - A_{out}/A_{in}}{2 + A_{out}/A_{in}}}, \quad (2)$$

where A_{in} and A_{out} are the areas under the in-plane and out-of-plane component of the extinction coefficient, respectively (see Figure 2). The resulting average angles between the molecules and the substrate plane can be found in Figure 3. The Sessoli group reported $TbPc_2$ molecules which lay in a monolayer evaporated on polycrystalline gold and cobalt as well as standing molecules in a 200 nm thick film by exploiting synchrotron methods [17,18]. Thus, we expect that the first $TbPc_2$ layers will similarly lie on the polycrystalline Co films due to their low roughness (rms: 0.4 nm, obtained by AFM measurements). At this point it should be mentioned that the ellipsometry investigations of the molecular orientation in films with smaller thickness is difficult due to the low sensitivity to the out-of-plane component of the optical constants. In particular, this is due to the presence of a metallic layer beneath the organic layer. The molecular tilt angle increases with increasing films thickness, which was also shown for H_2Pc on PTCDA by utilizing spectroscopic ellipsometry and magneto-optical Kerr effect spectroscopy (MOKE) [16]. According to Equation 2, only values between 0 and 2 are allowed for A_{out}/A_{in}. Nevertheless, for the thickest $TbPc_2$ layer, the ratio A_{out}/A_{in} slightly exceeds the limit of 2. This could be related to errors in the ellipsometry fit. Therefore, we assume standing molecules for films thicker than 80 nm.

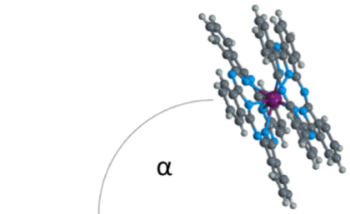

Thickness d / nm	Ratio A_{out} / A_{in}	Angle α / deg
18 ± 1	1.48 ± 0.05	67 ± 2
41 ± 1	1.87 ± 0.05	79 ± 2
58 ± 2	1.97 ± 0.05	85 ± 4
87 ± 3	2.02 ± 0.05	90 ± 5

Figure 3: Definition of the molecular tilt angle (top). Average tilt angle of the $TbPc_2$ molecules on cobalt (bottom). The thickness of the films was estimated from the ellipsometry data.

Topography characteristics

To investigate the topographic characteristics of the $TbPc_2$ thin films on Co substrates, a detailed analysis of the grain size evolution is performed as a function of the organic film thickness. Figure 4 shows AFM images with areas of 2 × 2 μm² for $TbPc_2$ films as well as the Co substrates. An increase of the roughness is observed as a function of the thickness of the organic film (see inset in Figure 5a). Scan profiles in Figure 4 show the average grain heights over the sample surface. These profiles also support a clear variation of the topographic characteristics of the $TbPc_2$ films as the thickness is increased.

In order to perform a detailed quantification of the $TbPc_2$ topographic grain characteristics, a statistical analysis via

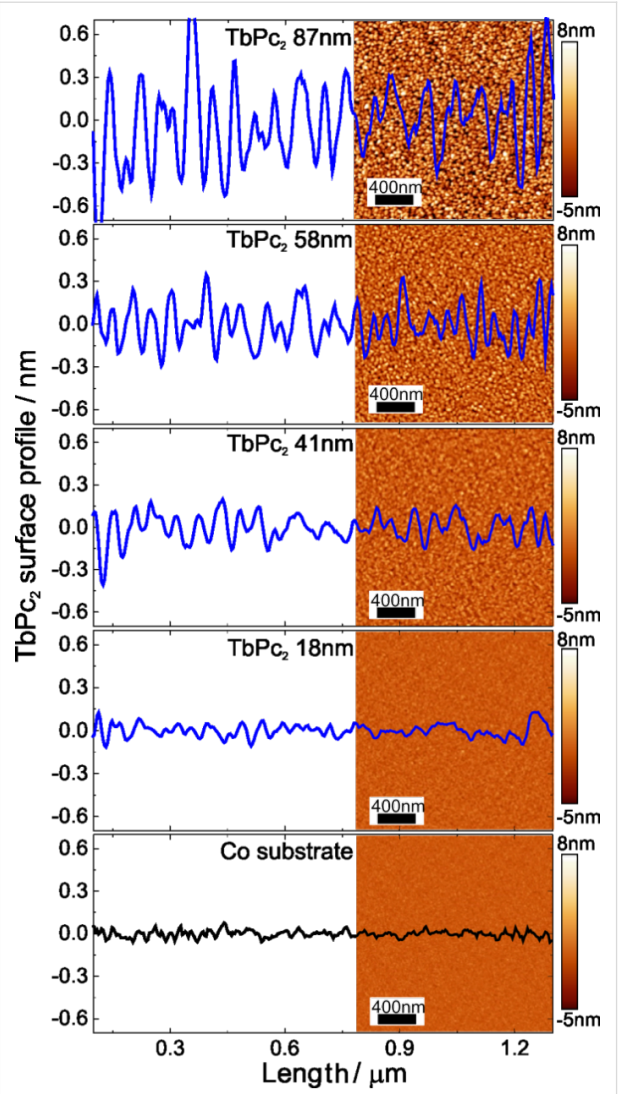

Figure 4: AFM topography characteristics of $TbPc_2$ thin films. Line scan profiles and AFM surface images for $TbPc_2$ films of 18, 41, 58 and 87 nm deposited on a 25 nm thick Co film.

histograms is used to calculate the average grain diameter and height from the topography images shown in Figure 4. Figure 5a shows that the height of the grains follows a linear increase while the average grain diameter tends to reach a maximum size of about 38–40 nm with increasing organic film thickness, as expected for an unheated substrate during the deposition [19]. As an example of the statistical analysis performed, Figure 5b shows a histogram of the grain height and diameter for the case of the 87 nm $TbPc_2$ film. This analysis considers areas of 2×2 µm^2 shown in Figure 4, which contain approximately 2×10^3 grains on the surface. The statistical analysis was performed on different locations of the organic films, revealing similar results. This reinforces the reliability of the data and dismisses the possibility of error during the AFM measurements on a particular location of the sample surface. Further information on the statistical analysis can be found in Supporting Information File 1, Figure S2 and Figure S3.

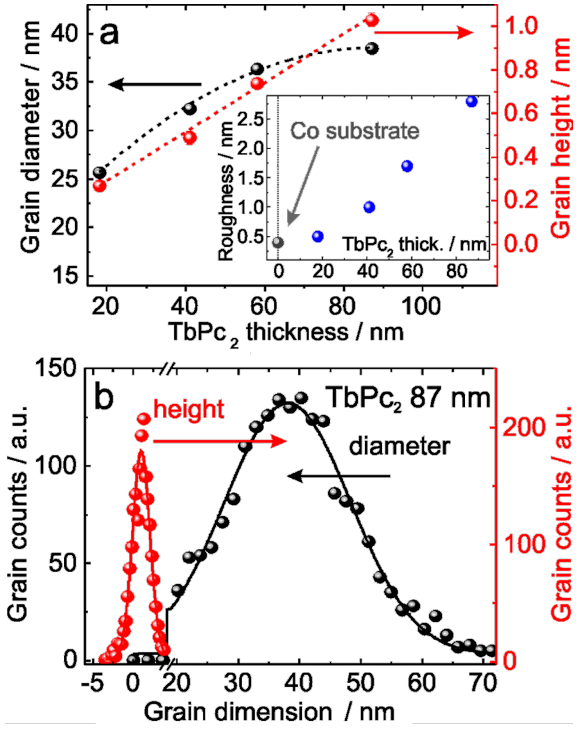

Figure 5: AFM statistical analysis of $TbPc_2$ thin films. (a) Average grain diameter and height as a function of the organic film thickness. Dotted lines are guide to the eye to show the tendency of the grain height and grain diameter with the thickness. The inset shows the dependence of the roughness of the organic films thickness. (b) Diameter and height histograms for an 87 nm $TbPc_2$ film. Error bars (with sizes comparable to plotted dot symbols) in (a) are obtained from Gaussian fits in histograms as shown in (b).

Current sensing atomic force microscopy

Conductive atomic force microscopy techniques are well-established methods for local electrical characterization in organic materials [20-24]. In this work, we employ the cs-AFM technique in order to investigate the local transport properties of $TbPc_2$ thin films on Co substrates. Due to its high reproducibility and versatility, cs-AFM allows for local current–voltage (I–V) spectroscopy as well as current mapping of particular areas of interest on the organic film. I–V spectroscopy is realized by subsequent sweeping of the applied bias while the AFM conductive probe is located at a fixed location on the sample surface. This procedure is repeated several times over different locations to ensure the reproducibility of the electrical response. On the other hand, in current mapping experiments, a fixed voltage is applied at the probe–sample interface while the probe is scanned over a specific area of the sample surface. These high resolution current maps (512 × 512 points) allow simultaneous information to be obtained regarding

topographic and electrical current through the organic material, and establish a direct correlation of the organic topography with electrical characteristics. Also, by repeating current mapping at different locations and with different voltages, we are able to reconstruct the I–V characteristics.

Figure 6a shows a schematic diagram of the set up for local electrical measurements. A conductive AFM probe placed directly in contact with the $TbPc_2$ surface plays the role of the top electrode, while the Co bottom film acts as a back electrode. Samples for cs-AFM measurements were deposited on a Si substrate with a top SiO_2 layer of 1 µm in order to eliminate possible leakage current.

Figure 6b shows a 5 × 5 μm^2 topography image of an 80 nm thick $TbPc_2$ film which has the highest roughness, with respect to Figure 4 and Figure 5. It is worth pointing out that for the case of electrical AFM measurements, special conductive probes with a larger radius compared to the high resolution probes used in the topographic studies (see Experimental section for more details) are utilized. Therefore, a lower topography resolution is expected in topography images acquired during electrical measurements (e.g., Figure 6b). The electrical response of the film, for the same location indicated in Figure 6b, is explored under different applied voltages, as indicated in Figure 6c–e. We observe highly stable and uniformly transport characteristics for all $TbPc_2$ film thicknesses investigated. This suggests a uniform distribution of the electrical charge flow through the organic film.

To further investigate the transport mechanism in $TbPc_2$ thin films, a series of local I–V spectroscopy measurements on different locations along the organic material were performed. Figure 7a shows the transport response for the case of 20 and 80 nm thick $TbPc_2$ films. Here, the AFM probe is fixed at one single point on the surface while the voltage is swept for around 20 consecutive cycles (grey and black areas). Solid lines show the average electrical current. In order to verify the reproducibility of the I–V spectroscopy results, a series of current maps were also obtained at different applied voltages for both organic films. I–V characteristics were then reconstructed by obtaining the average current corresponding to 512 × 512 data

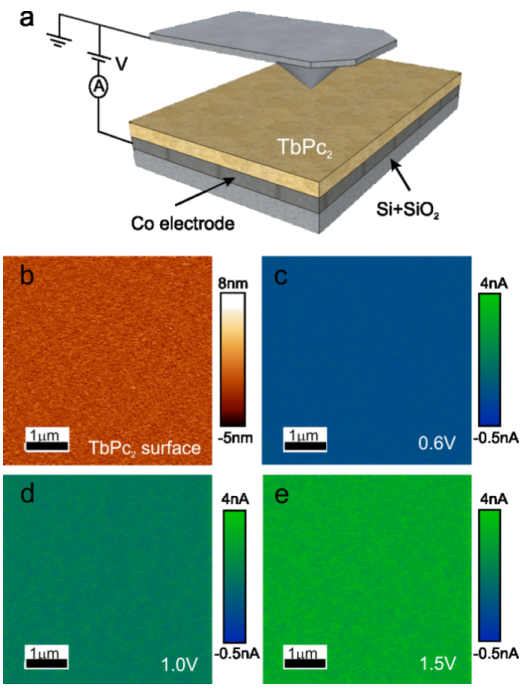

Figure 6: cs-AFM electrical measurements. (a) Electrical setup employed for local electrical measurements via cs-AFM. (b) AFM topography image of an 87 nm thick $TbPc_2$ film (5 × 5 μm^2). Current maps for the same location indicated in (b) for the case of an applied voltage of 0.6 V (c), 1.0 V (d) and 1.5 V (e).

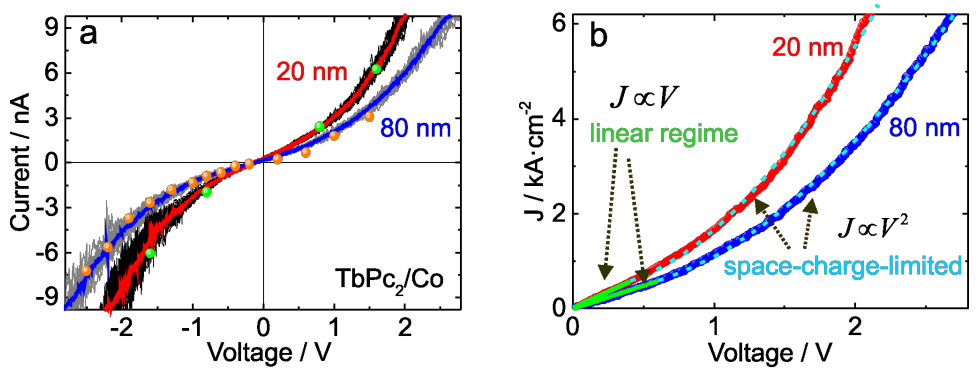

Figure 7: Transport mechanism for $TbPc_2$ thin films. Red and blue solid lines indicate the average of 20 local I–V spectroscopy cycles. (a) Current–voltage characteristics for $TbPc_2$ thin films. Grey and black data in (a) represent the local I–V spectroscopy cycles. Dotted data represent the current value obtained via current maps. Each dot represents the average of 512 × 512 data points acquired during the AFM scanning. (b) Current density response. Solid green lines and dashed blue lines correspond to the linear and space-charge-limited transport regimes, respectively.

points from current maps as the ones shown in Figure 6c–e. Solid dots in Figure 7a correspond to the I–V characteristics reconstructed with current maps and indicate the high reproducibility of the transport measurements for $TbPc_2$ organic films performed via cs-AFM.

The current values measured for the $TbPc_2$ thin films are close to those reported for the case of CuPc [23] and up to three orders of magnitude higher than those reported for similar organic films investigated via cs-AFM techniques such as metalloporphyrin thin films on Ni substrates [20]. In general, due to their planar structure, phthalocyanines are known to exhibit a higher hole mobility as compared to the porphyrins [25], which could lead to a higher current. When comparing the topographic characteristics of $TbPc_2$ samples with 20 nm and 80 nm (see Figures 4 and 5), the variation with grain size would induce more grain boundaries for electron scattering in the thinner samples when compared with the ticker samples. Thus, a different amount of scattering centers might be responsible for the fact that the electric current scales gentler than the expected laws with the film thickness ($1/L$).

Figure 7b shows the current density–voltage characteristics for the $TbPc_2$ films. In order to obtain the current density from the cs-AFM measurements, we follow a similar approach as presented by Reid et al. [26], where the contact area between probe and sample is determined assuming a tip indentation of 1 nm for the same kind of Pt-coated hemispherical probes used in this work. This results in a circular contact area with a diameter (P_d) of 14 nm. Here, we ensure that the probe–sample force is kept constant during the electrical measurements and no extra force, which could eventually modify the contact area, is applied.

The electrical response of the $TbPc_2$ thin films presents a transition from a linear ohmic-like transport regime for low voltages to a square law dependence for high voltages. These results appear to be in agreement with a space-charge-limited current process (SCLC). According to G. Horowitz et al., the linear current–voltage characteristics can exist in the SCLC model and come from electrons hopping from one insulating state to the next [27]. Hence, the transport regime of $TbPc_2$ thin films would follow such transition behavior:

$$J_{\text{ohmic}} = \frac{\sigma V}{L}, \qquad J_{\text{sc}} = \frac{9}{8}\varepsilon\varepsilon_0\mu\frac{V^2}{L^3}, \tag{3}$$

where J_{ohmic} and J_{SC} are the current densities for each regime, σ is the low voltage conductivity, L is the thickness of the organic film, ε is the relative dielectric constant, ε_0 is the permittivity of free space, μ is the charge carrier mobility and V is the applied voltage. From the ohmic-like regime (see Figure 7b) we obtained parameters of σ/L equal to 1.38 and 0.97 kA/cm^2 V for the samples of 20 and 80 nm, respectively. If the mobility is higher along the crystalline direction, where an overlap of the π orbitals of the neighboring molecules exists, then the mobility might be higher perpendicular to the molecular plane as opposed to parallel to it. Assuming the same kind of charge for the carriers and the same charge density per unit volume in all films, a reduction in the ratio σ/L corresponds to a reduction in the carrier mobility in the direction perpendicular to the substrate. This is in agreement with the increasingly standing molecules. The validity of the model applied for the ohmic region should be granted in both cases, since the condition is that the amount of injected carriers is low compared to that of thermally generated carriers.

Once the modelling of the current density characteristics for $TbPc_2$ thin films is derived from cs-AFM measurements, it is necessary to account for the electrode geometry in the AFM electrical experiments (AFM probe geometry). We apply the modelling approach described in [26], as we use the same AFM probe geometry. Here, the system is treated as an intermediate case between a situation with infinite plane–plane electrodes and a situation with point–plane electrodes. For the electrode-modified electrical characteristics, a semi-empirical expression for the current density determined via cs-AFM is given by [23,26]:

$$J_{\text{sc}} = 8.2\varepsilon\varepsilon_0\mu V^2\left(7.8\pm1\right)\left(\frac{1}{P_{\text{d}}}\right)^{1.6\pm0.1} L^{-1.4}. \tag{4}$$

By comparing Equations 3 and 4, one can see that current density measurements via cs-AFM consider a thickness dependence from L^{-3} to $L^{-1.4}$ for the case of the Pt-coated AFM probes used in this work [26]. Applying this geometry-corrected model to our current density measurements, it is possible to quantify the charge carrier mobility for the $TbPc_2$ thin films on a nanometer scale. The values of L and P_d are fixed by the film thickness and tip geometry, respectively. For the dielectric constant we consider a minimum value of ε = 4.5, which is the real part of the dielectric function at the lowest photon energy (1.3 eV) used in our ellipsometry experiment (see Figure 2). As a maximum value for the dielectric constant we used ε = 13, which was previously proposed to describe the hole transport along the phthalocyanine ligand plane in CuPc films [28]. This would be the case if all phthalocyanine molecules were perfectly aligned with their ligand plane perpendicular to the electrodes. From the SCLC fitting in Figure 7b we obtain charge carrier mobility values from 0.80×10^{-4} cm^2 V^{-1} s^{-1}

(for ε = 13) to 2.31 × 10^{-4} cm^2 V^{-1} s^{-1} (for ε = 4.5) for the 20 nm $TbPc_2$ film. For the 80 nm thick film, the mobility values range from 0.35 × 10^{-4} cm^2 V^{-1} s^{-1} (for ε = 13) to 1.01 × 10^{-4} cm^2 V^{-1} s^{-1} (for ε = 4.5). The variation of the mobility values across the film surface in a scan window of 5 × 5 μm^2 is below 15% (see Supporting Information File 1, Figure S4). These values are comparable to the hole field effect mobility values determined from OFET measurements by Katoh et al. [10] Noteworthy, the mobility is expected to increase with increasing size of the crystalline grains in the film [29]. A decrease in the hole mobility values with increasing film thickness is therefore at a first glance surprising. However, considering the anisotropic hole transport in the phthalocyanines (with higher mobility in the direction of the π–π stacking in a molecular crystal, i.e., perpendicular to the Pc ligand), a change in the molecular orientation from more lying to more standing molecules with increasing film thickness can be responsible for the decrease in the hole mobility values with increasing film thickness. By taking into account the homogeneous current maps recorded at different voltages (see Figure 6), the excellent agreement between the local I–V characteristics and the average current values obtained via current maps (Figure 7), we conclude that the mobility values estimated above are representative for the area of the respective $TbPc_2$ film.

Conclusion

In this work we present the optical, topographic and electrical properties of $TbPc_2$ thin films on cobalt by utilizing ellipsometry and AFM techniques. The ellipsometric studies allowed us to determine the average molecular tilt angle in the $TbPc_2$ films and this evaluation revealed an evolution from nearly lying molecules in the first layers to standing molecules in a thick film. The current flow through our organic layers is homogeneous within a standard deviation of about 10%, with lower values at the grain boundaries as compared to the top of the grains (see Figure S5 of Supporting Information File 1). A statistical analysis was conducted to determine the size of the grains and it was shown that the lateral expansion of the grains appears to saturate in films at a thickness higher than 58 nm. The I–V characteristics indicate that the transport through the films with thicknesses of 20 nm and 80 nm is governed by the SCLC regime. By applying a SCLC model adapted for the I–V characteristics obtained from cs-AFM measurements, we estimate the hole mobility in $TbPc_2$ films on cobalt substrates to be in the range from 0.35 × 10^{-4} cm^2 V^{-1} s^{-1} to 2.31 × 10^{-4} cm^2 V^{-1} s^{-1}, depending on the film thickness and the dielectric constant considered. The AFM-based approach implemented here allows important transport properties such as current density homogeneity and the local charge carrier mobility to be quantified. The nanoscale resolution achieved here for the characterization of organic systems such as $TbPc_2$ thin films is crucial for future molecular spintronics applications.

Experimental

Sample preparation

Cobalt films were grown by electron beam evaporation on a Si(111) substrate covered by a oxide layer with different thickness (VASE, AFM: 1.5 nm and cs-AFM: 1 μm) at a rate of 1.25 nm/min under UHV conditions (10^{-8} mbar). The substrates were cleaned in acetone and ethanol for 5 minutes each in an ultrasonic bath. On top of the cobalt, the $TbPc_2$ films were prepared by organic molecular beam deposition at a rate of 0.5 nm/min at a pressure below 10^{-7} mbar. The evaporation took place at a temperature of about 400 °C in the Knudsen cell. The samples were kept at room temperature during all depositions. The preservation of the molecules in a film was checked by UV–vis and Raman spectroscopy.

Ellipsometry measurements

VASE measurements were performed ex situ with a Woollam T-Solar Ellipsometer in the spectral range of 0.7–5.0 eV with an energy step width of 0.02 eV. Three different angles of incidence (50°, 60° and 70°) were exploited for increased sensitivity of the optical anisotropy of the films. The initially linear polarized light becomes elliptically polarized light after reflection on the sample. The elliptical polarization state is described by the experimentally measured quantities Ψ and Δ, according to

$$\rho = \frac{r_p}{r_s} = \tan(\Psi)e^{i\Delta}, \tag{5}$$

where ρ is the ratio between the Fresnel reflection coefficients for p- and s-polarized light. The ellipsometry data were analyzed using the WVASE 32 software from J. A. Woollam Co. [30].

AFM measurements

AFM measurements for topography analysis and electrical characterization were performed on an Agilent 5500 AFM system. Measurements were performed under a controlled N_2 environment to preserve the integrity and avoid exposure of the organic films to ambient conditions. Topography measurements were performed in AC tapping mode, which guarantees minimal contact between the AFM probe and the organic film. Ultra sharp (4–10 nm radius) Olympus cantilevers allowed high sensitivity measurements. cs-AFM measurements were performed in contact mode using special Pt-coated Si cantilevers with a spring constant of 0.2 N/m and typical radii of about 20–25 nm. The voltage is applied directly to the

bottom Co electrode. The grounded conductive cantilever is therefore used as a top electrode for local I–V spectroscopy as well as current mapping experiments. AFM topography analysis and current maps images were analyzed using WSxM and Gwyddion software packages [31,32].

Supporting Information

The Supporting Information shows the raw data obtained from ellipsometry and the corresponding model fit for one sample. Furthermore, a statistical analysis of the AFM data is included.

Supporting Information File 1

Ellipsometry and AFM analysis.
[http://www.beilstein-journals.org/bjnano/content/supplementary/2190-4286-5-215-S1.pdf]

Acknowledgements

We gratefully acknowledge the financial support from the Deutsche Forschungsgemeinschat (DFG) in the frames of the Research Unit FOR 1154 “Towards Molecular Spintronics”.

References

1. Rocha, A. R.; Garcia-Suárez, V. M.; Bailey, S. W.; Lambert, C. J.; Ferrer, J.; Sanvito, S. *Nat. Mater.* **2005,** *4,* 335–339. doi:10.1038/nmat1349
2. Bogani, L.; Wernsdorfer, W. *Nat. Mater.* **2008,** *7,* 179–186. doi:10.1038/nmat2133
3. Gambardella, P.; Stepanow, S.; Dmitriev, A.; Honolka, J.; de Groot, F. M. F.; Lingenfelder, M.; Sen Gupta, S.; Sarma, D. D.; Bencok, P.; Stanescu, S.; Clair, S.; Pons, S.; Lin, N.; Seitsonen, A. P.; Brune, H.; Barth, J. V.; Kern, K. *Nat. Mater.* **2009,** *8,* 189–193. doi:10.1038/nmat2376
4. Mannini, M.; Pineider, F.; Sainctavit, P.; Danieli, C.; Otero, E.; Sciancalepore, C.; Talarico, A. M.; Arrio, M.-A.; Cornia, A.; Gatteshi, D.; Sessoli, R. *Nat. Mater.* **2009,** *8,* 194–197. doi:10.1038/nmat2374
5. Urdampilleta, M.; Klyatskaya, S.; Cleuziou, J.-P.; Ruben, M.; Wernsdorfer, W. *Nat. Mater.* **2011,** *10,* 502–506. doi:10.1038/nmat3050
6. Candini, A.; Klyatskaya, S.; Ruben, M.; Wernsdorfer, W.; Affronte, M. *Nano Lett.* **2011,** *11,* 2634–2639. doi:10.1021/nl2006142
7. Vincent, R.; Klyatskaya, S.; Ruben, M.; Wernsdorfer, W.; Balestro, F. *Nature* **2012,** *488,* 357–360. doi:10.1038/nature11341
8. Schwöbel, J.; Fu, Y.; Brede, J.; Dilullo, A.; Hoffmann, G.; Klyatskaya, S.; Ruben, M.; Wiesendanger, R. *Nat. Commun.* **2012,** *3,* 953. doi:10.1038/ncomms1953
9. Ganzhorn, M.; Klyatskaya, S.; Ruben, M.; Wernsdorfer, W. *Nat. Nanotechnol.* **2013,** *8,* 165–169. doi:10.1038/nnano.2012.258
10. Katoh, K.; Komeda, T.; Yamashita, M. *Dalton Trans.* **2010,** *39,* 4708–4723. doi:10.1039/b926121d
11. Klar, D.; Klyatskaya, S.; Candini, A.; Krumme, B.; Kummer, K.; Ohresser, P.; Corradini, V.; de Renzi, V.; Biagi, R.; Joly, L.; Kappler, J.-P.; del Pennino, U.; Affronte, M.; Wende, H.; Ruben, M. *Beilstein J. Nanotechnol.* **2013,** *4,* 320–324. doi:10.3762/bjnano.4.36
12. Palik, E. D. *Handbook of Optical Constants of Solids II;* Academic Press, 1991.
13. Gordan, O. D.; Friedrich, M.; Zahn, D. R. T. *Org. Electron.* **2004,** *5,* 291–297. doi:10.1016/j.orgel.2004.10.001
14. Gordan, O. D.; Friedrich, M.; Zahn, D. R. T. *Thin Solid Films* **2004,** *455,* 551–556. doi:10.1016/j.tsf.2003.11.209
15. Yoshino, K.; Lee, S. B.; Sonoda, T.; Kawagishi, H.; Hidayat, R.; Nakayama, K.; Ozaki, M.; Ban, K.; Nishizawa, K.; Ohta, K.; Shirai, H. *J. Appl. Phys.* **2000,** *88,* 7137–7143. doi:10.1063/1.1316050
16. Bräuer, B.; Fronk, M.; Lehmann, D.; Zahn, D. R. T.; Salvan, G. *J. Phys. Chem. B* **2009,** *113,* 14957–14961. doi:10.1021/jp9073224
17. Margheriti, L.; Chiappe, D.; Mannini, M.; Car, P.-E.; Sainctavit, P.; Arrio, M.-A.; de Mongeot, F. B.; Cezar, J. C.; Piras, F. M.; Magnani, A.; Otero, E.; Caneschi, A.; Sessoli, R. *Adv. Mater.* **2010,** *22,* 5488–5493. doi:10.1002/adma.201003275
18. Malavolti, L.; Poggini, L.; Margheriti, L.; Chiappe, D.; Graziosi, P.; Cortigiani, B.; Lanzilotto, V.; Buatier de Mongeot, F.; Ohresser, P.; Otero, E.; Choueikani, F.; Sainctavit, Ph.; Bergenti, I.; Dediu, V. A.; Mannini, M.; Sessoli, R. *Chem. Commun.* **2013,** *49,* 11506–11508. doi:10.1039/c3cc46868b
19. Khrishnakumar, K. P.; Menon, C. S. *Mater. Lett.* **2001,** *48,* 64–73. doi:10.1016/S0167-577X(00)00281-0
20. Siles, P. F.; Bof Bufon, C. C.; Grimm, D.; Jalil, A. R.; Mende, C.; Lungwitz, F.; Salvan, G.; Zahn, D. R. T.; Lang, H.; Schmidt, O. G. *Org. Electron.* **2014,** *15,* 1432–1439. doi:10.1016/j.orgel.2014.04.004
21. Vervacke, C.; Bof Bufon, C. C.; Thurmer, D. J.; Siles, P. F.; Schmidt, O. G. *Anal. Chem.* **2012,** *84,* 8399–8406. doi:10.1021/ac301959e
22. Alexeev, A.; Loos, J.; Koetse, M. M. *Ultramicroscopy* **2006,** *106,* 191–199. doi:10.1016/j.ultramic.2005.07.003
23. MacDonald, G. A.; Veneman, P. A.; Placenica, D.; Armstrong, N. R. *ACS Nano* **2012,** *6,* 9623–9636. doi:10.1021/nn303043y
24. Hendriksen, B. L. M.; Martin, F.; Qi, Y.; Mauldin, C.; Vukmirovic, N.; Ren, J.; Wormeester, H.; Katan, A. J.; Altoe, V.; Aloni, S.; Fréchet, J. M. J.; Wang, L.-W.; Salmeron, M. *Nano Lett.* **2011,** *11,* 4107–4112. doi:10.1021/nl202720y
25. Walter, M. G.; Rudine, A. B.; Wamser, C. C. *J. Porphyrins Phthalocyanines* **2010,** *14,* 759–792. doi:10.1142/S1088424610002689
26. Reid, O. G.; Munechika, K.; Ginger, D. S. *Nano Lett.* **2008,** *8,* 1602–1609. doi:10.1021/nl080155l
27. Horowitz, G.; Fichou, D.; Peng, X.; Delannoy, P. *J. Phys. France* **1990,** *51,* 1489–1499. doi:10.1051/jphys:0199000510130148900
28. Bof Bufon, C. C.; Vervacke, C.; Thurmer, D. J.; Fronk, M.; Salvan, G.; Lindner, S.; Knupfer, M.; Zahn, D. R. T.; Schmidt, O. G. *J. Phys. Chem. C* **2014,** *118,* 7272–7279. doi:10.1021/jp409617r
29. Yakuphanoglu, F.; Caglar, M.; Caglar, Y.; Ilican, S. *Synth. Met.* **2010,** *160,* 1520–1523. doi:10.1016/j.synthmet.2010.05.013
30. *WVASE®;* J.A. Woollam Co. Inc.: Lincoln, NE, 2014.
31. Horcas, I.; Fernández, R.; Gómez-Rodríguez, J. M.; Colchero, J.; Gómez-Herrero, J.; Baro, A. M. *Rev. Sci. Instrum.* **2007,** *78,* 013705. doi:10.1063/1.2432410
32. *Gwyddion,* 2.38; Klapetek, P.; Nečas, D.: Brno, Czech Republic, 2014.

BEILSTEIN JOURNAL OF NANOTECHNOLOGY

UHV deposition and characterization of a mononuclear iron(III) β-diketonate complex on Au(111)

Irene Cimatti[1], Silviya Ninova[1], Valeria Lanzilotto[1], Luigi Malavolti[1], Luca Rigamonti[2], Brunetto Cortigiani[1], Matteo Mannini[1], Elena Magnano[3], Federica Bondino[3], Federico Totti[1], Andrea Cornia[2] and Roberta Sessoli*[1]

Full Research Paper

Open Access

Address:
[1]Laboratory of Molecular Magnetism, Department of Chemistry "Ugo Schiff", University of Florence & INSTM RU of Florence, Via della Lastruccia 3, 50019 Sesto Fiorentino, Italy, [2]Department of Chemical and Geological Sciences, University of Modena and Reggio Emilia & INSTM RU of Modena and Reggio Emilia, Via G. Campi 183, 41125 Modena, Italy, and [3]CNR-IOM, Laboratorio TASC, Basovizza SS-14, Km 163.5, 34149 Trieste, Italy

Email:
Roberta Sessoli* - roberta.sessoli@unifi.it

* Corresponding author

Keywords:
Au(111); β-diketonate complexes; DFT; STM; thin films; UPS; XMCD; XPS

Beilstein J. Nanotechnol. **2014,** *5,* 2139–2148.
doi:10.3762/bjnano.5.223

Received: 31 July 2014
Accepted: 23 October 2014
Published: 18 November 2014

This article is part of the Thematic Series "Molecular materials – towards quantum properties".

Guest Editor: M. Ruben

Abstract

The adsorption of the sterically hindered β-diketonate complex $Fe(dpm)_3$, where Hdpm = dipivaloylmethane, on Au(111) was investigated by ultraviolet photoelectron spectroscopy (UPS) and scanning tunnelling microscopy (STM). The high volatility of the molecule limited the growth of the film to a few monolayers. While UPS evidenced the presence of the β-diketonate ligands on the surface, the integrity of the molecule on the surface could not be assessed. The low temperature STM images were more informative and at submonolayer coverage they showed the presence of regular domains characterized by a flat morphology and height of ≈0.3 nm. Along with these domains, tetra-lobed features adsorbed on the kinks of the herringbone were also observed. DFT-simulated images of the pristine molecule and its possible decomposition products allowed to assess the partial fragmentation of $Fe(dpm)_3$ upon adsorption on the Au(111) surface. Structural features with intact molecules were only observed for the saturation coverage. An ex situ prepared thick film of the complex was also investigated by X-ray magnetic circular dichroism (XMCD) and features typical of high-spin iron(III) in octahedral environment were observed.

Introduction

A renewed interest in mononuclear metal complexes has recently arisen due to the observation that systems of this class can behave as single molecule magnets (SMMs) [1-6]. SMMs are molecules whose magnetic moment reorients orders of magnitude slower than in normal paramagnets and results in a memory effect at low temperature. Such a behaviour is often

accompanied by spectacular quantum features, for example, resonant quantum tunnelling of the magnetization [7-9], and has attracted practical interest in the areas of ultra-high-density information storage devices, quantum computing and spintronics [10]. Although the SMM behaviour was first observed in polynuclear systems, the investigation was extended to simple mononuclear complexes of either lanthanide or transition-metal ions, which are better suited for vapour-phase processing, in particular when β-diketonate ligands are present [11].

This work exploits the high volatility of the iron(III) tris-β-diketonate complex, $Fe(dpm)_3$ (Hdpm = dipivaloylmethane), in order to perform a detailed in situ ultra-high vacuum (UHV) characterization. In $Fe(dpm)_3$ the three dipivaloylmethanide ligands chelate a high-spin (HS) Fe^{3+} ion, producing a distorted octahedral coordination environment. $Fe(dpm)_3$ is of specific importance because in a previous study it was suggested as a possible contaminant in thin films of $[Fe_4(Ph\text{-}C(CH_2O)_3)_2(dpm)_6]$ (Fe_4Ph) [12], a tetrairon(III) star-shaped SMM that can be sublimated in vacuum conditions. This class of molecules provided the first evidence that SMMs can retain their memory effect once grafted onto a metallic substrate. The magnetic properties of individual Fe_4 molecules have also been addressed using electro-migrated nanojunctions [13-16]. We present here a detailed scanning tunneling microscopy (STM) and photoelectron spectroscopy investigation, in the ultraviolet (UPS) and X-ray (XPS) ranges, on ultra-thin films of $Fe(dpm)_3$ sublimated on Au(111) surfaces. The non-trivial interpretation of the STM images and the spectroscopic data, supported by theoretical simulations, evidence a pronounced reactivity of this species with gold surface.

Results and Discussion

Electronic characterization

The $Fe(dpm)_3$ adsorption mechanism onto the Au(111) surface was studied by means of UPS and XPS measurements. Due to the high volatility of the compound, low deposition rates (LR) were obtained by keeping the crucible at room temperature and varying the exposure time, namely, t_1 = 30 min, t_2 = 60 min, t_3 = 90 min, t_4 = 13 h. The corresponding UPS sequence is reported in the left panel of Figure 1.

The spectrum recorded at t_1 is almost identical to the one collected for the clean substrate. Only a slight attenuation of the gold features and the appearance of a small peak near −15.7 eV can be noticed. Longer exposure times (t_2 and t_3) lead to a clear development of the deeper molecular states and a more evident smearing of the gold valence band (VB). Finally, the spectrum shape of the sample dosed for ca. 13 h remains practically unchanged if compared with the t_3 deposition. This result suggests a self-limiting adsorption mechanism of $Fe(dpm)_3$ on the Au(111) surface. With the aim of collecting more material, the deposition rate (high rate, HR) was increased by heating the crucible up to 338 K. In this case, relatively short exposure times (t_5 = 1 min) already show the typical features observed for the t_4 sample (compare the right and left panel of Figure 1). Despite the high deposition rate, longer doses (t_6 = 10 min and t_7 = 20 min) do not produce thicker films, which confirms that

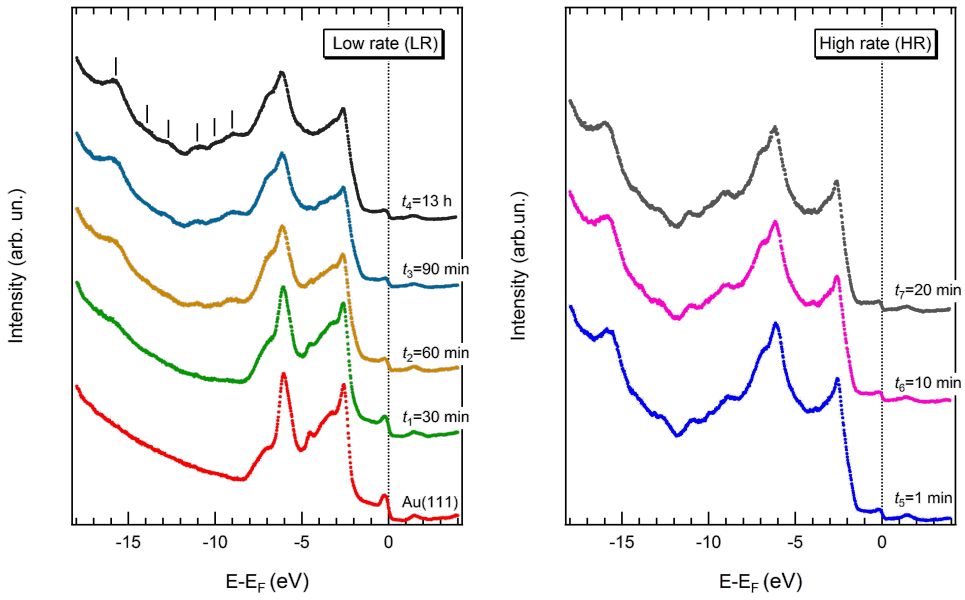

Figure 1: UPS spectra acquired for the Au(111) sample exposed to increasing doses of $Fe(dpm)_3$ with low (left) and high (right) deposition rates.

saturation of the coverage has been achieved. This behaviour is fully consistent with that reported for other metal β-diketonate complexes. Saturation coverage has been observed for $Cu(hfac)_2$, adsorbed onto the $TiO_2(110)$ substrate [17], while multilayers of $Pd(hfac)_2$ can be obtained by cooling Cu surfaces at 120 K [18].

As shown in Figure 2 (top panel), the spectrum corresponding to the saturation coverage (t_7) still displays some features related to the gold substrate; in particular, the Fermi edge (Au#1) and the most prominent peaks (Au#2 and Au#3) of the spectra between −2 and −7 eV can be clearly identified. On the other hand, the smooth trend of the inelastic electron tail allows observation of the molecular features labelled as a, b, c and d. To gain a deeper insight, the density of states (DOS) for the $Fe(dpm)_3$@Au(111) system was computed through a periodic density functional approach (see details in Experimental section). The comparison between the experimental and computed DOS spectra (Figure 2) shows a good correlation between the main features. The DOS region between −2 and −7 eV is strongly dominated by the gold features while few molecular states are clearly visible only at higher binding energies, that is, at more negative values of $E - E_F$ (see inset in the bottom panel of Figure 2). These deeper molecular states can be easily associated to those observed in the inelastic tail of the experimental spectrum, despite the contraction of the theoretical energy scale. The observed slight mismatch between experimental and theoretical energy scale can be related to possible deficiencies in the used exchange-correlation functional/basis sets combination [19]. However, it should be considered that the calculated DOS do not take into account that during the photoexcitation process the creation of a hole reduces the electron screening, the so-called final state effects in photoemission [20]. This effect becomes larger with a deeper created hole, justifying the larger discrepancies observed at higher binding energies.

By plotting the projected density of states (PDOS) on the ligands and the iron ion (see Figure 3a), it is evident that dpm^- ligands provide the main orbital contributions to the energy region where the molecular peaks (a, b, c, d) can be identified at the UPS level. More information on the coordination environment of the iron ion could be extracted from the frontier molecular orbitals which are also expected to bear the fingerprint of any possible molecule–substrate interaction. However, at low molecular coverage, the UPS spectra are dominated by the gold signal and no information on the molecule's Fermi region could

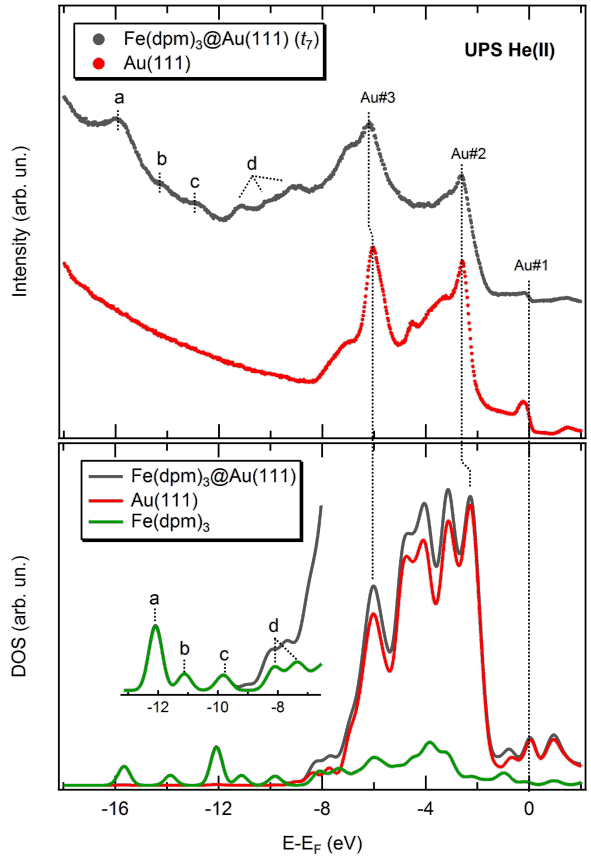

Figure 2: (Top panel) UPS spectra relative to the $Fe(dpm)_3$ saturation coverage (grey curve) and the clean substrate (red curve). (Bottom panel) Theoretical density of states for the system $Fe(dpm)_3$@Au(111) (grey curve) and decomposition into Au and $Fe(dpm)_3$ contributions.

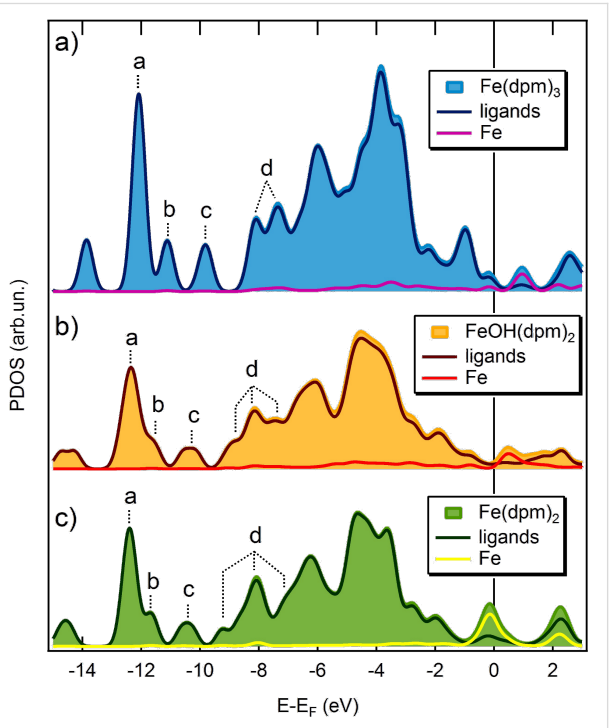

Figure 3: Projected DOS of the molecules in $Fe(dpm)_3$@Au(111) (a), $FeOH(dpm)_2$@Au(111) (b), and $Fe(dpm)_2$@Au(111) (c), in which further separation of PDOS coming from the Fe ion and the ligands is presented.

be obtained. Therefore, it seems that UPS spectra are unable to unambiguously assess the integrity of $Fe(dpm)_3$ once adsorbed on the gold surface.

Samples labelled as t_1, t_6, and t_7 were also characterized by XPS spectroscopy, and the results are reported in Figure 4. As expected, no intensity variations occur when passing from t_6 to t_7. For the t_1 coverage, lower than the saturation one, the C 1s and O 1s peaks do not show significant changes in terms of line shape and binding energy with respect to the thicker films. As for the Fe 2p region, the signal is detectable but quite noisy at saturation coverage, and practically negligible at t_1. Therefore, no useful information about the Fe oxidation state could be retrieved.

STM and DFT characterization

Spectroscopic characterization indicates that $Fe(dpm)_3$ adsorbs on the gold surface up to a saturation coverage, probably one or two layers, but no definitive conclusions could be drawn about the molecule–substrate interaction. With the aim of identifing the nature of the deposited film, samples with saturation and submonolayer coverage were studied by means of low temperature STM measurements.

A representative STM image (400 × 400 nm^2) for submonolayer coverage (t_1 = 30 min) is presented in Figure 5a. Upon adsorption, the surface is characterized by the presence of molecular patches with regular shape and variable size. Reactive sites on the Au substrate, such as the kinks of the herringbone reconstruction and terrace steps, seem to be necessary for the nucleation of molecular domains. Extended islands can grow in the middle of a gold terrace starting from the isolated objects initially adsorbed on the herringbone kinks. Molecular assembly can also occur starting from the lower side of step edges. An enlarged view of the surface reveals that the molecular islands are mainly characterized by a flat morphology and an ordered internal structure (see Figure 5b). However, given the limited resolution, it is not possible to address the individual units

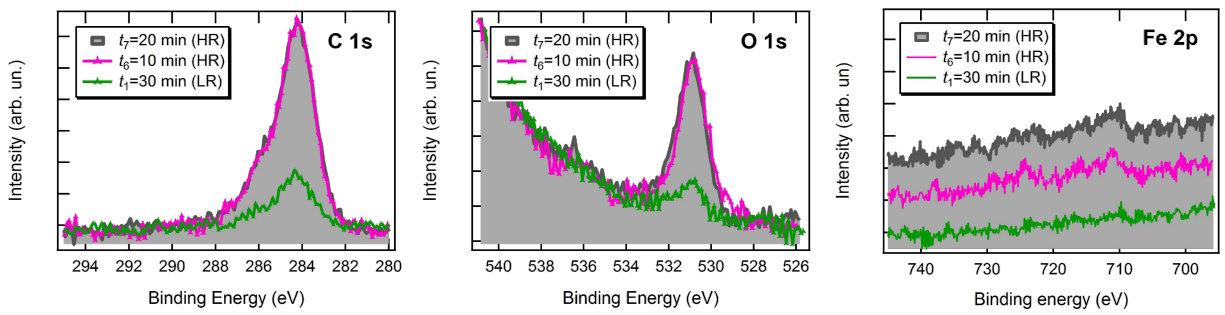

Figure 4: C 1s, O 1s and Fe 2p XPS spectra for the Au(111) substrate exposed to increasing doses of $Fe(dpm)_3$.

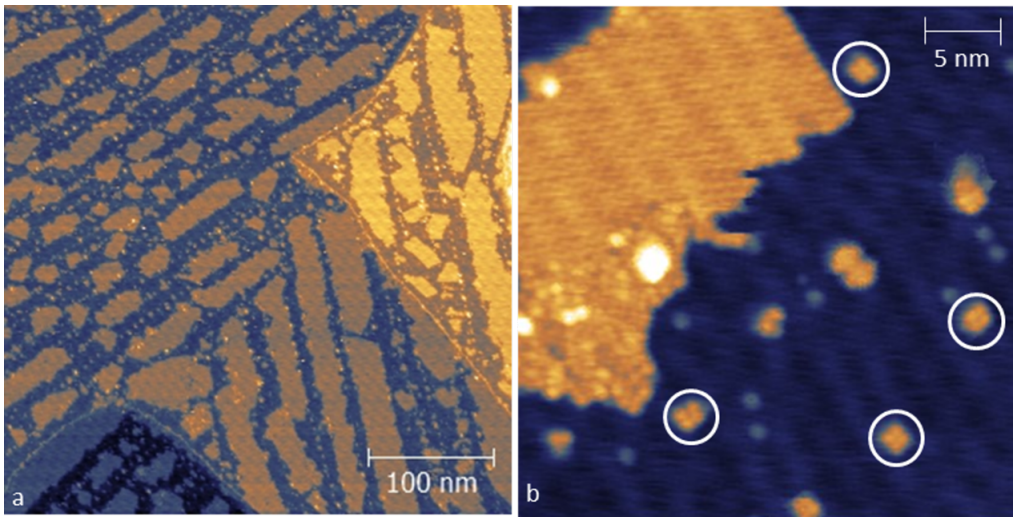

Figure 5: STM image of Au(111) surface after exposure to $Fe(dpm)_3$ for t_1 = 30 min (LR) at T = 30 K. (a) Size = 400 × 400 nm^2, bias = −2 V (empty states), I = 10 pA. (b) Size = 34 × 34 nm^2, bias = −2 V (empty states), I = 5 pA.

forming these domains. On the other hand, their flatness and ordering suggest that these features could arise from the self-assembly of highly symmetric building blocks. Indeed, most of the isolated objects, which are believed to be the starting point of the molecular self-assembly, are characterized by a four-fold symmetry (indicated with open circles in Figure 5b). Moreover, both islands and isolated objects are 0.29 ± 0.02 nm high, therefore confirming the common nature of their building blocks. The ordered domains present also less ordered portions (see the bottom part of the island in Figure 5b). In some areas of the sample, a second layer is also observed and has the same ordered domains in addition to sporadic disordered dendritic regions. By comparing the height of ordered and disordered regions (both at the submonolayer and second layer domains) we can conclude that they might be constituted of the same units (see Figure S1 in Supporting Information File 1).

The situation is different for STM images corresponding to the saturation coverage, that is, t_6 and t_7 (see Figure 6). Both samples are characterized by a wetting layer whose dendritic morphology is reminiscent of the second layer disordered regions, which were occasionally detected at the submonolayer regime. This finding suggests that high deposition rates prevent the molecules from self-assembling in ordered domains. On top of this disordered layer we also observed quasi-spherical objects with a height of 0.35 ± 0.06 nm and a diameter of 1.57 ± 0.21 nm.

To get a deeper insight in the adsorption process, the STM image of $Fe(dpm)_3$ was simulated by DFT calculations. At the experimental bias of 1.5 V (negative values for simulations), an almost spherical multi-lobe image with height of about 0.92 nm and diameter of approximately 1.37 nm is calculated (see Figure 7a). A reasonable agreement between the calculated image and the round features of Figure 6 was found. However, the limited experimental resolution and the approximation in the calculation approach do not allow for an unambiguous conclusion. Because of the low resolution, it is much more difficult to find correlations with the features observed within the dendritic layer or other disordered regions.

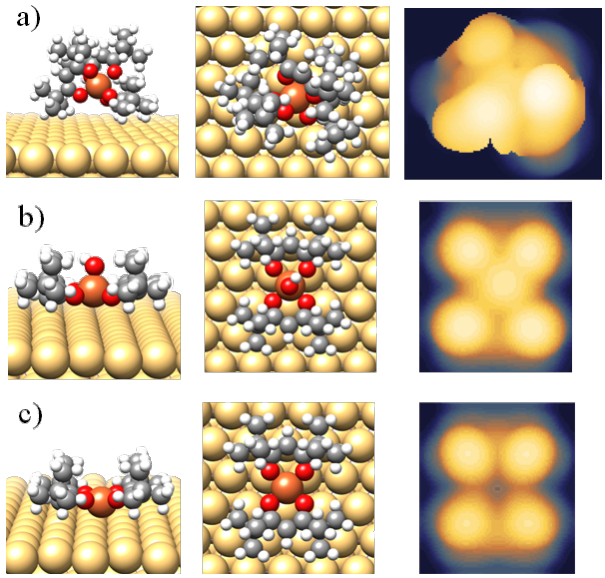

Figure 7: Optimized geometries of the three theoretical models $Fe(dpm)_3$@Au(111) (a), $FeOH(dpm)_2$@Au(111) (b), and $Fe(dpm)_2$@Au(111) (c) presented as side (left column) and top views (middle column). Simulated STM images at experimental bias are also reported in the right column. (a) Bias = −1.5 eV (filled states); size = 17.31 × 14.99 Å^2. (b), (c) Bias = 2 eV (empty states); size = 14.44 × 14.99 Å^2.

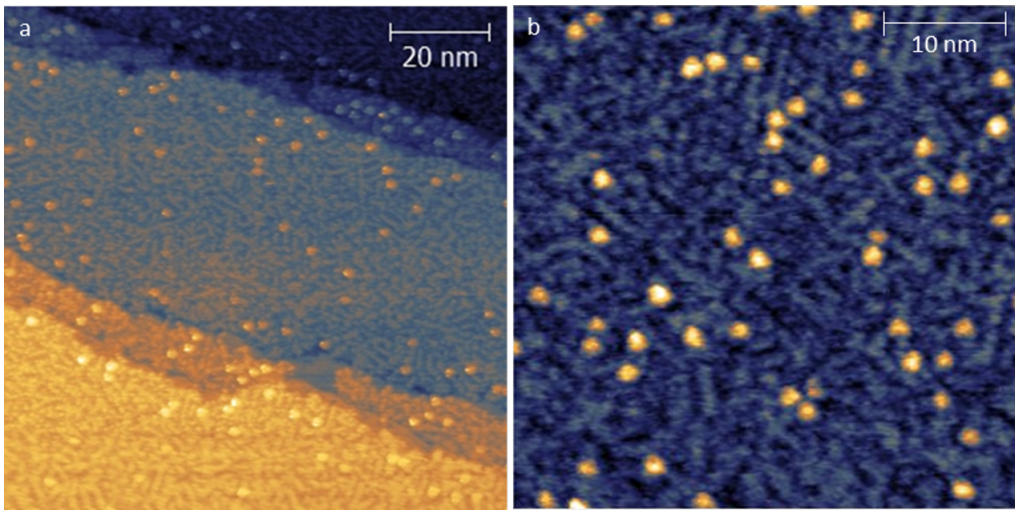

Figure 6: STM images for saturation coverage of $Fe(dpm)_3$ on Au(111) at T = 30 K. (a) t_6 = 10 min (HR); size = 100 × 100 nm^2, bias = 1.5 V (filled states), I = 10 pA. (b) t_7 = 1 min (HR); size = 45 × 45 nm^2, bias = 1.5 V (filled states), I = 10 pA.

As for the submonolayer coverage (Figure 5b), the observed tetra-lobed features (and probably the flat domains) are not compatible with the spherical calculated aspect for intact $Fe(dpm)_3$ molecules, suggesting that major structural changes occur on the gold substrate, namely, decomposition. To better understand the features observed at low coverage deposition, two molecular fragments were theoretically investigated as possible intermediate or end products in the $Fe(dpm)_3$ decomposition process: $FeOH(dpm)_2$@Au(111) and $Fe(dpm)_2$@Au(111). Indeed, the high-spin (HS) Fe^{3+} ion in $FeOH(dpm)_2$ can undergo reduction to HS Fe^{2+} in $Fe(dpm)_2$ via $Fe(d_z^2)$–Au(s) interaction and result in low-spin (LS) Fe^{2+} with a concurrent release of the OH^- group. $FeOH(dpm)_2$ considers a penta-coordinated complex of HS Fe^{3+} with two dpm^- ligands forming the basis of a square pyramid and the OH^- group acting as an apical ligand. $Fe(dpm)_2$ corresponds to a LS Fe^{2+} square planar complex. The optimized geometries as well as the computed STM images are reported in Figure 7b,c. The computed STM image of $Fe(dpm)_2$@Au(111) (Figure 7c) matches very closely to the observed tetra-lobed units with no detectable contribution from the iron d_z^2 orbital. $FeOH(dpm)_2$@Au(111) also affords a tetra-lobed pattern, but with an extra spot in the middle. This shows that $FeOH(dpm)_2$ is unlikely to be the end product of $Fe(dpm)_3$ decomposition.

The TDOS and PDOS for the two fragments were also computed and compared to the ones of pristine $Fe(dpm)_3$ in Figure 3. The largest differences are expected in the valence band region involving the coordination site (i.e., molecules Fermi region). Unfortunately, as mentioned above, these features are hidden by the gold contribution. Even if some minor differences are computed for the inner levels corresponding to the dpm^- ligands, again the overwhelming contribution from the substrate does not allow for unambiguous identification of the species present on the surface from UPS experiments.

Thanks to the combined STM and DFT investigation we partially rationalized the adsorption mechanism of $Fe(dpm)_3$ on the Au(111) surface in terms of a "dissociative adsorption process". This is also supported by the exhaustive literature which can be found on the surface reactivity of metal β-diketonates in relation with their use as metallic precursors in coating technology, such as chemical vapour deposition (CVD) and atomic layer deposition (ALD) [21,22]. For instance, the reactivity of $Cu^{II}(hfac)_2$, $hfac^-$ = hexafluoroacetylacetonate, was found to critically depend on the nature of the molecule–substrate interaction. Using TiO_2(110) [17], Ag [23], TiN [24,25], and Ta [26] as substrates, the molecule dissociatively chemisorbs giving rise to “activated” species (Cu^Ihfac and $hfac^-$) which favour the subsequent reduction to Cu^0 by chemical processing [23,25] or thermal treatment [17,26]. On the contrary, $Cu(hfac)_2$ adsorbs on SiO_2 without fragmentation, thus making reduction to Cu metal less favoured [27]. In the case of $Cr(dbm)_3$, dbm^- = dibenzoylmethanide, the STM investigation revealed bi-lobed features associated with free dbm^-, suggesting that the molecule dissociatively interacts with the Cu(100) surface, while the less reactive dbm-based Ru complexes seem to adsorb as intact molecules on Ag(111) [28,29].

A different situation is observed for complexes based on Fe(II) and bearing pyridine ligands, such as $Fe((H_2B\text{-}pz)_2)_2(bipy)$, $Fe((H_2B\text{-}pz)_2)_2(phen)$ or $Fe(phen)_2(NCS)_2$, where H_2B-pz = bis(hydrido)bis(1*H*-pyrazol-1-yl)borate, bipy = 2,2’-bypiridine and phen = 1,10-phenanthroline. This class of compounds, known as spin crossover (SCO) [30], can be reversibly switched between two distinct spin states, low-spin (LS) and high-spin (HS), by means of a variety of external inputs, such as temperature, light and charge flow. Recently many efforts have been made to study SCO molecules adsorbed on solid surfaces with the aim to exploit their conversion properties in nanoscale devices [31-36]. Many of these studies have systematically shown the presence of intact molecules even if the switching properties can be dramatically altered by the interaction of the organic ligands with the surface. For instance, the electrical switching of $Fe((H_2B\text{-}pz)_2)_2(phen)$ can be observed in the second molecular layer deposited on Au(111), but the molecules of the first layer cannot be switched [36]. Similarly, isolated $Fe(phen)_2(NCS)_2$ molecules cannot be switched on Cu(100). On the other hand, the introduction of an interfacial layer of CuN on Cu(100) allows switching between the HS and the LS state [33,35]. A slightly different situation was observed for a submonolayer of $Fe((H_2B\text{-}pz)_2)_2(bipy)$ on Au(111) [34], where 20% of the molecules are able to preserve the SCO behavior.

XMCD of a $Fe(dpm)_3$ thick film

Given the interest in $Fe(dpm)_3$ as a potential contaminant of evaporable Fe_4 SMMs [12], the magnetic characterization of an ex situ preparation was also attempted. Considering that the high coverages compatible with an ex situ prepared sample cannot be achieved by UHV sublimation, a thick film sample of $Fe(dpm)_3$ was prepared by drop-casting. XAS spectra at the Fe $L_{2,3}$ edge, acquired at the BACH beamline of the Elettra synchrotron for both circular left (σ^+) and circular right (σ^-) polarization, are reported in the top panel of Figure 8. These absorption spectra were measured at 4 K under an external field of 3 T applied parallel to the light propagation vector. They show the expected features for HS Fe^{3+} ions in octahedral coordination geometry with two distinct peaks at the L_3 edge [37-39]. From these data the XMCD signal can be extracted as the difference ($\sigma^- - \sigma^+$).

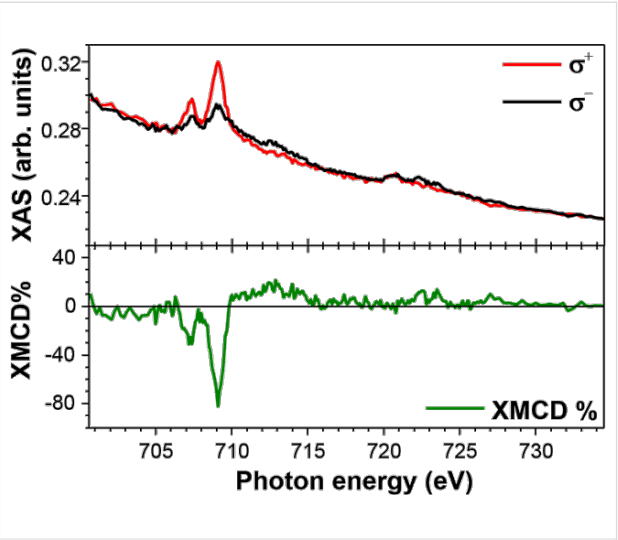

Figure 8: X-ray absorption spectra for a bulk sample of $Fe(dpm)_3$ acquired using the left (σ^+) and right (σ^-) circular polarisation (upper panel) and the derived XMCD% spectrum calculated by dividing the XMCD signal ($\sigma^- - \sigma^+$) by the L_3 edge jump of the isotropic spectrum ($\sigma^- + \sigma^+$)/2 (lower panel).

Similarities between the presented XMCD spectra, featuring the largest intensity at 709.1 eV, and those reported for the Fe_4 family of molecules [13,14,40] are evident thus excluding radiation damage for $Fe(dpm)_3$ molecules in the adopted experimental conditions. The amplitude of the XMCD% signal reaches approximately 80% of the isotropic contribution ($\sigma^- + \sigma^+$)/2, as expected for a set of independent HS Fe^{3+} ions with their magnetic moment fully aligned in the direction of the externally applied magnetic field [37,38]. Interestingly this value is comparable to the one recorded at the Fe $L_{2,3}$ edge on the heteronuclear Fe_3Cr systems [41], the isostructural chromium centred analogues of Fe_4 SMMs. On the other hand, the XMCD% intensity observed here is almost twice as large as in Fe_4 SMMs. We reiterate here that in star-shaped Fe_4 SMMs, the field-opposing contribution of the central spin halves the average magnetic polarization per iron site. Full polarization is instead achieved in these conditions for non-interacting Fe^{3+} ions, as in the present case, or for the peripheral and parallel aligned Fe^{3+} spins of Fe_3Cr.

It is interesting to point out that also the XMCD profile observed in $Fe(dpm)_3$ is very close to that of Fe_3Cr. In particular, for both $Fe(dpm)_3$ and Fe_3Cr, the XMCD signal remains negative in the saddle between the two main peaks at the L_3 edge (707.9 eV). By contrast, the XMCD signal at 707.9 eV vanishes in Fe_4 SMMs [13,14,40]. The different behaviour of the latter can be justified by a non-perfect cancellation of the magnetic contribution of central and peripheral Fe^{3+} ions, thus confirming that this spectral feature is a diagnostic signal for intact star-shaped Fe_4 molecules [41].

Conclusion

Our multi-technique investigation revealed, notwithstanding from the sterically hindered β-diketonate ligands, $Fe(dpm)_3$ undergoes a partial decomposition upon adsorption on the Au(111) surface. The high volatility of the complex limits the deposition to only a few layers. Photoelectron spectroscopy of valence and core states proved to be unable to assess the presence of intact complexes on the surface. More informative was an in situ, low temperature STM investigation, which showed the presence of both tetra-lobed and approximately spherical objects, the latter only visible for higher coverages on top of a wetting layer. The comparison of the experimental topography with DFT-simulated STM images of the pristine $Fe(dpm)_3$ complex, as well as those of two possible fragments, suggests that the observed tetra-lobed features are compatible with the formation of $Fe(dpm)_2$ species on the surface, while the spherical spots visible at higher coverages reveal some resemblance with the simulated images for $Fe(dpm)_3$. Despite the important information obtained by combining STM microscopy and DFT calculations, a definitive assessment of decomposition products in terms of redox and spin state could only be achieved through a detailed synchrotron investigation on in situ prepared samples.

Experimental

Synthesis of [$Fe(dpm)_3$]

A solution of Hdpm (160.2 mg, 0.8693 mmol) in acetonitrile (5 mL) and NEt_3 (0.4 mL) was added dropwise to a solution of sublimed $FeCl_3$ (48.0 mg, 0.296 mmol) in acetonitrile (1 mL). A red, microcrystalline solid was formed and was collected and washed with acetonitrile (2 mL) and dried in vacuum (113.7 mg, 64.79%). Stoichiometric calculations for $C_{33}H_{57}FeO_6$ (605.66) were: C, 65.44; H, 9.49, while experimental values revealed C, 65.01; H, 9.66. NMR studies revealed: ^{1}H NMR (200 MHz, C_6D_6, 293 K, δ): 12.9 ppm (54 H, *t*-Bu) with mp 171–172 ºC. The unit cell of the crystals was checked by X-ray diffraction and found to coincide with that reported in the literature [42].

Sample preparation

All UHV-based depositions were performed on a Au(111) single crystal. The surface was cleaned by repeated Ar^+ sputtering (2 μA, 1 keV) and annealing (720 K) cycles. Considering that $Fe(dpm)_3$ and most β-diketonates show high volatility [43,44], the sublimation was performed in a dedicated preparation chamber with a base pressure of 1×10^{-7} mbar. Low deposition rates were obtained by keeping the molecular powders, hosted in a quartz crucible, at room temperature. In order to achieve higher deposition rates, the powders were heated to a temperature of about 338 K. During the sublimation, the substrate was kept a room temperature. A K-type thermocouple, buried into the powder, allowed for temperature control.

STM studies

The STM images were obtained by an UHV scanning tunnelling microscope (Omicron VT-STM) operating at 30 K in the constant current mode with electrochemically-etched W tips. The applied tip bias voltage and the tunnelling current of each image are given in the figure caption.

Photoelectron spectroscopy

XPS and UPS measurements were carried out in an UHV chamber with a base pressure in the low 10^{-10} mbar range. The chamber is equipped with a hemispherical analyser (VSW HA100) with a 16-channel detector, a monochromatic X-ray source (Al Kα source, E = 1486.6 eV), and a helium discharge lamp. The X-ray source was assembled at 54.44º with respect to the analyser and operated at a power of 100 W (13 kV and 7.7 mA). For the UPS spectra, the He II line (40.8 eV) was used for excitation. In order to ensure that all photoelectrons generated by the He II line were detected, a fixed bias of −30 V was applied to the sample. Both XPS and UPS spectra were recorded in normal emission with circular 5 mm entrance and exit slits. The pass energy was set to 44 and 10 eV for XPS and UPS spectra, respectively. For the XPS spectra, the binding energy scale was calibrated by setting the Au $4f_{7/2}$ peak at 80.04 eV. UPS spectra were calibrated such that the Fermi level was located at 0 eV.

X-ray absorption spectroscopy

The deposition was prepared by drop-casting using a 2 mM dichloromethane solution on a gold film grown on mica.

The Fe $L_{2,3}$ XMCD measurements were performed in total electron yield using a ±6.5 Tesla, 2 K cryomagnet endstation at the BACH beamline of the Elettra synchrotron facility in Trieste (Italy) [45]. For the measurements we used magnetic fields of ±3 T applied in the same direction of the synchrotron light propagation, sample temperature of 4 K, energy resolution below 100 meV and theoretical 100% degree of circular polarization. In order to suppress beam damage, the flux was reduced to have sample drain currents below 11 pA. The data were normalized using a Au grid located between the sample and the last focusing mirror of the beamline.

DFT calculations

The calculations for all model structures were performed with the Cp2k program package [46] within the DFT framework. The Grimme's D3 parameterization approach [47] was used to introduce the dispersion correction term. Norm-conserving Goedecker–Teter–Hutter (GTH) pseudopotentials [48] were used together with GTH double-ζ polarized molecularly optimized basis sets for all atomic species. The energy cut-off applied to the plane wave basis sets was set to 400 Ry. Geometry optimizations were performed with the PBEsol functional [49]. In all cases, the convergence criteria were fixed at 1×10^{-6} Hartree for the SCF energy and 1×10^{-3} Hartree $Bohr^{-1}$ for the atomic forces. A Fermi–Dirac distribution was used with a broadening (electronic temperature) of 300 K.

The following simulation cells sizes were used: $Fe(dpm)_3$@Au(111) – (17.3 × 15.0 × 40.0) $Å^3$ $FeOH(dpm)_2$@Au(111) and $Fe(dpm)_2$@Au(111) – (14.4 × 15.0 × 40.0) $Å^3$. During the geometry optimization, the atomic positions of the bottom Au layer were kept fixed to the bulk experimental distances (2.885 Å), whereas the other two layers were allowed to relax. In all simulated DOS studies, the Gaussian width of the convolution, σ, was set to 0.30 eV. The STM images were simulated according to the Tersoff–Hamman approximation [50] as implemented in Cp2k.

Supporting Information

Supporting information contains STM images of low rate deposition of Fe(dpm)3. An additional second layer of ordered and disordered domains is visible.

Supporting Information File 1

Additional STM images.
[http://www.beilstein-journals.org/bjnano/content/supplementary/2190-4286-5-223-S1.pdf]

Acknowledgements

We are grateful to Silvia Nappini (IOM-CNR), Igor Píš (Sincrotrone Trieste) and Federico Salvador (IOM-CNR) for their assistance during the experiment at the BACH beamline of the ELETTRA synchrotron. Funding from the European Research Council through the Advanced Grant "MolNanoMas" (267746) and from the Italian MIUR through FIRB projects "NanoPlasMag" (RBFR10OAI0) and "Nanomagneti molecolari su superfici metalliche e magnetiche per applicazioni nella spintronica molecolare" (RBAP117RWN) is acknowledged. The support of Ente Cassa di Risparmio di Firenze is also acknowledged.

References

1. Zadrozny, J. M.; Liu, J.; Piro, N. A.; Chang, C. J.; Hill, S.; Long, J. R. *Chem. Commun.* **2012,** *48,* 3927–3929. doi:10.1039/c2cc16430b
2. Zadrozny, J. M.; Atanasov, M.; Bryan, A. M.; Lin, C.-Y.; Rekken, B. D.; Power, P. P.; Neese, F.; Long, J. R. *Chem. Sci.* **2013,** *4,* 125–138. doi:10.1039/c2sc20801f
3. Huang, W.; Liu, T.; Wu, D.; Cheng, J.; Ouyang, Z. W.; Duan, C. *Dalton Trans.* **2013,** *42,* 15326–15331. doi:10.1039/c3dt51801a

4. Vallejo, J.; Castro, I.; Ruiz-García, R.; Cano, J.; Julve, M.; Lloret, F.; De Munno, G.; Wernsdorfer, W.; Pardo, E. *J. Am. Chem. Soc.* **2012,** *134,* 15704–15707. doi:10.1021/ja3075314
5. Gomez-Coca, S.; Cremades, E.; Aliaga-Alcalde, N.; Ruiz, E. *J. Am. Chem. Soc.* **2013,** *135,* 7010–7018. doi:10.1021/ja4015138
6. Gómez-Coca, S.; Urtizberea, A.; Cremades, E.; Alonso, P. J.; Camón, A.; Ruiz, E.; Luis, F. *Nat. Commun.* **2014,** *5,* No. 4300. doi:10.1038/ncomms5300
7. Sessoli, R.; Gatteschi, D.; Caneschi, A.; Novak, M. A. *Nature* **1993,** *365,* 141–143. doi:10.1038/365141a0
8. Gatteschi, D.; Caneschi, A.; Pardi, L.; Sessoli, R. *Science* **1994,** *265,* 1054–1058. doi:10.1126/science.265.5175.1054
9. Gatteschi, D.; Sessoli, R. *Angew. Chem., Int. Ed. Engl.* **2003,** *42,* 268–297. doi:10.1002/anie.200390099
10. Bogani, L.; Wernsdorfer, W. *Nat. Mater.* **2008,** *7,* 179–186. doi:10.1038/nmat2133
11. Siddiqi, M. A.; Siddiqui, R. A.; Atakan, B. *Surf. Coat. Technol.* **2007,** *201,* 9055–9059. doi:10.1016/j.surfcoat.2007.04.036
12. Margheriti, L.; Mannini, M.; Sorace, L.; Gorini, L.; Gatteschi, D.; Caneschi, A.; Chiappe, D.; Moroni, R.; de Mongeot, F. B.; Cornia, A.; Piras, F. M.; Magnani, A.; Sessoli, R. *Small* **2009,** *5,* 1460–1466. doi:10.1002/smll.200801594
13. Mannini, M.; Pineider, F.; Sainctavit, P.; Danieli, C.; Otero, E.; Sciancalepore, C.; Talarico, A. M.; Arrio, M.-A.; Cornia, A.; Gatteschi, D.; Sessoli, R. *Nat. Mater.* **2009,** *8,* 194–197. doi:10.1038/nmat2374
14. Mannini, M.; Pineider, F.; Danieli, C.; Totti, F.; Sorace, L.; Sainctavit, Ph.; Arrio, M. A.; Otero, E.; Joly, L.; Cezar, J. C.; Cornia, A.; Sessoli, R. *Nature* **2010,** *468,* 417–421. doi:10.1038/nature09478
15. Burzurí, E.; Zyazin, A. S.; Cornia, A.; van der Zant, H. S. J. *Phys. Rev. Lett.* **2012,** *109,* 147203. doi:10.1103/PhysRevLett.109.147203
16. Burzurí, E.; Yamamoto, Y.; Warnock, M.; Zhong, X.; Park, K.; Cornia, A.; van der Zant, H. S. J. *Nano Lett.* **2014,** *14,* 3191–3196. doi:10.1021/nl500524w
17. Mulley, J. S.; Bennett, R. A.; Dhanak, V. R. *Surf. Sci.* **2008,** *602,* 2967–2974. doi:10.1016/j.susc.2008.07.026
18. Lin, W.; Wiegand, B. C.; Nuzzo, R. G.; Girolami, G. S. *J. Am. Chem. Soc.* **1996,** *118,* 5977–5987. doi:10.1021/ja944130h
19. Ninova, S.; Lanzilotto, V.; Malavolti, L.; Rigamonti, L.; Cortigiani, B.; Mannini, M.; Totti, F.; Sessoli, R. *J. Mater. Chem. C* **2014,** *2,* 9599–9608. doi:10.1039/C4TC01647E
20. Petrova, N. V.; Yakovkin, I. N. *Eur. Phys. J. B* **2013,** *86,* 303. doi:10.1140/epjb/e2013-40105-5
21. Tiitta, M.; Niinistou, L. *Chem. Vap. Deposition* **1997,** *3,* 167–182. doi:10.1002/cvde.19970030404
22. Turnipseed, S. B.; Barkley, R. M.; Sievers, R. E. *Inorg. Chem.* **1991,** *30,* 1164–1170. doi:10.1021/ic00006a003
23. Cohen, S. L.; Liehr, M.; Kasi, S. *Appl. Phys. Lett.* **1992,** *60,* 50–52. doi:10.1063/1.107370
24. Donnelly, V. M.; Gross, M. E. *J. Vac. Sci. Technol., A* **1993,** *11,* 66–77. doi:10.1116/1.578721
25. Nuesca, G.; Prasad, J.; Kelber, J. A. *Appl. Surf. Sci.* **1994,** *81,* 237–249. doi:10.1016/0169-4332(94)00168-5
26. Nuesca, G. M.; Kelber, J. A. *Thin Solid Films* **1995,** *262,* 224–233. doi:10.1016/0040-6090(94)05811-3
27. Cohen, S. L.; Liehr, M.; Kasi, S. *Appl. Phys. Lett.* **1992,** *60,* 1585–1587. doi:10.1063/1.107259
28. Munery, S.; Ratel-Ramond, N.; Benjalal, Y.; Vernisse, L.; Guillermet, O.; Bouju, X.; Coratger, R.; Bonvoisin, J. *Eur. J. Inorg. Chem.* **2011,** *2011,* 2698–2705. doi:10.1002/ejic.201100116
29. Vernisse, L.; Munery, S.; Ratel-Ramond, N.; Benjalal, Y.; Guillermet, O.; Bouju, X.; Coratger, R.; Bonvoisin, J. *J. Phys. Chem. C* **2012,** *116,* 13715–13721. doi:10.1021/jp304523f
30. Garcia, Y.; Niel, V.; Muñoz, M. C.; Real, J. A. Spin Crossover in 1D, 2D and 3D Polymeric Fe(II) Networks. In *Spin Crossover in Transition Metal Compounds I;* Gütlich, P.; Goodwin, H. A., Eds.; Topics in Current Chemistry, Vol. 233; Springer Verlag: Berlin-Heidelberg, Germany, 2004; pp 229–257. doi:10.1007/b95408
31. Bernien, M.; Wiedemann, D.; Hermanns, C. F.; Krüger, A.; Rolf, D.; Kroener, W.; Müller, P.; Grohmann, A.; Kuch, W. *J. Phys. Chem. Lett.* **2012,** *3,* 3431–3434. doi:10.1021/jz3011805
32. Palamarciuc, T.; Oberg, J. C.; El Hallak, F.; Hirjibehedin, C. F.; Serri, M.; Heutz, S.; Létard, J.-F.; Rosa, P. *J. Mater. Chem.* **2012,** *22,* 9690. doi:10.1039/c2jm15094h
33. Miyamachi, T.; Gruber, M.; Davesne, V.; Bowen, M.; Boukari, S.; Joly, L.; Scheurer, F.; Rogez, G.; Yamada, T. K.; Ohresser, P.; Beaurepaire, E.; Wulfhekel, W. *Nat. Commun.* **2012,** *3,* No. 938. doi:10.1038/ncomms1940
34. Warner, B.; Oberg, J. C.; Gill, T. G.; El Hallak, F.; Hirjibehedin, C. F.; Serri, M.; Heutz, S.; Arrio, M.-A.; Sainctavit, P.; Mannini, M.; Poneti, G.; Sessoli, R.; Rosa, P. *J. Phys. Chem. Lett.* **2013,** *4,* 1546–1552. doi:10.1021/jz4005619
35. Gruber, M.; Davesne, V.; Bowen, M.; Boukari, S.; Beaurepaire, E.; Wulfhekel, W.; Miyamachi, T. *Phys. Rev. B* **2014,** *89,* 195415. doi:10.1103/PhysRevB.89.195415
36. Gopakumar, T. G.; Matino, F.; Naggert, H.; Bannwarth, A.; Tuczek, F.; Berndt, R. *Angew. Chem., Int. Ed. Engl.* **2012,** *51,* 6262–6266. doi:10.1002/anie.201201203
37. Brice-Profeta, S.; Arrio, M. A.; Tronc, E.; Menguy, N.; Letard, I.; Cartier dit Moulin, C.; Nouguès, M.; Chanéac, C.; Jolivet, J.-P.; Sainctavit, P. *J. Magn. Magn. Mater.* **2005,** *288,* 354–365. doi:10.1016/j.jmmm.2004.09.120
38. Carvallo, C.; Sainctavit, P.; Arrio, M.-A.; Menguy, N.; Wang, Y.; Ona-Nguema, G.; Brice-Profeta, S. *Am. Mineral.* **2008,** *93,* 880–885. doi:10.2138/am.2008.2713
39. Hocking, R. K.; Wasinger, E. C.; de Groot, F. M. F.; Hodgson, K. O.; Hedman, B.; Solomon, E. I. *J. Am. Chem. Soc.* **2006,** *128,* 10442–10451. doi:10.1021/ja061802i
40. Mannini, M.; Pineider, F.; Sainctavit, P.; Joly, L.; Fraile-Rodríguez, A.; Arrio, M.-A.; Cartier dit Moulin, C.; Wernsdorfer, W.; Cornia, A.; Gatteschi, D.; Sessoli, R. *Adv. Mater.* **2009,** *21,* 167–171. doi:10.1002/adma.200801883
41. Mannini, M.; Tancini, E.; Sorace, L.; Sainctavit, P.; Arrio, M.-A.; Qian, Y.; Otero, E.; Chiappe, D.; Margheriti, L.; Cezar, J. C.; Sessoli, R.; Cornia, A. *Inorg. Chem.* **2011,** *50,* 2911–2917. doi:10.1021/ic102184n
42. Baidina, I. A.; Stabnikov, P. A.; Alekseev, V. I.; Igumenovand, I. K.; Borisov, S. V. *J. Struct. Chem.* **1986,** *27,* 427–433. doi:10.1007/BF00751824
43. Evans, S.; Hamnett, A.; Orchard, A. F.; Lloyd, D. R. *Faraday Discuss. Chem. Soc.* **1972,** *54,* 227–250. doi:10.1039/dc9725400227
44. da Silva, M. A. V. R.; Monte, M. J. S.; Huinink, J. *J. Chem. Thermodyn.* **1996,** *28,* 413–419. doi:10.1006/jcht.1996.0041

45. Zangrando, M.; Zacchigna, M.; Finazzi, M.; Cocco, D.; Rochow, R.; Parmigiani, F. *Rev. Sci. Instrum.* **2004,** *75,* 31–36. doi:10.1063/1.1634355
46. Mundy, C. T.; Mohamed, F.; Schiffman, F.; Tabacchi, G.; Forbert, H.; Kuo, W.; Hutter, J.; Krack, M.; Iannuzzi, M.; McGrath, M.; Guidon, M.; Kuehne, T. D.; VandeVondele, J.; Weber, V. CP2K, version 2.6.
47. Grimme, S.; Antony, J.; Ehrlich, S.; Krieg, H. *J. Chem. Phys.* **2010,** *132,* 154104. doi:10.1063/1.3382344
48. Goedecker, S.; Teter, M.; Hutter, J. *Phys. Rev. B* **1996,** *54,* 1703–1710. doi:10.1103/PhysRevB.54.1703
49. Perdew, J. P.; Ruzsinszky, A.; Csonka, G. I.; Vydrov, O. A.; Scuseria, G. E.; Constantin, L. A.; Zhou, X.; Burke, K. *Phys. Rev. Lett.* **2008,** *100,* 136406. doi:10.1103/PhysRevLett.100.136406
50. Tersoff, J.; Hamann, D. R. *Phys. Rev. B* **1993,** *31,* 805–813. doi:10.1103/PhysRevB.31.805

License and Terms

BEILSTEIN JOURNAL OF NANOTECHNOLOGY

In situ metalation of free base phthalocyanine covalently bonded to silicon surfaces

Fabio Lupo[1], Cristina Tudisco[1], Federico Bertani[2], Enrico Dalcanale[2] and Guglielmo G. Condorelli[*1]

Full Research Paper

Open Access

Address:
[1]Dipartimento di Scienze Chimiche, Università di Catania and INSTM UdR di Catania, v.le A. Doria 6, 95125 Catania, Italy and
[2]Dipartimento di Chimica and INSTM UdR di Parma Università of Parma Parco Area delle Scienze 17/A, 43124 Parma, Italy

Email:
Guglielmo G. Condorelli[*] - guido.condorelli@unict.it

* Corresponding author

Keywords:
metalation; phthalocyanine; silicon surface; surface functionalization; X-ray photoelectron spectroscopy (XPS)

Beilstein J. Nanotechnol. **2014,** *5,* 2222–2229.
doi:10.3762/bjnano.5.231

Received: 09 July 2014
Accepted: 03 November 2014
Published: 25 November 2014

This article is part of the Thematic Series "Molecular materials – towards quantum properties".

Guest Editor: M. Ruben

Abstract

Free 4-undecenoxyphthalocyanine molecules were covalently bonded to Si(100) and porous silicon through thermic hydrosilylation of the terminal double bonds of the undecenyl chains. The success of the anchoring strategy on both surfaces was demonstrated by the combination of X-ray photoelectron spectroscopy with control experiments performed adopting the commercially available 2,3,9,10,16,17,23,24-octakis(octyloxy)-29*H*,31*H*-phthalocyanine, which is not suited for silicon anchoring. Moreover, the study of the shape of the XPS N 1s band gave relevant information on the interactions occurring between the anchored molecules and the substrates. The spectra suggest that the phthalocyanine ring interacts significantly with the flat Si surface, whilst ring–surface interactions are less relevant on porous Si. The surface-bonded molecules were then metalated in situ with Co by using wet chemistry. The efficiency of the metalation process was evaluated by XPS measurements and, in particular, on porous silicon, the complexation of cobalt was confirmed by the disappearance in the FTIR spectra of the band at 3290 cm^{-1} due to –NH stretches. Finally, XPS results revealed that the different surface–phthalocyanine interactions observed for flat and porous substrates affect the efficiency of the in situ metalation process.

Introduction

Free (Pc) and metallophthalocyanines (M–Pc) are molecules of great interest because of their versatile optical and electronic properties as well as their thermal stability [1]. These properties make them attractive molecular materials for applications in photovoltaic cells [2], sensing devices [3,4], catalysis [5], cancer therapy [6] and molecular electronics [3,7,8]. The most promising architecture for the exploitation of the potentialities of Pc and M–Pc is the organization of the molecules in a suit-

able and accessible way on a solid surface. Therefore, phthalocyanine thin films have been deposited by using different techniques including Langmuir–Blodgett deposition [9], spin-coating [10] and vapor deposition [10,11]. Well-organized monolayers and multilayers have been also obtained through self-assembly [12,13]. Among the various approaches adopted to organize phthalocyanines on surfaces, covalent grafting on H-terminated silicon through hydrosilylation reaction has the advantage to form robust and highly stable Si–C bonds. For this reason, a device based on silicon-grafted molecules possesses a much greater robustness and reliability compared to van der Waals films or Au-bonded layers, which makes these systems suited for application in aggressive environments [14-16]. In addition, the possible use of differently doped silicon substrates could influence the electronic properties of grafted Pc and M–Pc [3], and, in turn, the device properties. Furthermore, the overall chemical and physical properties of M–Pc can be easily tuned by varying the nature of the coordinated metal, thus making phthalcyanine-based systems suitable for a wide range of applications. In particular, transition metal Pc have attracted great interest for their optical and magnetic properties [8,17] as well as for their potential catalytic [5] and sensing applications [4]. Various metallophthalocyanines (Zn, Fe, Co, Cu, Sn) have been deposited as monolayers and multilayers on various surfaces [13,18] and, in some cases, free base Pc have been metalated directly on the metal surface from vapor-deposited atoms [19,20]. However, no report of the direct metalation of covalently bonded Pc on inorganic surfaces has been reported, yet.

In this work we study the silicon grafting of the tetra-4-(ω-undecenyloxy)phthalocyanine (thereafter **1-Pc**) (Figure 1) and its interaction with a silicon surface. **1-Pc** was synthesized to allow for a silicon grafting by functionalization with four undecenyl chains each having a terminal double bond. Phthalocyanine covalent anchoring was performed through thermic hydrosilylation on flat Si(100) and on porous silicon (**Si-1-Pc** and **PSi-1-Pc**, respectively). The success of the anchoring strategy on both surfaces was demonstrated by the combination of X-ray photoelectron spectroscopy (XPS) with control experiments performed adopting the commercially available 2,3,9,10,16,17,23,24-octakis(octyloxy)-29*H*,31*H*-phthalocyanine (thereafter **2-Pc**), which is not suited for silicon anchoring (Figure 1).

1-Pc covalently bonded to silicon surface was in situ metalated with Co by using a solution of cobalt chloride. The direct formation of Co-Pc on flat and porous Si **(Si-Co-Pc** and **PSi-Co-Pc**, respectively) was monitored by XPS and FTIR. In particular, for phthalocyanines anchored on porous Si, transmission FTIR represents a suitable technique to monitor the formation

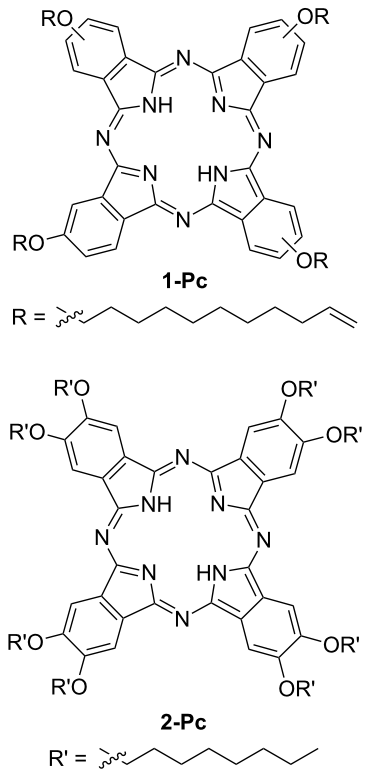

Figure 1: Chemical structures of **1-Pc** and **2-Pc**.

M–Pc through the disappearance of the band at 3290 cm^{-1}, corresponding to the pyrrolic –NH streches [21]. Differences in the metalation efficiency between porous and flat silicon were evaluated by XPS and explained in terms of different surface interactions.

Results and Discussion

Synthesis of **1-Pc**

Phthalocyanine **1-Pc** was prepared according to a slightly modified literature procedure [22] starting from the 4-(ω-undecenyloxy)phthalonitrile in refluxing 1-pentanol in presence of a catalytic amount of 1,8- diazabicyclo[5.4.0]undec-7-ene (DBU) as a basic catalyst. The target compound was isolated in 58% yield as a dark-green powder after purification. **1-Pc** was successfully characterized by ^{1}H NMR and MALDI–TOF mass spectrometry (see Experimental section).

XPS characterization of Si-bonded phthalocyanine

Covalent anchoring of **1-Pc** on flat Si(100) and porous Si was performed through thermally activated hydrosilylation and the functionalized samples (**Si-1-Pc** and **PSi-1-Pc**, respectively) were characterized through XPS. In addition, further experiments were performed to demonstrate that the surface anchoring is not due to physisorption but it is due to the hydrosilylation reaction. Control samples were, therefore, prepared by treating

flat and porous silicon surfaces with a phthalocyanine (**2-Pc**), in which no double bonds are present in the lateral chains, under the same experimental conditions adopted for **1-Pc** anchoring. Elemental compositions of **1-Pc** and **2-Pc** treated samples are reported in Table 1.

Table 1: Atomic compositions (%) evaluated through XPS of **1-Pc** treated flat (**Si-1-Pc**) and porous (**PSi-1-Pc**) silicon samples. Analogous samples obtained from **2-Pc** treatment (**Si-2-Pc** and **PSi-2-Pc**) have been also reported as control experiments.

	Si-1-Pc	Si-2-Pc	PSi-1-Pc	PSi-2-Pc
C	36.6	11.8	56.5	30.5
N	2.4	0.5	4.6	0.6
Si	38.8	46.7	29.6	34.3
O	22.2	41.0	9.3	34.6

XPS data show that **Pc**-related signals (C 1s and N 1s) are higher for the **1-Pc** treated samples compared to the **2-Pc** treated samples. Since the C 1s signal is affected by the presence of ubiquitous adventitious carbon [23,24], the success of Pc anchoring route can be evaluated from the N 1s signal, which is very low for **Si-2-Pc** and **PSi-2-Pc** samples while it is about 5 and 8 times higher for **1-Pc** treated surfaces. These data point to a surface-anchoring process determined by the hydrosilylation reaction of the double bonds while physisorption phenomena play a much less relevant role.

The surface density of **1-Pc** on flat Si(100) was estimated from XPS data (Table 1) [25-27]. The obtained value, ca. 2×10^{13} molecules/cm^2, points to a molecular footprint of 5 nm^2 for each molecular unit, which is intermediate between the cross-sectional areas expected for a configuration with the side chains vertical with respect to the phthalocyanine ring (ca. 1 nm^2) and a configuration in which all four alkyl side chains are full extended in the same plane of the ring (ca. 9 nm^2).

Useful information about the nature of the grafted layers was obtained from high-resolution spectra of the relevant photoemission bands. Figure 2 reports the C 1s photoelectron spectra of **Si-1-Pc** (a) and **PSi-1-Pc** (b). The observed bands do not show significant differences between flat and porous samples. For both samples, a careful deconvolution of the band envelope reveals three components: a main peak centered at 285.0 eV, due to both aliphatic and aromatic carbons [11]; a band at a binding energy (B.E.) of 286.5 eV due to the pyrrole carbons and to the shake-up related to benzene carbons, in tune with literature data [11]; and finally, a band at 288.3 eV (288.1 eV for **PSi-1-Pc**) due to the shake-up transition associated with the photoionization of pyrrole [11].

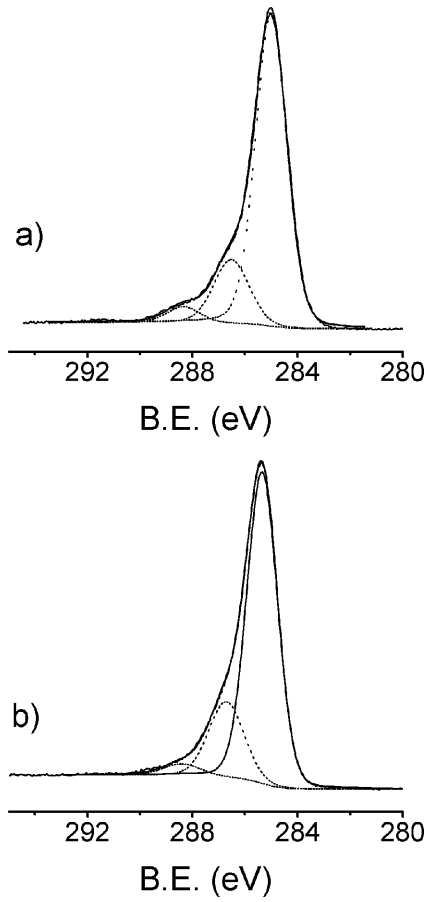

Figure 2: C1s XPS spectral region of **Si-1-Pc** (a) and **PSi-1-Pc** (b).

The N 1s XPS spectral regions of **Si-1-Pc** and **PSi-1-Pc** are reported in Figure 3a and 3b, respectively. The spectrum collected from **Si-1-Pc** shows two bands, at B.E. values of 398.8 and 400.4 eV. The first signal is due to non-protonated pyrrolic nitrogen atoms and due to iminic bridges, whilst the high B.E. signal is due to protonated pyrrolic nitrogen atoms [28-30]. However the intensity ratio between the 398.8 and 400.6 eV bands is 2:3, which is significantly different from the value (3:1) expected for free-base phthalocyanines [28-30]. The increase of the high B.E signal can be explained as a consequence of the interaction with the silicon surface. The effects of various surfaces on the shape of the N 1s band have been already observed and discussed for other metal phthalocyanine monolayers adsorbed on oxide semiconductors [28-30] and, recently, reported also for double-decker complexes on silicon [31]. In general, according to the mentioned studies, the interaction between the fraction of anchored phthalocyanine lying down close to the surface and the semiconductors surface itself, induce an electron depletion in the phthalocyanine ring and, in turn, a high energy shift (about 1.5 eV) from 398.8 to about 400.3 eV of the main N 1s component due to deprotonated

nitrogen atoms [28,29,31]. Possible local interactions (i.e., H-bonds) between the phthalocyanine ring lying down close to the surface and the Si surface itself could contribute to a similarly high B.E. shift [32] and cannot be excluded. In any case, the surface-induced shift can explain the increase of the component at 400.4 eV and also the presence of a low shoulder at around 401.8 eV due to protonated nitrogen atoms.

The N 1s XPS spectrum of **Psi-1-Pc** (Figure 3b) shows a different situation. The N 1s band consists of the same two components at 398.6 and 400.4 eV observed for **Si-1-Pc**, but in this case the component ratio is 2:1, which is closer to the value expected for free phthalocyanine, thus indicating that there are no strong interactions between the surface of PSi and the Pc molecules.

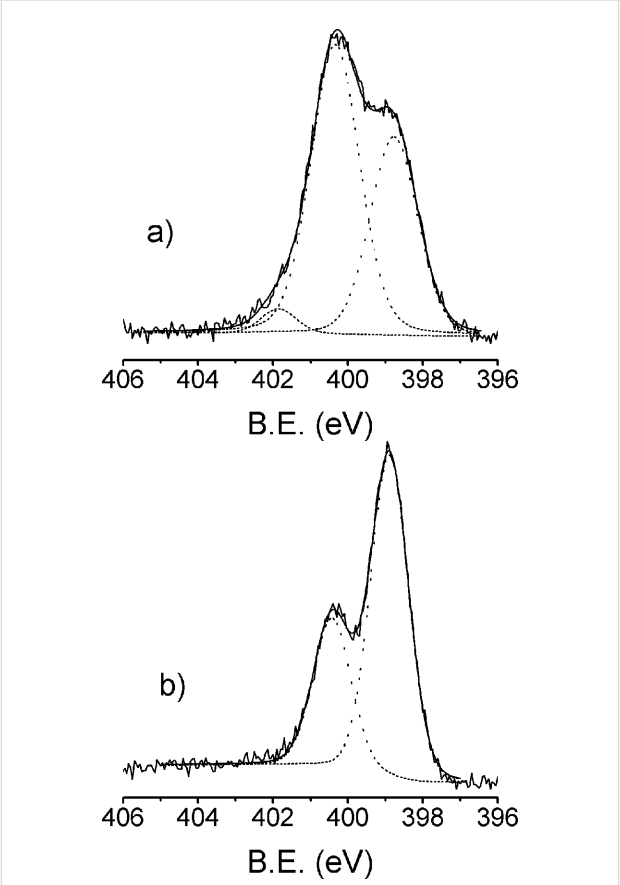

Figure 3: N 1s XPS spectral region of **Si-1-Pc** (a) and **PSi-1-Pc** (b).

Metalation of SAM

The possibility to induce a direct metalation of the grafted Pc was explored for both **Si-1-Pc** and **PSi-1-Pc** samples. **1-Pc** that was covalently bonded to Si and PSi surfaces has been treated with a solution of $CoCl_2$ in diglyme in the presence of triethylamine and then accurately sonicated to remove any physisorbed salt. XPS characterization of cobalt treated **Si-1-Pc** and **PSi-1-Pc** samples (**Si-Co-Pc** and **PSi-Co-Pc**, respectively) clearly showed the presence of Co, whilst no Cl could be detected (Cl content < 0.1% noise level). Similar bands centered at 781.2 eV are present in the spectra of both **Si-Co-Pc** and **PSi-Co-Pc** (Figure 4a and Figure 4b). Although this band position is consistent with the presence of Co(II) atoms, the peak position and, in particular, the absence of the intense shake-up typical of Co(II) compounds such as $CoCl_2$ (Figure 4c) indicate that Co signal is not due to physisorbed $CoCl_2$. The observed band shape and position are consistent with spectra reported for Co-phthalocyanine thin films [33-35].

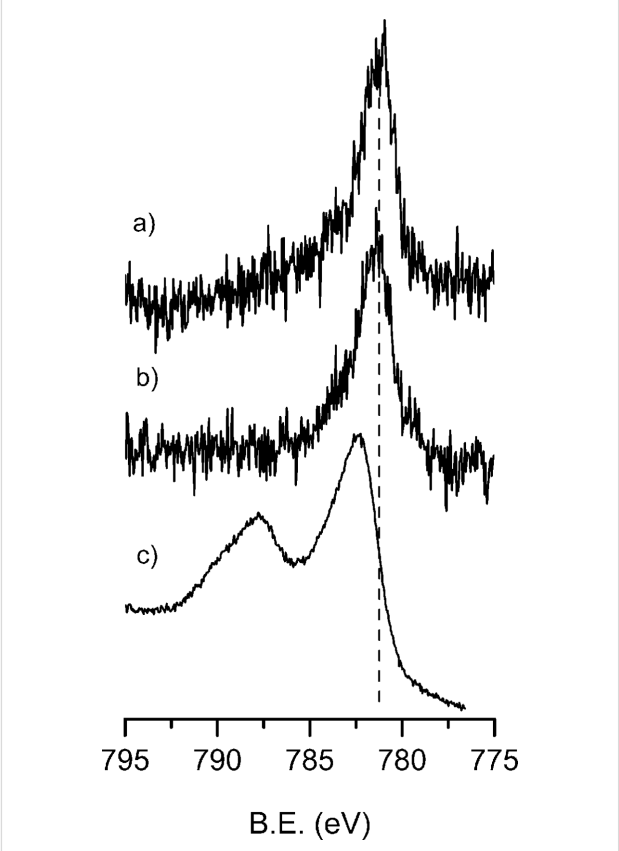

Figure 4: Co 2p3/2 XPS spectral region of **Si-Co-Pc** (a) and **PSi-Co-Pc** (b). The Co 2p3/2 region of $CoCl_2$ powder (c) has been added as reference.

In addition, complexation efficiency was estimated from the N/Co atomic ratio determined through XPS. Considering a theoretical N/Co ratio of 8 expected for 100% of complexation, N/Co ratios obtained for **Si-Co-Pc** and **PSi-Co-Pc** (28.6 and 10.7, respectively) indicate a percentage of metalation of 28% and 75%, respectively.

Further indication of Co complexation in the Pc-ring was obtained from the analysis of the N 1s spectra (Figure 5) after

metalation. Clearly the presence of cobalt gives rise to a modification on the N 1s band shape compared to spectra before metalation (Figure 3). As expected, after metalation the intensity of the component at 400.4 eV due to –NH pyrrolic nitrogen atoms decreases compared to the low B.E. component at 398.8 eV since the metal coordination is associated to the deprotonation of pyrrolic nitrogen atoms to form N–Co [36]. In particular, for **PSi-Co-Pc,** for which the metalation efficiency is higher than that of **Si-Co-Pc,** the 400.4 eV signal becomes much lower and the spectrum becomes similar to the typical spectra of M–Pc in which a single band at low B.E. is present [36]. Note, in addition, that eventual interferences due to triethylamine physisorption on **PSi,** which would lead to the increase of the N 1s component around 400 eV**,** can be ruled out since the reverse trend was observed for **PSi-1-Pc**. Overall the metalation appears more efficient in the case of the porous silicon substrate compared to flat Si(100). This behavior is likely to be associated to the different surface interactions observed for **Si-1-Pc** and **PSi-1-Pc**. In the case of a flat substrate the proposed strong surface interaction of the fraction of **1-Pc** lying down close the substrate prevents an efficient insertion of Co in the Pc ring, whilst in the case of porous samples, less strong surface interactions allow for a more efficient metalation.

Further information about the grafting of **1-Pc** on porous silicon and about the in situ metalation could be obtained from transmission FTIR spectra by taking advantage of the high surface area of **PSi**. Figure 6 compares the FTIR region of 3400–2800 cm^{-1} in which $–CH_x$ and –NH stretches are present before and after the metalation. Typical bands present before the metalation are the strong CH_2 stretches $\nu_{as}(CH_2)$ at 2925 cm^{-1} and $\nu_{sym}(CH_2)$ at 2854 cm^{-1}, the weak =CH

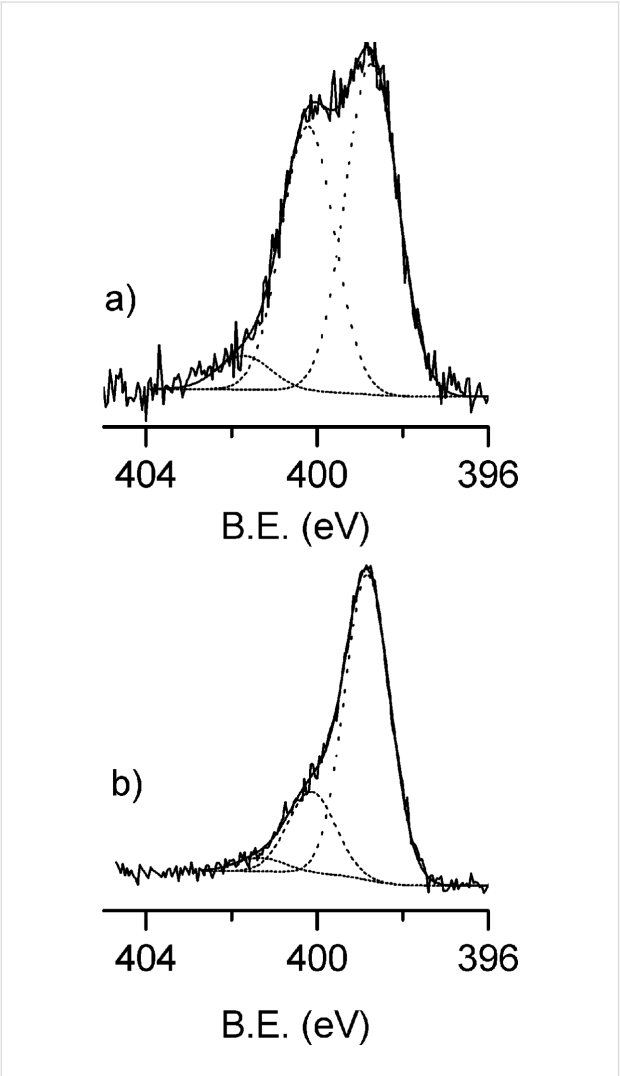

Figure 5: N 1s XPS region of **Si-Co-Pc** (a) and **PSi-Co-Pc** (b).

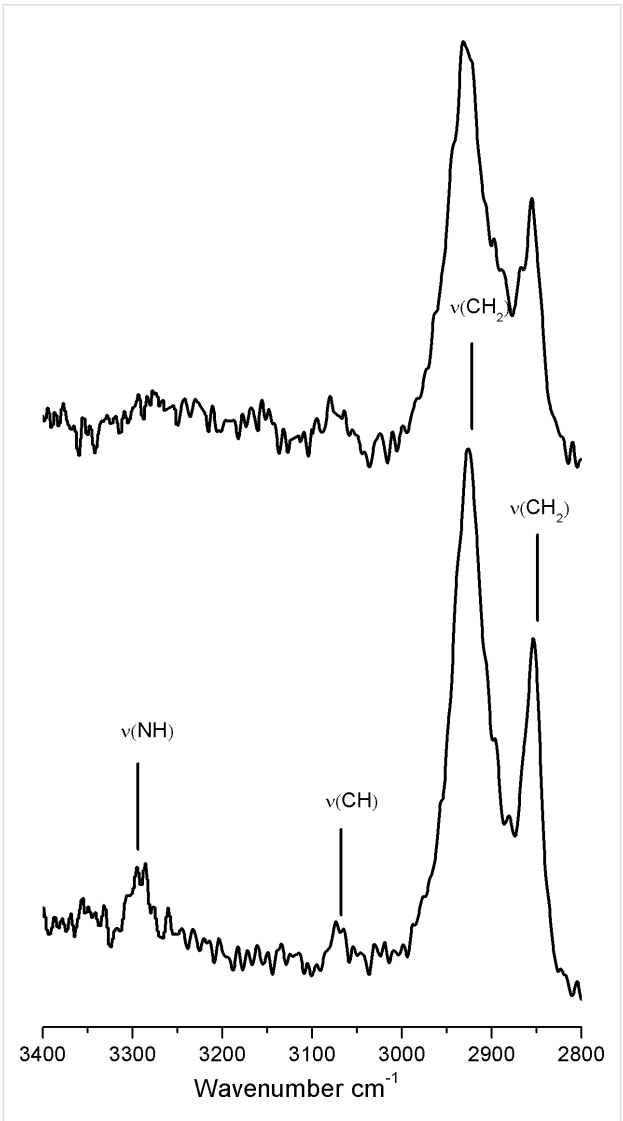

Figure 6: FTIR spectral region between 3400–2800 cm^{-1} (CH_x stretching region) of **PSi-1-Pc** (below) and **PSi-Co-Pc** (above).

stretches ν(=CH) of the aromatic rings at 3070 cm^{-1} and the characteristic –NH stretch of pyrrolic nitrogen atoms at about 3290 cm^{-1}. After metalation, –NH stretch vibrations cannot longer be clearly detected, whilst the other bands are still observed. Since triethylamine is unable to deprotonate the phthalocyanine, the absence of N–H bonds is exclusively due to the Co complexation [21].

Conclusion

The results presented here report on a grafting route to covalent anchor phthalocyanine on flat and porous silicon surfaces. The grafting route was validated by XPS characterization and control experiments that were performed by adopting a phthalocyanine inert towards hydrosilylation. XPS results also suggest that on flat substrates a relevant fraction of phthalocyanine interacts significantly with the silicon surface, thus inducing evident modifications of the N 1s band shape. On porous silicon, surface interactions are less relevant and the N 1s band shape is similar to the typical shape of free Pc.

In situ complexation of Co was achieved with phthalocyanine bonded to both flat and porous silicon surfaces. However, the metalation efficiency is higher in the case of porous samples. These differences were attributed to the different surface interactions observed for the two samples. If strong surface interactions are present, as in the case of flat silicon, metalation is less efficient, whilst if Pc does not interact significantly with the surface, as in the case of PSi, the efficiency of the metalation improves. Although further work is required to better clarify the nature of interaction between the silicon surface and the molecular system, these results represent a step forward in the understanding of the chemistry of phthalocyanine covalently bonded to inorganic surfaces.

Experimental

Reagents

All chemicals, unless otherwise noted, were commercially available and used as received. Water used for porous silicon and monolayer preparations was a Milli-Q grade (18.2 MΩ·cm) with a final filtering step through a 0.22 μm filter. **2-Pc** was purchased from Aldrich chemicals.

1-Pc synthesis

To a stirred solution of 4-(ω-undecenyloxy)phthalonitrile [22] (300.0 mg, 1.01 mmol) in 1-pentanol (10 mL) a catalytic amount of DBU was added. The resulting solution was stirred at 135 °C for 14 h under N_2. After cooling, methanol was added to the residue until a precipitate formed. The green finely dispersed mixture was filtered off and purified by flash chromatography (DCM as eluent) to give **1-Pc** as a green solid (174.0 mg, 58% yield). ^{1}H NMR (400 MHz, $CDCl_3$) δ 6.91–6.72 (br), 5.99–5.93 (m, 4H), 5.16–5.05 (m, 8H), 3.98 (bs, 8H), 2.22 (m, 8H), 2.01 (bs, 8H), 1.71–1.54 (m, 48H); MALDI–TOF (*m*/*z*): $[M]^+$ calcd for $C_{76}H_{98}N_8O_4$, 1186.77; found, 1186.79.

Preparation of **Si-1-Pc** and **PSi-1-Pc**

The anchoring of **1-Pc** on a single crystalline, Czochralski grown, p-type boron-doped, (100)-oriented silicon substrate was performed through a well establish thermal hydrosilylation route [37,38]. Similarly to the procedure described in [38], Si(100) substrates were first cleaned with ''piranha'' solution (H_2SO_4 (30%)/H_2O_2 70:30, v/v) at room temperature for 12 min, rinsed in double distilled water for 2 min, etched in 2% hydrofluoric acid for 90 s, washed with double distilled water for 20 s, accurately dried with pre-purified N_2, and immediately placed in a three neck flask containing 10 mL of anhydrous mesitylene (Sigma-Aldrich) in which was dissolved 25 mg of **1-Pc** (2.1 mmol/L). The solution was then refluxed at 190 °C for 2 h, under slow N_2 bubbling. After cooling to room temperature, the substrates were removed from the flask, rinsed, and repeatedly sonicated in dichloromethane, pentane, and toluene to remove any residual unreacted Pc.

Porous Si (PSi) was prepared by a metal-assisted chemical etching method [39]. A Czochralski grown, p-type boron-doped, Si(100) substrate was immersed in an aqueous solution of 0.14 M HF and 5×10^{-4} M in $AgNO_3$ for 5 min, washed in water and then immersed for 1 min in a solution of HF (65%)/H_2O_2 (25%)/H_2O (10%), washed in water and then left for 1 h in a solution of HF (20%)/H_2O (80%). At the end, the substrate was washed, dried and placed in a three-neck flask containing a solution of **1-Pc** in mesitylene (2.1 mmol/L) and treated as described for flat Si(100) grafting. In this case the reaction time was increased to 4 h.

Control experiments were performed by placing non-etched Si(100) or PSi substrates in a three-neck flask containing a **2-Pc** solution (2.1 mmol/L) in mesitylene and treated as described for Si(100) or PSi grafting.

Direct metalation

Metalation of the silicon-anchored Pc was obtained by wet chemistry. The freshly prepared **Si-1-Pc** and **PSi-1-Pc** were immersed in a flask containing a cobalt solution and then refluxed at 160 °C for 8 h, under slow N_2 bubbling. The solution was prepared by dissolving 80 mg of $CoCl_2$ in 20 mL of anhydrous diglyme and 3 mL of TEA (triethylamine). The substrates were finally washed several times with diglyme and sonicated first in CH_2Cl_2 and then in EtOH.

Material characterisations

X-ray photoelectron spectra (XPS) were measured at a take-off angle of 45°, relative to the surface plane, with a PHI 5600 Multi Technique System (base pressure of the main chamber 2×10^{-10} Torr). The spectrometer is equipped with a dual Mg/Al standard X-ray source and a monochromatized Al source, a spherical capacitor analyzer (SCA) with a mean diameter of 279.4 mm. The samples were excited with monochromatized Al Kα radiation. The XPS peak intensities were obtained after Shirley background removal. No relevant charging effect was observed. Freshly prepared samples were quickly transferred to the XPS main chamber. The XPS binding energy scale was calibrated by centering the C 1s peak (due to hydrocarbon moieties and adventitious carbon) at 285.0 eV [24,40]

Infrared attenuated total reflectance spectra of the monolayers were recorded by using a Jasco FT/IR-430 spectrometer (100 scans collected per spectrum, scan range 560–4000 cm^{-1}, resolution 4 cm^{-1}).

Acknowledgements

The authors thank Ministero dell'Istruzione, dell'Università e della Ricerca (MIUR) for financial support through FIRB "RINAME Rete Integrata per la NAnoMEdicina" (RBAP114AMK). F. Lupo also thanks Università degli Studi di Catania for financial support.

References

1. Baran, J. D.; Larsson, J. A. *J. Phys. Chem. C* **2013,** *117,* 23887–23898. doi:10.1021/jp409127e
2. Walter, M. G.; Rudine, A. B.; Wamser, C. C. *J. Porphyrins Phthalocyanines* **2010,** *14,* 759–792. doi:10.1142/S1088424610002689
3. Claessens, C. G.; Hahn, U.; Torres, T. *Chem. Rec.* **2008,** *8,* 75–97. doi:10.1002/tcr.20139
4. Bohrer, F. I.; Colesniuc, C. N.; Park, J.; Ruidiaz, M. E.; Schuller, I. K.; Kummel, A. C.; Trogler, W. C. *J. Am. Chem. Soc.* **2009,** *131,* 478–485. doi:10.1021/ja803531r
5. Sorokin, A. B. *Chem. Rev.* **2013,** *113,* 8152–8191. doi:10.1021/cr4000072
6. Dolmans, D. E. J. G. J.; Fukumura, D.; Jain, R. K. *Nat. Rev. Cancer* **2003,** *3,* 380–387. doi:10.1038/nrc1071
7. Cárdenas-Jirón, G. I.; Leon-Plata, P.; Cortes-Arriagada, D.; Seminario, J. M. *J. Phys. Chem. C* **2011,** *115,* 16052–16062. doi:10.1021/jp2041026
8. Klar, D.; Klyatskaya, S.; Candini, A.; Krumme, B.; Kummer, K.; Ohresser, P.; Corradini, V.; de Renzi, V.; Biagi, R.; Joly, L.; Kappler, J. P.; del Pennino, U.; Affronte, M.; Wende, H.; Ruben, M. *Beilstein J. Nanotechnol.* **2013,** *4,* 320–324. doi:10.3762/bjnano.4.36
9. Chen, S.; Liu, Y.; Xu, Y.; Sun, Y.; Qiu, W.; Sun, X.; Zhu, D. *Synth. Met.* **2006,** *156,* 1236–1240. doi:10.1016/j.synthmet.2006.09.004
10. Li, Z.; Lieberman, M.; Hill, W. *Langmuir* **2001,** *17,* 4887–4894. doi:10.1021/la010203g
11. Alfredsson, Y.; Åhlund, J.; Nilson, K.; Kjeldgaard, L.; O'Shea, J. N.; Theobald, J.; Bao, Z.; Mårtensson, N.; Sandell, A.; Puglia, C.; Siegbahn, H. *Thin Solid Films* **2005,** *493,* 13–19. doi:10.1016/j.tsf.2005.05.012
12. Huc, V.; Armand, F.; Bourgoin, J. P.; Palacin, S. *Langmuir* **2001,** *17,* 1928–1935. doi:10.1021/la001237b
13. Trelka, M.; Urban, C.; Rogero, C.; de Mendoza, P.; Mateo-Marti, E.; Wang, Y.; Silanes, I.; Écija, D.; Alcamì, M.; Yndurain, F.; Arnau, A.; Martın, F.; Echavarren, A. M.; Martın-Gago, J. A.; Gallego, J. M.; Otero, R.; Miranda, R. *CrystEngComm* **2011,** *13,* 5591. doi:10.1039/c1ce05494e
14. Buriak, J. M. *Chem. Rev.* **2002,** *102,* 1271–1308. doi:10.1021/cr000064s
15. Biavardi, E.; Tudisco, C.; Maffei, F.; Motta, A.; Massera, C.; Condorelli, G. G.; Dalcanale, E. *Proc. Natl. Acad. Sci. U. S. A.* **2012,** *109,* 2263–2268. doi:10.1073/pnas.1112264109
16. Biavardi, E.; Federici, S.; Tudisco, C.; Menozzi, D.; Massera, C.; Sottini, A.; Condorelli, G. G.; Bergese, P.; Dalcanale, E. *Angew. Chem., Int. Ed.* **2014,** *53,* 9183–9188. doi:10.1002/anie.201404774
17. Kumar, G. A.; Thomas, J.; Unnikrishnan, N. V.; Nampoori, V. P. N.; Vallabhan, C. P. G. *J. Porphyrins Phthalocyanines* **2001,** *5,* 456–459. doi:10.1002/jpp.339
18. Massimi, L.; Lisi, S.; Pacilè, D.; Mariani, C.; Betti, M. G. *Beilstein J. Nanotechnol.* **2014,** *5,* 308–312. doi:10.3762/bjnano.5.34
19. Sperl, A.; Kröger, J.; Berndt, R. *Angew. Chem., Int. Ed.* **2011,** *50,* 5294–5297. doi:10.1002/anie.201100950
20. Bai, Y.; Buchner, F.; Wendahl, M. T.; Kellner, I.; Bayer, A.; Steinrück, H.-P.; Marbach, H.; Gottfried, J. M. *J. Phys. Chem. C* **2008,** *112,* 6087–6092. doi:10.1021/jp711122w
21. Leclaire, J.; Dagiral, R.; Pla-Quintana, A.; Caminade, A.-M.; Majoral, J.-P. *Eur. J. Inorg. Chem.* **2007,** 2890–2896. doi:10.1002/ejic.200601235
22. Görlach, B.; Hellriegel, C.; Steinbrecher, S.; Yüksel, H.; Albert, K.; Plies, E.; Hanack, M. *J. Mater. Chem.* **2001,** *11,* 3317–3325. doi:10.1039/B104554G
23. Boukherroub, R.; Morin, S.; Sharpe, P.; Wayner, D. D. M.; Allongue, P. *Langmuir* **2000,** *16,* 7429–7434. doi:10.1021/la991678z
24. Swift, P. *Surf. Interface Anal.* **1982,** *4,* 47–51. doi:10.1002/sia.740040204
25. Killampalli, A. S.; Ma, P. F.; Engstrom, J. R. *J. Am. Chem. Soc.* **2005,** *127,* 6300–6310. doi:10.1021/ja047922c
26. Dube, A.; Chadeayne, A. R.; Sharma, M.; Wolczanski, P. T.; Engstrom, J. R. *J. Am. Chem. Soc.* **2005,** *127,* 14299–14309. doi:10.1021/ja054378e
27. Condorelli, G. G.; Motta, A.; Bedoya, C.; Di Mauro, A.; Pellegrino, G.; Smecca, E. *Inorg. Chim. Acta* **2007,** *360,* 170–178. doi:10.1016/j.ica.2006.07.079
28. Palmgren, P.; Nilson, K.; Yu, S.; Hennies, F.; Angot, T.; Nlebedim, C. I.; Layet, J.-M.; Le Lay, G.; Göthelid, M. *J. Phys. Chem. C* **2008,** *112,* 5972–5977. doi:10.1021/jp711311s
29. Yu, S.; Ahmadi, S.; Sun, C.; Adibi, P. T. Z.; Chow, W.; Pietzsch, A.; Göthelid, M. *J. Chem. Phys.* **2012,** *136,* 154703. doi:10.1063/1.3699072
30. Mattioli, G.; Filippone, F.; Giannozzi, P.; Caminiti, R.; Bonapasta, A. A. *Chem. Mater.* **2009,** *21,* 4555–4567. doi:10.1021/cm9014755
31. Mannini, M.; Bertani, F.; Tudisco, C.; Malavolti, L.; Poggini, L.; Misztal, K.; Menozzi, D.; Motta, A.; Otero, E.; Ohresser, P.; Sainctavit, P.; Condorelli, G. G.; Dalcanale, E.; Sessoli, R. *Nat. Commun.* **2014,** *5,* No. 4582. doi:10.1038/ncomms5582

32. Tudisco, C.; Trusso Sfrazzetto, G.; Pappalardo, A.; Motta, A.; Tomaselli, G. A.; Fragalà, I. L.; Ballistreri, F. P.; Condorelli, G. G. *Eur. J. Inorg. Chem.* **2011,** 2124–2131. doi:10.1002/ejic.201001239
33. Petraki, F.; Peisert, H.; Uihlein, J.; Aygül, U.; Chassé, T. *Beilstein J. Nanotechnol.* **2014,** *5,* 524–531. doi:10.3762/bjnano.5.61
34. Petraki, F.; Peisert, H.; Biswas, I.; Chassé, T. *J. Phys. Chem. C* **2010,** *114,* 17638–17643. doi:10.1021/jp104141s
35. Guo, J.; Li, H.; He, H.; Chu, D.; Chen, R. *J. Phys. Chem. C* **2011,** *115,* 8494–8502. doi:10.1021/jp112197f
36. Shubina, T. E.; Marbach, H.; Flechtner, K.; Kretschmann, A.; Jux, N.; Buchner, F.; Steinrück, H.-P.; Clark, T.; Gottfried, J. M. *J. Am. Chem. Soc.* **2007,** *129,* 9476–9483. doi:10.1021/ja072360t
37. Condorelli, G. G.; Motta, A.; Favazza, M.; Fragala, I. L.; Busi, M.; Menozzi, E.; Dalcanale, E.; Cristofolini, L. *Langmuir* **2006,** *22,* 11126–11133. doi:10.1021/la060682p
38. Gulino, A.; Lupo, F.; Condorelli, G. G.; Fragalà, M. E.; Amato, M. E.; Scarlata, G. *J. Mater. Chem.* **2008,** *18,* 5011–5018. doi:10.1039/b809037h
39. Tudisco, C.; Betti, P.; Motta, A.; Pinalli, R.; Bombaci, L.; Dalcanale, E.; Condorelli, G. G. *Langmuir* **2012,** *28,* 1782–1789. doi:10.1021/la203797b
40. Briggs, D.; Beamson, G. *Anal. Chem.* **1992,** *64,* 1729–1736. doi:10.1021/ac00039a018

License and Terms

BEILSTEIN JOURNAL OF NANOTECHNOLOGY

Hybrid spin-crossover nanostructures

Carlos M. Quintero[1], Gautier Félix[2], Iurii Suleimanov[2,3], José Sánchez Costa[2], Gábor Molnár[2], Lionel Salmon[2], William Nicolazzi[2] and Azzedine Bousseksou[*2]

Review

Open Access

Address:
[1]LAAS, CNRS & Université de Toulouse (UPS, INSA, LAES), 7 Av de Colonel Roche, 31077 Toulouse, France, [2]LCC, CNRS & Université de Toulouse (UPS, INPT), 205 route de Narbonne, 31077 Toulouse, France and [3]Department of Chemistry, National Taras Shevchenko University of Kiev, 62 Volodymyrska St. 01601, Ukraine

Email:
Azzedine Bousseksou[*] - boussek@lcc-toulouse.fr

* Corresponding author

Keywords:
core–shell particle; multifunctionality; nanomaterials; spin-crossover

Beilstein J. Nanotechnol. **2014,** *5,* 2230–2239.
doi:10.3762/bjnano.5.232

Received: 15 July 2014
Accepted: 04 November 2014
Published: 25 November 2014

This article is part of the Thematic Series "Molecular materials – towards quantum properties".

Guest Editor: M. Ruben

Abstract

This review reports on the recent progress in the synthesis, modelling and application of hybrid spin-crossover materials, including core–shell nanoparticles and multilayer thin films or nanopatterns. These systems combine, often in synergy, different physical properties (optical, magnetic, mechanical and electrical) of their constituents with the switching properties of spin-crossover complexes, providing access to materials with unprecedented capabilities.

Review

Introduction

More than 15 years ago, Olivier Kahn highlighted the great potential of the so-called spin-crossover (SCO) materials on the nanoscale [1]. Indeed, there are interesting fundamental questions with regards to the size effect on the phase transition temperature, on the hysteresis width, on the kinetics of the spin transition, etc. On the other hand, SCO nanomaterials are also attractive candidates for integration into a variety of emerging micro- and nano-technologies. The notable characteristics of SCO materials include: i) reversible changes in their various physical properties (magnetic, optical, electrical and mechanical), ii) diverse external stimuli to drive their transition, iii) their versatility, i.e., there are multiple complexes with different transition properties, iv) room temperature operation and v) their bistability can be kept down to the nanoscale.

In the last few years, diverse pathways for the production of SCO nanomaterials as colloidal suspensions, thin films and other types of nanoscale assemblies have been established using different chemical and/or lithographic approaches for controlling the size, shape and even the organization of SCO nano-objects [2-11]. Furthermore, there is an active quest for developing novel methods which are sensitive enough to probe

extremely small quantities of SCO materials for a better understanding of these materials at the nanoscale. All of these recent results have been extensively reviewed in [12-16]. In the present review, we focus on new types of emerging, hybrid nano-objects that involve SCO nanomaterials in complex structures, which reveal unique functionalities due to the synergy between the SCO properties and the physical properties (magnetic, photonic, charge transport, etc.) of the surrounding matter. The present review constitutes an overview of these systems including their synthesis, theoretical modelling and future possible technological applications.

Indeed, a recent strategy to access the multifunctional potential of novel nanomaterials was the development of nanohybrid or nanocomposite structures that are able to combine different materials with different properties. Typically, in this approach, at least one of the components is organic while the other is inorganic in nature. A nanocomposite is a multiphase solid material where one of the phases has one, two or three dimensions in the size range of 1–100 nm. Additionally, it is worth noting that the molecular building blocks that constitute these hybrid materials can be as big as inorganic clusters, typically in the nanometer range. The most notable advantage of controlling their mutual arrangement is that they can effectively combine the properties of both components into one material with the additional possibility to present synergetic effects, and thus properties which were unattainable in the constituent parent materials [17]. The properties of these hybrid structures are not only interesting from a fundamental point of view, but are currently envisaged to be applied in various fields of technology.

Synthesis of hybrid SCO nanostructures

The development of functionalized nano-composite materials with potential applications in the field of switchable materials has recently attracted great attention mainly due to the development of hybrid nanoparticle molecules (HNMs) [18] and hybrid nanoparticle-coordination network structures (HNCNSs) [19]. Here, some remarkable examples of sophisticated structures involving SCO activity recently appeared in the literature and are examined according to a simple classification based on the position of the active SCO species on the core–shell nanostructure. One can thus envision a case in which the switchable active species is placed at the core, a second type where the active species is at the shell, and finally, a third type where both the core and the shell substructures are active (see Figure 1).

To our knowledge, for the first type, only three examples have been reported. Raza et al. [20] produced core–shell nanostructures based on a Hofmann-type clathrate SCO core with different shell materials. Although they observed a very interesting effect of the shell thickness on the SCO properties, their study did not aim for development of multifunctional materials. Titos-Padilla et al. [21] reported a core–shell nanocomposite with a SCO core synthetized from the coordination polymer $[Fe(Htrz)_2(trz)](BF_4)$ (Htrz = 1,2,4-triazole and trz = 1,2,4-triazolato), known to show a memory effect above room temperature [22], and SiO_2 shell grown around it. The use of silica is of great interest because of its high porosity and the possibility of grafting other functionalities onto its surface. In this case, the luminophore 3-(dansylamido)propyltrimethoxysilane was grafted onto the surface of the nanoparticles (NPs) using a straightforward chemical reaction (see Figure 2). The luminescent signal from these core–shell particles during the thermal cycles follows the SCO curve obtained from magnetic studies. Consequently, the authors affirm that the grafting process did not significantly affect either the morphology or the magnetic properties of the NPs. In this system, the luminescent signal from the dansyl is quenched by the Fe(II) low-spin state (LS) centers of the coordination polymer as a consequence of the spectral overlap between the dansyl emission and the absorption band of the LS ions.

Figure 1: Classification of core–shell SCO systems.

Following this synthetic strategy, a new nano-composite material with the same SCO complex $\{[Fe(Htrz)_2(trz)](BF_4)\}$ was reported by our team, which associated the SCO complex with gold NPs by means of an intermediate decorated silica shell [23]. Briefly, SCO@SiO_2 particles were synthetized using the reverse micelle technique by mixing two microemulsions: one containing the triazole ligand and the other the iron(II) salt, using Triton and TEOS (tetraethoxysilane) as tensioactive and silica sources, respectively. The SCO nano-composite particles were combined with gold NPs with the aim of using the properties of the gold to absorb light and convert it to heat (via a strong photothermal effect). Despite the small volume fraction of gold NPs within the nanocomposite (around 0.5%), the laser power required for a complete spin-state switching process was reduced by around 70%. It is interesting to note here that a similar strategy for low power, laser switching was also developed using the strong infrared absorption of the polymer matrix in a polymer–SCO composite material [24]. This work revealed exciting applications for high density read/write optical memory devices based on SCO compounds.

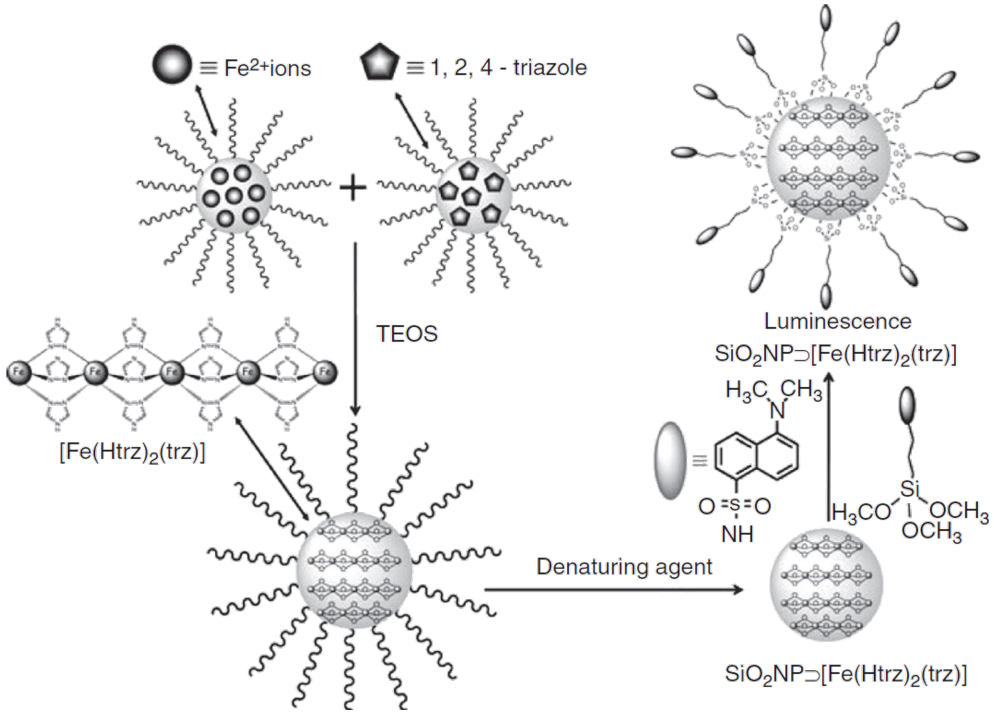

Figure 2: Synthesis route and schematic representation of the luminescent, SCO, SiO_2 nanoparticles. Reproduced with permission from [21], copyright 2011 Wiley-VCH.

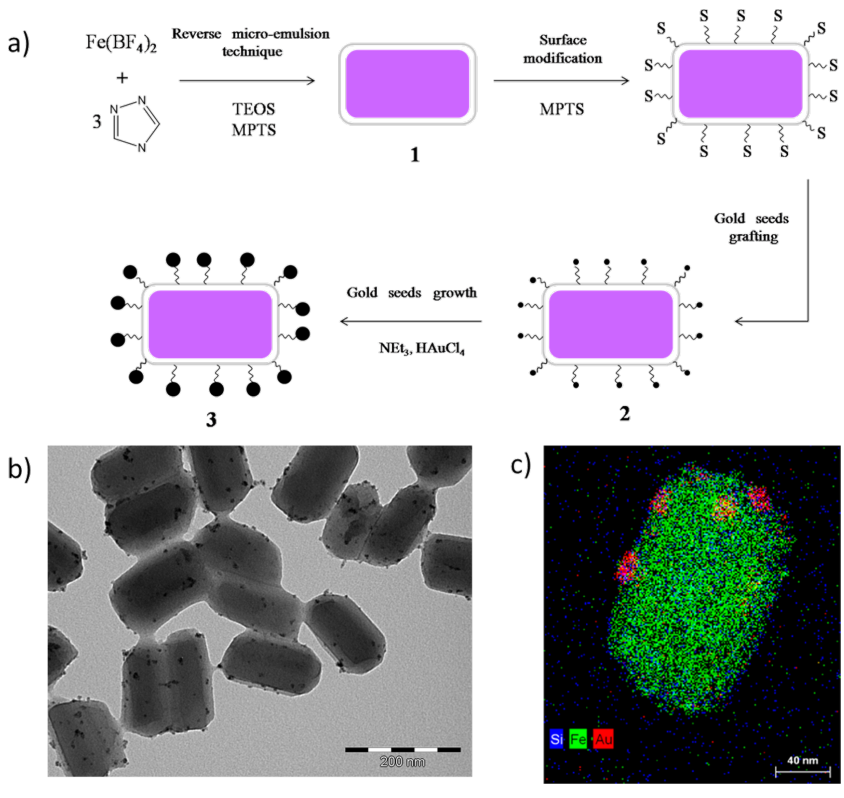

Figure 3: a) Schematic overview of the formation of the nanocomposite, gold-decorated SCO–SiO_2 nanoparticles. b) TEM and c) STEM–EDX images of the particles. Adapted with permission from [23], copyright 2014 The Royal Society of Chemistry.

As far as we know, the second and third types of core–shell structures were only achieved thus far by using Prussian blue analog complexes (PBA). While not all of these compounds are switchable, some can exhibit a charge transfer-induced, SCO phenomenon.

Guari et al. [25] has described a practical approach for the synthesis of single layer Au@PBA and double layer Au@PBA@PBA core–shell NPs. The synthesis route developed by the authors is a two-step process: first, an aqueous synthesis of cyanide gold NPs was performed and second, a cyano-bridged polymer shell was grown on the surface of the Au NPs by controlling the time of the reaction process. Following these procedures, two more remarkable processes were achieved: a second layer of PBA was inserted into the previous architecture in a controlled manner and additionally, the gold was removed from the core (Figure 4). As expected by the authors, the new NPs containing a gold core display both properties: the plasmonic optical property provided by the gold and the magnetic interactions from the PBA compound on the shell. In summary, the single layer NPs seem to behave differently from the double layer nanostructures. Namely, the single layer NPs exhibit a paramagnetic behavior while the double layer NPs exhibit ferromagnetism. Therefore, these new hybrid materials may be considered as multifunctional.

The third type of core–shell or core–multishell NPs contains two active magnetic species. Catala and Mallah reported that it is possible to carry out epitaxial growth of a 3D PBA different from that used for the core in the case of 10 nm $Cs[Ni^{II}Cr^{III}(CN)_6]$@$Cs[Co^{II}Cr^{III}(CN)_6]$ heterostructures [19] or 50 nm $Cs^{I}[Co^{II}Cr^{III}(CN)_6]$@$Cs^{I}[Fe^{II}Cr^{III}(CN)_6]$@-$Cs^{I}[Ni^{II}Cr^{III}(CN)_6]$ systems [26]. These core–multishell coordination nanoparticles were fabricated using a straightforward, surfactant-free manipulation with precise size control of the sample by controlling the addition rate and the concentration of the components. It is worth noting that these new combined materials present a different magnetic behavior than the associated pure nanoparticles. The authors attributed this result to a synergetic effect between the different ultrathin shells, allowing a modulation of the magnetic response of the nanoparticles. This method was also used by Talham to

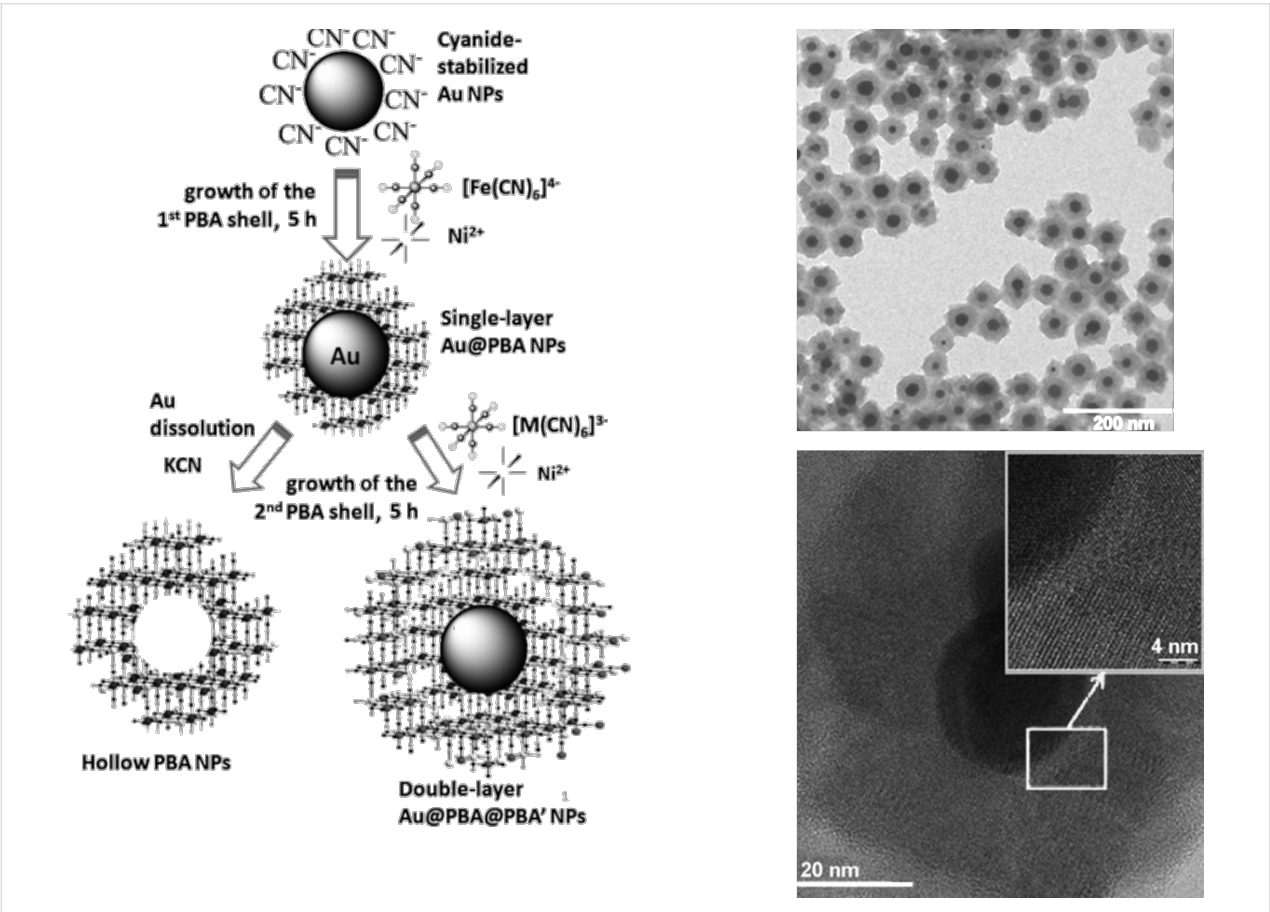

Figure 4: Schematic representation of single layer Au@PBA nanoparticles, double layer Au@PBA@PBA core–shell NPs, and hollow PBA NPs. On the right, TEM and HRTEM images of the Au@KNiFe NPs. Adapted with permission from [25], copyright 2014 Wiley-VCH.

study the photoinduced switching of the magnetism of $K_jNi_k[Cr(CN)_6]_l@Rb_aCo_b[Fe(CN)_6]$ heterostructures [27]. These nanoscale heterostructures exhibited a photo-response not seen in either constituent on its own (Figure 5). The changes induced by the light irradiation occur in the RbCoFe lattice, which experiences a charge transfer-induced spin transition from the Fe^{II}-CN-Co^{III}(LS) to the Fe^{III}-CN-Co^{II}(HS) state. According to the authors, the increase in the volume during this photo-switching process modifies the magnetism of the inner KNiCr layer due to magnetostrictive effects.

Devices based on hybrid SCO nanostructures

Luminescent devices

Matsuda et al. proposed a synthesis strategy that exploits the synergy between the charge carrier orbitals of a SCO complex and a light emitting material. They developed a concept for an organic light emitting diode (OLED) that consists of a 50 nm light emitting thin film composed of chlorophyll *a* (Chl *a*) mixed with the SCO complex $[Fe(dpp)_2](BF)_4$ (dpp = 2,6-di(pyrazol-1-yl)pyridine) spin-coated on an indium tin oxide (ITO) substrate (anode) and then covered by a 30 nm thick Al cathode (see Figure 6a) [28]. With this configuration, the electroluminescence (EL) of the device can be reproducibly switched on/off as a function of temperature due to the thermal spin state switching. Indeed, the light emission of this type of OLED is severely quenched if the $[Fe(dpp)_2](BF)_4$ is in its LS form ($T < 260$ K). After a photoluminescence study of identical films of $[Fe(dpp)_2](BF)_4$ and Chl *a,* the authors excluded the possibility of an energy transfer from the excited Chl *a* to the SCO complex in the LS state. These observations suggests that the excited form of Chl *a* does not exist in the OLEDs at low temperatures [29].

To explain these findings, the authors proposed two mechanisms: first, since the oscillator strength of the charge transfer (CT) bands increases in the LS state, it is possible that the injected electrons transit from the π orbital of the dpp ligand to the d orbital of the iron centers, giving an additional electron transport path from the cathode to the anode through the SCO complex. Second, a shift in the energy level of the molecular orbital concerning the electron transport in the SCO complex relative to that of Chl *a* (Figure 6b) [30] is possible. Thus, at high temperatures (HS state) the injected electrons effectively excite the Chl *a* molecules, leading to EL emission. Conversely, at low temperatures (LS state) the electron transport orbital of the $[Fe(dpp)_2](BF)_4$ shifts to a level lower than that of Chl *a* and as a result, the electrons flow exclusively into the SCO complex, preventing the formation of excited Chl *a*. Even though the shift of this orbital in the SCO complex is unknown, the authors confirmed their model by changing the light emitting compound to Nile Red (NR). This dye presents an electron transport orbital below that of Chl *a*; in consequence, in spite the change of the electronic configuration of the $[Fe(dpp)_2](BF)_4$, the EL emission persists at all temperatures (Figure 6c).

In a different approach, the luminescent response of a luminophore can also be effectively quenched if its emission/excitation displays an adequate spectral overlap with one of the distinctive LS or HS absorption bands of a SCO complex. In this manner, the luminescence will be modulated as the complex switches its spin state. Nonetheless, in order to render this approach valuable at the nanoscale, it is imperative to place the luminophore close to the metallic centers of the complex (≈1–3 nm) to establish a non-radiative energy transfer [31]. In our research, we exploited this idea by using an acridine orange dye as the luminescent doping agent for the SCO complex

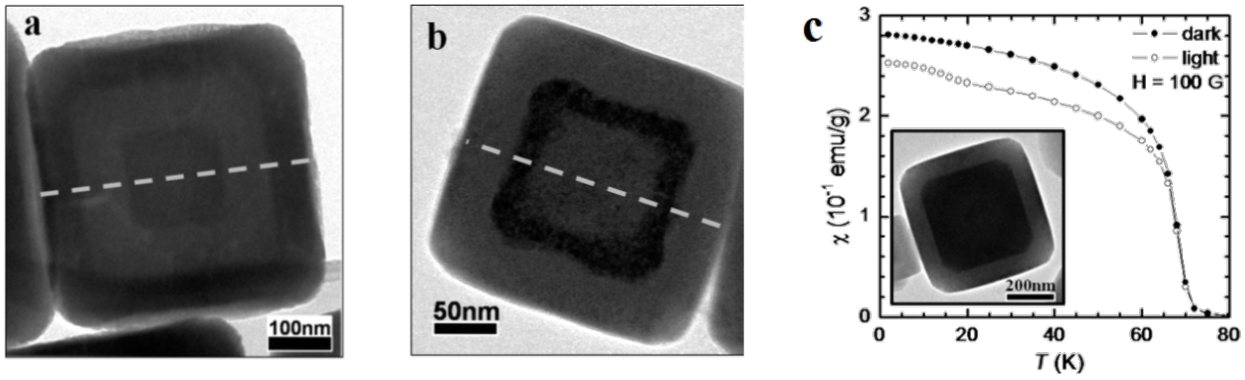

Figure 5: HRTEM images of core–multishell PBA nanoparticles a) RbCoFe@KNiCr@RbCoFe and b) KNiCr@RbCoFe@KNiCr, and c) shows the field-cooled magnetic susceptibility as a function of temperature before and after light irradiation of RbCoFe@KNiCr. Adapted with permission from [27], copyright 2011 American Chemical Society.

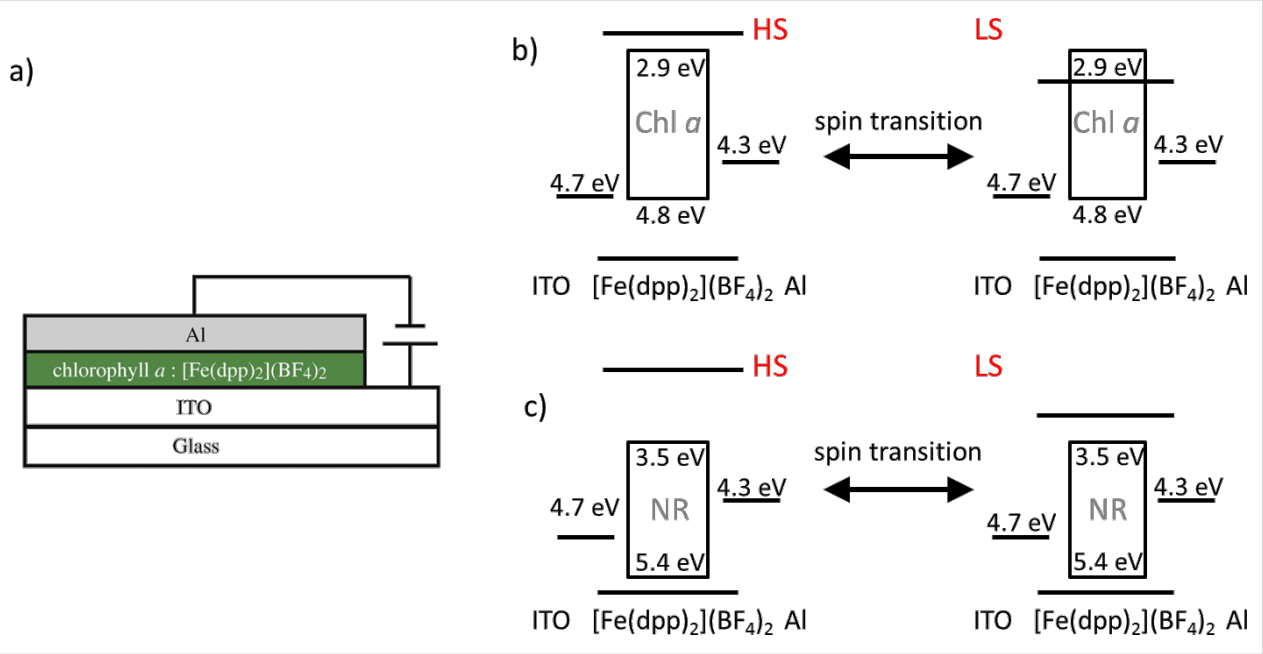

Figure 6: a) Architecture of the OLED device constructed by Matsuda et al. [28]. b) A schematic representation of the mechanism proposed for the EL, on/off switching, based on an energy level diagram of a device using Chl *a* and $[Fe(dpp)_2](BF)_4$. c) Energy level diagram for an analog device but employing NR as the emitting material [30]. Adapted with permission from [28] and [30], copyright 2008 and 2013 Elsevier.

$Fe(hptrz)_3(OTs)_2$ (hptrz = 4-heptyl-1,2,4-triazole) [32]. In addition to its strong emission in the green spectral range that overlaps with the characteristic LS absorption band of the SCO complex (centered at 543 nm), these molecules may serve as ligands in substitution for hptrz and thus, they are likely to approach the Fe(II) centers during the synthesis. Regular arrays of luminescent, SCO, nano-objects with an average size of 200 × 150 nm were patterned by employing a nano-patterned polydimethylsiloxane (PDMS) stamp. The luminescence of the isolated dots as a function of temperature increased upon the LS to HS spin transition and decreased as the LS state was restored at low temperatures. The synergy between luminescence and SCO properties in these hybrid systems also has interesting potential for thermal imaging applications. Molnár et al. demonstrated that thin films of the system as employed in [32] can be successfully used as luminescent surface temperature sensors with high spatial resolution [33]. The greatest benefit from this luminescent, SCO-based probe lies in the fact that the speed and temperature range (where the spin transition takes place) can be tuned by well-known chemical synthesis methods and without necessarily modifying the luminescent agent. This can be translated into a flexible design when it comes to sensitivity and working range of the probe at fixed wavelengths.

Active plasmonic devices

Currently, one of the most dynamic research area in the nanosciences is plasmonics. Surface plasmons provide unprecedented capabilities for manipulating electromagnetic waves at the nanoscale and have opened the door to unique photonic applications involving biological/chemical sensors, signal processing and solar energy harvesting. In particular, emerging, active, plasmonic devices employ hybrid nanostructures consisting of at least one metallic nanostructure and one dielectric compound with externally tunable dielectric properties. From this point of view, SCO complexes are of great interest due to the substantial variation of the real part of their refractive index (n) throughout the entire UV, visible and IR frequency ranges. In our research, we proposed a hybrid, SCO–plasmonic device based on gold nanostructures. Employing electron beam lithography (EBL) and lift off strategies, we developed localized surface plasmon (LSP) substrates consisting of a series of arrays of gold nanorods with different aspect ratios (Figure 7a) [34]. After this, the photonic device was finalized with a 60 nm thin film of the SCO complex, $Fe(hptrz)_3(OTs)_2$, spin-coated onto the top.

For a given particle size, aspect ratio and distance between particles, each array of gold nanorods have a characteristic LSP resonance (LSPR) wavelength that will also depend on the refractive index value of the surrounding media (Figure 7b). As a result, the LSPR of these devices can be tuned by varying n, due to the spin-state change of the SCO film. Figure 7c displays the LSPR response of the array shown in Figure 7a (covered with a SCO film) as a function of temperature. It was demonstrated that under those experimental conditions, the confined electromagnetic field around the metallic nanostructures can be

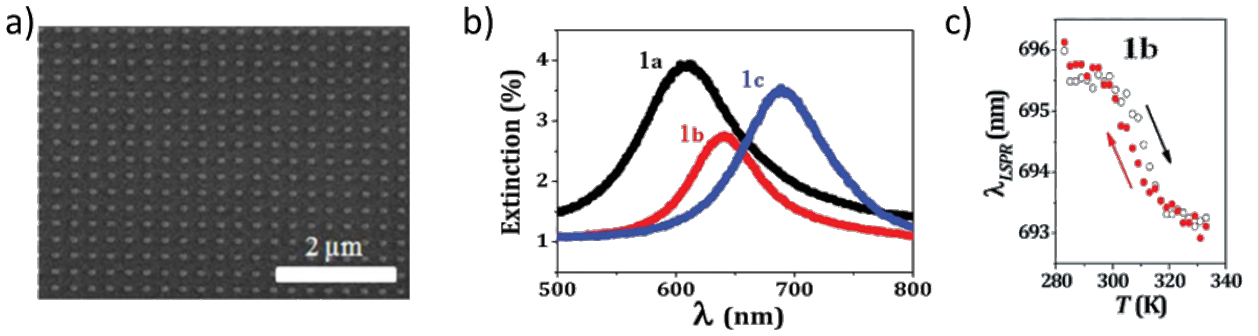

Figure 7: a) SEM image of a gold nanorod array with 200 nm pitch. b) Extinction spectra of three nanorod arrays with different aspect ratios. c) Plasmon resonance shift associated with the spin crossover of a 60 nm thin film deposited onto the nano-dot array displayed in a) as a function of temperature. Adapted with permission from [34], copyright 2013 The Royal Society of Chemistry.

successfully coupled to the molecular spin state changes brought on by the Fe centers of the SCO film. The LSPR technique was sensitive enough to detect the thermal spin transitions in thin films of up to 60 nm with a conventional optical absorption setup. Furthermore, the spin-state switching behavior was also observed due to plasmonic heating. Such devices that display synergy between plasmon resonance and molecular spin states may be of great interest for implementing detection or self-regulation strategies on-chip for the photothermal effect or, with an appropriate design, even for the development of photonic self-oscillators.

Nanoelectronic devices

The act of inducing an SCO transition with an electric field could provide the breakthrough necessary for the development of working molecular memory devices. With this in mind, Zhang et al. designed an experiment where the spin state of a thin film can be controlled by the ferroelectric polarization of the underlying substrate [35]. Through variations observed from inverse photoemeision spectroscopy (IPES) of the film, they inferred the signature of a voltage-controlled, spin-crossover transition that was later validated using magnetometry. For this purpose, 3 nm thick, organic copolymer, ferroelectric polyvinylidene fluoride trifluoroethylene films (PVDF:TrFE, 70:30) were deposited on graphite substrates using the Langmuir–Blodgett technique (Figure 8). Then, an up or down ferroelectric polarization state was preprogrammed into these substrates by scanning a probe (±900 V) before deposition of a SCO layer. The complex $[Fe(H_2B(pz)_2(bipy)]$ (pz = pyrazol-1-yl, bipy = 2,2'-bipyridine) was sublimated onto these substrates to form different thin films of 10 to 25 molecular layers in thickness and also onto gold substrates as control samples. It was found that there was a shift in the density of unoccupied states during the spin transition that leads to a significant loss in

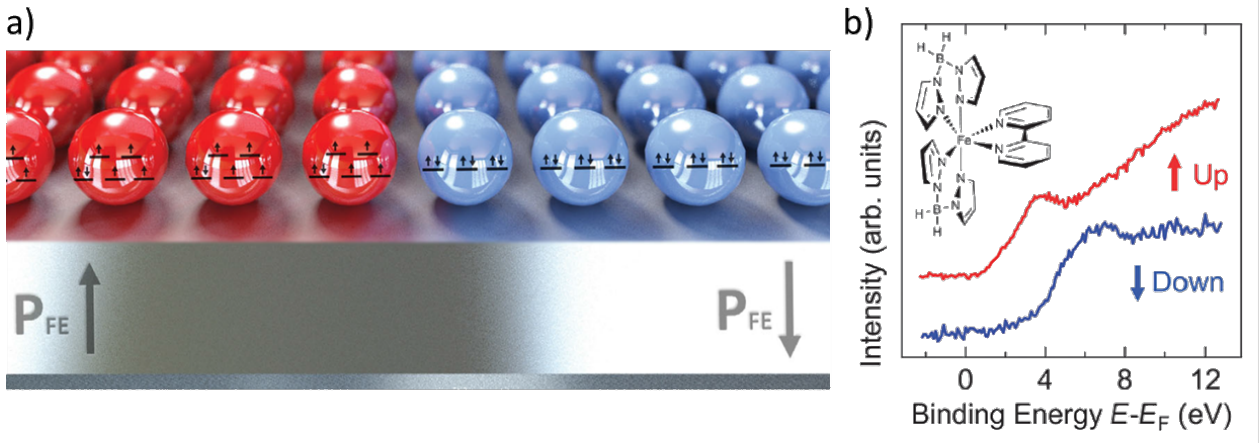

Figure 8: a) Schematic view of the molecular memory proposed by Zhang et al. At low temperatures, the spin state is determined by the polarization of the ferroelectric substrate. If the substrate is poled "up", the SCO molecules will remain HS; conversely, the SCO molecules will adopt the LS form for a substrate poled "down". b) Inverse photoemission spectrum at 170 K for a 25 molecule thick layer of $[Fe(H_2B(pz)_2(bipy)]$ deposited on PVDF–TrFE poled "up" (red) and "down" (blue). Each spectrum corresponds to the characteristic signature of the complex in the HS and LS form, respectively. Adapted with permission from [35], copyright 2014 The Royal Society of Chemistry.

the density of states just above the Fermi energy level in a HS to LS transition. This situation was observed in SCO films deposited on the gold and the graphite substrates where the ferroelectric PVDF–TrFE film was poled "down". However, if the interfacial dipoles of the PVDF–TrFE film are poled "up" instead, the characteristic inverse photoemission (IPES) signature of the SCO complex in the HS form persists down to 100 K, well below the thermal spin crossover (Figure 8). These observations in this hybrid device constitute one of the first evidences that electric fields can be effectively employed to address and manipulate spin states in molecular SCO systems on the nanometer scale.

Theoretical studies of spin-crossover nano-objects: towards modelling hybrid systems

A reduction in dimensions leads to an inevitable change in the bistability phenomenon for SCO nano-objects [36]. This idea has been experimentally confirmed with the study of spin-crossover nanoparticles [2-5]. The main observations include the shrinking of the thermal hysteresis loop, a downshift in the transition temperature, and an increase of the high spin (HS) residual fraction at low temperature. On the other hand, against all predictions, a surprising cooperative behavior has been observed in very small nanoparticles (2–4 nm) [6-11]. The origin of this effect is not well understood and different explanations can be proposed. For instance, the hysteresis loop in small objects could be the consequence of interactions between particles through the matrix, an interaction between the particle and the matrix [20], or a size dependent variation of the mechanical properties of the particle [37]. Of course all of these phenomena can be coupled, which leads to considerable complexity for the study of size effects in spin-crossover nanoparticles.

In any case, the pervasiveness of the surface-to-volume ratio at the nanometer scale has a major impact on the spin-crossover behavior. Thus, the SCO phenomenon can be controlled by clever engineering of the nanoparticle interface. To this regard, theoretical studies can be very useful to predict the various interface effects. In general, the presence of the surface leads to new energy terms that are added to the internal energy of the system. As a consequence, the internal energy becomes nonextensive, which leads to the modification of the thermodynamic properties of the SCO particles [37,38]. The degree to which the system becomes nonextensive depends on the surface-to-volume ratio. The modulation of the spin-crossover behavior in nanoparticles can be realized by modification of the surface energy terms in the HS and LS states. This energy depends on two different parameters: the energy per surface, γ, and the area of the particle, A. The energy per surface term depends on several complicated phenomena which happen at the surface. For instance, coordination defects the surface, the relaxation or reconstruction of the surface, the chemical or physical interaction between the nanoparticle and the environment can all contribute, in a rather complex way, to γ. The theoretical prediction of these phenomena and, even more importantly, their spin-state dependence is currently not possible. On the other hand, the spin-crossover behavior of particles can be altered when their shape is modified [38,39].

Beyond the modulation of the surface-to-volume ratio, in the case of hybrid core–shell particles, the interaction between the core and the shell can be used to further tune the spin-crossover phenomenon. Oubouchou et al. have shown the impact of an inactive HS shell on an active SCO core [40]. Figure 9 displays thermal SCO curves of a square-shaped SCO core surrounded by 0, 5, 10, 15 and 20 layers of an inactive HS shell. The authors explain the downshift in the transition temperature by a negative elastic pressure applied by the shell, leading to the widening of the thermal hysteresis loop. In another point of view, the downshift in the transition temperature and the cooperative change of the SCO behavior can be understood by additional deformation energies in the internal energy of the core, depending on the core spin state. Félix et al. have shown that the misfit between the lattice parameters of the core and the shell leads to a modification of the spin transition temperature

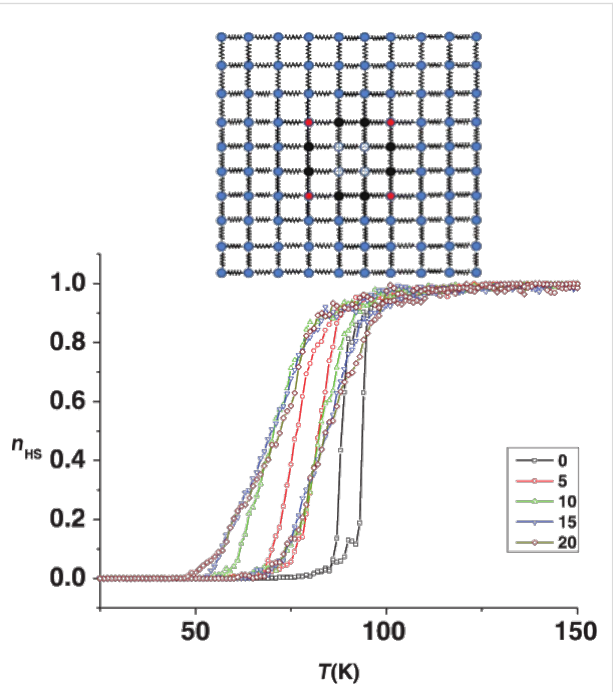

Figure 9: Thermal SCO curves for different thicknesses of an inactive HS shell, calculated with a compressible Ising-like model with harmonic potential. Top panel: core–shell system with an SCO active core and an inactive HS shell. Adapted with permission from [40], copyright 2013 American Physical Society.

[41]. In the case of an inactive HS shell, the misfit between a LS core and the shell is higher than the misfit between a HS core and the shell. The consequence of this misfit is a downshift in the transition temperature of the core. As shown in Figure 10, the authors have also shown that the synergy between an SCO active shell and an SCO active core leads to a modulation of the SCO behavior, and furthermore, to a new kind of bistability at the nanometer scale.

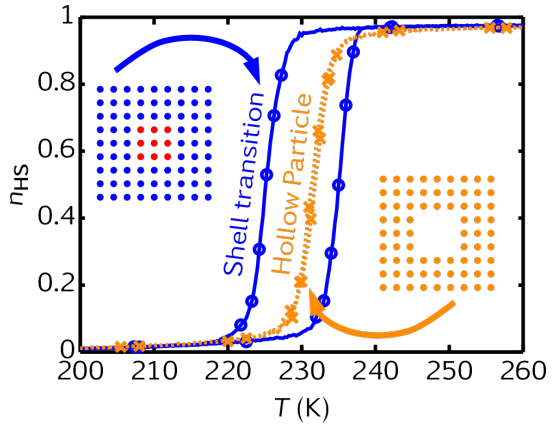

Figure 10: Comparison between the thermal SCO curves of a 9 × 9 hollow particle with a 3 × 3 hole and a 9 × 9 shell surrounding a 3 × 3 active core. Adapted with permission from [41], copyright 2014 Elsevier.

Conclusion

The fundamental and technological developments associated with the vast hybrid materials domain are limited only by the imagination of researchers. In the SCO field, thus far, chemists have focused mainly on the elaboration of core–shell or doped, hybrid nanoparticles. While low-level doping is not expected to significantly influence the SCO properties, theoretical models predict important effects in the case of core–shell systems that must be taken into account for the design of such nano-objects. On the other hand, physicists have produced different multilayer structures involving electroluminescent, plasmonic and ferroelectric thin films in interaction with SCO films. The results prove that SCO materials are attractive candidates for integration into photonic and electronic devices. In addition we believe that interesting applications of SCO hybrids can be anticipated in mechanical actuator technology as well. Indeed, the huge spontaneous strain during the spin transition was recently employed by Shepherd et al. through the integration of SCO materials in bimorph cantilevers, which were actuated both thermally and by light irradiation [42]. While these systems used macroscopic materials, in principle, true nanoscale operation is also possible. Exciting strain-induced coupling of SCO with electrical [43] and magnetic properties [44] has also been very recently reported using polymer composite and multilayer heterostructure systems, respectively. Finally, let us note that spintronics may also benefit from SCO nanohybrids as was highlighted by a scanning tunneling microscopy experiment [45].

Acknowledgements

Financial support from the project “ANR Nanohybrid” is acknowledged. JSC thanks the Marie-Curie research program (NanoSCOpe 328078).

References

1. Kahn, O.; Martinez, C. J. *Science* **1998,** *279,* 44–48. doi:10.1126/science.279.5347.44
2. Martínez, V.; Boldog, I.; Gaspar, A. B.; Ksenofontov, V.; Bhattacharjee, A.; Gütlich, P.; Real, J. A. *Chem. Mater.* **2010,** *22,* 4271–4281. doi:10.1021/cm101022u
3. Boldog, I.; Gaspar, A. B.; Martínez, V.; Pardo-Ibañez, P.; Ksenofontov, V.; Bhattacharjee, A.; Gütlich, P.; Real, J. A. *Angew. Chem., Int. Ed.* **2008,** *120,* 6533–6537. doi:10.1002/ange.200801673
4. Volatron, F.; Catala, L.; Rivière, E.; Gloter, A.; Stéphan, O.; Mallah, T. *Inorg. Chem.* **2008,** *47,* 6584–6586. doi:10.1021/ic800803w
5. Forestier, T.; Mornet, S.; Daro, N.; Nishihara, T.; Mouri, S.; Tanaka, K.; Fouche, O.; Freysz, E.; Letard, J. F. *Chem. Commun.* **2008,** 4327–4329. doi:10.1039/b806347h
6. Larionova, J.; Salmon, L.; Guari, Y.; Tokarev, A.; Molvinger, K.; Molnár, G.; Bousseksou, A. *Angew. Chem., Int. Ed.* **2008,** *47,* 8236–8240. doi:10.1002/anie.200802906
7. Galán-Mascarós, J. R.; Coronado, E.; Forment-Aliaga, A.; Monrabal-Capilla, M.; Pinilla-Cienfuegos, E.; Ceolin, M. *Inorg. Chem.* **2010,** *49,* 5706–5714. doi:10.1021/ic100751a
8. Tokarev, A.; Salmon, L.; Guari, Y.; Nicolazzi, W.; Molnár, G.; Bousseksou, A. *Chem. Commun.* **2010,** *46,* 8011–8013. doi:10.1039/c0cc02606a
9. Durand, P.; Pillet, S.; Bendeif, E.-E.; Carteret, C.; Bouazaoui, M.; El Hamzaoui, H.; Capoen, B.; Salmon, L.; Hebert, S.; Ghanbaja, J.; Aranda, L.; Schaniel, D. *J. Mater. Chem. C* **2013,** *1,* 1933–1942. doi:10.1039/c3tc00546a
10. Gural'skiy, I. A.; Quintero, C. M.; Molnár, G.; Fritsky, I. O.; Salmon, L.; Bousseksou, A. *Chem. – Eur. J.* **2012,** *18,* 9946–9954. doi:10.1002/chem.201201063
11. Peng, H.; Tricard, S.; Félix, G.; Molnár, G.; Nicolazzi, W.; Salmon, L.; Bousseksou, A. *Angew. Chem., Int. Ed.* **2014,** *126,* 11074–11078. doi:10.1002/ange.201406710
12. Bousseksou, A.; Molnár, G.; Salmon, L.; Nicolazzi, W. *Chem. Soc. Rev.* **2011,** *40,* 3313–3335. doi:10.1039/c1cs15042a
13. Cavallini, M. *Phys. Chem. Chem. Phys.* **2012,** *14,* 11867–11876. doi:10.1039/c2cp40879a
14. Shepherd, H. J.; Molnár, G.; Nicolazzi, W.; Salmon, L.; Bousseksou, A. *Eur. J. Inorg. Chem.* **2013,** *2013,* 653–661. doi:10.1002/ejic.201201205
15. Molnár, G.; Salmon, L.; Nicolazzi, W.; Terki, F.; Bousseksou, A. *J. Mater. Chem. C* **2014,** *2,* 1360–1366. doi:10.1039/c3tc31750a
16. Mikolasek, M.; Félix, G.; Nicolazzi, W.; Molnár, G.; Salmon, L.; Bousseksou, A. *New J. Chem.* **2014,** *38,* 1834–1839. doi:10.1039/c3nj01268a
17. Hoffmann, F.; Cornelius, M.; Morell, J.; Fröba, M. *Angew. Chem., Int. Ed.* **2006,** *45,* 3216–3251. doi:10.1002/anie.200503075

18. Dadosh, T.; Gordin, Y.; Krahne, R.; Khivrich, I.; Mahalu, D.; Frydman, V.; Sperling, J.; Yacoby, A.; Bar-Joseph, I. *Nature* **2005,** *436,* 677–680. doi:10.1038/nature03898
19. Prado, Y.; Dia, N.; Lisnard, L.; Rogez, G.; Brisset, F.; Catala, L.; Mallah, T. *Chem. Commun.* **2012,** *48,* 11455–11457. doi:10.1039/c2cc35929d
20. Raza, Y.; Volatron, F.; Moldovan, S.; Ersen, O.; Huc, V.; Martini, C.; Brisset, F.; Gloter, A.; Stephan, O.; Bousseksou, A.; Catala, L.; Mallah, T. *Chem. Commun.* **2011,** *47,* 11501–11503. doi:10.1039/c1cc14463d
21. Titos-Padilla, S.; Herrera, J. M.; Chen, X.-W.; Delgado, J. J.; Colacio, E. *Angew. Chem., Int. Ed.* **2011,** *50,* 3290–3293. doi:10.1002/anie.201007847
22. Kroeber, J.; Audiere, J.-P.; Claude, R.; Codjovi, E.; Kahn, O.; Haasnoot, J. G.; Groliere, F.; Jay, C.; Bousseksou, A. *Chem. Mater.* **1994,** *6,* 1404–1412. doi:10.1021/cm00044a044
23. Suleimanov, I.; Sánchez Costa, J.; Molnár, G.; Salmon, L.; Bousseksou, A. *Chem. Commun.* **2014,** *50,* 13015–13018. doi:10.1039/C4CC02652G
24. Hellel, W.; Ould Hamouda, A.; Degert, J.; Létard, J. F.; Freysz, E. *Appl. Phys. Lett.* **2013,** *103,* 143304. doi:10.1063/1.4824028
25. Maurin-Pasturel, G.; Long, J.; Guari, Y.; Godiard, F.; Willinger, M.-G.; Guerin, C.; Larionova, J. *Angew. Chem., Int. Ed.* **2014,** *53,* 3872–3876. doi:10.1002/anie.201310443
26. Catala, L.; Brinzei, D.; Prado, Y.; Gloter, A.; Stéphan, O.; Rogez, G.; Mallah, T. *Angew. Chem., Int. Ed.* **2009,** *48,* 183–187. doi:10.1002/anie.200804238
27. Dumont, M. F.; Knowles, E. S.; Guiet, A.; Pajerowski, D. M.; Gomez, A.; Kycia, S. W.; Meisel, M. W.; Talham, D. R. *Inorg. Chem.* **2011,** *50,* 4295–4300. doi:10.1021/ic1022054
28. Matsuda, M.; Isozaki, H.; Tajima, H. *Thin Solid Films* **2008,** *517,* 1465–1467. doi:10.1016/j.tsf.2008.09.034
29. Matsuda, M.; Isozaki, H.; Tajima, H. *Chem. Lett.* **2008,** *37,* 374–375. doi:10.1246/cl.2008.374
30. Matsuda, M.; Kiyoshima, K.; Uchida, R.; Kinoshita, N.; Tajima, H. *Thin Solid Films* **2013,** *531,* 451–453. doi:10.1016/j.tsf.2013.01.094
31. Shepherd, H. J.; Quintero, C. M.; Molnár, G.; Salmon, L.; Bousseksou, A. Luminescent Spin-Crossover Materials. In *Spin-Crossover Materials: Properties and Applications;* Halcrow, M. A., Ed.; John Wiley & Sons: Oxford, UK, 2013; pp 347–373. doi:10.1002/9781118519301.ch13
32. Quintero, C. M.; Gural'skiy, I. A.; Salmon, L.; Molnár, G.; Bergaud, C.; Bousseksou, A. *J. Mater. Chem.* **2012,** *22,* 3745–3751. doi:10.1039/c2jm15662h
33. Molnár, G.; Gural'skiy, I. A.; Salmon, L.; Nicolazzi, W.; Quintero, C.; Akou, A.; Abdul-kader, K.; Félix, G.; Mahfoud, T.; Bergaud, C.; Bartual-Murgui, C.; Thibault, C.; Vieu, C.; Bousseksou, A. Bistable photonic nanostructures based on molecular spin crossover complexes. In *Proc. SPIE 8425, Photonic Crystal Materials and Devices X,* Brussels, Belgium, April 16–19, 2012; Míguez, H. R.; Romanov, S. G.; Andreani, L. C.; Seassal, C., Eds.; . doi:10.1117/12.921849
34. Abdul-Kader, K.; Lopes, M.; Bartual-Murgui, C.; Kraieva, O.; Hernández, E. M.; Salmon, L.; Nicolazzi, W.; Carcenac, F.; Thibault, C.; Molnár, G.; Bousseksou, A. *Nanoscale* **2013,** *5,* 5288–5293. doi:10.1039/c3nr01337e
35. Zhang, X.; Palamarciuc, T.; Létard, J.-F.; Rosa, P.; Lozada, E. V.; Torres, F.; Rosa, L. G.; Doudin, B.; Dowben, P. A. *Chem. Commun.* **2014,** *50,* 2255–2257. doi:10.1039/c3cc46892e
36. Kawamoto, T.; Abe, S. *Chem. Commun.* **2005,** *31,* 3933–3935. doi:10.1039/b506643c
37. Félix, G.; Nicolazzi, W.; Salmon, L.; Molnár, G.; Perrier, M.; Maurin, G.; Larionova, J.; Long, J.; Guari, Y.; Bousseksou, A. *Phys. Rev. Lett.* **2013,** *110,* 235701. doi:10.1103/PhysRevLett.110.235701
38. Félix, G.; Nicolazzi, W.; Mikolasek, M.; Molnár, G.; Bousseksou, A. *Phys. Chem. Chem. Phys.* **2014,** *16,* 7358–7367. doi:10.1039/c3cp55031a
39. Chiruta, D.; Jureschi, C.-M.; Linares, J.; Garcia, Y.; Rotaru, A. *J. Appl. Phys.* **2014,** *115,* 053523. doi:10.1063/1.4864035
40. Oubouchou, H.; Slimani, A.; Boukheddaden, K. *Phys. Rev. B* **2013,** *87,* 104104. doi:10.1103/PhysRevB.87.104104
41. Félix, G.; Mikolasek, M.; Molnár, G.; Nicolazzi, W.; Bousseksou, A. *Chem. Phys. Lett.* **2014,** *607,* 10–14. doi:10.1016/j.cplett.2014.05.049
42. Shepherd, H. J.; Gural'skiy, I. A.; Quintero, C. M.; Tricard, S.; Salmon, L.; Molnár, G.; Bousseksou, A. *Nat. Commun.* **2013,** *4,* 2607. doi:10.1038/ncomms3607
43. Koo, Y.-S.; Galán-Mascarós, J. R. *Adv. Mater.* **2014,** *26,* 6785–6789. doi:10.1002/adma.201402579
44. Gros, C. R.; Peprah, M. K.; Hosterman, B. D.; Brinzari, T. V.; Quintero, P. A.; Sendova, M.; Meisel, M. W.; Talham, D. R. *J. Am. Chem. Soc.* **2014,** *136,* 9846–9849. doi:10.1021/ja504289p
45. Miyamachi, T.; Gruber, M.; Davesne, V.; Bowen, M.; Boukari, S.; Joly, L.; Scheurer, F.; Rogez, G.; Yamada, T. K.; Ohresser, P.; Beaurepaire, E.; Wulfhekel, W. *Nat. Commun.* **2012,** *3,* 938. doi:10.1038/ncomms1940

License and Terms

BEILSTEIN JOURNAL OF NANOTECHNOLOGY

Spectroscopic mapping and selective electronic tuning of molecular orbitals in phosphorescent organometallic complexes – a new strategy for OLED materials

Pascal R. Ewen[1], Jan Sanning[2], Tobias Koch[3], Nikos L. Doltsinis[3], Cristian A. Strassert[*2] and Daniel Wegner[*1]

Full Research Paper

Open Access

Address:
[1]Institut for Molecules and Materials, Radboud Universiteit Nijmegen, P.O. Box 9010, 6500 GL Nijmegen, The Netherlands, [2]Physikalisches Institut, Westfälische Wilhelms Universität Münster, Wilhelm-Klemm-Straße 10, 48149 Münster, Germany and [3]Institut für Festkörpertheorie and Center for Multiscale Theory and Computation, Westfälische Wilhelms Universität Münster, Wilhem-Klemm-Straße 10 and Corrensstraße 40, 48149 Münster, Germany

Email:
Cristian A. Strassert[*] - ca.s@wwu.de; Daniel Wegner[*] - d.wegner@science.ru.nl

* Corresponding author

Keywords:
charge transfer; density-functional theory; frontier orbitals; hybridization; OLED; Pt(II) complex; scanning tunneling microscopy; scanning tunneling spectroscopy; triplet emitters

Beilstein J. Nanotechnol. **2014,** *5,* 2248–2258.
doi:10.3762/bjnano.5.234

Received: 31 July 2014
Accepted: 24 October 2014
Published: 26 November 2014

This article is part of the Thematic Series "Molecular materials – towards quantum properties".

Guest Editor: M. Ruben

Abstract

The improvement of molecular electronic devices such as organic light-emitting diodes requires fundamental knowledge about the structural and electronic properties of the employed molecules as well as their interactions with neighboring molecules or interfaces. We show that highly resolved scanning tunneling microscopy (STM) and spectroscopy (STS) are powerful tools to correlate the electronic properties of phosphorescent complexes (i.e., triplet emitters) with their molecular structure as well as the local environment around a single molecule. We used spectroscopic mapping to visualize several occupied and unoccupied molecular frontier orbitals of Pt(II) complexes adsorbed on Au(111). The analysis showed that the molecules exhibit a peculiar localized strong hybridization that leads to partial depopulation of a d_{z^2} orbital, while the ligand orbitals are almost unchanged. We further found that substitution of functional groups at well-defined positions can alter specific molecular orbitals without influencing the others. The results open a path toward the tailored design of electronic and optical properties of triplet emitters by smart ligand substitution, which may improve the performance of future OLED devices.

Introduction

Organic light emitting diodes (OLEDs) based on phosphorescent Ir(III) or Pt(II) complexes (also referred to as triplet emitters) are a very promising alternative to current devices for highly efficient lighting and display technologies [1]. In the quest to improve OLEDs, a fundamental understanding of the nature and interactions of the involved molecular orbitals (MO) is crucial both within each organic layer and at the interfaces of the multilayer device [2]. Cyclic voltammetry (CV) is widely used to determine the oxidation and reduction potentials of organometallic molecules and has rightfully become a very popular technique for electrochemical studies [3,4]. However, interactions of the molecules with their environment (e.g., host–guest interactions, hybridization at surfaces and interfaces, interaction in aggregates) can significantly change the energetic position and order of molecular orbitals, but CV cannot always provide information on such effects whenever the local environment is not well known. Moreover, CV depends delicately on many parameters and necessitates great care during execution and analysis [5], but the major popularity of CV and its transformation as a quick tool in many labs entails the risk of disregarding this [6].

Looking at alternative surface science-based methods, photoemission and inverse photoemission spectroscopy techniques are common to address the electronic properties of molecular systems under well defined conditions [7,8]. As a drawback, these methods are each limited to the occupied or unoccupied states, respectively. Moreover, in a structurally complex or inhomogeneous sample the spectra display the average of distributed MO levels due to a lack of spatial resolution. This has led to controversies as to how the MO levels should be deduced from the spectra [9,10]. In this context, the combined power of atomic and high energy resolution in scanning tunneling microscopy (STM) and spectroscopy (STS) makes it an ideal tool to study the electronic properties of adsorbed molecules with precise knowledge and control of the local environment around a single molecule. Although this method is limited to an energy range a few eV around the Fermi energy E_F, this is usually sufficient to probe the relevant frontier orbitals [11-15]. Several studies have performed STM and STS on organometallic compounds, mainly on porphyrins and phthalocyanines [16-22]. Considering this general success, it is surprising that phosphorescent complexes have barely been investigated via scanning probe methods. Almost all studies are limited to the analysis of thin film and crystal growth of Pt(II) or Ir(III) complexes via atomic force microscopy [23,24] or STM [25-28] and lack the submolecular resolution to address specific parts of a molecule. Only a single study employed STS [29], but without showing STM images or stating where on the molecule the data had been acquired. Essentially, prior to our involvement [30] no publication has utilized the advantages of combined STM and STS to study triplet emitters.

We have performed STM and STS measurements at cryogenic temperatures on submonolayer amounts of various square-planar Pt(II) complexes on a Au(111) single-crystal surface. These complexes coordinate a Pt atom to a tridentate ligand (TL, with substituents R^1 and R^2) and an ancillary ligand (AL, substituent R^3), see Figure 1, and are known to be highly efficient (phosphorescent) triplet emitters both in monomeric and aggregated form [31,32]. We identified a number of occupied and unoccupied frontier orbitals. Comparison with density functional theory (DFT) calculations allows the unambiguous assignment of all MOs from the HOMO–2 to the LUMO+2. We found that the complexes show a peculiar site-specific hybridization to the Au(111) substrate that only involves the Pt atom but leaves the ligand orbitals essentially unaltered. We also show that different substituents at particular positions of the molecular structure alter the HOMO and LUMO levels, and we propose a strategy of fine-tuning both levels independently, which should permit the tunability of the HOMO–LUMO gap (and thus the emission color) as well as charge-injection barriers in a device.

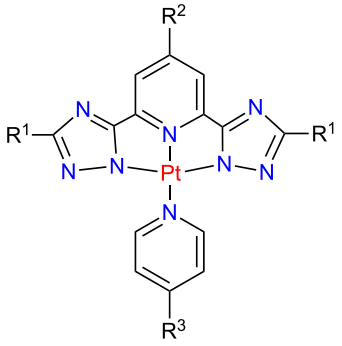

C1 $R^1 = CF_3$; R^2 = H; R^3 = H

C2 $R^1 = CF_3$; R^2 = H; $R^3 = C_5H_{11}$

C3 R^1 = *t*-Bu; R^2 = H; $R^3 = C_5H_{11}$

C4 $R^1 = CF_3$; R^2 = OMe; $R^3 = C_5H_{11}$

Figure 1: Molecular structure of the complexes **C1** to **C4**. In all cases the Pt atom is fourfold coordinated by N atoms, stemming from a tridendate ligand (TL, containing two triazole groups and one pyridine) and an ancillary ligand (AL, containing a pyridine group). The substituents R^1 to R^3 are varied in order to investigate their influence on the adsorption as well as the electronic structure.

Results and Discussion

Methods and sample preparation

The experiments were performed under ultrahigh vacuum conditions (base pressure $<10^{-10}$ mbar) using a commercial low-temperature scanning tunneling microscope (Createc LT-STM). The synthesis of the complexes is described elsewhere [32,33]. The sample preparation was done by repeated sputter-annealing cycles of the Au(111) single-crystal substrate followed by thermal evaporation of the molecules from a commercial evaporator (Createc TUBOmini) at about 420 K to 470 K, while the substrate was held at room temperature. Typical deposition times were on the order of 20 to 30 seconds, leading to sub-monolayer coverage on the metal surface. Subsequently, the sample was transferred in situ into the cold STM (T = 5 K).

All images where taken in constant-current mode. For the tunneling spectra the current I and the differential conductance dI/dV (via lock-in technique, modulation voltage 10–20 mV) were measured simultaneously as a function of sample bias V under open-feedback conditions. The bias voltage is always given with respect to the sample, i.e., positive sample bias corresponds to electrons tunneling from occupied electronic states of the tip into unoccupied states of the sample, and $V = 0$ corresponds to the Fermi energy E_F. In good approximation, dI/dV is proportional to the local density of states of the sample. Energy-resolved spectral maps (that visualize the spatial distribution of molecular orbitals) were acquired by measuring dI/dV at a fixed bias as a function of lateral position in constant-current mode.

For the DFT calculations shown here, Kohn–Sham molecular orbitals were calculated in the gas phase with the Gaussian 09 package [34] using the PBE0 hybrid exchange-correlation functional [35] and the SDD basis set [36]. The molecular orbitals were visualized using the VMD 1.9 software. The orbital energies in the gas-phase calculations are computed with respect to the vacuum level. For a comparison with the measured values from STS (which are given relative to E_F), a constant corresponding to the work function of 5.1 eV has to be added to the calculated values (cf. details in the discussion).

Structural analysis

For the the structural characterization of as-grown molecular films, we focus on the two Pt complexes **C1** and **C2** (see Figure 1). STM images of the first monolayer of **C1** (Figure 2a,b) and **C2** (Figure 2c–f) on Au(111) reveal that the underlying Au(111) herringbone reconstruction is essentially unaffected by the adsorbed layer. This is indicative of an overall weak adsorbate-substrate interaction [37]. The close-up images exhibit submolecular resolution and clearly reflect the chemical building blocks. By superimposing the corresponding molecular structures we can attribute the highest round protrusions to the Pt atom in the center of the complexes. This bright feature is surrounded by the TL that appears as a slightly dimmer protrusion at the top of the molecule (pyridine-R^2) and two lobes at the left- and the right-hand side (triazole-R^1). The different substituents R^3 of **C1** and **C2** are clearly visible in the appearance of the AL: while **C1** exhibits a round feature next to the Pt atom stemming from the pyridine (Figure 2b), **C2** features an additional "tail" stemming from the C_5H_{11} alkyl chain (Figure 2d–f).

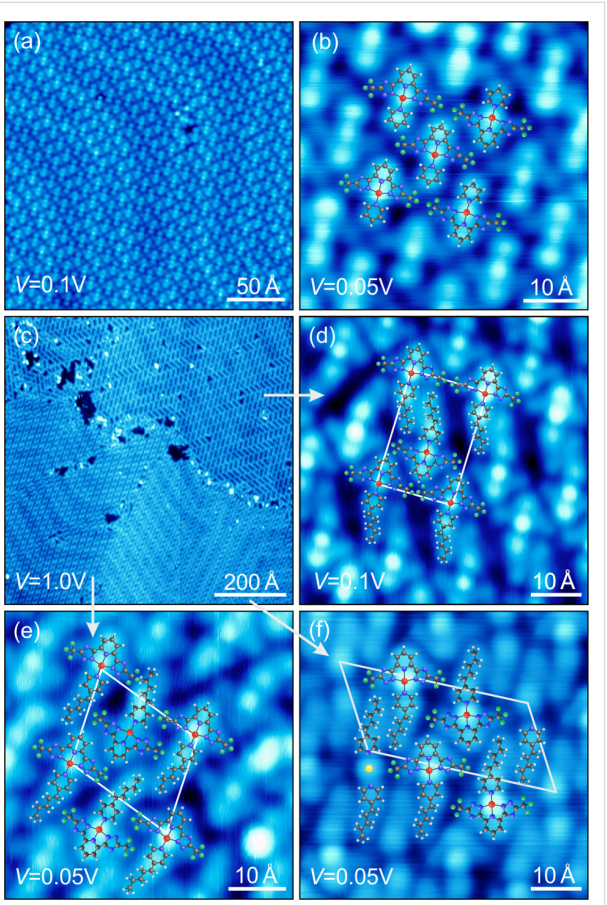

Figure 2: Topography analysis of a monolayer of **C1** (a,b) and **C2** (c–f) on Au(111). **C1** grows in only one close-packed structure probably due to steric packing. **C2** shows three different ordered structures, indicating the additional role of van der Waals forces between neighboring R^3 alkyl chains for the self-assembly.

We can evaluate the driving force of self-assembly and gain information about the intermolecular interactions within the first monolayer by focussing on the different packing structures. **C1** appears densely packed in a rhombic lattice with side lengths of 11.5 ± 0.3 Å and an angle of 86 ± 4° (Figure 2b). The symmetry axis of the molecule is tilted by 12.0 ± 0.5° relative to the Au$\{11\bar{2}\}$ direction. However, the orientation of neigh-

boring molecules to each other can be either parallel or antiparallel. We did not find any nearest or next-nearest neighbor correlation, i.e., the orientation in the lattice seems to be purely random. While we only found one packing for **C1**, we observed three different local patterns for **C2** within a single preparation (Figure 2c). The rectangular unit cell (Figure 2d) has a lower nominal coverage and exhibits pores with an irregular distribution. At maximum coverage the unit cell becomes oblique (Figure 2e,f). Each unit cell contains two **C2** molecules and in one case two additional elongated features (see below). The adsorption angle relative to the Au$\{11\bar{2}\}$ direction differs for each structure (9 ± 3° (Figure 2d), 4 ± 3° (Figure 2e) and 15 ± 3° (Figure 2f)). This is another indication for a weak overall molecule–substrate coupling. Furthermore, the lateral intermolecular interaction also seems to be relatively weak. TLs of neighboring molecules as well as the pyridine AL of complex **C1** seem to be packed in a steric fashion. However, we attribute the different patterns of **C2** to additional van der Waals forces between the amyl chains [38,39].

We note that an additional molecular structure is evident in the third pattern of **C2** (Figure 2f). Next to two rows of **C2** molecules with alternating orientation a row of paired elongated protrusions appears. This feature is quite similar in size, shape and intensity to the AL of **C2**, i.e., 4-pentylpyridine. On the other hand, isolated TLs could not be observed in any STM images. As STS spectra of these unknown elongated molecular structures remain featureless, we cannot clarify their composition or origin at this point. Nevertheless, we only observed these units at low coverages. Therefore, we suggest that a small ratio of molecules dissociates by breaking the bond between the Pt atom and the AL. This may occur when a molecule diffuses to an elbow site of the Au(111) herringbone reconstruction or a monatomic step edge, where the Au atoms have a lower coordination and hence interact stronger with adsorbates. At higher coverages, diffusion (and thus dissociation) is hindered. In fact, we cannot observe the unknown elongated molecular structures at high nominal coverages close to a complete monolayer. Occasionally, the supposed 4-pentylpyridine pairs are separated by a round protrusions. We speculate that these are Au atoms bound to the two adsorbates [40], as depicted in the model structure in Figure 2f. We note that these extra molecular structures did not have any measurable impact on the STS spectra of the **C2** complex and therefore will not be discussed any further.

Spectroscopic analysis – molecule-substrate interactions

Figure 3 shows an overview of the results from DFT calculations of **C1** in the gas phase (Figure 3a) and *dI*/*dV* maps of the first monolayer of **C1** on Au(111). The theoretical results contain the shapes and energies of five molecular orbitals with respect to E_F . While only one MO (HOMO–1) is exclusively localized at the Pt atom, all other given MOs exhibit a significant contribution at the ligands.

We first focus our discussion on the ligands (i.e., excluding the Pt site). The depicted seven *dI*/*dV* maps in Figure 3b reveal the local density of states (LDOS) of several MOs between −3.2 V and +3.2 V. Below −3.0 V the *dI*/*dV* intensity is most dominant at both pyridine rings while the triazole rings are low in intensity. Between −2.8 V and −1.8 V, the intensity distribution is reversed, i.e., triazoles now appear bright while all pyridines are dim. At positive bias voltages the triazole groups and the AL have no or weak intensities in all *dI*/*dV* maps, and features are exclusively observed at the pyridine group of the TL. Between 1.6 V and 2.3 V the signal is found centered above this pyridine ring, but above 2.3 V the *dI*/*dV* intensity is found to its left and right.

We are able to link the calculated orbitals to the measured spectroscopic maps by comparing their spatial distributions and symmetries. The calculated HOMO–2 exhibits an elongated LDOS distribution along the molecular symmetry axis with main intensities at both pyridine groups of the TL and the AL. This is in excellent agreement with the observed *dI*/*dV* maps below −3.0 V. Moreover, the HOMO shows an LDOS distribution at the two triazole groups, which is in good agreement with the experimental maps around −2.1 V. At positive energies, the calculated LUMO has an antinode along the symmetry axis of the molecule with major LDOS contribution at the TL pyridine. Again, this distribution agrees well with the spectroscopic maps seen around 2.0 V. Finally, the LUMO+1 is also localized mainly at the TL pyridine but now the orbital is antisymmetric with respect to the molecular symmetry axis. This is in very good agreement with the *dI*/*dV* distribution measured around 2.6 V. As a guide to the eye for the comparison of theory and experiment, we have schematically depicted the energetic visibility range of the described *dI*/*dV* features as Lorentzian peaks in Figure 3b that can be considered as (qualitative and schematic) experimental LDOS vs energy plots. The arrows between Figure 3a and Figure 3b display the MO assignments. As the DFT calculations only consider free molecules in the gas phase, differences originate from molecule–molecule or molecule–substrate interactions of the molecules adsorbed as a monolayer on the Au(111) surface.

We can rule out any significant lateral molecule–molecule interactions, because a comparison of **C1** and **C2** reveals virtually identical spectroscopic results despite different adsorption geometries and packing densities [30]. This also means that the molecular orientation with respect to the substrate does not seem to play a role, i.e., the overall molecule–substrate inter-

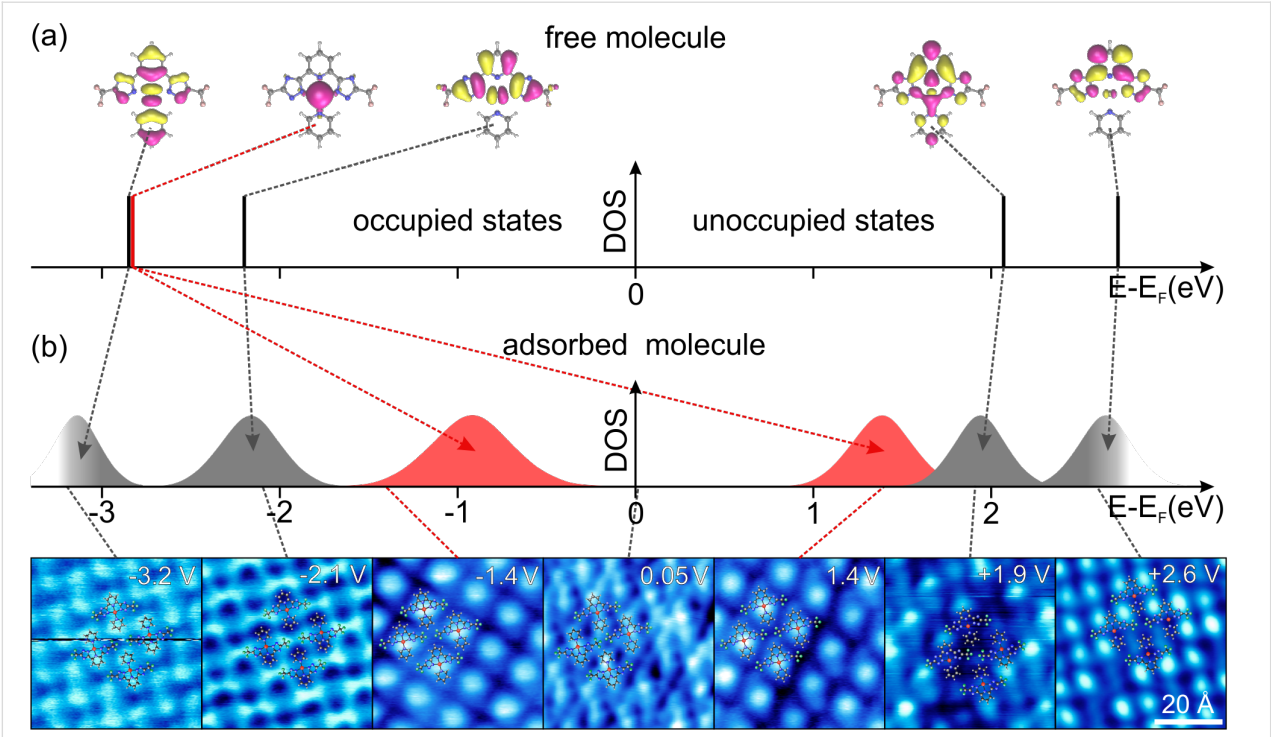

Figure 3: (a) Energy and LDOS of calculated orbitals for **C1** in the gas phase. Here, a work function of 5.1 eV was assumed. This value results from minimizing the energy differences between calculated and measured energies of the HOMO and the LUMO, respectively. (b) Series of *dI*/*dV* maps (bottom) and corresponding schematic representation of energetic distribution (top). Molecular states related to the Pt d_{z^2} orbital are colored in red, while ligand centered orbitals are grey-shaded. The arrows between (a) and (b) indicate the orbital shifts caused by the hybridization with the substrate states.

action cannot be large. This is indeed reflected in the above comparison. For the ligand orbitals, the major consequence of adsorbing the complex onto the Au substrate is a broadening of the levels due to weak hybridization with substrate states (i.e., physisorption) and only relatively small shifts in the energetic positions but no effect on the orbital order or occupancy.

The situation is dramatically different when focussing on the orbital features at the Pt atom. The DFT calculations show that the HOMO–1 is spatially confined to the Pt position of the complex. Further inspection reveals that this is the Pt d_{z^2} state, whose lobes extend much further out of the molecular plane compared to the other frontier orbitals. In the experiment, however, we could not find any additional new feature in our spectroscopic maps between the HOMO and the HOMO–2. Instead, a spectroscopic map exhibiting intensity exclusively at the Pt site (i.e., matching the HOMO–1) was found in the range between −1.4 V and −0.4 V, i.e., higher in energy as the HOMO map! The situation is – at first glance – more confusing at positive sample bias, where we also find an identical spectroscopic map in the range from 1.0 V to 1.8 V. In fact, these two features are the first arising MOs below and above E_F, respectively. In the intermediate region around E_F the *dI*/*dV* maps reflect the topographic information without a dominating contribution of a chemical group. This behavior is typical when measuring *dI*/*dV* maps within the HOMO–LUMO gap where no resonant tunneling into MO occurs [41]. Therefore, the HOMO–1 is observed twice, below and above E_F. This situation is again schematically depicted in Figure 3b, where two red-colored broadened peaks represent the observed MOs at the Pt site.

The fact that the Pt-based state is visible in spectroscopic maps but not in local point spectroscopy should be discussed in more detail. Sometimes features observed in *dI*/*dV* maps taken in constant current mode can strongly depend on the choice of set-point current and bias, which may lead to artifacts that are not related to any electronic state [42,43]. To exclude this possibility, we additionally recorded constant-height *dI*/*dV* maps. Figure 4 shows a comparison of *dI*/*dV* maps of **C1** at 1.4 V acquired in constant-current (Figure 4a) and constant-height mode (Figure 4b). Both images show exactly the same feature with a bright protrusion at the platinum position while the rest of the molecule is low in intensity. Furthermore, we have studied four different Pt-based complexes with tremendous variations of the apparent molecular shape, and in all these complexes we observed this Pt-based spectroscopic feature. We note that it is not entirely uncommon that a spectroscopic feature might be hard to see or even entirely obscured in point

spectroscopy but can be observed in *dI*/*dV* maps. This has, for instance, been found for surface states on W(110) [44] and Ni(111) [45]. Also tetracyanoethylene molecules on Cu(100) do not show any resonance in STS point spectroscopy [13], although DFT predicts at least two molecular states within the experimentally accesable energy range [46] and spectroscopic maps at E_F show the LUMO. Therefore, we conclude that the Pt-centered feature observed here is not an experimental artifact but an intrinsic and robust feature representing an orbital state.

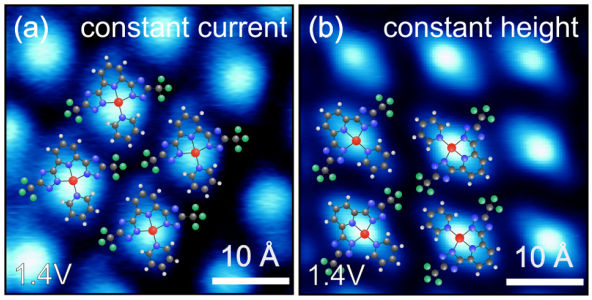

Figure 4: *dI*/*dV* maps of **C1** at 1.4 V recorded in constant current (a) and constant height (b) mode, respectively. 83 pA were choosen as the current setpoint.

Our observations summarized in Figure 3 can be understood when considering that the Pt d_{z^2} orbital exhibits a much larger overlap with the electronic wavefunctions of the Au(111) substrate compared to the ligand orbitals (sp-like states extending less far out of the molecular plane). If the overlap is large enough, the states can hybridize, leading to a partial charge transfer from the HOMO–1 into the substrate. Essentially, two different scenarios can explain our data. In the first scenario, the hybridization may lead to a singly occupied molecular orbital (SOMO). It has been shown that a SOMO is observed twice in STS [47]: at negative bias it is probed by a tunneling process of the SOMO-electron to the tip; at positive bias a second electron is injected into the SOMO. Due to the localized nature of this MO, the Coulomb repulsion between the two electrons has to be overcome. The separation of the two peaks in Figure 3b would then correspond to the Coulomb energy. Typical Coulomb energies for d_{z^2} states of organometallic complexes are around 2 eV [48,49], in agreement with the 2.4(7) eV for **C1**. In the second scenario, the Pt d_{z^2} orbital may strongly hybridize with a Au state to form a (occupied) bonding and an (unoccupied) antibonding orbital [50].

In order to evaluate which of the two scenarios is more likely, we can have a detailed look at the results of local STS spectroscopy (Figure 5). Spectra taken over the Pt atom only reveal a peak at about 1.9 V but no peaks around −0.9 or 1.4 V. In comparison, the spectrum on bare Au(111) is featureless at this energy, i.e., the peak is clearly a molecular state. However, it is not a state solely located at the Pt atom, because the spectrum on the pyridine group of the TL also shows a peak at the same energy and the *dI*/*dV* map at 1.9 V has almost exclusively intensity at the latter. We therefore assign the measured peak in the spectrum to the LUMO that also shows some finite contribution at the Pt site but is mainly located at the TL pyridine group (see DFT results in Figure 3a). Yet, we do not see any appearance of further peaks in the spectra between −1.5 V and 1.5 V at the Pt although the *dI*/*dV* maps unambiguously show two MO features.

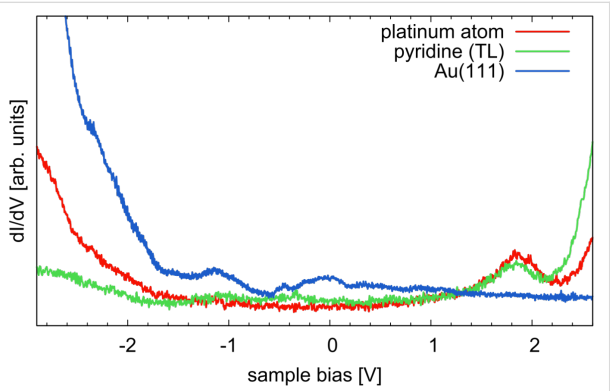

Figure 5: *dI*/*dV* spectra taken over the Pt atom and the pyridine group of **C1** exhibit a peak at 1.9 V that we assign to the LUMO of the free molecule (see discussion in the text). For comparison, a spectrum of the bare Au(111) surface is also shown. Results for complex **C2** are almost identical.

Why can we observe the d_{z^2} state in *dI*/*dV* maps but not in the spectra, whereas we can observe the ligand states in both measurements? For this we have to consider the possibility of strong physisorption (or even chemisorption). While weak physisorption only leads to a broadening of the MO levels (as described above), a strong molecule–substrate hybridization (i.e., strong physisorption or chemisorption) can lead to a strong broadening of a MO level as well as significant shifts in binding energy even to a degree that this state changes its occupancy due to charge transfer with the substrate [48,51-54]. For the SOMO scenario, we would expect the transfer of one electron from the Pt d_{z^2} state to the Au substrate, but the emergence of a Coulomb blockade would require that the MO is still well localized and should be clearly visible as peaks in STS spectra. On the other hand, in the scenario of bonding and antibonding states the d_{z^2} orbital of the Pt atom may hybridize and broaden in such a strong manner that no significant feature arises from the underground signal in the tunneling spectra. Nevertheless, in the *dI*/*dV* maps the very low intensity may still be imaged over a wide range (in our case about 1 eV). We also note that first DFT calculations including the surface do not support the formation of a SOMO. Therefore we conclude that the experi-

mental findings are in favor of the second scenario, the formation of bonding and antibonding states.

Independent of the mechanism, we can summarize that Pt(II) complex **C1** exhibits a peculiar site-specific strong hybridization accompanied by a charge transfer that only involves the Pt atom but leaves the ligand orbitals essentially unaltered. We note that this effect has some interesting consequences in possible device applications. The shift of the Pt d_{z^2} state reduces the charge-injection barrier dramatically: now the first accessible states to inject holes or electrons are not the HOMO and LUMO at about −2 and +2 eV, respectively, but the hybridized Pt MO at −0.9 and +1.4 eV. The exact energies should even be tunable in a controlled fashion by altering the degree of molecule–substrate coupling. This could be achieved by using different substrates [13,54] or alternatively by a systematic variation of the vertical Pt-substrate separation. The latter could be achieved sterically by using ligand side groups with different degrees of bulkiness. For instance, replacing the CF_3 by *tert*-butyl or adamantyl groups [32] would lift the molecular plane further away from the substrate surface. We emphasize that our analysis of electronic properties is identical (and thus highly reproducible) for all complexes within the monolayer; i.e., the molecules interact in a well-defined way with the substrate. This is only possible due to its planar structure that leads to distinct orbital overlaps. Hence, we expect that well-defined interactions also occur in host–guest environments as well as within aggregated structures of Pt(II) complexes.

Spectroscopic analysis - intramolecular tuning

The electronic properties of Pt(II) complexes can, of course, also be tuned by alteration of the chemical structure. In order to understand the intramolecular interactions in more detail, we have decided to only apply a fine-tuning of the substituents. For this study we measured two modified complexes **C3** and **C4** where either R^1 or R^2 are substituted in comparison to **C2**. Figure 6 depicts submolecularly resolved STM images of the molecules on Au(111). Both molecules are found in self-assembled monolayer islands containing only intact molecules. The overlay of the corresponding molecular structures again allows a straight-forward identification of each molecule. **C3** (Figure 6a) exhibits two bright lobes to the left and right of a dimmer protrusion. We attribute these to the two bulky *tert*-butyl groups at R^1 and the central Pt atom, respectively, i.e., the *tert*-butyl substituents dominate the topography. The AL and the pyridine of the TL appear as a dim elongated and round feature below and above the Pt site, respectively. In contrast, **C4** (Figure 6b) exhibits the brightest protrusion at the top of the molecule (i.e., at R^2) where a single hydrogen atom is replaced by a methoxy group. As observed for **C1** and **C2**, the triazole groups with the CF_3 substituent at R^1 show only a low apparent height. The unaltered Pt atom and AL appear similar to **C2** and **C3**. The packing of both molecules in the self-assembled islands consists of interlocked double rows where R^2 is pointing towards R^3 of a neighboring molecule. Apart from the molecular size, the different substituents do not show any influence on the measured structures. We suggest that only weak lateral interactions, most likely van der Waals forces (especially between neighboring amyl groups), and steric effects drive the self-assembly, similar to the situation of complex **C2**.

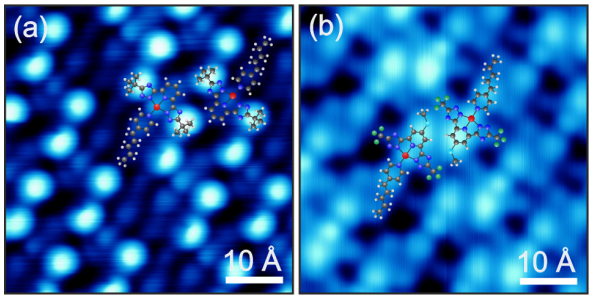

Figure 6: STM images of self-assembled monolayers of **C3** (a) and **C4** (b). Due to the rotational degree of freedom around the O–C bonds, the exact position of the methoxy group cannot be given here. Despite the different substituents R^1 and R^2 the complexes show similar packing structures indicated by the overlaid molecular models.

For **C3**, one may think that equally detailed STS mapping of the molecular orbitals as in Figure 3 may be prohibited by the topography-dominating *tert*-butyl groups. Nevertheless, we performed energy resolved *dI*/*dV* measurements on **C3** ranging from −2.55 V to +2.95 V. Figure 7 contains the corresponding series of *dI*/*dV* maps. An overlay of molecular structures in each map (where exact positions are again extracted from the simultaneously acquired topography images) permits the correlation of features to specific molecular parts. For comparison, the respective DFT MOs (calculated for gas-phase molecules) are reproduced in the insets. At +2.95 V (Figure 7a) a high signal is found at the AL, especially between the two neighboring amyl groups. Additionally, two lobes with low intensity show up on both sides of the TL pyridine. At +2.45 V (Figure 7b) the AL becomes dimmer while the sides of the TL pyridine are brighter. We suggest that the lack of *dI*/*dV* signal on top of the pyridine is due to a nodal line along the symmetry axis of the underlying MO. This changes at +1.95 V (Figure 7c), where a bright intensity is found above the center of the TL pyridine but not on its sides anymore. There is also a smaller signal located at the Pt atom and between the amyl groups. The situation is almost reversed at voltages of +1.45 V (Figure 7d): now the Pt position is most dominant and the top of the pyridine lost intensity. We could not find any evidence for unoccupied molecular states at the triazole groups in the given voltage range.

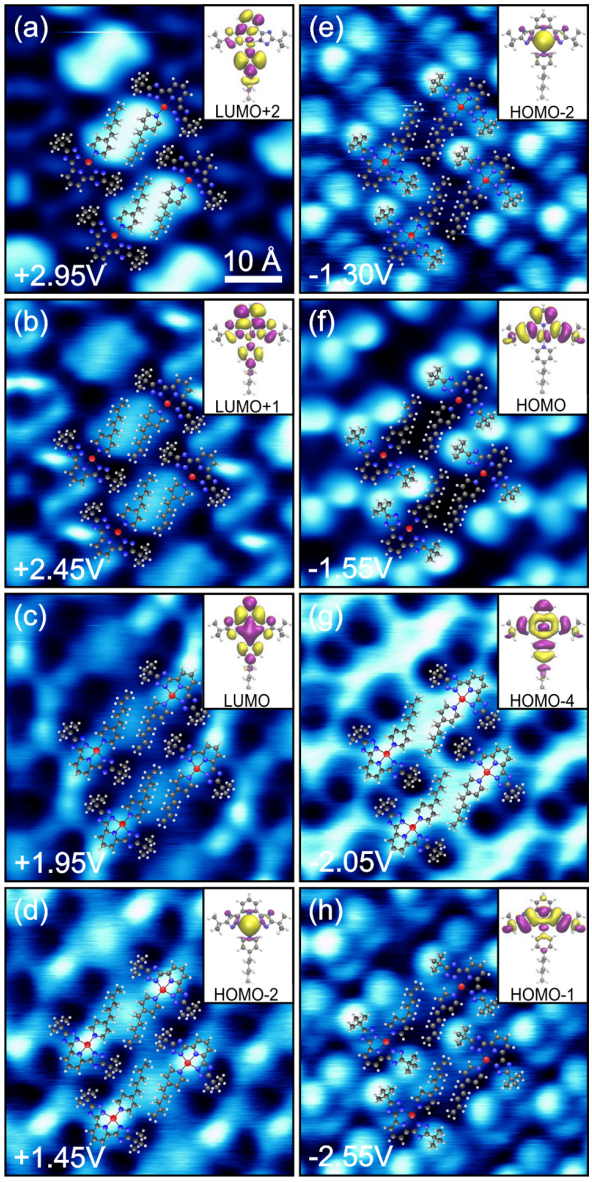

Figure 7: Series of *dI*/*dV* maps of complex **C3** and corresponding calculated orbitals of gas-phase molecules.

At negative sample bias of −1.30 V (Figure 7e) we observed waisted features at both *tert*-butyl groups and the Pt position whereas the pyridines and the amyl group are very low in intensity. The *dI*/*dV* signal at −1.55 V (Figure 7f) is concentrated at the left- and right-hand side of the TL while we do not detect any signal at the other positions. Compared to this, the *dI*/*dV* map at −2.05 V (Figure 7g) is completely inverted. Finally, at −2.55 V (Figure 7e) an asymmetric distribution of the *dI*/*dV* signal is found. The brightest features stem from the *tert*-butyl groups, but there are additional sickle-like features with lower intensity to the bottom right. The simultaneously recorded topography (not shown here) looks similar to that of Figure 6a. Therefore it is unclear whether this asymmetry is an artifact caused by the STM tip.

Essentially, despite the bulky *tert*-butyl groups, the *dI*/*dV* maps again reveal various spatial LDOS distributions that can be assigned to the simulated MOs analogous to the procedure for **C1** (Figure 5). The LUMO+2 is mainly localized at the AL and shows minor LDOS at the TL pyridine. The LUMO+1 is antisymmetric with respect to the mirror plane of the TL and has the highest LDOS at the TL pyridine. We assign these two orbitals to the features measured in the *dI*/*dV* maps at +2.95 V and +2.45 V, respectively. In the gas phase, the calculated energy levels of the LUMO+2 and LUMO+1 are quasi degenerate. Considering a much larger level broadening, we expect both MOs to be detected simultaneously but with varying relative intensity for different voltages. The symmetric LUMO exhibits a high LDOS at the pyridine extending further to the Pt atom. This is in good agreement with the map in Figure 7c. Overall, the three lowest lying unoccupied molecular orbitals reflect the results of the *dI*/*dV* measurement both in order and occupancy.

Nevertheless, the features in Figure 7d are best described by the Pt d_{z^2} orbital, which is the HOMO–2 in the gas-phase calculations. This indicates a scenario analogous to **C1** where a charge transfer from the molecule to the substrate occurs. However, this does not explain why we still observe a significant *dI*/*dV* contribution at (or between) the amyl groups. This could only be understood by assuming that the LUMO+2 exhibits a relatively strong level broadening. Alternatively, an artifact of scanning the sample in constant-current mode may be possible: the signal can be increased when the tip is approached toward the substrate at these positions between two neighboring amyl groups.

At negative bias the intensities at the Pt atom and both sides of the TL (Figure 7e) can be described by a superposition of the Pt d_{z^2} orbital (HOMO–2) and the antisymmetric HOMO. We suggest that the occupied MO closest to E_F is again the shifted HOMO–2 (cf. **C1**) showing a significant energetic overlap with the lower lying HOMO. In comparison to **C1** this orbital is calculated to be higher in energy which explains the simultaneous observation of both orbitals. The HOMO is individually reproduced in Figure 7f, only 0.25 eV below Figure 7e. The inverted intensity along the symmetry axis of the TL in Figure 7g is best reproduced by the calculated HOMO–4, while Figure 7h resembles the symmetry of the HOMO–1 or the HOMO–3 (not shown here) with LDOS distributed along the triazole-Pt-triazole axis. This observation provides indications for an orbital shift of the HOMO–4 towards E_F.

Our analysis shows that the characterization and visualization of molecular orbitals by STS is not limited to entirely flat molecules, but can also be applied when bulky chemical groups are used. Moreover, seven different MOs were measured, which even exceeds the previous result of the flat complex (cf. Figure 3). The unoccupied MOs of **C1** and **C3** show a similar behavior and seem to be almost unaffected by the adsorption. The Pt d_{z^2} orbital appears likewise below and above E_F, which is why we also assume a charge transfer toward the substrate for **C3**. However, we observed an alteration of the orbital order for the occupied states of **C3**. At this point, the origin for this different behavior from **C1** is unclear, but we assume that only the MOs exhibiting a huge contribution at the Pt site (HOMO–2 and HOMO–4) are likely to be significantly influenced by the Au(111) surface, while ligand-centered states remain essentially unchanged.

Despite the substrate-induced alterations, the HOMO and LUMO orbitals of **C3** can be clearly identified. This becomes even clearer when looking at local tunneling spectra. As shown in Figure 8, a spectrum taken above the triazole group (red line) reveals a peak at about −1.5 V. This peak is almost invisible at the TL pyridine site (blue line), which confirms the strong localization of the HOMO at the triazole groups as observed in the corresponding spectroscopic map (see Figure 7f). On the other hand, the pyridine spectrum exhibits a broad peak at about 1.9 V that is not present on the triazole group. This is a clear manifestation of the LUMO orbital (Figure 7c). We can compare the HOMO and LUMO energies with those of complex **C1** and **C2** that were also quantified via local *dI*/*dV* spectroscopy [30]. We find that the LUMO level of **C3** is virtually identical to that of **C1** and **C2**, whereas the HOMO level is significantly shifted toward E_F by about 0.6 eV. In order to understand why only the HOMO level is altered, we have to discuss the effect of the different substituents. Compared to a CH_3 or, in our case, a *tert*-butyl group, the CF_3 group is known to have an electron-withdrawing impact on an aromatic group (here: the triazole) which can stabilize associated MOs [55,56]. The calculated frontier orbitals show that several MOs have finite LDOS at the triazole groups. However, a closer inspection reveals that the carbon atom to which the R^1 substituents are attached only exhibits an antinode with large LDOS contribution in case of the HOMO but not the LUMO. Indeed, our spectroscopic maps of MOs show that the HOMO is localized at the triazole groups, while the LUMO shows no contribution there. Therefore it is reasonable to assume that the CF_3 group of **C2** will only stabilize the HOMO, i.e., it shifts further away from the Fermi energy compared to **C3**. This is indeed what we see in our STS data.

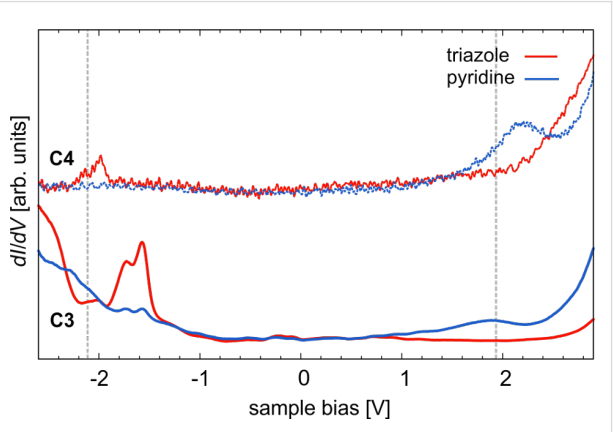

Figure 8: Tunneling spectra of **C3** and **C4** each acquired at the pyridine and triazole groups of the TL. For comparison, the vertical lines indicate the HOMO and LUMO levels of **C1** and **C2** [30].

We have also looked at another complex **C4** where the substituent R^2 was changed from a hydrogen atom to a methoxy (OCH_3) group. The latter is known to donate electrons into the π-electronic system of the attached aromatic (here: a pyridine) group, leading to a destabilization of associated unoccupied MOs. Indeed, looking at the tunneling spectra of **C4** (Figure 8), we find that the LUMO is shifted further away from E_F by about 0.4 eV, while now the HOMO is unaffected. Similar to the above discussion, this can be explained by the fact that the LUMO has a significant contribution at the TL pyridine group but none at the triazole (and vice versa). Interestingly, the DFT calculations show that both HOMO and LUMO have strong contributions at the pyridine group. However, the HOMO shows a node, the LUMO an antinode along the molecular symmetry plane, and the corresponding carbon atom of R^2 is located right there. This subtle difference seems to decide whether the R^2 moiety has an impact on the MO. Our finding is rather exciting as it may open the possibility to independently tune the HOMO and the LUMO levels by substitution of R^1 and R^2, respectively. This may have powerful consequences for OLED materials design because it should be feasible to set and tune the charge-injection barriers and the HOMO–LUMO gap, and hence the emission color, independently. We will perform further investigations on this matter to test the validity of this concept.

Conclusion

We showed that various phosphorescent Pt(II) complexes can be deposited reliably and without dissociation onto a Au(111) surface by thermal sublimation inside an ultrahigh vacuum environment. These planar molecules are well-suited for a thorough analysis by STM and STS. We can simultaneously identify and visualize the molecular structure as well as various occupied and unoccupied molecular frontier orbitals with high submolecular spatial and meV energy resolution. We found that

molecule–substrate coupling as well as specific substitution of functional groups can alter the occupation and alignment of molecular orbital levels. We emphasize the complementary benefit of combined STM and STS compared to CV or (inverse) photoemission studies whose results are often flawed by difficulties and ambiguities in the analysis due to a major lack of knowledge regarding structural integrity, homogeneity and cleanliness of samples. In a truly interlocked interdisciplinary effort, we have identified the fundamental mechanisms of external and intramolecular interactions that determine the electronic structure of the complexes, especially the HOMO and LUMO levels as well as the HOMO–LUMO gap. The results open a path toward the tailored design of triplet emitters for improving the performance of future OLED devices.

Acknowledgements

This work was supported by the Deutsche Forschungsgemeinschaft (DFG) through the Transregional Collaborative Research Center TRR61, project B13. T.K. and N.L.D. acknowledge computer time at the University of Münster's high performance facility PALMA.

References

1. Müllen, K.; Scherf, U., Eds. *Organic Light-Emitting Devices;* Wiley-VCH: Weinheim, 2006.
2. Ishii, H.; Sugiyama, K.; Ito, E.; Seki, K. *Adv. Mater.* **1999,** *11,* 605–625. doi:10.1002/(SICI)1521-4095(199906)11:8<605::AID-ADMA605>3.0.CO;2-Q
3. Heinze, J. *Angew. Chem., Int. Ed. Engl.* **1984,** *23,* 831–847. doi:10.1002/anie.198408313
4. Rusling, J. F.; Suib, S. L. *Adv. Mater.* **1994,** *6,* 922–930. doi:10.1002/adma.19940061204
5. Hamelin, A. *J. Electroanal. Chem.* **1996,** *407,* 1–11. doi:10.1016/0022-0728(95)04499-X
6. Holze, R. *J. Solid State Electrochem.* **2009,** *13,* 1629–1632. doi:10.1007/s10008-008-0753-6
7. Takahashi, T.; Suzuki, S.; Morikawa, T.; Katayama-Yoshida, H.; Hasegawa, S.; Inokuchi, H.; Seki, K.; Kikuchi, K.; Suzuki, S.; Ikemoto, K.; Achiba, Y. *Phys. Rev. Lett.* **1992,** *68,* 1232–1235. doi:10.1103/PhysRevLett.68.1232
8. Wu, C. I.; Hirose, Y.; Sirringhaus, H.; Kahn, A. *Chem. Phys. Lett.* **1997,** *272,* 43–47. doi:10.1016/S0009-2614(97)00481-8
9. Krause, S.; Casu, M. B.; Schöll, A.; Umbach, E. *New J. Phys.* **2008,** *10,* 085001. doi:10.1088/1367-2630/10/8/085001
10. Sharifzadeh, S.; Biller, A.; Kronik, L.; Neaton, J. B. *Phys. Rev. B* **2012,** *85,* 125307. doi:10.1103/PhysRevB.85.125307
11. Lu, X.; Grobis, M.; Khoo, K. H.; Louie, S. G.; Crommie, M. F. *Phys. Rev. Lett.* **2003,** *90,* 096802. doi:10.1103/PhysRevLett.90.096802
12. Repp, J.; Meyer, G.; Stojković, S. M.; Gourdon, A.; Joachim, C. *Phys. Rev. Lett.* **2005,** *94,* 026803. doi:10.1103/PhysRevLett.94.026803
13. Wegner, D.; Yamachika, R.; Wang, Y.; Brar, V. W.; Bartlett, B. M.; Long, J. R.; Crommie, M. F. *Nano Lett.* **2008,** *8,* 131–135. doi:10.1021/nl072217y
14. Weber-Bargioni, A.; Auwärter, W.; Klappenberger, F.; Reichert, J.; Lefrançois, S.; Strunskus, T.; Wöll, C.; Schiffrin, A.; Pennec, Y.; Barth, J. V. *ChemPhysChem* **2008,** *9,* 89–94. doi:10.1002/cphc.200700600
15. Kim, H.; Son, W.-j.; Jang, W. J.; Yoon, J. K.; Han, S.; Kahng, S.-J. *Phys. Rev. B* **2009,** *80,* 245402. doi:10.1103/PhysRevB.80.245402
16. Scudiero, L.; Barlow, D. E.; Mazur, U.; Hipps, K. W. *J. Am. Chem. Soc.* **2001,** *123,* 4073–4080. doi:10.1021/ja0100726
17. Iancu, V.; Deshpande, A.; Hla, S.-W. *Phys. Rev. Lett.* **2006,** *97,* 266603. doi:10.1103/PhysRevLett.97.266603
18. Barth, J. V. *Annu. Rev. Phys. Chem.* **2007,** *58,* 375–407. doi:10.1146/annurev.physchem.56.092503.141259
19. Bai, Y.; Buchner, F.; Wendahl, M. T.; Kellner, I.; Bayer, A.; Steinrück, H.-P.; Marbach, H.; Gottfried, J. M. *J. Phys. Chem. C* **2008,** *112,* 6087–6092. doi:10.1021/jp711122w
20. Chang, S.-H.; Kuck, S.; Brede, J.; Lichtenstein, L.; Hoffmann, G.; Wiesendanger, R. *Phys. Rev. B* **2008,** *78,* 233409. doi:10.1103/PhysRevB.78.233409
21. Chen, X.; Fu, Y.-S.; Ji, S.-H.; Zhang, T.; Cheng, P.; Ma, X.-C.; Zou, X.-L.; Duan, W.-H.; Jia, J.-F.; Xue, Q.-K. *Phys. Rev. Lett.* **2008,** *101,* 197208. doi:10.1103/PhysRevLett.101.197208
22. Franke, K. J.; Schulze, G.; Pascual, J. I. *Science* **2011,** *332,* 940–944. doi:10.1126/science.1202204
23. Yoshida, K.; Isoda, S.; Kamata, T. *Cryst. Growth Des.* **2009,** *9,* 2582–2587. doi:10.1021/cg7010887
24. Campione, M.; Fumagalli, E.; Raimondo, L.; Monguzzi, A.; Meinardi, F.; Sassella, A. *Chem. Mater.* **2011,** *23,* 832–840. doi:10.1021/cm102139h
25. Gersen, H.; Schaub, R.; Xu, W.; Stensgaard, I.; Laegsgaard, E.; Linderoth, T. R.; Besenbacher, F.; Nazeeruddin, M. K.; Graetzel, M. *Appl. Phys. Lett.* **2006,** *89,* 264102. doi:10.1063/1.2424675
26. Otsuki, J.; Tokimoto, T.; Noda, Y.; Yano, T.; Hasegawa, T.; Chen, X.; Okamoto, Y. *Chem. – Eur. J.* **2007,** *13,* 2311–2319. doi:10.1002/chem.200600972
27. Oncel, N.; Bernasek, S. L. *Appl. Phys. Lett.* **2008,** *92,* 133305. doi:10.1063/1.2904622
28. Yokoyama, T.; Takahashi, T.; Shinozaki, K. *Phys. Rev. B* **2010,** *82,* 155414. doi:10.1103/PhysRevB.82.155414
29. Ng, Z.; Loh, K. P.; Li, L.; Ho, P.; Bai, P.; Yip, J. H. K. *ACS Nano* **2009,** *3,* 2103–2114. doi:10.1021/nn900570v
30. Ewen, P. R.; Sanning, J.; Doltsinis, N. L.; Mauro, M.; Strassert, C. A.; Wegner, D. *Phys. Rev. Lett.* **2013,** *111,* 267401. doi:10.1103/PhysRevLett.111.267401
31. Strassert, C. A.; Chien, C.-H.; Galvez Lopez, M. D.; Kourkoulos, D.; Hertel, D.; Meerholz, K.; De Cola, L. *Angew. Chem., Int. Ed.* **2011,** *50,* 946–950. doi:10.1002/anie.201003818
32. Mydlak, M.; Mauro, M.; Polo, F.; Felicetti, M.; Leonhardt, J.; Diener, G.; De Cola, L.; Strassert, C. A. *Chem. Mater.* **2011,** *23,* 3659–3667. doi:10.1021/cm2010902
33. De Cola, L.; Strassert, C. A.; Mathias, M.; Mauro, M.; Felicetti, M.; Diener, G.; Leonhardt, J. DE 10 2011 001 007, 2012.
34. *Gaussian 09;* Gaussian, Inc.: Pittsburgh, PA, 2009.
35. Adamo, C.; Barone, V. *J. Chem. Phys.* **1999,** *110,* 6158–6170. doi:10.1063/1.478522
36. Andrae, D.; Häußermann, U.; Dolg, M.; Stoll, H.; Preuss, H. *Theor. Chem. Acc.* **1990,** *77,* 123–141. doi:10.1007/BF01114537
37. Kühnle, A. *Curr. Opin. Colloid Interface Sci.* **2009,** *14,* 157–168. doi:10.1016/j.cocis.2008.01.001
38. Qiu, X.; Wang, C.; Yin, S.; Zeng, Q.; Xu, B.; Bai, C. *J. Phys. Chem. B* **2000,** *104,* 3570–3574. doi:10.1021/jp993501j

39. Furukawa, S.; Tahara, K.; De Schryver, F. C.; Van der Auweraer, M.; Tobe, Y.; De Feyter, S. *Angew. Chem., Int. Ed.* **2007,** *46,* 2831–2834. doi:10.1002/anie.200604782
40. Maksymovych, P.; Sorescu, D. C.; Yates, J. T., Jr. *Phys. Rev. Lett.* **2006,** *97,* 146103. doi:10.1103/PhysRevLett.97.146103
41. When measuring a *dI*/*dV* map within the HOMO–LUMO gap, the arising signal is based on the current variations due to the feedback loop. The features in such a map correspond to the derivative of the topography along the fast scan direction. When measuring a *dI*/*dV* map within the HOMO–LUMO gap, the arising signal is based on the current variations due to the feedback loop. The features in such a map correspond to the derivative of the topography along the fast scan direction.
42. Feenstra, R. M. *Surf. Sci.* **1994,** *299–300,* 965–979. doi:10.1016/0039-6028(94)90710-2
43. Ziegler, M.; Néel, N.; Sperl, A.; Kröger, J.; Berndt, R. *Phys. Rev. B* **2009,** *80,* 125402. doi:10.1103/PhysRevB.80.125402
44. Bode, M.; Krause, S.; Berbil-Bautista, L.; Heinze, S.; Wiesendanger, R. *Surf. Sci.* **2007,** *601,* 3308–3314. doi:10.1016/j.susc.2007.06.017
45. Braun, K.-F.; Rieder, K.-H. *Phys. Rev. B* **2008,** *77,* 245429. doi:10.1103/PhysRevB.77.245429
46. Bedwani, S.; Wegner, D.; Crommie, M. F.; Rochefort, A. *Phys. Rev. Lett.* **2008,** *101,* 216105. doi:10.1103/PhysRevLett.101.216105
47. Repp, J.; Meyer, G.; Paavilainen, S.; Olsson, F. E.; Persson, M. *Science* **2006,** *312,* 1196–1199. doi:10.1126/science.1126073
48. Mugarza, A.; Robles, R.; Krull, C.; Korytár, R.; Lorente, N.; Gambardella, P. *Phys. Rev. B* **2012,** *85,* 155437. doi:10.1103/PhysRevB.85.155437
49. Lukasczyk, T.; Flechtner, K.; Merte, L. R.; Jux, N.; Maier, F.; Gottfried, J. M.; Steinrück, H.-P. *J. Phys. Chem. C* **2007,** *111,* 3090–3098. doi:10.1021/jp0652345
50. Hoffmann, R. *Rev. Mod. Phys.* **1988,** *60,* 601–628. doi:10.1103/RevModPhys.60.601
51. Lu, X.; Grobis, M.; Khoo, K. H.; Louie, S. G.; Crommie, M. F. *Phys. Rev. B* **2004,** *70,* 115418. doi:10.1103/PhysRevB.70.115418
52. Wang, L.; Liu, L.; Chen, W.; Feng, Y.; Wee, A. T. S. *J. Am. Chem. Soc.* **2006,** *128,* 8003–8007. doi:10.1021/ja061741o
53. Koch, N. *J. Phys.: Condens. Matter* **2008,** *20,* 184008. doi:10.1088/0953-8984/20/18/184008
54. Harutyunyan, H.; Callsen, M.; Allmers, T.; Caciuc, V.; Blügel, S.; Atodiresei, N.; Wegner, D. *Chem. Commun.* **2013,** *49,* 5993–5995. doi:10.1039/c3cc42574f
55. Kiplinger, J. L.; Richmond, T. G.; Osterberg, C. E. *Chem. Rev.* **1994,** *94,* 373–431. doi:10.1021/cr00026a005
56. Joshi, H. K.; Arvin, M. E.; Durivage, J. C.; Gruhn, N. E.; Carducci, M. D.; Westcott, B. L.; Lichtenberger, D. L.; Enemark, J. H. *Polyhedron* **2004,** *23,* 429–438. doi:10.1016/j.poly.2003.11.027

License and Terms

The definitive version of this article is the electronic one which can be found at:
doi:10.3762/bjnano.5.234

BEILSTEIN JOURNAL OF NANOTECHNOLOGY

Influence of the supramolecular architecture on the magnetic properties of a Dy^{III} single-molecule magnet: an ab initio investigation

Julie Jung[1], Olivier Cador[1], Kevin Bernot[2], Fabrice Pointillart[1], Javier Luzon[3,4] and Boris Le Guennic[*1]

Full Research Paper

Open Access

Address:
[1]Institut des Sciences Chimiques de Rennes, UMR 6226 CNRS - Université de Rennes 1, 263 Avenue du Général Leclerc, 35042 Rennes Cedex, France, [2]INSA, ISCR, UMR 6226, Université Européenne de Bretagne, 35708 Rennes, France, [3]Instituto de Ciencia de Materiales de Aragon, CSIC–Universidad de Zaragoza, Pedro Cerbuna 12, 50009 Zaragoza, Spain and [4]Centro Universitario de la Defensa, Academia General Militar, Zaragoza, Spain

Email:
Boris Le Guennic[*] - boris.leguennic@univ-rennes1.fr

* Corresponding author

Keywords:
ab initio calculations; dysprosium; magnetic properties; single-molecule magnets; supramolecular effects

Beilstein J. Nanotechnol. **2014,** *5,* 2267–2274.
doi:10.3762/bjnano.5.236

Received: 24 July 2014
Accepted: 05 October 2014
Published: 27 November 2014

This article is part of the Thematic Series "Molecular materials – towards quantum properties".

Guest Editor: M. Ruben

Abstract

Single-crystal angular-resolved magnetometry and wavefunction-based calculations have been used to reconsider the magnetic properties of a recently reported Dy^{III}-based single-molecule magnet, namely $[Dy(hfac)_3(L^1)]$ with $hfac^-$ = 1,1,1,5,5,5-hexafluoro-acetylacetonate and L^1 = 2-(4,5-bis(propylthio)-1,3-dithiol-2-ylidene)-6-(pyridin-2-yl)-5H-[1,3]dithiolo[4',5':4,5]benzo[1,2-d]imidazole. The magnetic susceptibility and magnetization at low temperature are found to be strongly influenced by supramolecular interactions. Moreover, taking into account the hydrogen-bond networks in the calculations allows to explain the orientation of the magnetic axes. This strongly suggests that hydrogen bonds play an important role in the modulation of the electrostatic environment around the Dy^{III} center that governs the nature of its magnetic ground-state and the orientation of its anisotropy axes. We thus show here that SMM properties that rely on supramolecular organization may not be transferable into single-molecule devices.

Introduction

At the molecular level, single-molecule magnets (SMMs) can be seen as magnets in which the magnetic information relies on the magnetic moment of the molecule and its magnetic anisotropy [1]. Most of SMMs have been characterized as bulk crystalline material in which intermolecular magnetic interactions are expected to be negligible when compared to the

intramolecular ones. The magnetic properties of a compound have then a molecular origin. However the "single-molecule" terminology can be misleading. In fact, in some particular cases, supramolecular interactions have been evidenced to play a significant role in SMM behavior. For instance, in Mn aggregates, supramolecular organization generates exchange-biased quantum tunneling [2]. The easiest way to evidence these supramolecular effects is to design a diamagnetic solid solution in which the sample is present at a doping level [3-12]. The investigation of such sample shows drastic differences from the bulk and highlights that a "single-molecule" when embedded in its crystalline matrix does not behave as an isolated object. This sensitivity of SMM to their environment makes their insertion into devices [13-15] trickier than expected. If SMM are considered for quantum information processing [16-19], supramolecular interactions are expected to generate decoherence [20]. If spin-based devices [13] are considered, the influence of supramolecular interactions has to be characterized very well before deposition of the molecule on a surface. This implies new strategies and new investigation tools [21,22]. When the molecule benefits from a well-known architecture [23,24] that can be optimized for grafting [25,26] the magnetic properties of the molecular object can be kept at the surface [27,28]. This is a tremendous breakthrough in magnetic molecular science that opens the way to molecular surface magnetometry [29]. However, in a "core-shell" picture, where the core is the magnetic ion and the shell its organic surrounding, shell deformation upon grafting can drastically impact the properties of the molecule. A good example is Tb-phthalocyanine molecule, which is one of the most efficient SMM [30]. Depending on the surface and the grafting or deposition mode [25,31-33], it can show erratic hysteresis and even some depth- dependence of the magnetic behavior when multilayers are considered [34]. In order to overcome these drawbacks and to understand their origin, many studies have been undertaken on single-crystals to extensively characterize the magnetic anisotropy of the molecules [9,10,35-38] and its evolution with ligand modifications [39-41]. These studies have been performed mainly on lanthanide-based SMMs as these ions are expected to be extremely sensitive to modifications of the surrounding [42,43]. The first strong experimental evidence has been given by the investigation of DyDOTA (where H_4DOTA = 1,4,7,10-tetraazacyclododecane *N*,*N*′,*N*″,*N*‴-tetraacetic acid) the Dy derivative of the famous GdDOTA that is a commercial contrast agent used in MRI [44]. In this molecule, lanthanide coordination is ensured by one DOTA ligand and one water molecule which provides the "contrast properties" of the compound [45]. A general assumption was that these properties were governed by the Ln–O bond that was supposed to be close to the easy magnetization axis of the molecule. Synergistic investigation by single-crystal magnetometry, low temperature luminescence, and wavefunction-based ab initio calculations, has demonstrated that subtle modification of the Dy^{III} environment such as the rotation of the water molecule is enough to be the driving force of the easy-axis orientation in such a molecule [40]. Subsequent investigations have shown that all lanthanides from Tb to Yb are affected in the same way [36]. This reveals that this subtle effect can be considered as a general property of 4f open-shell ions whatever their ground-state parity. This opens the way to close theoretical examinations of Ln-based SMMs as simple electrostatic approaches were not able to reproduce such results [46].

The influence of the surrounding on Ln-based SMM can also be highlighted through a supramolecular point of view. As an example, the special packing of two analogous Yb-based molecules in which H-bonds are present or not, drastically influences the orientation of the magnetic easy axis [12,39]. In the latter, multiconfigurational post-Hartree–Fock calculations demonstrated that the relative position of one hydrogen atom along the N–H···O bonding mode tailors its orientation.

In the present article, a Dy^{III}-based SMM in which supramolecular effects impact the magnetic properties is investigated on the basis of single-crystal angular-resolved magnetometry and ab initio calculations.

Results and Discussion

We have focused our investigation on two Dy^{III}-based complexes that were reported by some of us recently [12]. As a short reminder, both complexes are mononuclear species of the general formula $[Dy(hfac)_3(L^1)]$ (**Dy1**) and $[Dy(hfac)_3(L^2)]$ (**Dy2**). **Dy1** crystallizes in the triclinic *P*–1 (No. 2) space group with a unit cell composed of mononuclear complexes of the formula $[Dy(hfac)_3(L^1)]$ with $hfac^-$ = 1,1,1,5,5,5-hexafluoroacetylacetonate and L^1 = 2-(4,5-bis(propylthio)-1,3-dithiol-2-ylidene)-6-(pyridin-2-yl)-5H-[1,3]dithiolo[4',5':4,5]benzo[1,2-d]imidazole. In this complex, the Dy^{III} ion is surrounded by six oxygen atoms and two nitrogen atoms belonging to three $hfac^-$ ligands and one bis-chelating L^1 ligand (Figure 1). The average Dy–O distances are shorter (2.35(3) Å) than the average Dy–N distances (2.50(6) Å). **Dy2** crystallizes in the monoclinic $P2_1/c$ (No. 14) space group and the unit cell is composed of mononuclear complexes of the formula $[Dy(hfac)_3(L^2)]$ with L^2 = 2-(4,5-bis(propylthio)-1,3-dithiol-2-ylidene)-6-(pyridin-2-yl)-5-(pyridin-2-ylmethyl)-5H-[1,3]dithiolo[4',5':4,5]benzo[1,2-d]imidazole (Figure S1, Supporting Information File 1). As for **Dy1**, the Dy^{III} ion is surrounded by six oxygen atoms and two nitrogen atoms belonging to three $hfac^-$ ligands and one bis-chelating L^2 ligand. The average Dy–O and Dy–N distances are equal to 2.34(4) Å and 2.49(5) Å, respectively. The formation of "head to tail" dimers is observed in both compounds.

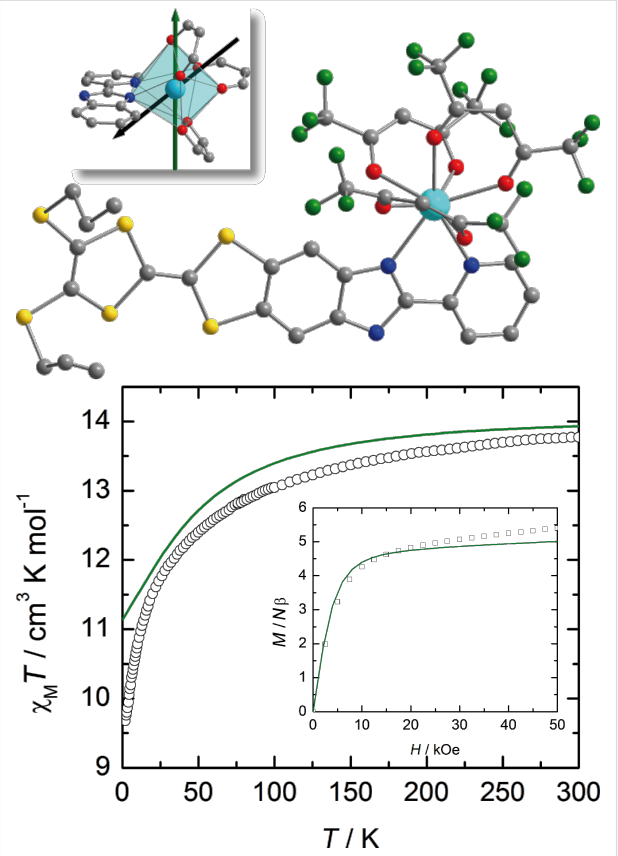

Figure 1: Molecular structure of **Dy1** (top). Dy, O, N, C, S and F atoms are depicted in light blue, red, blue, grey, yellow and green, respectively. H atoms are omitted for clarity. Inset: Experimental (black) and theoretical (green) ground state anisotropy axes are shown on the coordination polyhedron. Thermal variation of $\chi_M T$ of a solid-state sample of **Dy1** (black circles) with the curve (in green) calculated on the basis of SA-CASSCF/RASSI-SO data (bottom). Inset: field variation of the magnetization at 2 K (black squares) with the computed curve (in green) obtained at the same level of calculation.

Despite their identical coordination spheres the experimental magnetic properties of the two compounds differ significantly. Indeed, in the condensed phase the thermal variations of $\chi_M T$ as well as the field variations of the magnetization at 2 K do not match (Figure 1 and Figure S1, Supporting Information File 1). While for both complexes the high temperature values of $\chi_M T$ coincide and are close to the expected value for a $^6H_{15/2}$ multiplet (14.17 $cm^3 \cdot K \cdot mol^{-1}$) [47], on cooling the values of $\chi_M T$ of **Dy1** is far below the ones of **Dy2**. On the other hand, the magnetization at 2 K increases linearly for **Dy1** at fields higher than 1 T while it saturates for **Dy2**. The consequences of these differences is that **Dy2** behaves as a SMM in the solid state while **Dy1** does not [12]. However, the latter behaves as a SMM in CH_2Cl_2 solution. This drastic difference of behavior between solid state and solution was attributed, with no clear experimental evidence, to the breaking of the hydrogen-bond network in solution. This is what we would like to clarify in the present work.

Following this first investigation [12], we took advantage of the uniqueness of the molecule in the *P*–1 space group to perform single-crystal angular-resolved magnetometry for **Dy1** (see Experimental section) as already done in the case of the Yb^{III} derivative [39]. After indexation of the crystal faces through single-crystal diffraction (Figure S2, Supporting Information File 1), the angular dependence of the magnetization was measured in three orthogonal planes (XY, YZ and XZ) at 2 K with an applied magnetic field of 1 kOe (Figure 2). The data were then fitted assuming that $M = \chi_M H$. Rotation of H in the αβ-plane changes the expression of the magnetization to $M/H = \chi_{\alpha\alpha}(\cos\theta)^2 + \chi_{\beta\beta}(\sin\theta)^2 + 2\chi_{\alpha\beta}(\sin\theta\cos\theta)$, where α and β are the directions of the vectors X, Y and Z in a cyclic permutation and θ is the angle between H and α (Figure 2). The principal values of the Zeeman tensor in the 1/2 effective spin approximation (g_z = 14.22, g_y = 3.96 and g_x = 9.43) as well as its orientation are extracted (see Supporting Information File 1). First of all, the principal values do not fit with an Ising-type anisotropy (g_z = 20, $g_y = g_x$ = 0) which agrees with the non-SMM behavior of this compound in the solid state. Secondly, the tensor orientation of the ground state is not lying in any special direction (Figure 1).

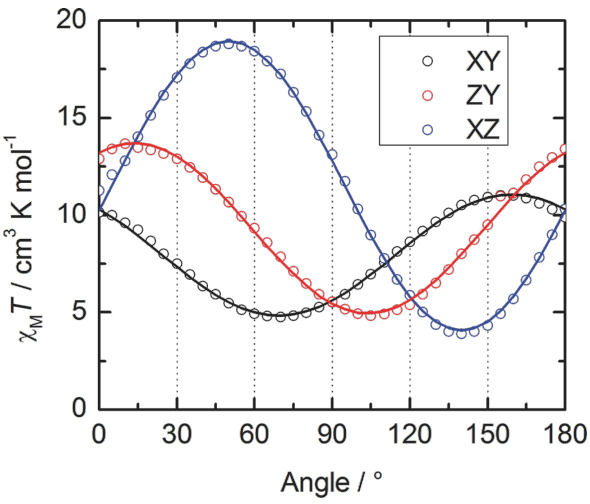

Figure 2: Angular dependence of $\chi_M T$ measured for **Dy1** in the three orthogonal planes with the best fitted curves as solid lines.

Relativistic ab initio calculations (SA-CASSCF/RASSI-SO) have been performed in order to rationalize the observed magnetic properties of both compounds **Dy1** and **Dy2**. We first attempted to reproduce the magnetic data in solely considering isolated molecules (see Experimental section). For **Dy2** the computed $\chi_M T$ vs T and M vs H curves almost perfectly match the experimental ones (Figure S1, Supporting Information File 1). On the contrary, this "molecular" approach dramati-

cally fails in the case of **Dy1** with a significant discrepancy between calculated and experimental values at the low temperature limit for $\chi_M T$ (computed: $\chi_M T$ = 11.135 $cm^3 \cdot K \cdot mol^{-1}$; experimental: $\chi_M T$ = 9.67 $cm^3 \cdot K \cdot mol^{-1}$, Figure 1). Also, at 2 K the computed *M* vs *H* curve saturates contrary to the experimental one (Figure 1), a behavior that was already observed for the Yb parents [Yb(hfac)$_3$(L^1)] and [Yb(hfac)$_3$(L^2)] [39]. The disagreement for [Yb(hfac)$_3$(L^1)] was attributed to intermolecular interactions that seem to play a key role in the magnetic properties of this series of complexes. Moreover, the calculated ground state of **Dy1** is almost Ising (see below in Table 1) in contradiction to the solid-state experiments (see above). This result is confirmed by the nature of the calculated ground-state wavefunction that is mainly composed of M_J = 15/2 state with a small contribution of the M_J = 11/2 state. Finally, the orientation of the calculated easy axis differ by more than 57° from the experiment. In short, whereas this "molecular" computational results do not reproduce the solid-state behavior, they are in line with the observations made in solution [12]. The above results showed that a "local" description that only takes into account intramolecular interactions is not able to explain the solid-state magnetism of this complex. As already mentioned in the introduction, subtle geometric effects may change both magnetic susceptibility and orientation of the easy axis [39,40]. Contrary to **Dy2**, intermolecular hydrogen bond networks organize the three dimensional edifice in **Dy1** (Figure 3) [12]. We thus revisit the theoretical interpretation on the basis of these supramolecular interactions.

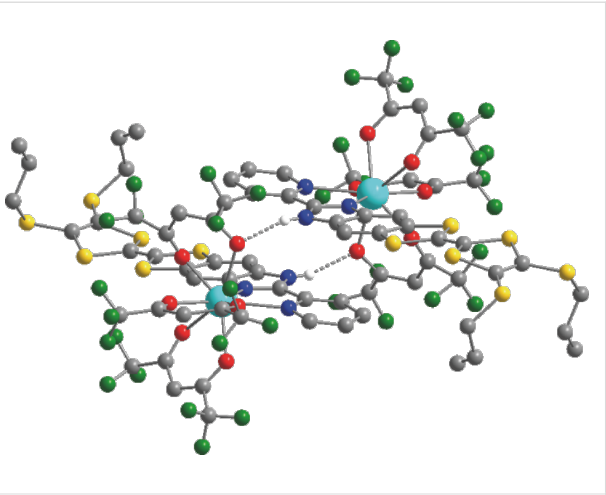

Figure 3: Representation of supramolecular interactions in **Dy1**. Dy, O, N, C, S and F atoms are depicted in light blue, red, blue, grey, yellow and green, respectively. H atoms (except the H atoms involved in hydrogen bonds) are omitted for clarity.

In **Dy1**, a hydrogen bond is formed between the protonated imidazole ring and the oxygen atom of the neighboring molecule. On the contrary, in **Dy2**, the presence of the 2-methylpyridine arm prevents such weak interactions between neighboring molecules [12]. To mimic this hydrogen bond in the calculations, the neighboring complex in **Dy1** was modeled by an imidazole molecule. Various arbitrary positions of the H atom were considered, i.e., i) at the position calculated from single-crystal X-ray diffraction (H_N), ii) along the O···N axis at a classical O–H distance (H_O) and iii) equidistant to N and O (H_m). In order to cover as much as possible of both the long-range interactions and the electronic reorganization that might be induced by this weak interaction, the hydrogen atom involved in the hydrogen bond was described with an extended [3s2p1d] basis set (see Experimental section). First, the presence of this hydrogen bond in the calculations slightly affects the relative energy splitting of the ground-state multiplet. Compared with the non-protonated situation, the whole splitting is slightly reduced for H_m and H_N whereas it increases for H_O (Table 1 and Figure S3, Supporting Information File 1). More importantly, the energy gap between the ground and first excited states is much smaller when the H atom is positioned close to the N atom of the imidazole or in the median position. Thus, the weight of the M_J = ±15/2 state in the ground-state wavefunction is significantly lowered and mixing with other M_J states is observed (Table 1). Concomitantly, the magnetic susceptibility and magnetization curves are progressively closer to the experimental ones (Figure 4). In particular, for the hydrogen atom at the H_m position, the low temperature limit for $\chi_M T$ is well reproduced (computed: $\chi_M T$ = 9.40 $cm^3 \cdot K \cdot mol^{-1}$; experimental: $\chi_M T$ = 9.67 $cm^3 \cdot K \cdot mol^{-1}$), as well as the *M* vs *H* curve at 2 K. As shown in Figure 4 the location of the proton has a non-negli-

Table 1: Computed ground-state anisotropy tensor for **Dy1** for different positions of the hydrogen atom involved in the hydrogen bond. The weights of the ± M_J components of the calculated ground-state wavefunction, the relative energy of the first excited-state (ΔE, cm^{-1}) and the angle (α, degrees) between the experimental and computed easy axes are also given.

H atom position	g_x	g_y	g_z	± M_J weights of the GS wavefunction	ΔE	α
no H	0.08	0.16	18.87	0.85|±15/2>; 0.11|±11/2>; 0.03|±7/2>	91.1	56.9
H_O	0.02	0.03	19.51	0.94|±15/2>; 0.03|±9/2>; 0.02|±11/2>	109.7	27.1
H_m	0.83	3.05	17.05	0.77|±15/2>; 0.10|±9/2>; 0.03|±5/2>; 0.03|±1/2>; 0.03|±3/2>	34.1	28.5
H_N	0.39	1.25	17.94	0.78|±15/2>; 0.12|±11/2>; 0.06|±7/2>; 0.03|±3/2>	48.1	67.0

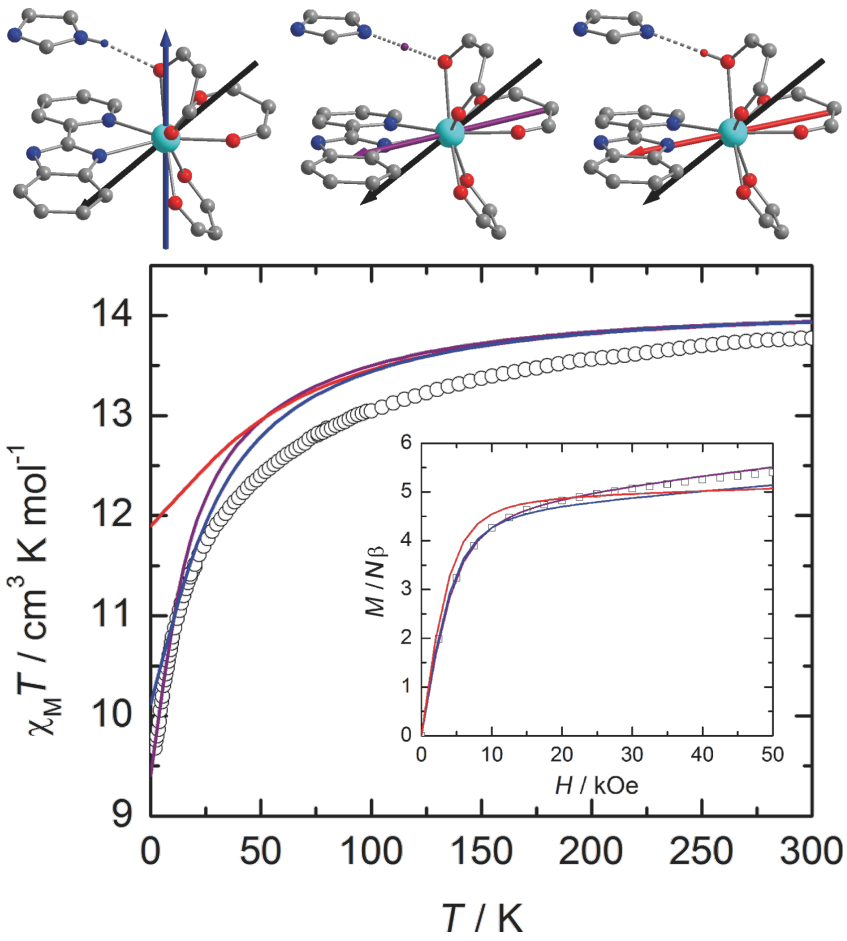

Figure 4: Orientation of the experimental (black) and calculated ground-state anisotropy axes for **Dy1** (top). The orientation of the calculated axis is given for the different positions of the hydrogen atom involved in the hydrogen bond, i.e., from left to right: H_N (blue), H_m (purple) and H_O (red). Thermal variation of $\chi_M T$ of a solid-state sample of **Dy1** (black circles) with the curve calculated on the basis of SA-CASSCF/RASSI-SO data for the various positions of the H atom (bottom). Inset: field variation of the magnetization at 2 K (black squares) with the computed curve obtained at the same level of calculation.

gible effect on the orientation of the ground state magnetic axis. Whereas this axis is calculated far away from the experimental one if the hydrogen bond is not taken into account (α = 57°) or for H_N (α = 67°), the discrepancy is much weaker for H_O (α = 27°) and H_m (α = 29°, Table 1). As described previously [10,39,41], the orientation of the axis is governed by the variation of the electrostatic potentials generated by the coordinated atoms on the Dy^{III} center (Table S1, Supporting Information File 1). In particular, the charge on the oxygen atom (O5) involved in the hydrogen-bond evolves significantly. This induces large modifications of the charge distribution around Dy^{III} with respect to the position of the hydrogen atom. Based on these observations, it seems thus that H_m is the most suited position for this particular H atom. It may signify that at the time scale of the magnetic measurements an "averaged" position of the H atom along the N–H···O bond has to be considered.

Conclusion

The understanding of the subtle mechanisms at the origin of the magnetic properties of molecular materials is a prerequisite before anchoring/grafting these molecular architectures onto surfaces, nanoparticles or graphene-based devices. In this work, we have used wavefunction-based calculations combined with single-crystal angular-resolved magnetometry to reconsider the magnetic properties of a recently proposed Dy^{III}-based single-molecule magnet [12]. The magnetic susceptibility and magnetization at low temperature are found to be strongly influenced by supramolecular interactions. Moreover, taking into account the hydrogen-bond networks allows to explain the orientation of the magnetic axes. The computational results suggest that hydrogen bonds have an important influence on the modulation of the electrostatic environment of the Dy^{III} ion. As a consequence it also impacts the nature of the Dy magnetic ground state and the orientation of the magnetic axes. Further investi-

gation of the dynamics of the N–H···O bonds and its implication on the magnetic behavior is thus envisaged.

Experimental

Computational details. Ab initio calculations were carried out on model structures of **Dy1** and **Dy2** (see below) by using the SA-CASSCF/RASSI-SO approach, as implemented in the MOLCAS quantum chemistry package (versions 7.6) [48]. In this approach, the relativistic effects are treated in two steps on the basis of the Douglas–Kroll Hamiltonian. First, the scalar terms were included in the basis-set generation and were used to determine the spin-free wavefunctions and energies in the complete active space self consistent field (CASSCF) method [49]. Next, spin-orbit coupling was added within the restricted-active-space-state-interaction (RASSI-SO) method, which uses the spin-free wavefunctions as basis states [50,51]. The resulting wavefunctions and energies are used to compute the magnetic properties and the g-tensors of the lowest states from the energy spectrum by using the pseudo-spin $S = 1/2$ formalism in the SINGLE-ANISO routine [52,53]. The calculated ground state wavefunction were obtained from the RASSI-SO results by using a custom-made program. Cholesky decomposition of the bielectronic integrals was employed to save disk space and speed-up the calculations [54]. For similar reasons, the donor part of the TTF ligand in **Dy1** and **Dy2** was replaced by H atoms [39]. All atoms were represented by ANO-type basis sets from the ANO-RCC library [55,56]. The following contractions were used: [9s8p5d4f3g1h] for the Dy ion, [4s3p2d] for the O and N atoms of the first coordination sphere of the Dy ion, [3s2p] for the C, F and remaining N atoms, [3s2p1d] for the H atom involved in the hydrogen bond and [2s] for all the other H atoms. The active space of the self consistent field (CASSCF) method consisted of the nine 4f electrons of the Dy ion spanning the seven 4f orbitals. State-averaged CASSCF calculations were performed for all of the sextets (21 roots) and quadruplets (224 roots) of the Dy ion. Only 148 quadruplets were added to the 21 sextets to mix through spin–orbit coupling in RASSI-SO. In this case, there was no need to add more quadruplet or doublet roots to converge the wavefunctions and energies of the ground multiplet ($^6H_{15/2}$) of the Dy ion. The anisotropy tensor, the energy of the eight Kramer doublets of the ground spin–orbit state, as well as the temperature-dependent magnetic susceptibility and the molar magnetization at 2 K were computed to support experimental results. Atomic charges were computed by using the LoProp approach [57].

Magnetic measurements. Angular-resolved magnetometry was performed on a single-crystal of **Dy1** with a Quantum Design MPMS-XL SQUID magnetometer by using the horizontal-rotator option. The background of the sample holder was subtracted.

Supporting Information

Supporting information features molecular structure and magnetic properties of **Dy2**, as well as susceptibility tensor and calculated charges and potentials of **Dy1**.

Supporting Information File 1

Additional experimental data.
[http://www.beilstein-journals.org/bjnano/content/supplementary/2190-4286-5-236-S1.pdf]

Acknowledgements

This work was supported by the Centre National de la Recherche Scientifique (CNRS), Rennes Métropole, Université de Rennes 1, Région Bretagne, the Fonds Européen de Développement Economique et Régional (FEDER) and the Agence Nationale de la Recherche (No. ANR-13-BS07-0022-01). B. L. G. thanks the French GENCI-CINES center for high-performance computing resources (grant x2014080649).

References

1. Gatteschi, D.; Sessoli, R.; Villain, J. *Molecular Nanomagnets;* Oxford University Press, 2006.
2. Wernsdorfer, W.; Aliaga-Alcalde, N.; Hendrickson, D. N.; Christou, G. *Nature* **2002,** *416,* 406–409. doi:10.1038/416406a
3. Habib, F.; Lin, P.-H.; Long, J.; Korobkov, I.; Wernsdorfer, W.; Murugesu, M. *J. Am. Chem. Soc.* **2011,** *133,* 8830–8833. doi:10.1021/ja2017009
4. Giraud, R.; Wernsdorfer, W.; Tkachuk, A. M.; Mailly, D.; Barbara, B. *Phys. Rev. Lett.* **2001,** *87,* 057203. doi:10.1103/PhysRevLett.87.057203
5. Johnson, R. C.; Malkin, B. Z.; Lord, J. S.; Giblin, S. R.; Amato, A.; Baines, C.; Lascialfari, A.; Barbara, B.; Graf, M. J. *Phys. Rev. B* **2012,** *86,* 014427. doi:10.1103/PhysRevB.86.014427
6. Ishikawa, N.; Sugita, M.; Wernsdorfer, W. *J. Am. Chem. Soc.* **2005,** *127,* 3650–3651. doi:10.1021/ja0428661
7. Vergnani, L.; Barra, A.-L.; Neugebauer, P.; Rodriguez-Douton, M. J.; Sessoli, R.; Sorace, L.; Wernsdorfer, W.; Cornia, A. *Chem. – Eur. J.* **2012,** *18,* 3390–3398. doi:10.1002/chem.201103251
8. Moro, F.; Kaminski, D.; Tuna, F.; Whitehead, G. F. S.; Timco, G. A.; Collison, D.; Winpenny, R. E. P.; Ardavan, A.; McInnes, E. J. L. *Chem. Commun.* **2014,** *50,* 91–93. doi:10.1039/c3cc46326e
9. Yi, X.; Bernot, K.; Cador, O.; Luzon, J.; Calvez, G.; Daiguebonne, C.; Guillou, O. *Dalton Trans.* **2013,** *42,* 6728–6731. doi:10.1039/C3DT50762A
10. da Cunha, T. T.; Jung, J.; Boulon, M.-E.; Campo, G.; Pointillart, F.; Pereira, C. L. M.; Le Guennic, B.; Cador, O.; Bernot, K.; Pineider, F.; Golhen, S.; Ouahab, L. *J. Am. Chem. Soc.* **2013,** *135,* 16332–16335. doi:10.1021/ja4089956
11. Jiang, S.-D.; Wang, B.-W.; Su, G.; Wang, Z.-M.; Gao, S. *Angew. Chem., Int. Ed.* **2010,** *49,* 7448–7451. doi:10.1002/anie.201004027
12. Cosquer, G.; Pointillart, F.; Golhen, S.; Cador, O.; Ouahab, L. *Chem. – Eur. J.* **2013,** *19,* 7895–7903. doi:10.1002/chem.201300397

13. Bogani, L.; Wernsdorfer, W. *Nat. Mater.* **2008,** *7,* 179–186. doi:10.1038/nmat2133
14. Candini, A.; Klyatskaya, S.; Ruben, M.; Wernsdorfer, W.; Affronte, M. *Nano Lett.* **2011,** *11,* 2634–2639. doi:10.1021/nl2006142
15. Urdampilleta, M.; Klyatskaya, S.; Cleuziou, J.-P.; Ruben, M.; Wernsdorfer, W. *Nat. Mater.* **2011,** *10,* 502–506. doi:10.1038/nmat3050
16. Troiani, F.; Affronte, M. *Chem. Soc. Rev.* **2011,** *40,* 3119–3129. doi:10.1039/C0CS00158A
17. Timco, G. A.; Faust, T. B.; Tuna, F.; Winpenny, R. E. P. *Chem. Soc. Rev.* **2011,** *40,* 3067–3075. doi:10.1039/C0CS00151A
18. Ardavan, A.; Rival, O.; Morton, J. J. L.; Blundell, S. J.; Tyryshkyn, A. M.; Timco, G. A.; Winpenny, R. E. P. *Phys. Rev. Lett.* **2007,** *98,* 057201. doi:10.1103/PhysRevLett.98.057201
19. Aromi, G.; Aguila, D.; Gamez, P.; Luis, F.; Roubeau, O. *Chem. Soc. Rev.* **2012,** *41,* 537–546. doi:10.1039/C1CS15115K
20. Takahashi, S.; Tupitsyn, I. S.; van Tol, J.; Beedle, C. C.; Hendrickson, D. N.; Stamp, P. C. E. *Nature* **2011,** *476,* 76–79. doi:10.1038/nature10314
21. Cornia, A.; Mannini, M.; Sainctavit, P.; Sessoli, R. *Chem. Soc. Rev.* **2011,** *40,* 3076–3091. doi:10.1039/C0CS00187B
22. Mannini, M.; Pineider, F.; Sainctavit, P.; Joly, L.; Fraile-Rodriguez, A.; Arrio, M.-A.; Cartier dit Moulin, C.; Wernsdorfer, W.; Cornia, A.; Gatteschi, D.; Sessoli, R. *Adv. Mater.* **2009,** *21,* 167–171. doi:10.1002/adma.200801883
23. Barra, A.-L.; Caneschi, A.; Cornia, A.; de Biani, F. F.; Gatteschi, D.; Sangregorio, C.; Sessoli, R.; Sorace, L. *J. Am. Chem. Soc.* **1999,** *121,* 5302–5310. doi:10.1021/ja9818755
24. Accorsi, S.; Barra, A.-L.; Caneschi, A.; Chastanet, G.; Cornia, A.; Fabretti, A. C.; Gatteschi, D.; Mortalo, C.; Olivieri, E.; Parenti, F.; Rosa, P.; Sessoli, R.; Sorace, L.; Wernsdorfer, W.; Zobbi, L. *J. Am. Chem. Soc.* **2006,** *128,* 4742–4755. doi:10.1021/ja0576381
25. Margheriti, L.; Mannini, M.; Sorace, L.; Gorini, L.; Caneschi, A.; Chiappe, D.; Moroni, R.; Buatier de Mongeot, F.; Cornia, A.; Piras, F. M.; Magnani, N.; Sessoli, R. *Small* **2009,** *5,* 1460–1466. doi:10.1002/smll.200801594
26. Pineider, F.; Mannini, M.; Danieli, C.; Armelao, L.; Piras, F. M.; Magnani, N.; Cornia, A.; Sessoli, R. *J. Mater. Chem.* **2010,** *20,* 187–194. doi:10.1039/B916895H
27. Mannini, M.; Pineider, F.; Sainctavit, P.; Danieli, C.; Otero, E.; Sciancalepore, C.; Talarico, A. M.; Arrio, M.-A.; Cornia, A.; Gatteschi, D.; Sessoli, R. *Nat. Mater.* **2009,** *8,* 194–197. doi:10.1038/nmat2374
28. Mannini, M.; Pineider, F.; Danieli, C.; Totti, F.; Sorace, L.; Sainctavit, P.; Arrio, M.-A.; Otero, E.; Joly, L.; Cezar, J. C.; Cornia, A.; Sessoli, R. *Nature* **2010,** *468,* 417–422. doi:10.1038/nature09478
29. Tancini, E.; Mannini, M.; Sainctavit, P.; Otero, E.; Sessoli, R.; Cornia, A. *Chem. – Eur. J.* **2013,** *19,* 16902–16905. doi:10.1002/chem.201303585
30. Ishikawa, N.; Sugita, M.; Ishikawa, T.; Koshihara, S.-y.; Kaizu, Y. *J. Am. Chem. Soc.* **2003,** *125,* 8694–8695. doi:10.1021/ja029629n
31. Malavolti, L.; Mannini, M.; Car, P.-E.; Campo, G.; Pineider, F.; Sessoli, R. *J. Mater. Chem. C* **2013,** *1,* 2935–2942. doi:10.1039/C3TC00925D
32. Margheriti, L.; Chiappe, D.; Mannini, M.; Car, P.-E.; Sainctavit, P.; Arrio, M.-A.; Buatier de Mongeot, F.; Cezar, J. C.; Piras, F. M.; Magnani, N.; Otero, E.; Caneschi, A.; Sessoli, R. *Adv. Mater.* **2010,** *22,* 5488–5493. doi:10.1002/adma.201003275
33. Klar, D.; Candini, A.; Joly, L.; Klyatskaya, S.; Krumme, B.; Ohresser, P.; Kappler, J.-P.; Ruben, M.; Wende, H. *Dalton Trans.* **2014,** *43,* 10686–10689. doi:10.1039/C4DT01005A
34. Hofmann, A.; Salman, Z.; Mannini, M.; Amato, A.; Malavolti, L.; Morenzoni, E.; Prokscha, T.; Sessoli, R.; Suter, A. *ACS Nano* **2012,** *6,* 8390–8396. doi:10.1021/nn3031673
35. Bernot, K.; Luzon, J.; Bogani, L.; Etienne, M.; Sangregorio, C.; Shanmugam, M.; Caneschi, A.; Sessoli, R.; Gatteschi, D. *J. Am. Chem. Soc.* **2009,** *131,* 5573–5579. doi:10.1021/ja8100038
36. Boulon, M.-E.; Cucinotta, G.; Luzon, J.; Degl'Innocenti, C.; Perfetti, M.; Bernot, K.; Calvez, G.; Caneschi, A.; Sessoli, R. *Angew. Chem., Int. Ed.* **2013,** *52,* 350–354. doi:10.1002/anie.201205938
37. Boulon, M.-E.; Cucinotta, G.; Liu, S.-S.; Jiang, S.-D.; Ungur, L.; Chibotaru, L.; Gao, S.; Sessoli, R. *Chem. – Eur. J.* **2013,** *19,* 13726–13731. doi:10.1002/chem.201302600
38. Hewitt, I. J.; Tang, J.; Madhu, N. T.; Anson, C. E.; Lan, Y.; Luzon, J.; Etienne, M.; Sessoli, R.; Powell, A. K. *Angew. Chem., Int. Ed.* **2010,** *49,* 6352–6356. doi:10.1002/anie.201002691
39. Cosquer, G.; Pointillart, F.; Jung, J.; Le Guennic, B.; Golhen, S.; Cador, O.; Guyot, Y.; Brenier, A.; Maury, O.; Ouahab, L. *Eur. J. Inorg. Chem.* **2014,** 69–82. doi:10.1002/ejic.201301358
40. Cucinotta, G.; Perfetti, M.; Luzon, J.; Etienne, M.; Car, P.-E.; Caneschi, A.; Calvez, G.; Bernot, K.; Sessoli, R. *Angew. Chem., Int. Ed.* **2012,** *51,* 1606–1610. doi:10.1002/anie.201107453
41. Jung, J.; da Cunha, T. T.; Le Guennic, B.; Pointillart, F.; Pereira, C. L. M.; Luzon, J.; Golhen, S.; Cador, O.; Maury, O.; Ouahab, L. *Eur. J. Inorg. Chem.* **2014,** *24,* 3888–3894. doi:10.1002/ejic.201400121
42. Rinehart, J. D.; Long, J. R. *Chem. Sci.* **2011,** *2,* 2078–2085. doi:10.1039/C1SC00513H
43. Luzon, J.; Sessoli, R. *Dalton Trans.* **2012,** *41,* 13556–13567. doi:10.1039/c2dt31388j
44. Viswanathan, S.; Kovacs, Z.; Green, K. N.; Ratnakar, S. J.; Sherry, A. D. *Chem. Rev.* **2010,** *110,* 2960–3018. doi:10.1021/cr900284a
45. Bottrill, M.; Kwok, L.; Long, N. J. *Chem. Soc. Rev.* **2006,** *35,* 557–571. doi:10.1039/B516376P
46. Chilton, N. F.; Collison, D.; McInnes, E. J. L.; Winpenny, R. E. P.; Soncini, A. *Nat. Commun.* **2013,** *4,* No. 2551. doi:10.1038/ncomms3551
47. Kahn, O. *Molecular Magnetism;* Wiley-VCH: New York, 1993.
48. Aquilante, F.; De Vico, L.; Ferré, N.; Ghigo, G.; Malmqvist, P.-å.; Neogrády, P.; Bondo Pedersen, T.; Pitoňák, M.; Reiher, M.; Roos, B. O.; Serrano-Andrés, L.; Urban, M.; Veryazov, V.; Lindh, R. *J. Comput. Chem.* **2010,** *31,* 224–247. doi:10.1002/jcc.21318
49. Roos, B. O.; Taylor, P. R.; Siegbahn, P. E. M. *Chem. Phys.* **1980,** *48,* 157–173. doi:10.1016/0301-0104(80)80045-0
50. Malmqvist, P.-å.; Roos, B. O. *Chem. Phys. Lett.* **1989,** *155,* 189–194. doi:10.1016/0009-2614(89)85347-3
51. Malmqvist, P. Å.; Roos, B. O.; Schimmelpfennig, B. *Chem. Phys. Lett.* **2002,** *357,* 230–240. doi:10.1016/S0009-2614(02)00498-0
52. Chibotaru, L.; Ungur, L.; Soncini, A. *Angew. Chem., Int. Ed.* **2008,** *47,* 4126–4129. doi:10.1002/anie.200800283
53. Chibotaru, L. F.; Ungur, L. *J. Chem. Phys.* **2012,** *137,* 064112. doi:10.1063/1.4739763
54. Aquilante, F.; Malmqvist, P.-Å.; Pedersen, T. B.; Ghosh, A.; Roos, B. O. *J. Chem. Theory Comput.* **2008,** *4,* 694–702. doi:10.1021/ct700263h

55. Roos, B. O.; Lindh, R.; Malmqvist, P.-Å.; Veryazov, V.; Widmark, P.-O.; Borin, A. C. *J. Phys. Chem. A* **2008,** *112,* 11431–11435. doi:10.1021/jp803213j
56. Widmark, P.-O.; Malmqvist, P.-Å.; Roos, B. O. *Theor. Chim. Acta* **1990,** *77,* 291–306. doi:10.1007/BF01120130
57. Gagliardi, L.; Lindh, R.; Karlström, G. *J. Chem. Phys.* **2004,** *121,* 4494–4500. doi:10.1063/1.1778131

BEILSTEIN JOURNAL OF NANOTECHNOLOGY

Poly(styrene)/oligo(fluorene)-intercalated fluoromica hybrids: synthesis, characterization and self-assembly

Giuseppe Leone[*1], Francesco Galeotti[*1], William Porzio[1], Guido Scavia[1], Luisa Barba[2], Gianmichele Arrighetti[2], Giovanni Ricci[1], Chiara Botta[1] and Umberto Giovanella[*1]

Full Research Paper

Open Access

Address:
[1]CNR, Istituto per lo Studio delle Macromolecole (ISMAC), via E. Bassini 15, 20133 Milano, Italy and [2]CNR, Institute of Crystallography, UOS Trieste, Strada Statale 14, 34149 Basovizza, Trieste, Italy

Email:
Giuseppe Leone[*] - g.leone@ismac.cnr.it;
Francesco Galeotti[*] - f.galeotti@ismac.cnr.it;
Umberto Giovanella[*] - u.giovanella@ismac.cnr.it

* Corresponding author

Keywords:
breath figures; fluoromica; layered silicates; oligo(fluorene); photostability; self-assembly

Beilstein J. Nanotechnol. **2014,** *5,* 2450–2458.
doi:10.3762/bjnano.5.254

Received: 04 July 2014
Accepted: 18 November 2014
Published: 19 December 2014

This article is part of the Thematic Series "Molecular materials – towards quantum properties".

Guest Editor: M. Ruben

Abstract

We report on the intercalation of a cationic fluorescent oligo(fluorene) in between the 2D interlayer region of a fluoromica type silicate. The formation of intercalated structures with different fluorophore contents is observed in powders by synchrotron radiation XRD. Successively, the hybrids are dispersed in poly(styrene) through in situ polymerization. Such a procedure allows us to synthesize the materials from solution, to achieve solid films, and to characterize them by optical and morphologic techniques. The polymeric films with homogeneous distribution of the hybrids exhibit ultraviolet–blue photoluminescence with a significantly enhanced photostability compared to the bare oligo(fluorene)s. Finally, under specific conditions, the polymer hybrid with higher oligo(fluorene) content spontaneously assembles into highly ordered microporous films.

Introduction

The functionalization of inorganic structures is an effective approach for enriching the potential applications of existing nanomaterials [1-7]. Among the inorganic nano-scaled materials, layered silicates have been widely used as hosts for functional π-conjugated molecules (dyes) [8-10], and polymers [11-15], owing to their adsorption properties, ion-exchange ability, high specific surface area, and a two-dimensional (2D) expandable interlayer space. The combination of these features permits the easy tuning of the interaction between the emitting centers by surface chemistry (i.e., ion-exchange and grafting reactions), and a sandwich-type intercalation. In particular, the intercalation of functional molecular species within the silicate inter-

layer region is expected (i) to improve the photo-, thermo-, and chemical stability of the dye, which is generally insufficient for a use in applied optoelectronic devices, and (ii) to control the accommodation of the guest for organizing efficient dye assemblies, thus allowing the tuning of the photo-functions of the hybrid [16,17].

Herein we report the intercalation of a cationic oligo(fluorene) (Figure 1) in between the interlayer region of a fluoromica type silicate. A series of three samples has been synthesized with different amounts of the dye with respect to the fluoromica maximum cation exchange capacity (CEC), and the formation of intercalated structures has been observed in powders by synchrotron radiation X-ray diffraction (XRD). Successively, in order to enhance the solution processability of the material, the resulting intercalated hybrids were dispersed in a poly(styrene) (PS) matrix by in situ thermal polymerization. Such a procedure allowed us to process the materials as solid films and to characterize them by optical, structural, and morphologic analyses. In addition, we explored the possibility of organizing these materials in ordered honeycomb structures through a self-assembly approach.

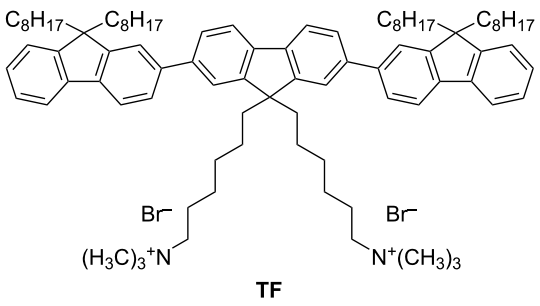

Figure 1: Chemical structure of the cationic oligo(fluorene) (TF).

Results and Discussion

Synthesis and characterization of TF-intercalated SME Hybrids

Sodium-exchanged Somasif ME100 (SME) has been chosen to intercalate a fluorescent oligo(fluorene) cation (hereafter named TF) thanks to its very low iron impurities and low charge density [18-20]. The organo-modified SME hybrids were synthesized by a cation-exchange reaction following the procedure reported elsewhere [8]. In Table 1 the amount of charged TF with respect to the CEC of pristine SME is shown.

Structural investigation through XRD studies

Evidence of the intercalation of the oligo(fluorene) (TF) cation was first provided by XRD analysis (Figure 2 and Table 1). The sample profiles have been treated according to Enzo et al. [21] to derive relevant parameters reported in Table 1. As reported on our previous works [8,9], SME shows two diffraction peaks at 7.30 and 9.40°, corresponding to the interlayer spacing of 1.22 and 0.95 nm of hydrated and dehydrated layers, respectively, while for DHS (dehydrated SME) only the peak at about 9.40° [$d(001)$ = 0.95 nm] is observed.

The XRD pattern of TF-intercalated SME samples (T5, T15, and T30) are reported in Figure 2. T5 exhibits a broader peak centered at ca. 5.88°, and a second one at about 7.1°. The former (marked with an asterisk and equivalent to pristine SME [9]) stems from the layer which retains water molecules (meaning that the cation-exchange is incomplete), while the latter reflection, shifted to lower a Bragg angles compared to SME (7.30°), is associated with a layer repetition of 1.46 nm (d-free value of 0.51 nm) thus suggesting that the TF cation is

Table 1: Cation-exchange reaction conditions, and XRD results.

sample	cation exchange	XRD data			
	(% vs CEC)	2θ (°)	d spacing[b] (nm)	d-free[c] (nm)	L[d] (nm)
SME[e]		7.26/9.36	1.22/0.95		50/45
DHS[e]		9.40/9.20	0.94		
T5	5	5.88/7.1	1.51	0.55	10
T15	15	2.65/5.85[e]	3.3/1.51	2.34/0.55	13/30
T30	30	2.87/5.75/8.5[f]	3.15	2.18	13

[a]The XRD data for SME and DHS, reported in [9], are added to help the comparison with the TF-intercalated samples. Peaks other than those indicated observed in the patterns are possibly attributable to a mixed reflection of fluoromica [20].
[b]The basal spacing, $d(001)$, is determined by Bragg's equation $2d(hkl) \sin\theta = \lambda$.
[c]The lamellae clearance (d-free) is determined by subtracting the thickness of the SME layer (0.94 nm) from the basal spacing determined from the (001) diffraction peak.
[d]L is the crystallite size determined by using the package described in [21];
[e]Two spacings related to different arrangements are observed.
[f]Three orders of [00l] are detected.

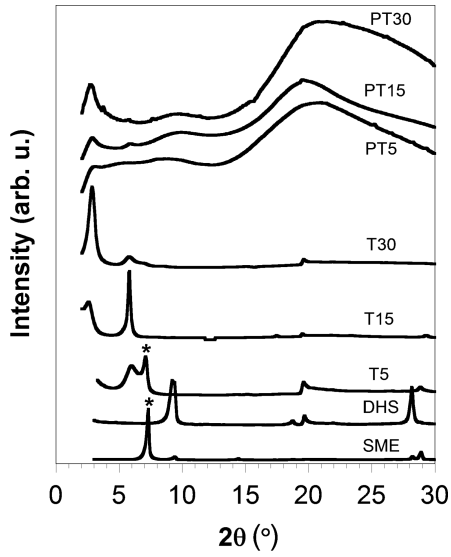

Figure 2: XRD spectra of SME, dehydrated SME (DHS), TF-intercalated hybrids (T5, T15, and T30), and the PS/TF–intercalated SME materials (PT5, PT15 and PT30).

intercalated in between the SME galleries. To propose a reasonable interlayer arrangement of TF molecules, the steric limitations between TF and the SME charged sites should be examined. Indeed, steric limitations are determined by the SME equivalent area for the charge deficit layer (A_e) and the minimum area demand (A_d) of intercalated molecules. In the case of sample T5, according to the XRD data (d-free = 0.51 nm), and TF size [22], a monolayer arrangement with the alkyl chains extending nearly parallel to the SME lamellae is in agreement with XRD data. In such a configuration the evaluated A_d value of the oligo(fluorene) can range from 0.4 to 0.5 nm^2 according to the available space to extend the lateral chains, which is smaller than the SME equivalent area for the charge deficit layer (assuming an average layer charge density of 0.77 nm^2 as reported by Choy et al. [23]).

When the TF loading is increased up to 15% and 30% CEC the XRD spectra change. T15 shows two uncorrelated peaks at 2.65 and 5.85°, indicating that different intercalating arrangements are obtained (in a forthcoming paper a detailed analysis will be reported). T30 exhibits a diffraction peak having a maximum at 2.9°, strongly shifted to lower angle with respect to the neat SME, which indicates a successful oligo(fluorene) intercalation. An approximate doubling of the interlayer height up to 3.1 nm was observed, and it can be explained if a tilted interlayer distribution of the TF cation is considered. Indeed, such an interlayer spacing (d-free = 2.14 nm) is attributable to the intercalation of TF molecules with a position far from flat inside the SME interlayers, and it becomes coherently positioned with second and third order appearance [d(002) = 5.7° 2θ, d(003) = 8.5° 2θ, see also Table 1]. This fact possibly suggests that a sequence of ordered TF molecules standing-up between layers is formed. For such an inclination, the evaluated A_d can exceed 1 nm^2 for each TF molecule; therefore, considering an average layer charge density of 0.77 nm^2, the area available of SME surface is oversaturated by the oligo(fluorene) cation with a loading of 30% CEC.

Synthesis and characterization of PS/TF-intercalated SME hybrids

Aiming to improve the processability of the TF-intercalated SME material in solution, we believed that an intriguing strategy would be to use a polymer as dispersing agent. Our previous results [8-10] caused us to regard the in situ polymerization as a potent tool to improve the intimate mixing between the polymer and the inorganic component. Thus, we synthesized the polymer directly by mixing the TF-intercalated SME hybrid with styrene monomer that polymerizes when the temperature is increased to about 120 °C.

The PS/TF-intercalated SME materials (hereafter named PT5, PT15, and PT30) were first characterized by XRD analysis. All the materials still show the presence of a diffraction peak in the low-angle region, clearly related to the precursor features. Similarly to what observed earlier, no XRD peaks of pristine crystalline SME were observed after the polymerization due to the distribution of intercalated SME tactoids within the continuous polymer phase [24,25]. As an example, the XRD pattern of the PT30 material, included in Figure 2, still reveals the presence of a peak in the low-angle region that corresponds to a layer periodicity of 3.14 nm. This peak is only marginally shifted to a lower diffraction angle than that of T30 (d_{001} = 3.10 nm), which is consistent with the partial intercalation of PS in between the enlarged SME layers.

Optical and morphological properties

The emission properties of the polymer hybrids were recorded in 220–230 nm thick spin-coated films. The fluorescence spectra of PT5, PT15, and PT30 films show maxima at 400 nm similar to neat TF, in turn unchanged compared to the terfluorene [26], with vibronic side bands typical of fluorene-based oligomers.

The PL intensity of PT15 film is higher than PT5 and PT30 likely due to the higher density of fluorescent intercalated tactoids. We recorded a PL quantum yield of 48% for PT15 (Figure 3).

Thicker films of PT5, PT15 and PT30 prepared by drop casting of toluene solutions, show a distribution of SME aggregates ranging from a few micrometers to a few tens of micrometers.

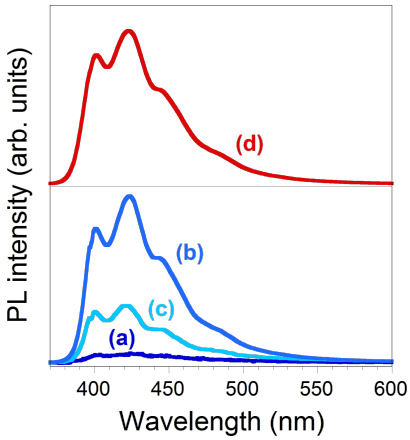

Figure 3: The fluorescence spectra of PT5 (a), PT15 (b), PT30 (c) and TF films (d).

As evidenced by the fluorescence microscope images in Figure 4, the blue emission comes solely from the silicates, while the polymer matrix is completely dark, which confirms that the whole amount of the emissive TF is confined in between the fluoromica layers. The AFM images reported as inset of Figure 4a–c confirm the large-scale morphology observed by fluorescence microscopy and reveal an organization and orientation of most of the silicates forming clusters (Figure 4d).

Self-assembly

We explored further possibilities of organization of these materials by drop casting dilute solutions in carbon disulfide under humid atmosphere. Under these conditions, the fast evaporation of the solvent and its consequent cooling trigger the condensation of micrometric water droplets on the polymer solution

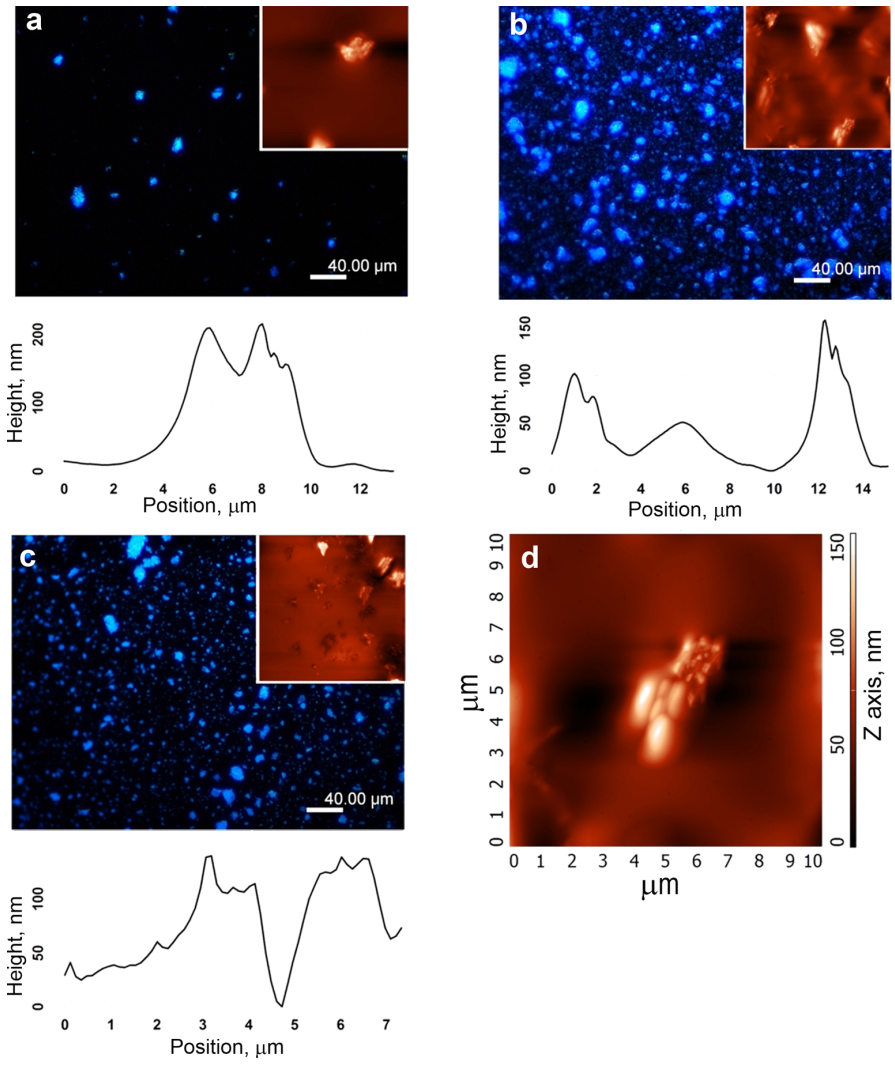

Figure 4: Fluorescence microscopy image, corresponding AFM magnification X,Y = 20 µm (inset) and cluster profile of PT5 (a) PT15 (b) and PT30 (c) films. d) AFM detail of a typical cluster.

surface, which leads to the spontaneous formation of breath figure (BF) patterns [27]. This self-assembly technique allows one to create patterned surfaces with highly regular geometry, in an custom-built microfabrication system. Such patterns hold great promise for several up-to-date applications, including nanostructures for optoelectronic devices [28-30], microfiltration membranes [31,32], and plasmonic sensors [33].

In a recently published study [11], we applied the BF pattering technique to a hybrid copolymer formed by a PS backbone and oligo(fluorene) branches, partially intercalated within the SME layers. The balanced combination of flexible coil, rigid rods, and silicates realized in that single material allowed us to prepare highly ordered BF patterns. By contrast, when we tried to organize PT5, PT15, and PT30 by using the same approach, we could not observe any ordered patterns. As shown in Figure 5a–c, all the films show unpacked and non-ordered cavities, with a wide diameter distribution, resembling what is normally obtained by casting linear PS without polar groups under the same conditions [34]. This is a clear indication that the polymer is not able to stabilize the water droplets forming at the solution/air interface, so that the microdroplets are free to float around and to coalesce in a disordered way. In order to increase the hydrophilicity of the system and hence the ability of the material to stabilize the water droplets, we added some free TF to the polymer solution.

As soon as a minimal amount of free TF is added to the system (0.02 mg·mL^{-1}, corresponding to 0.4% w/w with respect to the polymer hybrid), we could observe the formation of the densely packed cavities typical of BFs on the surface of the three films. The micrographs in Figure 5d–f show films of the three ma-

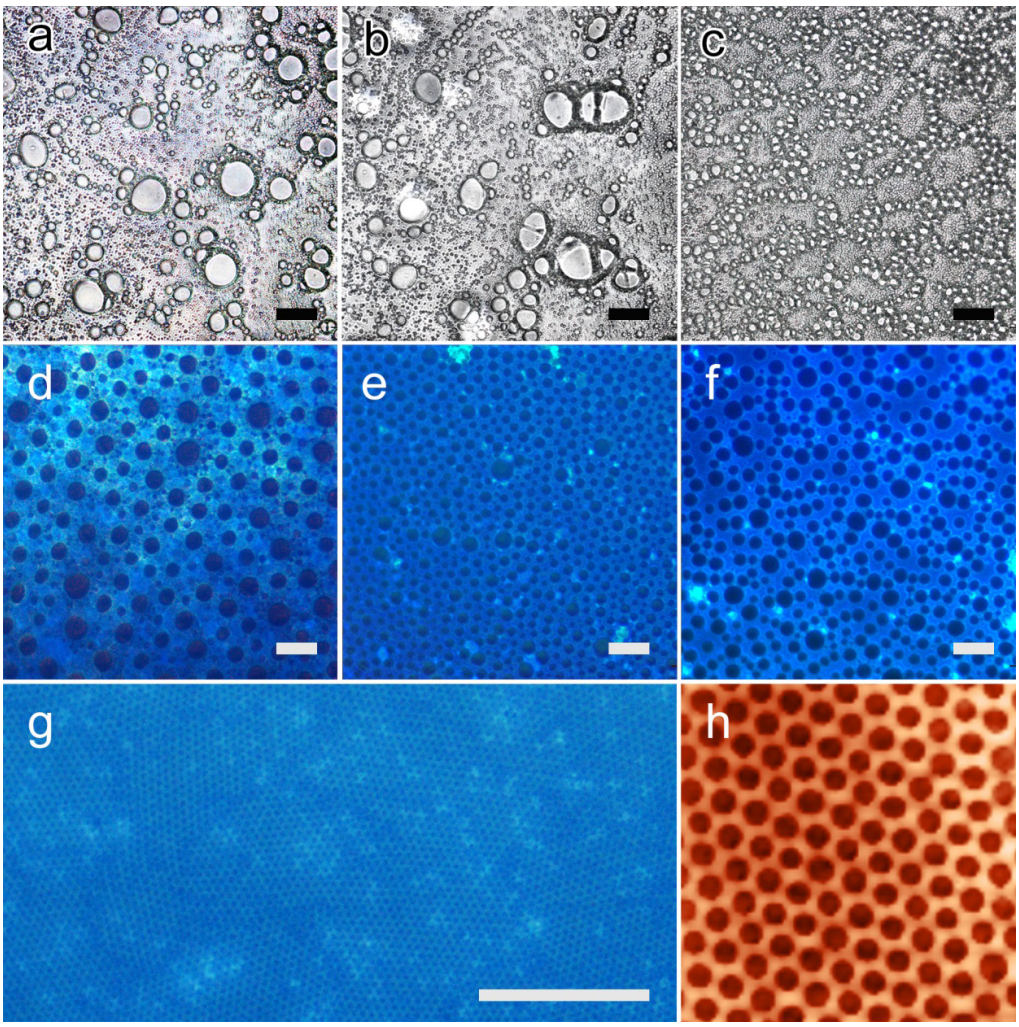

Figure 5: (a–c) Microscopy images of films of PT5, PT15 and PT30 cast under breath figure conditions. (d–f) Fluorescence microscopy images of PT5, PT15 and PT30 films prepared under the same conditions, after the addition of free TF (0.4% w/w). (g) Highly ordered microporous film of PT30 after optimization of parameters. (h) AFM view of a 10 × 10 μm^2 area of the same film. All scale bars are 20 μm long.

terials, which now emit blue light because of the presence of free TF blended with PS, homogeneously covered by cavities of 5–20 μm diameter. Even though the diameter distribution is not uniform in these films, the presence of free TF clearly aided the formation of BF. Underneath, the emitting SME clusters containing intercalated TF are still visible.

The process of BF formation is regulated by different parameters (polymer concentration, cast volume, solvent evaporation rate) that can be tuned to control both the degree of order in the arrangement of the micropores and their size [27]. Figure 5g shows a honeycomb film of PT30 prepared after the optimization of BF parameters; in particular, the concentration of TF blended with PT30 was raised up to 0.2 $mg \cdot mL^{-1}$, and the flow rate of humid nitrogen was set to 400 $L \cdot h^{-1}$. As evidenced by the AFM detail in Figure 5h, in this film cavities have an external diameter of 0.65 μm and a pitch of 1.0 μm and are arranged in a highly ordered hexagonal fashion, while bright SME aggregates are visible under the honeycomb structure, which indicates that a hierarchical organization of this material by the BF approach is feasible.

Photostability

The intercalation of the oligo(fluorene) molecules within the lamellae interlayers of the inorganic scaffold has dramatically improved their photophysical stability, a critical issue for fluorene-based materials [35]. PT15, selected as a representative sample, shows good chromatic stability when irradiated by a 100 mW/cm^2 UV lamp at 365 nm (Figure 6b), compared to the flat film of neat TF (Figure 6a). The photodegradation of fluorene-based compounds leads to a reduction of PL intensity together with the appearance of the keto-defects green emission band, peaked at around 530 nm, at the expense of the initial blue emission. In the flat PT15 film the contribution of keto-defects emission is almost suppressed and the decrease of PL intensity is slower (Figure 6c) with respect to neat TF film. In the nanoporous film (Figure 6d–f), the oxidation affects free TF oligomers dispersed in the polymer hybrid, while sharp blue emission from the intercalated TF is still observed, confirming the protecting role played by the silicate.

Conclusion

In summary, novel inorganic–organic hybrid composites have been prepared by intercalation of a cationic fluorescent oligo(fluorene) in between fluoromica-type silicate layers. The confined arrangement of the emitter is easily tuned by modulating the dye loading as demonstrated by XRD studies. Successively, the hybrids have been in situ dispersed in a PS matrix as a mean of making a composite that is processable from solution.

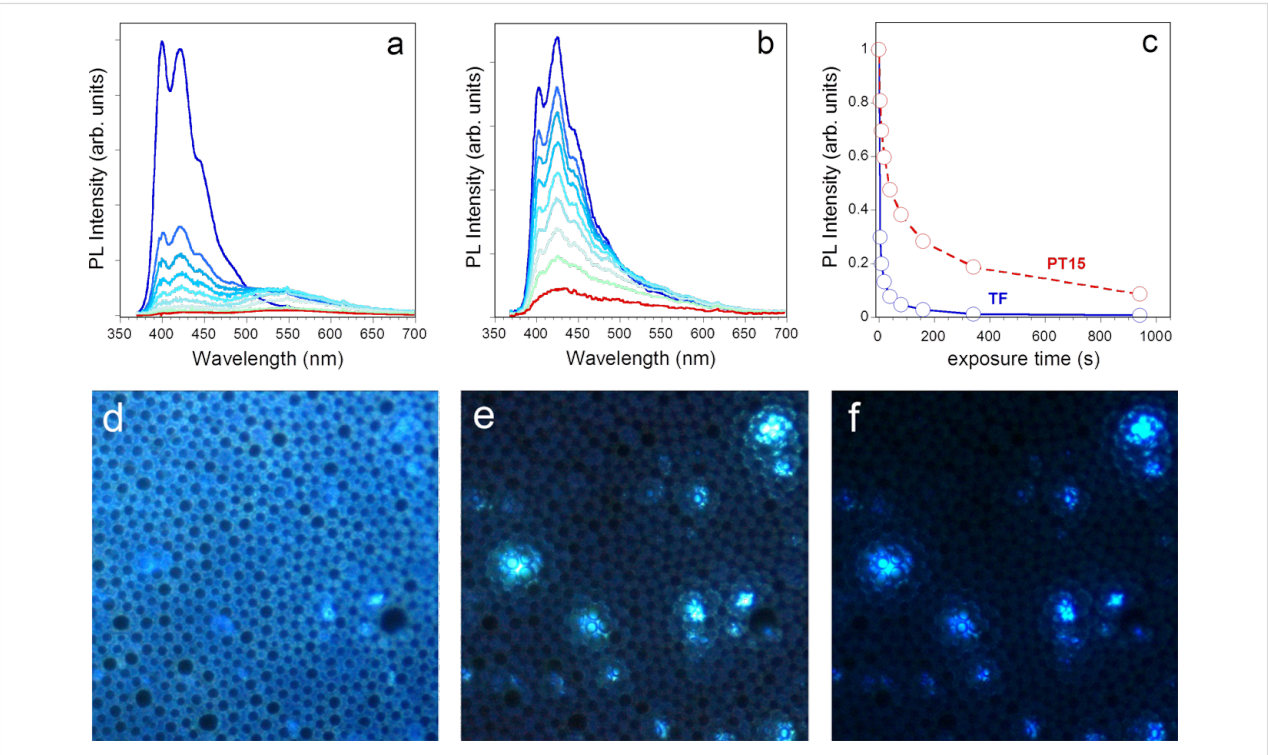

Figure 6: Chromatic stability of steady-state PL spectra upon UV exposure for 0 (dark blue line) to 20 min (red line) of neat flat TF film (a) and PT15 film (b). PL intensity of 400 nm peak of TF and PT15 film versus exposure time to UV light (c). PL images of the patterned PT15 film acquired during exposure to UV light are reported in (d–f).

The hybrid material films exhibit ultraviolet-blue photoluminescence with a significantly enhanced photostability with respect to the bare oligo(fluorene), thanks to the intercalation of the dye in between the inorganic layers which inhibits the photochemical oxidation by blocking the oxygen penetration.

The possibility to organize the polymer nanocomposite by BF technique opens to intriguing applications such as optoelectronic devices, microfiltration membranes, and plasmonic sensors.

Experimental

Reagents

Sodium-exchanged Somasif ME100 (SME, CO-OP Chemicals, CEC = 1.2 mmol·g^{-1}) was dried at 130 °C under reduced pressure (10^{-3} bar) for 2 weeks and then it was stored under nitrogen. Ethyl alcohol (Carlo Erba, 96% pure) was degassed under vacuum then by bubbling nitrogen, kept over molecular sieves and used without any further purification. Styrene (Aldrich, 99% pure) was refluxed for 4 h over CaH_2, then distilled trap-to-trap and stored under nitrogen. Distilled deionized water was used for all ion-exchange experiments. 2,7-dibromofluorene, 1,6-dibromohexane and trimethylamine were purchased from Sigma–Aldrich. 9,9-di-*n*-octylfluorene-2-boronic acid pinacol ester was purchased from Alfa Aesar. 2,7-dibromo-9,9-bis(6'-bromohexyl)fluorene was synthesized following the procedure reported elsewhere [36].

Materials preparation

Synthesis of 2,7-bis(9,9-dioctylfluorene-2-yl)-9,9-bis[6-(trimethylammonium)hexyl]fluorene dibromide (TF)

TF was synthesized by standard Suzuki coupling reaction of 2,7-dibromo-9,9-bis(6'-bromohexyl)fluorene and 9,9-di-*n*-octylfluorene-2-boronic acid pinacol ester and subsequent quaternization of the neutral precursor with trimethylamine, according to the following procedure. A mixture of 2,7-dibromo-9,9-bis(6'-bromohexyl)fluorene (173 mg, 0.266 mmol), 9,9-di-*n*-octylfluorene-2-boronic acid pinacol ester (302 mg, 0.585 mmol), $Pd(PPh_3)_4$ (6 mg, 0.005 mmol), aqueous potassium carbonate (2 M, 1.0 mL), and toluene (2.5 mL) was deoxygenated and then heated to 90 °C under nitrogen. The mixture was stirred for 48 h and then cooled to room temperature. The organic fraction was dried over Na_2SO_4 and purified by silica gel column chromatography, to afford 300 mg of product as pale powder (yield 87%). Condensed trimethylamine (2.5 mL) was added dropwise to a solution of the neutral precursor polymer (100 mg) in 7.5 mL of THF at −30 °C. The mixture was then allowed to warm up to room temperature for 30 min, and then cooled down again to −30 °C. More trimethylamine (5 mL) was added and the mixture was stirred at room temperature overnight. The obtained transparent gel was dried under a flux of N_2 to obtain TF as a white solid (93 mg; yield 96%).

1H NMR (600 MHz, CD_3OD) δ 7.85–7.69 (m, 14H, fluorene ring), 7.38–7.33 (m, 6H, fluorene ring), 3.14 (t, 4H, -CH_2N-), 2.98 (s, 18H,-NCH_3), 2.22–2.08 (m, 12H, C(CH_2-)$_2$), 1.55 (m, 4H, -CH_2-CH$_2$N-), 1.18–0.63 (m, 72H, -CH$_2$C$_7H_{15}$ and -CH$_2$C$_3H_6$C$_2$H$_4$N-); Anal. calcd for $C_{89}H_{130}Br_2N_2$: C, 77.02; H, 9.44; Br, 11.52; N, 2.02%; found: C, 77.95; H, 9.91; Br, 11.08; N, 1.93%.

Preparation of the intercalated SME hybrids

The synthesis of T30 is reported as standard procedure. To a 100 mL three-neck round bottom flask were added SME (50 mg) and H_2O (20 mL) and stirred for 5 days at room temperature. Meanwhile, an EtOH solution of TF (17 mg, 1.2×10^{-5} mol, 30% vs CEC) is prepared and then added to the SME suspension. The cation-exchange reaction proceeds for 3 h at 60 °C and then for additional 48 h at room temperature. The suspension was filtrated and washed with a H_2O/EtOH mixture (1:1) to collect the hybrid materials. Once the solvent was removed under reduced pressure, the product was extracted with EtOH by Soxhlet extraction for 8 h. The residual fraction was dried in vacuum and then ground in an agate mortar. T5 was prepared with the loading of 5% of CEC for TF (2.8 mg, 2.0×10^{-6} mol) and T15 was prepared with the loading of 15% of CEC for TF (8.1 mg, 5.9×10^{-6} mol) for 50 mg of SME.

The preparation of PT30 filled with T30 is reported as a standard procedure. The polymerization experiments were carried out in a 25 mL round-bottomed Schlenk flask, which had been dried on the high vacuum line by heating at 110 °C. The reactor was charged with T30 (10 mg) and styrene (2.20 mL, 1.98 g). The polymerization was carried out at 125 °C for 100 min. When the system was cooled to room temperature, polymerization was stopped by addition of methanol (20-fold excess). The precipitated polymer was collected by filtration, repeatedly washed with fresh MeOH and dried in vacuum to constant weight (yield = 0.615 g; styrene conversion = 31%; M_w = 30.3×10^4 g/mol; M_w/M_n = 2.0)

Preparation of films

Films for optical characterization were obtained by casting or spin-coating a 20 mg·mL^{-1} toluene solution of the compound on a glass substrate. Honeycomb structured films were obtained by following the procedure reported elsewhere [11], with few optimizations. In particular, to set the optimal conditions for BF formation, concentration of PT5, PT15 and PT30 was varied from 5 to 20 mg·mL^{-1}, while free TF was varied from 0.02 to 0.2 mg·mL^{-1}.

Characterization techniques

Size exclusion chromatography (SEC) measurements were carried out on a Waters SECV2000 system equipped with two PLGel Mixed C columns, a 2414 RI detector and a 490 UV diode-array detector. THF was used as solvent and poly(styrene) with molecular weights (M_w) ranging from 162 to 3.28 × 106 g·mol^{-1}, as standards. GIWAXS measurements were performed at the X-ray diffraction beamline 5.2 at the synchrotron radiation facility Elettra in Trieste (Italy). The X-ray beam emitted by the wiggler source on the Elettra 2 GeV electron storage ring was monochromatized by a Si(111) double crystal monochromator, focused on the sample and collimated by a double set of slits giving a spot size of 0.2 × 0.2 mm. Both spin-coated films (50–80 nm thick) and powders inserted into a sealed capillary were examined at 25 °C. The beam was monochromatized at energies of 8 keV for films or 10.33 keV for powders. The samples were oriented by means of a four-circle diffractometer with a motorized goniometric head. The X-ray beam direction was fixed, while the sample holder could be rotated about the different diffractometer axes, in order to reach the sample surface alignment in the horizontal plane containing the X-ray beam by means of laser light reflection. Subsequently it was possible to rotate it around an axis perpendicular to this plane or, alternatively, to vary the angle between beam and surface (angle of incidence). Bidimensional diffraction patterns were recorded with a 2M Pilatus silicon pixel X-ray detector (DECTRIS Ltd., Baden, Switzerland) positioned perpendicular to the incident beam, at 200 mm distance from the sample, to record the diffraction patterns in reflection mode. Sample and detector were kept fixed during the measurements. The sample inclination to the beam was changed from ω = −0.05° to ω = 0.25°, in steps of 0.05° yielding seven diffraction images. The q-resolution of the 2D images collected was estimated by means of lanthanum hexaboride powder (standard reference material 660a of NIST) and it has been evaluated ranging from 0.2 to 0.3 nm^{-1} both for q_z and q_{xy}, in agreement with other synchrotron measurements [37-39]. The same calibration standard allowed for the integration of 2D patterns by using the software Fit2D [40] yielding several series of powder-like patterns, corrected for geometry, Lorentz, and beam polarization effects. Peaks positions were extracted by means of the program Winplotr [41]. When sufficient amounts were available, the powders were examined by using an Anton Parr camera under nitrogen flux and a Siemens D-500 diffractometer (Cu Kα radiation, λ = 0.154 nm). The operating voltage and current were 40 kV and 40 mA, respectively. Data were collected from 3 to 33° at 0.05° intervals. PL spectra were recorded by using a Spex 270M monochromator combined with a CCD. UV irradiation of the film was performed by Hamamatsu Lightningcure^{TM} LC8. Atomic force microscopy investigations were performed by using a NT-MDT NTEGRA instrument in semicontact mode in ambient conditions.

Acknowledgements

This work was carried out with the financial support of Fondazione Cariplo project “EDONHIST” (ref. 2012-0844) and Regione Lombardia through Project “Tecnologie e materiali per l’utilizzo efficiente dell’energia solare” (decreto 3667/2013). Authors wish to thank Daniele Piovani for SEC analysis.

References

1. Ma, W.; Yah, W. O.; Otsuka, H.; Takahara, A. *Beilstein J. Nanotechnol.* **2012,** *3,* 82–100. doi:10.3762/bjnano.3.10
2. Sanchez, C.; Arribart, H.; Giraud-Guille, M. M. *Nat. Mater.* **2005,** *4,* 277–288. doi:10.1038/nmat1339
3. Descalzo, B.; Martínez-Máñez, R.; Sancenón, F.; Hoffmann, K.; Rurack, K. *Angew. Chem., Int. Ed.* **2006,** *45,* 5924–5948. doi:10.1002/anie.200600734
4. Yan, D.; Lu, J.; Mei, W.; Evans, D. G.; Duan, X. *J. Mater. Chem.* **2011,** *21,* 13128–13139. doi:10.1039/c1jm11594d
5. Sanchez, C.; Lebeau, B.; Chaput, F.; Boilot, J.-P. *Adv. Mater.* **2003,** *15,* 1969–1994. doi:10.1002/adma.200300389
6. Sanchez, C.; Julián, B.; Belleville, P.; Popall, M. *J. Mater. Chem.* **2005,** *15,* 3559–3592. doi:10.1039/b509097k
7. Fernandes, F. M.; Baradari, H.; Sanchez, C. *Appl. Clay Sci.* **2014,** *100,* 2–21. doi:10.1016/j.clay.2014.05.013
8. Leone, G.; Giovanella, U.; Bertini, F.; Porzio, W.; Meinardi, F.; Botta, C.; Ricci, G. *J. Mater. Chem. C* **2013,** *1,* 1450–1460. doi:10.1039/c2tc00533f
9. Leone, G.; Giovanella, U.; Porzio, W.; Botta, C.; Ricci, G. *J. Mater. Chem.* **2011,** *21,* 12901–12909. doi:10.1039/c1jm11281c
10. Giovanella, U.; Leone, G.; Ricci, G.; Virgili, T.; Suarez Lopez, I.; Rajendran, S. K.; Botta, C. *Phys. Chem. Chem. Phys.* **2012,** *14,* 13646–13650. doi:10.1039/c2cp42361h
11. Leone, G.; Giovanella, U.; Bertini, F.; Hoseinkhani, S.; Porzio, W.; Ricci, G.; Botta, C.; Galeotti, F. *J. Mater. Chem. C* **2013,** *1,* 6585–6593. doi:10.1039/c3tc31122h
12. Lee, T.-W.; Park, O. O.; Yoon, J.; Kim, J.-J. *Adv. Mater.* **2001,** *13,* 211–213. doi:10.1002/1521-4095(200102)13:3<211::AID-ADMA211>3.0.CO;2-H
13. Park, J. H.; Lim, Y. T.; Park, O. O.; Kim, J. K.; Yu, J.-W.; Kim, Y. C. *Adv. Funct. Mater.* **2004,** *14,* 377–382. doi:10.1002/adfm.200305045
14. Chakraborty, C.; Dana, K.; Malik, S. *J. Colloid Interface Sci.* **2012,** *368,* 172–180. doi:10.1016/j.jcis.2011.10.037
15. Chakraborty, C.; Sukul, P. K.; Dana, K.; Malik, S. *Ind. Eng. Chem. Res.* **2013,** *52,* 6722–6730. doi:10.1021/ie4000213
16. Ogawa, M.; Kuroda, K. *Chem. Rev.* **1995,** *95,* 399–438. doi:10.1021/cr00034a005
17. López Arbeloa, F.; Martínez Martínez, V.; Arbeloa, T.; López Arbeloa, I. *J. Photochem. Photobiol., C* **2007,** *8,* 85–108. doi:10.1016/j.jphotochemrev.2007.03.003
18. Auerbach, S. M.; Carrado, K. A.; Dutta, S. M. *Handbook of Layered Materials;* Marcel Dekker Inc.: New York, NY, U.S.A., 2004.
19. Utracki, L. A.; Broughton, B.; González-Rojano, N.; Hecker de Carvalho, L.; Achete, C. A. *Polym. Eng. Sci.* **2011,** *51,* 559–572. doi:10.1002/pen.21807

20. Cattaneo, A. S.; Bracco, S.; Comotti, A.; Galimberti, M.; Sozzani, P.; Eckert, H. *J. Phys. Chem. C* **2011,** *115,* 12517–12529. doi:10.1021/jp2020676
21. Enzo, S.; Fagherazzi, G.; Benedetti, A.; Polizzi, S. *J. Appl. Crystallogr.* **1988,** *21,* 536–542. doi:10.1107/S0021889888006612
22. Indeed the number of different conformations attainable by the alkyl chains of TF molecule provokes a large variability of values from the minimum A_d calculation.
23. Yang, J.-H.; Han, Y.-S.; Choy, J.-H.; Tateyama, H. *J. Mater. Chem.* **2001,** *11,* 1305–1312. doi:10.1039/b006059n
24. Leone, G.; Boglia, A.; Bertini, F.; Canetti, M.; Ricci, G. *J. Polym. Sci., Part A: Polym. Chem.* **2010,** *48,* 4473–4483. doi:10.1002/pola.24238
25. Alexandre, M.; Dubois, P. *Mater. Sci. Eng., R* **2000,** *28,* 1–63. doi:10.1016/S0927-796X(00)00012-7
26. Jaramillo-Isazaab, F.; Turner, M. L. *J. Mater. Chem.* **2006,** *16,* 83–89. doi:10.1039/b511349k
27. Wan, L.-S.; Zhu, L.-W.; Ou, Y.; Xu, Z.-K. *Chem. Commun.* **2014,** *50,* 4024–4039. doi:10.1039/c3cc49826c
28. Galeotti, F.; Mróz, W.; Scavia, G.; Botta, C. *Org. Electron.* **2013,** *14,* 212–218. doi:10.1016/j.orgel.2012.10.034
29. Galeotti, F.; Trespidi, F.; Timò, G.; Pasini, M. *ACS Appl. Mater. Interfaces* **2014,** *6,* 5827–5834. doi:10.1021/am500687f
30. Galeotti, F.; Mróz, W.; Bolognesi, A. *Soft Matter* **2011,** *7,* 3832–3836. doi:10.1039/c1sm05148b
31. Ma, H.; Gao, P.; Zhang, Y.; Fan, D.; Li, G.; Du, B.; Wei, Q. *RSC Adv.* **2013,** *3,* 25291–25295. doi:10.1039/c3ra44812f
32. Wan, L.-S.; Li, J.-W.; Ke, B.-B.; Xu, Z.-K. *J. Am. Chem. Soc.* **2011,** *134,* 95–98. doi:10.1021/ja2092745
33. Pisco, M.; Quero, G.; Iadicicco, A.; Giordano, M.; Galeotti, F.; Cusano, A. *Proc. SPIE* **2013,** *8774,* 87740R. doi:10.1117/12.2017538
34. Galeotti, F.; Calabrese, V.; Cavazzini, M.; Quici, S.; Poleunis, C.; Yunus, S.; Bolognesi, A. *Chem. Mater.* **2010,** *22,* 2764–2769. doi:10.1021/cm903652x
35. Polyfluorenes. Scherf, U.; Neher, D., Eds.; Advances in Polymer Science, Vol. 212; Springer: Berlin Heidelberg, Germany, 2008. doi:10.1007/978-3-540-68734-4
36. Liu, B.; Gaylord, B. S.; Wang, S.; Bazan, G. C. *J. Am. Chem. Soc.* **2003,** *125,* 6705–6714. doi:10.1021/ja028961w
37. Rivnay, J.; Noriega, R.; Northrup, J. E.; Kline, R. J.; Toney, M. F.; Salleo, A. *Phys. Rev. B* **2011,** *83,* 121306. doi:10.1103/PhysRevB.83.121306
38. Rivnay, J.; Noriega, R.; Kline, R. J.; Salleo, A.; Toney, M. F. *Phys. Rev. B* **2011,** *84,* 045203. doi:10.1103/PhysRevB.84.045203
39. Gozzo, F.; De Caro, L.; Giannini, C.; Guagliardi, A.; Schmitt, B.; Prodi, A. *J. Appl. Crystallogr.* **2006,** *39,* 347–357. doi:10.1107/S0021889806009319
40. Hammersley, A. P.; Svensson, S. O.; Hanfland, M.; Fitch, A. N.; Hausermannm, D. *High Pressure Res.* **1996,** *14,* 235–248. doi:10.1080/08957959608201408
41. Roisnel, T.; Rodriguez-Carvajal, J. *Mater. Sci. Forum* **2001,** *378–381,* 118–123. doi:10.4028/www.scientific.net/MSF.378-381.118

License and Terms

BEILSTEIN JOURNAL OF NANOTECHNOLOGY

Synthesis, characterization, monolayer assembly and 2D lanthanide coordination of a linear terphenyl-di(propiolonitrile) linker on Ag(111)

Zhi Chen[1], Svetlana Klyatskaya[*1], José I. Urgel[2], David Écija[2,3], Olaf Fuhr[1,4], Willi Auwärter[2], Johannes V. Barth[*2] and Mario Ruben[*1,5]

Full Research Paper

Open Access

Address:
[1]Institute of Nanotechnology (INT), Karlsruhe Institute of Technology (KIT), 76344 Eggenstein-Leopoldshafen, Germany, [2]Physik Department E20, Technische Universität München, 85748 Garching, Germany, [3]IMDEA Nanoscience, 28049, Madrid, Spain, [4]Karlsruhe Nano Micro Facility (KNMF), Karlsruhe Institute of Technology (KIT), 76344 Eggenstein-Leopoldshafen, Germany and [5]Universite de Strasbourg, Institut de Physique et de Chimie des Materiaux de Strasbourg, CNRS UMP 7504, 23 Rue du Loess, 67034 Strasbourg Cedex 2, France

Email:
Svetlana Klyatskaya[*] - svetlana.klyatskaya@kit.edu; Johannes V. Barth[*] - jvb@tum.de; Mario Ruben[*] - mario.ruben@kit.edu

* Corresponding author

Keywords:
di(propiolonitrile) linker; lanthanides; metal–organic networks; molecular self-assembly; organic monolayers; single crystal X-ray diffraction analysis; UHV-STM

Beilstein J. Nanotechnol. **2015,** *6,* 327–335.
doi:10.3762/bjnano.6.31

Received: 18 July 2014
Accepted: 19 December 2014
Published: 29 January 2015

This article is part of the Thematic Series "Molecular materials – towards quantum properties".

Associate Editor: S. R. Cohen

Abstract

As a continuation of our work employing polyphenylene-dicarbonitrile molecules and in particular the terphenyl derivative **1** (TDCN), we have synthesized a novel ditopic terphenyl-4,4"-di(propiolonitrile) (**2**) linker for the self-assembly of organic monolayers and metal coordination at interfaces. The structure of the organic linker **2** was confirmed by single crystal X-ray diffraction analysis (XRD). On the densely packed Ag(111) surface, the terphenyl-4,4"-di(propiolonitrile) linkers self-assemble in a regular, molecular chevron arrangement exhibiting a Moiré pattern. After the exposure of the molecular monolayer to a beam of Gd atoms, the propiolonitrile groups get readily involved in metal–ligand coordination interactions. Distinct coordination motifs evolve with coordination numbers varying between three and six for the laterally-bound Gd centers. The linker molecules retain an overall flat adsorption geometry. However, only networks with restricted local order were obtained, in marked contrast to previously employed, simpler polyphenylene-dicarbonitrile **1** linkers.

Introduction

The drive towards miniaturization of modern electronics has led to a growing interest in the development of memory units that can satisfy the ever-growing demand for information storage. In this context, rare-earth elements have been employed for the design of materials with extraordinary magnetic properties [1,2], including single molecular magnets (SMMs) [2,3], which serve as pivotal subunits for modern developments in spintronic devices [4-12].

Moreover, in recent years, significant strides have been made in the understanding and the application of nanofabrication from the "bottom-up" perspective [13-17]. The tailored design, controlled formation, and in-depth characterization of self-assembled, molecular and periodic heterostructures (ranging over several length scales on atomically well-defined surfaces under ultrahigh vacuum (UHV) conditions) have been achieved [13-15,18,19]. More recently, our groups have successfully extended this approach toward the on-surface coordination of f-block organic networks exhibiting five-vertex, Archimedean surface tessellation [20,21]. However, at least for the class of simple polyphenylene dicarbonitrile linkers, NC–Ph_n–CN (n = 3, **1**), the nature of the underlying mononuclear five-fold coordination motif is still unclear. It is notably an open question whether the nature of the surface interaction or the steric hindrances of the surface-confined groups are crucial factors favouring the expression of certain coordination motifs.

In this context, the nature of the organic linker molecule seems to play a crucial role in the tuning of the on-surface 2D self-assembly, by means of the intermolecular and substrate-mediated interactions [22-24]. A particular case is represented by molecules that show highly reactive functional units, such as terminal carbon–carbon triple bonds (–C≡CH) [25-32]. Notably, when working on a planar Ag(111) substrate, in addition to the reported butadiyne bridge formation via a homocoupling reaction, a clear tendency toward branching-side reactions involving three and four reacting monomers and leading to markedly reduced chemoselectivity is observed [25-28]. Interestingly, on a Au(111) substrate, the cyclotrimerisation of arylalkynes becomes the dominant reaction pathway with high selectivity [33]. The alkynyl activation leading to C–C coupling has been ascribed to the emergence of a double σ-bridge-bounded acetylene [25,26], or alternatively to the formation of an intermediary π-substrate complex [27,28,34].

The results presented herein focus on the design, synthesis, characterization and 2D Ag(111)-mediated self-assembly of a novel terphenyl-4,4"-di(propiolonitrile) (**2**) linker exhibiting a NC–C≡C–Ph_3–C≡C–CN structure. Based on previous work in our group employing dicarbonitriles, as well as diacetylenes, the linker **2** carries both a –C≡C– acetylene group and a terminal carbonitrile group (–C≡N). In bulk chemistry, this combination usually yields so-called propiolonitriles as versatile building blocks for highly functionalized derivatives [35-41]. The structure of the organic linker **2** was confirmed by single crystal X-ray diffraction analysis (XRD) along with other standard techniques (Supporting Information File 1).

The results of the surface-confined, molecular self-assembly and the lanthanide coordination reaction were analysed by using low-temperature scanning tunnelling microscopy (STM). The STM investigation of the self-assembly of the organic linker **2** on a Ag(111) surface revealed a densely packed, chevron monolayer exhibiting a Moiré pattern. In contrast, lanthanide coordination of the same ligand **2** with Gd atoms resulted in metal–organic networks with only local order. These latter results differ strongly from previous reports on 2D surface coordination of the related ligand terphenyl-4,4"-dicarbonitrile (**1**) linker by cerium or gadolinium atoms [20,21,42]. This indicates that the preference for the formation of extended metal–organic networks is not primarily a consequence of the geometrical footprint of the endgroups at the surface, but rather a generic property of carbonitrile–Ln coordination.

Results and Discussion

Synthesis

This work compares the 2D self-assembly and the coordination behaviour of two related ligand systems, namely the terphenyl-4,4"-dicarbonitrile (**1**) and the terphenyl-4,4"-di(propiolonitrile) (**2**) linker, whereby the latter has been synthesized and characterized herein (Figure 1). A class of terphenyl-4,4"-dicarbonitrile derivatives, NC–Ph_3–CN, was intensively studied as a linker in molecular and metal coordination assemblies under 2D

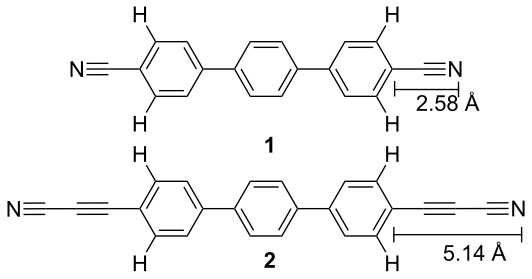

Figure 1: Representation of the structure of the molecular linkers: terphenyl-4,4"-dicarbonitrile (**1**) [24,43], terphenyl-4,4"-di(propiolonitrile) (**2**) showing the increased distance of the coordinating carbonitrile N-donor atom from the sterically hindering α-C–H group at the phenyl ring.

confinement [20,22,24,43]. With the goal to achieve increased coordination numbers (7–12) (typically for f-block elements in bulk chemistry [18,20,44]), the linker **2** was designed to reduce the steric repulsion induced by the α-C–H bonds at the terminal phenyl rings and the coordinating donor N-atom of the carbonitrile group. By incorporating the propiolonitrile groups into the terphenyl backbone of NC–C≡C–Ph_3–C≡C–CN (**2**), the distance between the coordination-active N-atom of the –C≡N group and the adjacent phenyl ring bearing the α-C–H group is consequently increased from 2.58 Å to 5.14 Å. (Figure 1).

During the synthesis, the diiodoterphenyl **4** was subjected to a cross-coupling reaction with propargyl alcohol in the presence of catalytic amounts of Pd(II) salts, leading to the formation of the intermediary compound **5**. This compound was subsequently reacted by a tandem manganese dioxide-mediated alcohol oxidation with in situ trapping of the resulting aldehydes with ammonia giving the final product **2** with a overall yield of 18% [45] (Scheme 1).

Additionally, a small amount of a byproduct, identified as terphenyl-4-propiolonitrile (**3**) (Ph_3–C≡C–C≡N), was separated and revealed to be a thus-far unreported decarboxylation reaction of the propiolonitrile group. The nature of this compound was confirmed by a blind synthesis starting from 4-bromoterphenyl (**6**) following a multistep protocol (Supporting Information File 1, Scheme S1). The nature of both compounds, the di- (**2**) and the mono-substituted linker (**3**), was substantiated by single crystal X-ray structure analysis at 180 K. Compound **2** crystallizes in a monoclinic system with space group $P2_1/n$, while **3** crystallizes in the triclinic system with space group P-1. The anisotropic displacement ellipsoids and atom labelling (ORTEP plots) of compounds **2** and **3** are shown in Figure 2a and Supporting Information File 1, Figure S2, respectively. Selected bond lengths of these molecules are listed in Supporting Information File 1, Tables S1–4.

The visualization of molecule **2** highlights a conformation, in which the central phenyl ring is rotated out of the plane of the two peripheral ones by a dihedral angle of 31.56(5)° (Figure 2b). In comparison, the mono-substituted compound **3** exhibits twist angles of 33° and 10° between phenyl rings A/B and B/C, respectively (Supporting Information File 1, Figure S3). In both cases the molecules arrange within the crystal in layers (Figure 2c and Supporting Information File 1, Figure S3) in an antiparallel organisation of the end standing CN groups by dipole–dipole interactions.

Formation of the self-assembled monolayer of **2** on Ag(111)

In recent years, systematic studies of the self-assembly behavior of the series of polyphenylene-dicarbonitrile linkers (NC–Ph_n–CN, n = 3–6) on the Ag(111) surfaces have been reported demonstrating the controlled formation of highly-ordered monolayers [43,46]. The structural diversity of the formed molecular monolayers was illustrated by (i) a strict dependence on the length of linker molecules resulting in either densely packed chevron patterns (n = 3), open rhombic networks (n = 4) or complex Kagomé lattices (n = 5, 6); (ii) changing the stereochemical position of the coordinating –CN groups leading to higher order complexities with partially systemic behavior [47-51].

The new linker **2** (NC–C≡C–Ph_3–C≡C–CN) was deposited by organic molecular beam epitaxy onto an atomically clean and flat Ag(111) surface kept at 300 K. After the deposition, the samples were cooled down to about 6 K for imaging. Similar to earlier studies on the terphenyl-dicarbonitrile analog **1** [43], the individual molecules of NC–C≡C–Ph_3–C≡C–CN (**2**) were clearly resolved as rod-like protrusions showing a chevron arrangement but now exhibiting an additional Moiré pattern (Figure 3). The latter results from the superposition of the monolayer and substrate symmetries, rotated by an angle

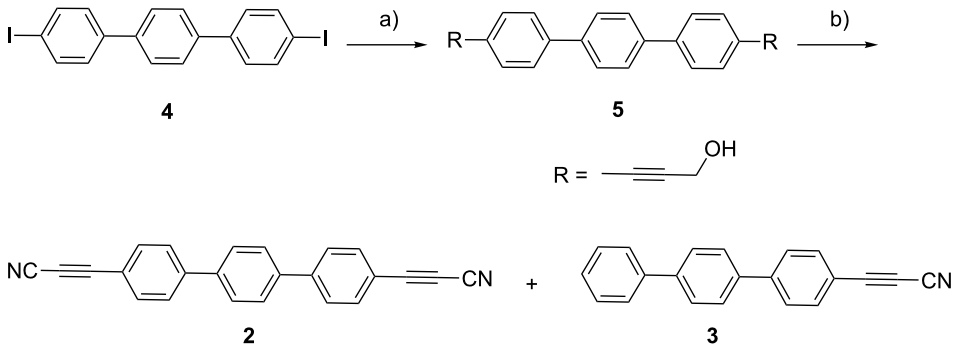

Scheme 1: Synthesis of the terphenyl-4,4"-di(propiolonitrile) linker (**2**). Reagents and conditions: a) propargyl alcohol, $Pd(PPh_3)_2Cl_2$/CuI, pyrrolidine/THF, 60 °C; b) NH_3–IPA, $MgSO_4$, MnO_2, THF, rt [45].

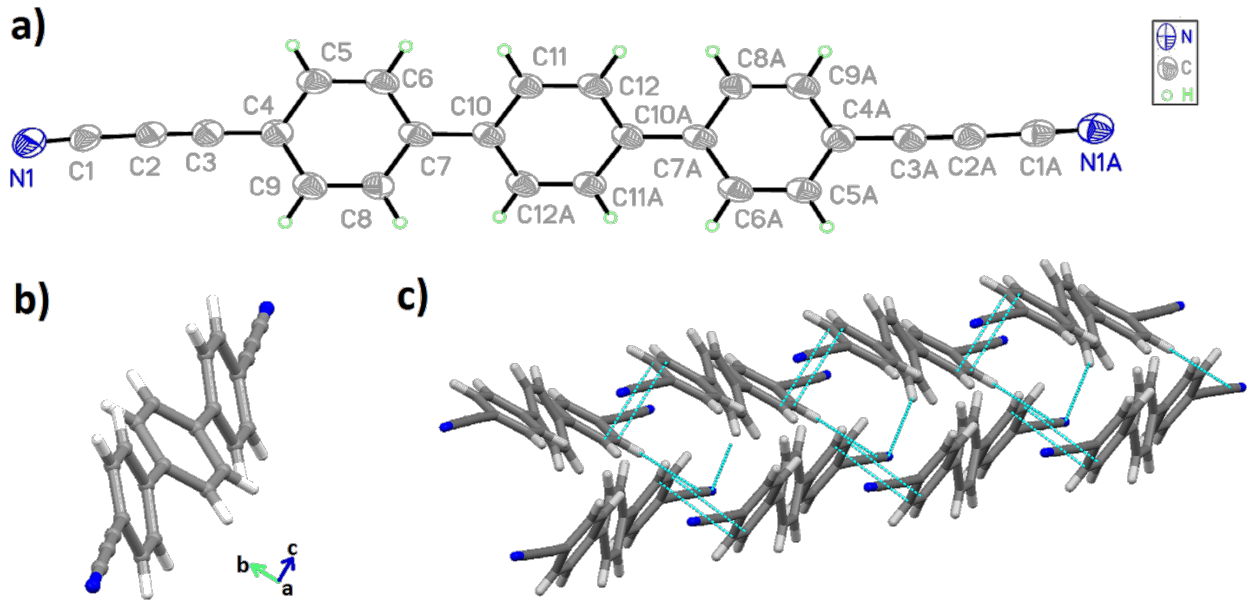

Figure 2: ORTEP plot of compound **2**. Ellipsoids were drawn at a 30% level of probability for all non-hydrogen atoms, indicating the numbering scheme (a); 3D visualization of the molecular conformation (view along direction *a*) (b); and the packing viewed along the *b** axis demonstrating the parallel layers arrangement (c).

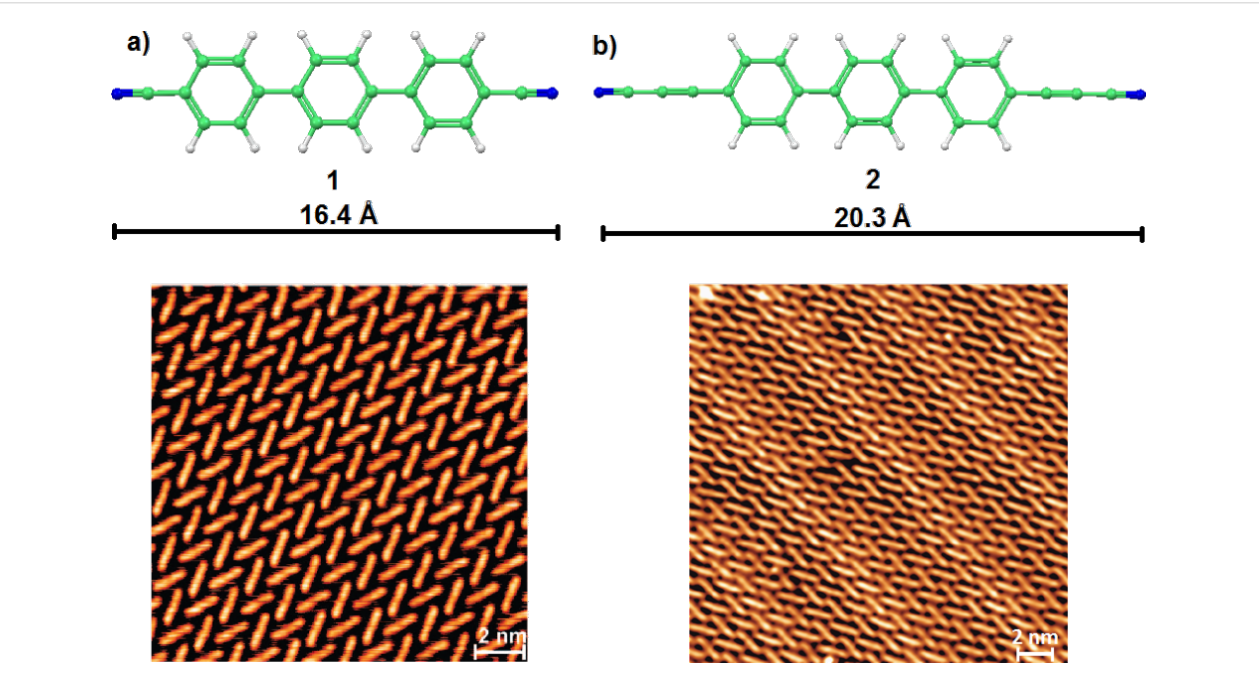

Figure 3: Comparison of the molecular self-assembled monolayers of **1** and **2** on a Ag(111) surface. a) Densely packed chevron layer formed by NC–Ph_3–CN (**1**), adapted from [43]; b) Densely packed chevron layer formed by the NC–C≡C–Ph_3–C≡C–CN (**2**) species (data measured at 6 K; image size: 239 × 239 $Å^2$; scanning parameters: V_{bias} = 0.3 V, I = 0.05 nA).

showing the very subtle balance between molecule–substrate and molecule–molecule interactions. Occasionally, deviations from molecular linearity as an S-shape of certain protrusions could be identified. Similar to the earlier observations for dicarbonitrile oligophenyls [43,46,52], this contrast can be ascribed to the rotation of the aromatic rings alternatively lifting the left and the right side of a phenyl rings up from the underlying substrate.

It was found that the chevron pattern assembled from **2** is similar to that earlier reported for NC–Ph_n–CN linkers (whereby n = 3, **1**) [43], where only two orientations of the molecules with the respect to the substrate within a given domain are present.

The high-resolution STM topograph depicted in Figure 4a clearly indicates that the monolayer pattern is determined by non-covalent interactions between adjacent linkers, in particular electrostatic interactions [43,47,53]. The packing is stabilized by the attractive interaction between the propilonitrile end groups, as proton acceptors, and H atoms of the phenylene rings. This reveals related ordering principles on the terminal alkynes, which is interpreted in terms of a proton acceptor–ring interaction [53].

Figure 4b represents the model based on the averaged bonding distances and angles between adjacent molecules gained from the STM data. The derived organic network model expresses a six-fold symmetry related to the substrate atomic arrangement. Based on the topography and assuming the same size of the molecules as in the gas phase, we obtained an average length of about 0.26 ± 04 nm for the phenylene–N distance, which is slightly shorter than in the earlier reported network of molecule **1** (0.33 ± 03 nm) [43].

Lanthanide-directed coordination of **2** on Ag(111)

In previous work, regular metallo–supramolecular nanomeshes were obtained on flat Ag(111) surfaces from the exposure of **1**-type NC–Ph_n–CN (n = 3, 4, 5, 6) linkers to cobalt atoms [22,23,48], while the use of lanthanide atoms (Ce, Gd) yielded an Archimedean snub square tiling [20,21]. The underlying driving force for the diversity in results is associated with the remarkable coordination reactivity of carbonitrile groups, which are very well known in bulk coordination chemistry.

The linker **2** was deposited by organic molecular beam epitaxy onto an atomically clean and flat Ag(111) surface kept at 300 K, followed by the controlled co-deposition of Gd atoms provided from an electron beam source. The samples were subsequently cooled down to $T \approx 6$ K for imaging.

In contrast to previous reports on NC–Ph_3–CN (**1**) (Figure 5a) [20,21], the co-evaporation of Gd atoms with linker **2** resulted in an irregular metal–organic pattern without expression of a translational spatial symmetry. Thus, nodes with variable coordination motifs, including clustering, can be found in the STM topographs (Figure 5b). Consequently, no clear preference of one coordination motif with higher coordination number was encountered, even in the presence of excess Gd (associated with cluster formation as shown by the emergence of white protrusions in Figure 5b). This provides an unintended route towards 2D, randomly reticulated coordination networks, which is in line with the usage of linear and nonlinear dicarbonitrile linkers as recently reported [48,50].

A model for a five-fold coordination vertex and detailed views of the respective STM data are reproduced in Figure 5b. Despite serious efforts, only surface-confined networks with limited length scales could be obtained. Obviously, the expression of regular metallo–supramolecular nanostructures or layers

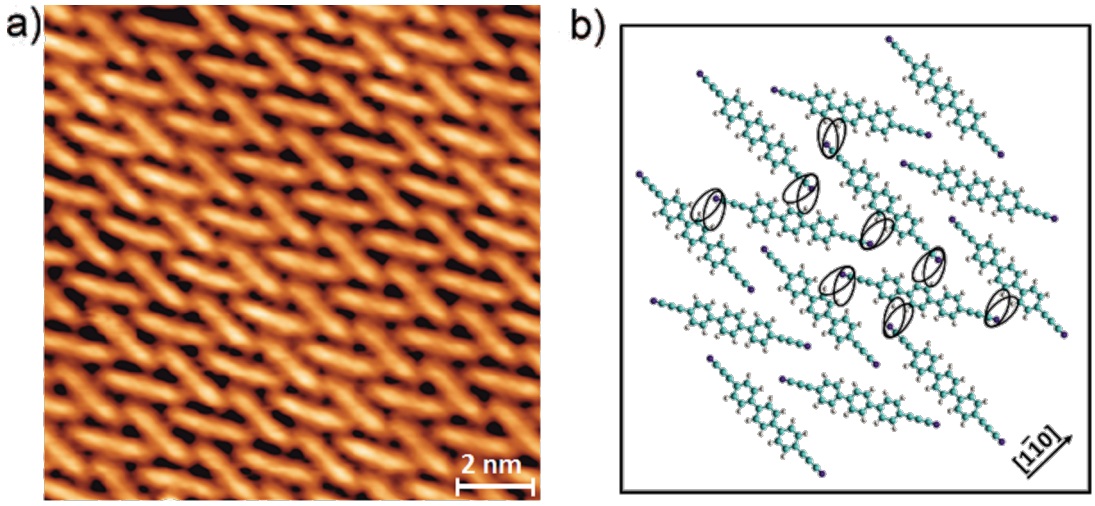

Figure 4: High-resolution STM image showing a) the molecular packing in chevron layers mediated by the propilonitrile end groups of the NC–C≡C–Ph_3–C≡C–CN (**2**) linker (data measured at 6 K; image size: 119 × 119 Å^2; scanning parameters: V_{bias} = 0.3 V, I = 0.05 nA); b) Corresponding model showing the interaction of adjacent propionitrile groups.

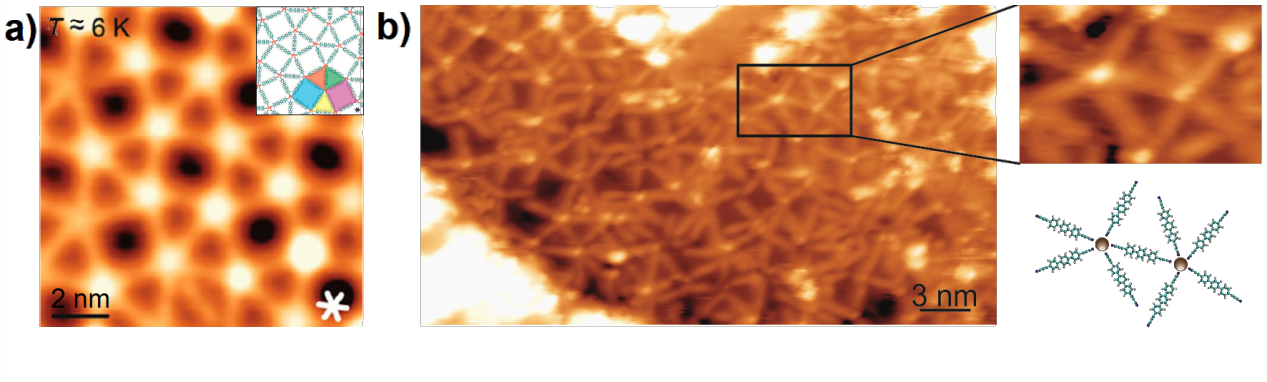

Figure 5: STM image of the lanthanide-directed assembly on Ag(111) for appreciable surface concentration (linker: Ln = 5:2). a) Snub square tiling motif comprised of NC–Ph_3–CN (**1**) linkers and Gd centers (atomistic model of the snub square Archimedean tessellation of the surface in insert), reprinted with permission from [21], copyright 2014 American Chemical Society; b) irregular metal–organic network comprised of NC–C≡C–Ph_3–C≡C–CN (**2**) molecules and Gd centers. In inset: model of one of the coordination units presented (the 5-fold linker Gd nonameric unit. Data was obtained at 6 K. Image size: 352 × 195 $Å^2$. Scanning parameters: V_{bias} = 0.7 V, I = 0.1 nA).

requires a careful balance of surface bonding, mobility and lateral interactions between metal centers and linkers [54]. We attribute the observed, reduced order to the high reactivity of the –C≡C– bonds in propiolonitrile groups. From bulk chemistry, it is well known that the activation of the acetylene group by noble metal substrates can occur [35-41]. This was demonstrated by on-surface homo-coupling of alkynes on planar surfaces with a clear tendency towards branching side reactions [25-28,34]. Although in the presented work we could not deduce any changes of the –C≡C– bonds from the STM investigations, we attribute the hampering of the expression of a regular network to the presence of active –C≡C– bonds close to the coordinating CN units.

Conclusion

The self-assembly of the new terphenyl-4,4”-di(propiolonitrile) (**2**) linker on the Ag(111) surface leads to a densely packed monolayer with chevron arrangement exhibiting a Moiré pattern. Gd-directed assembly resulted in an irregular metal–organic pattern with variable coordination motifs, but without any evidence of coordination numbers higher than five. The preference for the established mononuclear five-fold nodes, identified previously for the related class of linkers of type **1**, seems thus a generic property of the 2D carbonitrile–Ln coordination. Obviously, the high reactivity of the –C≡C– bonds in the propiolonitrile groups prevented the surface-confined molecular system from formation of regular metal–organic nanostructures or layers, instead resulting in reticulated Ln, organic networks with only local order. Our results highlight the paramount importance of the nature of the coordinating end groups for the surface-confined lanthanide coordination chemistry in attempts to design molecular architectures incorporating the sophisticated properties of f-elements [55].

Experimental

STM measurements

The STM measurements were performed using a CreaTec low temperature STM (LT-STM). The base pressure of the ultra-high vacuum system was below 2×10^{-10} mbar.

The Ag(111) substrate was prepared using standard cycles of Ar^+ sputtering (800 eV) and subsequent annealing at 723 K for 10 min. All STM images were taken in constant-current mode with an electrochemically etched tungsten tip.

The supramolecular networks based on Gd–ligand coordination motifs described in the manuscript were fabricated in a two-step process:

1. The molecular linkers NC–C≡C–Ph_3–C≡C–CN (**2**) were deposited from a quartz crucible held at T = 479 K by organic molecular beam epitaxy (OMBE) onto a clean Ag(111) crystal held at ≈300 K.
2. Subsequently, Gd atoms were sublimated by means of electron beam evaporation from an outgassed Gd rod (99.9%, MaTecK GmbH, 52428 Jülich, Germany) onto the sample held at ≈300 K.

X-ray crystallography

Crystals suitable for single crystal X-ray diffraction were obtained by slow diffusion of hexane into a 1,4-dioxane solution of **2** and by slow diffusion of hexane into a solution of **3** in the dichloromethane. Crystals were then selected in perfluoroalkyl ether oil. Single crystal X-ray diffraction data of compounds **2** and **3** were collected on a STOE IPDS II diffractometer with graphite monochromatic Mo Kα radiation (0.71073 Å) at 180 K.

Data were corrected for Lorentz and polarisation effects. Interframe scaling was performed with the program LANA. The structures were solved by direct methods (SHELX-97) [56]. Refinement was performed with anisotropic temperature factors for all non-hydrogen atoms. Crystal data and the results of the refinement are collected in Supporting Information File 1, Tables S1–4. Molecular diagrams were prepared using Diamond software [57].

CCDC-1026443 (**2**) and CCDC-1006987 (**3**) contain the supplementary reference crystallographic data for this paper. These data can be obtained free of charge at http://www.ccdc.cam.ac.uk/conts/retrieving.html (or from the Cambridge Crystallographic Data Centre, 12 Union Road, Cambridge CB2 1EZ, UK; fax: +44 1223/336-033; Email: deposit@ccdc.cam.ac.uk).

General synthesis remarks

Reactions requiring an inert gas atmosphere were conducted under argon, and the glassware was oven dried (140 °C). All reagents were purchased from commercial sources and used as received. Compound **4** was prepared according to previous literature [58].

^{1}H NMR and ^{13}C NMR spectra were recorded on a Bruker DRX 500 spectrometer. The chemical shifts are given in ppm and are referenced to residual proton resonances of the solvents. The mass spectroscopic data were acquired with a Voyager-DE PRO Bio spectrometry work station for MALDI–ToF. MALDI spectra were measured with no additional matrix compound other than the sample itself. Elemental analysis of carbon, hydrogen, and nitrogen were carried out in a Vario Micro Cube. Infrared spectra were measured in KBr pellets (MAGNA FTIR 750, Nicolet) in the 4000–400 cm^{-1} region.

3,3'-([1,1':4',1"-terphenyl]-4,4"-diyl)bis(prop-2-yn-1-ol) (**5**)

Under an argon atmosphere 4,4"-diiodo-1,1':4',1"-terphenyl (**4**, 192 mg, 1.0 mmol), prop-2-yn-1-ol (140 mg, 2.5 mmol), $Pd(PPh_3)_2Cl_2$ (40 mg), CuI (20 mg) were added to a mixture of 10 mL pyrrolidine and 10 mL THF and heated at 60 °C for 36 h. Next, hexane (50 mL) was added and the residue was filtered off and dissolved in THF. The solution was chromatographed on silica gel using dichloromethane/ethyl acetate 5:1 as eluent with a short column, affording 240 mg of **5** as yellow solid (yield 71%). ^{1}H NMR (500 MHz, DMSO-d_6) δ/ppm 4.34 (d, J = 5.96 Hz, 4H, –CH_2–), 5.37 (t, J = 5.96, 5.96 Hz, 2H, –OH), 7.54 (d, J = 8.37 Hz, 4H, Ar–H), 7.77 (d, J = 8.39 Hz, 4H, Ar–H), 7.82 (s, 4H, Ar–H); ^{13}C NMR (126 MHz, DMSO-d_6) δ/ppm 139.21, 138.43, 131.88, 127.20, 126.74, 121.62, 90.79, 83.39, 49.48; IR (KBr, cm^{-1}): 2184 (C≡C); MALDI–ToF (m/z): $[M]^+$ calcd for $C_{24}H_{18}O_2$, 338.1; found, 338.0.

3,3'-([1,1':4',1"-terphenyl]-4,4"-diyl)dipropiolonitrile (**2**)

Following [45] a 2 M solution of ammonia in 2-propanol (1.8 mL, 3.2 mmol) and anhydrous magnesium sulfate (1.5 g, 12.8 mmol) were added to a stirred solution of compound **5** (203 mg, 0.6 mmol) in THF (20 mL). Then, activated manganese dioxide (1.1 g, 12.8 mmol) was added. The resulting mixture was stirred at room temperature for 2 h and then diluted with dichloromethane (20 mL). The mixture was filtered through Celite, washed well with dichloromethane, and the combined filtrates were concentrated in vacuum. The residue was purified by column chromatography on silica gel (hexane/dichloromethane 2:1) affording 51 mg of **2** as light yellow solid (yield 26%). ^{1}H NMR (500 MHz, $CDCl_3$) δ/ppm 7.69–7.75 (m, 12H); ^{13}C NMR (126 MHz, $CDCl_3$) δ/ppm 143.69, 139.46, 134.11, 127.85, 127.41, 116.60, 105.54, 82.86, 63.95; IR (KBr, cm^{-1}): 2260 (C≡N), 2141, (C≡C); MALDI–ToF (m/z): $[M]^+$ calcd for $C_{24}H_{12}N_2$, 328.1; found, 328.1; Anal. calcd for $C_{24}H_{12}N_2$: C, 87.79; H, 3.68; N, 8.53; found: C, 87.63; H, 3.45; N 8.81.

Additionally, 10 mg of a white solid was separated. The analytical data were identical to terphenyl-4-propiolonitrile (**3**) prepared by the blind synthesis (Supporting Information File 1).

Supporting Information

Supporting Information File 1

Additional experimental data.
[http://www.beilstein-journals.org/bjnano/content/supplementary/2190-4286-6-31-S1.pdf]

Acknowledgements

This work was supported by the EC-MoQuaS (FP7-ICT-2013-10), the Marie Curie action EIF-041565 MoST, the ERC Advanced Grant MolArt (247299), and the China Scholarship Council.

References

1. Cotton, S. *Lanthanide and Actinide Chemistry;* John Wiley & Sons: Chichester, United Kingdom, 2006; pp 61–87. doi:10.1002/0470010088.ch5
2. Rinehart, J. D.; Long, J. R. *Chem. Sci.* **2011,** *2,* 2078–2085. doi:10.1039/c1sc00513h
3. Bogani, L.; Wernsdorfer, W. *Nat. Mater.* **2008,** *7,* 179–186. doi:10.1038/nmat2133

4. Urdampilleta, M.; Klyatskaya, S.; Cleuziou, J.-P.; Ruben, M.; Wernsdorfer, W. *Nat. Mater.* **2011,** *10,* 502–506. doi:10.1038/nmat3050
5. Urdampilleta, M.; Nguyen, N.-V.; Cleuziou, J.-P.; Klyatskaya, S.; Ruben, M.; Wernsdorfer, W. *Int. J. Mol. Sci.* **2011,** *12,* 6656–6667. doi:10.3390/ijms12106656
6. Ganzhorn, M.; Klyatskaya, S.; Ruben, M.; Wernsdorfer, W. *ACS Nano* **2013,** *7,* 6225–6236. doi:10.1021/nn402968k
7. Lopes, M.; Candini, A.; Urdampilleta, M.; Reserbat-Plantey, A.; Bellini, V.; Klyatskaya, S.; Marty, L.; Ruben, M.; Affronte, M.; Wernsdorfer, W.; Bendiab, N. *ACS Nano* **2010,** *4,* 7531–7537. doi:10.1021/nn1018363
8. Candini, A.; Klyatskaya, S.; Ruben, M.; Wernsdorfer, W.; Affronte, M. *Nano Lett.* **2011,** *11,* 2634–2639. doi:10.1021/nl2006142
9. Sanvito, S. *Nat. Mater.* **2011,** *10,* 484–485. doi:10.1038/nmat3061
10. Vincent, R.; Klyatskaya, S.; Ruben, M.; Wernsdorfer, W.; Balestro, F. *Nature* **2012,** *488,* 357–360. doi:10.1038/nature11341
11. Thiele, S.; Vincent, R.; Holzmann, M.; Klyatskaya, S.; Ruben, M.; Balestro, F.; Wernsdorfer, W. *Phys. Rev. Lett.* **2013,** *111,* 037203. doi:10.1103/PhysRevLett.111.037203
12. Thiele, S.; Balestro, F.; Ballou, R.; Klyatskaya, S.; Ruben, M.; Wernsdorfer, W. *Science* **2014,** *344,* 1135–1138. doi:10.1126/science.1249802
13. Barth, J. V.; Costantini, G.; Kern, K. *Nature* **2005,** *437,* 671–679. doi:10.1038/nature04166
14. Lin, N.; Stepanow, S.; Vidal, F.; Kern, K.; Alam, M. S.; Strömsdörfer, S.; Dremov, V.; Müller, P.; Landa, A.; Ruben, M. *Dalton Trans.* **2006,** *23,* 2794–2800. doi:10.1039/b515728e
15. Elemans, J. A. A. W.; Lei, S.; De Feyter, S. *Angew. Chem., Int. Ed.* **2009,** *48,* 7298–7332. doi:10.1002/anie.200806339
16. Bartels, L. *Nat. Chem.* **2010,** *2,* 87–95. doi:10.1038/nchem.517
17. Barth, J. V. *Surf. Sci.* **2009,** *603,* 1533–1541. doi:10.1016/j.susc.2008.09.049
18. Bünzli, J.-C. G. *Acc. Chem. Res.* **2006,** *39,* 53–61. doi:10.1021/ar0400894
19. Silly, F.; Castell, M. R. *Phys. Rev. Lett.* **2006,** *96,* 086104. doi:10.1103/PhysRevLett.96.086104
20. Écija, D.; Urgel, J. I.; Papageorgiou, A. C.; Joshi, S.; Auwärter, W.; Seitsonen, A. P.; Klyatskaya, S.; Ruben, M.; Fischer, S.; Vijayaraghavan, S.; Reichert, J.; Barth, J. V. *Proc. Natl. Acad. Sci. U. S. A.* **2013,** *110,* 6678–6681. doi:10.1073/pnas.1222713110
21. Urgel, J. I.; Ecija, D.; Auwärter, W.; Papageorgiou, A. C.; Seitsonen, A. P.; Vijayaraghavan, S.; Joshi, S.; Fischer, S.; Reichert, J.; Barth, J. V. *J. Phys. Chem. C* **2014,** *118,* 12908–12915. doi:10.1021/jp502901z
22. Schlickum, U.; Decker, R.; Klappenberger, F.; Zoppellaro, G.; Klyatskaya, S.; Ruben, M.; Silanes, I.; Arnau, A.; Kern, K.; Brune, H.; Barth, J. V. *Nano Lett.* **2007,** *7,* 3813–3817. doi:10.1021/nl072466m
23. Kühne, D.; Klappenberger, F.; Decker, R.; Schlickum, U.; Brune, H.; Klyatskaya, S.; Ruben, M.; Barth, J. V. *J. Am. Chem. Soc.* **2009,** *131,* 3881–3883. doi:10.1021/ja809946z
24. Klyatskaya, S.; Klappenberger, F.; Schlickum, U.; Kühne, D.; Marschall, M.; Reichert, J.; Decker, R.; Krenner, E.; Zoppellaro, G.; Brune, H.; Barth, J. V.; Ruben, M. *Adv. Funct. Mater.* **2011,** *21,* 1230–1240. doi:10.1002/adfm.201001437
25. Sohn, Y.; Wei; White, J. M. *Langmuir* **2007,** *23,* 12185–12191. doi:10.1021/la702241m
26. Sohn, Y.; Wei, W.; White, J. M. *J. Phys. Chem. C* **2007,** *111,* 5101–5110. doi:10.1021/jp068398u
27. Kepčija, N.; Zhang, Y.-Q.; Kleinschrodt, M.; Björk, J.; Klyatskaya, S.; Klappenberger, F.; Ruben, M.; Barth, J. V. *J. Phys. Chem. C* **2013,** *117,* 3987–3995. doi:10.1021/jp310606r
28. Zhang, Y.-Q.; Kepčija, N.; Kleinschrodt, M.; Diller, K.; Fischer, S.; Papageorgiou, A. C.; Allegretti, F.; Björk, J.; Klyatskaya, S.; Klappenberger, F.; Ruben, M.; Barth, J. V. *Nat. Commun.* **2012,** *3,* No. 1286. doi:10.1038/ncomms2291
29. Cirera, B.; Zhang, Y.-Q.; Klyatskaya, S.; Ruben, M.; Klappenberger, F.; Barth, J. V. *ChemCatChem* **2013,** *5,* 3281–3288. doi:10.1002/cctc.201300299
30. Cirera, B.; Zhang, Y.-Q.; Björk, J.; Klyatskaya, S.; Chen, Z.; Ruben, M.; Barth, J. V.; Klappenberger, F. *Nano Lett.* **2014,** *14,* 1891–1897. doi:10.1021/nl4046747
31. Gao, H.-Y.; Franke, J.-H.; Wagner, H.; Zhong, D.; Held, P.-A.; Studer, A.; Fuchs, H. *J. Phys. Chem. C* **2013,** *117,* 18595–18602. doi:10.1021/jp406858p
32. Gao, H.-Y.; Wagner, H.; Zhong, D.; Franke, J.-H.; Tuder, A.; Fuchs, H. *Angew. Chem., Int. Ed.* **2013,** *52,* 4024–4028. doi:10.1002/anie.201208597
33. Liu, J.; Ruffieux, P.; Feng, X.; Mülle, K.; Fasel, R. *Chem. Commun.* **2014,** *50,* 11200–11203. doi:10.1039/C4CC02859G
34. Eichhorn, J.; Heckl, W. M.; Lackinger, M. *Chem. Commun.* **2013,** *49,* 2900–2902. doi:10.1039/c3cc40444g
35. Chen, Y.-R.; Duan, W.-L. *J. Am. Chem. Soc.* **2013,** *135,* 16754–16757. doi:10.1021/ja407373g
36. Cheng, Z.-Y.; Li, W.-J.; He, F.; Zhou, J.-M.; Zhu, X.-F. *Bioorg. Med. Chem.* **2007,** *15,* 1533–1538. doi:10.1016/j.bmc.2006.09.041
37. Shi, Z.; Zhang, C.; Li, S.; Pan, D.; Ding, S.; Cui, Y.; Jiao, N. *Angew. Chem., Int. Ed.* **2009,** *48,* 4572–4576. doi:10.1002/anie.200901484
38. Reutenauer, P.; Kivala, M.; Jarowski, P. D.; Boundon, C.; Gisselbrecht, J.-P.; Gross, M.; Diederich, F. *Chem. Commun.* **2007,** 4898–4900. doi:10.1039/b714731g
39. Tanee Fomum, Z.; Forsche Asobo, P.; Landor, S. R.; Landor, P. D. *J. Chem. Soc., Perkin Trans. 1* **1984,** 1079–1083. doi:10.1039/P19840001079
40. Heard, N. E.; Turner, J. *J. Org. Chem.* **1995,** *60,* 4302–4304. doi:10.1021/jo00118a061
41. Rama Rao, V. V. V. N. S.; Lingaiah, B. P. V.; Ezikiel, G.; Yadla, R.; Shanthan Rao, P. *Heterocycl. Commun.* **2006,** *12,* 275–280. doi:10.1515/HC.2006.12.3-4.275,
42. Urgel, J. I.; Ecija, D.; Auwärter, W.; Barth, J. V. *Nano Lett.* **2014,** *14,* 1369–1373. doi:10.1021/nl4044339
43. Schlickum, U.; Decker, R.; Klappenberger, F.; Zoppellaro, G.; Klyatskaya, S.; Auwärter, W.; Kern, K.; Brune, H.; Ruben, M.; Barth, J. V. *J. Am. Chem. Soc.* **2008,** *130,* 11778–11782. doi:10.1021/ja8028119
44. Bünzli, J.-C. G.; André, N.; Elhabiri, M.; Muller, G.; Piguet, C. *J. Alloys Compd.* **2000,** *303–304,* 66–74. doi:10.1016/S0925-8388(00)00609-5
45. McAllister, G. D.; Wilfred, C. D.; Taylor, R. J. K. *Synlett* **2002,** *8,* 1291–1292. doi:10.1055/s-2002-32950
46. Kühne, D.; Klappenberger, F.; Decker, R.; Schlickum, U.; Brune, H.; Klyatskaya, S.; Ruben, M.; Barth, J. V. *J. Phys. Chem. C* **2009,** *113,* 17851–17859. doi:10.1021/jp9041217
47. Reichert, J.; Marschall, M.; Seufert, K.; Ecija, D.; Auwärter, W.; Arras, E.; Klyatskaya, S.; Ruben, M.; Barth, J. V. *J. Phys. Chem. C* **2013,** *117,* 12858–12863. doi:10.1021/jp4021273

48. Marschall, M.; Reichert, J.; Weber-Bargioni, A.; Seufert, K.; Auwärter, W.; Klyatskaya, S.; Zoppellaro, G.; Ruben, M.; Barth, J. V. *Nat. Chem.* **2010,** *2,* 131–137. doi:10.1038/nchem.503
49. Stepanow, S.; Strunskus, T.; Lingenfelder, M.; Dmitriev, A.; Spillmann, H.; Lin, N.; Barth, J. V.; Wöll, Ch.; Kern, K. *J. Phys. Chem. B* **2004,** *108,* 19392–19397. doi:10.1021/jp046766t
50. Schlickum, U.; Klappenberger, F.; Decker, R.; Zoppellaro, G.; Klyatskaya, S.; Ruben, M.; Kern, K.; Brune, H.; Barth, J. V. *J. Phys. Chem. C* **2010,** *114,* 15602–15606. doi:10.1021/jp104518h
51. Marschall, M.; Reichert, J.; Seufert, K.; Auwaerter, W.; Klappenberger, F.; Weber-Bargioni, A.; Klyatskaya, S.; Zoppellaro, G.; Nefedov, A.; Strunskus, T.; Woell, C.; Ruben, M.; Barth, J. V. *ChemPhysChem* **2010,** *11,* 1446–1451. doi:10.1002/cphc.200900938
52. Klappenberger, F.; Kühne, D.; Marschall, M.; Neppl, S.; Krenner, W.; Nefedov, A.; Strunskus, T.; Fink, K.; Wöll, C.; Klyatskaya, S.; Fuhr, O.; Ruben, M.; Barth, J. V. *Adv. Funct. Mater.* **2011,** *21,* 1631–1642. doi:10.1002/adfm.201001940
53. Arras, E.; Seitsonen, A. P.; Klappenberger, F.; Barth, J. V. *Phys. Chem. Chem. Phys.* **2012,** *14,* 15995–16001. doi:10.1039/c2cp42293j
54. Barth, J. V. *Annu. Rev. Phys. Chem.* **2007,** *58,* 375–407. doi:10.1146/annurev.physchem.56.092503.141259
55. Ruben, M. *Angew. Chem., Int. Ed.* **2005,** *44,* 1594–1596. doi:10.1002/anie.200462064
56. Sheldrick, G. M. *Acta Crystallogr., Sect. A: Found. Crystallogr.* **2008,** *A64,* 112–122. doi:10.1107/S0108767307043930
57. *Diamond,* Version 2.1d; Crystal Impact GbR: Bonn, Germany, 2000.
58. Sviridenko, F. B.; Stass, D. V.; Kobzeva, T. V.; Tretyakov, E. V.; Klyatskaya, S. V.; Mshvidobadze, E. V.; Vasilevsky, S. F.; Molin, Y. N. *J. Am. Chem. Soc.* **2004,** *126,* 2807–2819. doi:10.1021/ja037157m

License and Terms

BEILSTEIN JOURNAL OF NANOTECHNOLOGY

A versatile strategy towards non-covalent functionalization of graphene by surface-confined supramolecular self-assembly of Janus tectons

Ping Du[1,§], David Bléger[1,¶], Fabrice Charra[2], Vincent Bouchiat[3], David Kreher[1], Fabrice Mathevet[1] and André-Jean Attias[*1]

Review

Open Access

Address:
[1]Institut Parisien de Chimie Moléculaire, Chimie des Polymères, UMR CNRS 8232, Université Pierre et Marie Curie, 3 rue Galilée, 94200 Ivry, France, [2]Laboratoire de Nanophotonique, Service de Physique de l'Etat Condensé CEA/Saclay 91191 Gif sur Yvette Cedex, France and [3]Department Nanosciences Institut Neel, CNRS, Univ. Grenoble-Alpes, 38042 Grenoble Cedex 09, France

Email:
André-Jean Attias[*] - andre-jean.attias@upmc.fr

* Corresponding author
§ Current address: Karlsruher Institut für Technologie, Institut für Nanotechnologie Hermann-von-Helmholtz-Platz 1, 76344 Eggenstein-Leopoldshafen, Germany
¶ Current address: Laboratory of Organic Chemistry and Functional Materials, Department of Chemistry, Humboldt Universität zu Berlin, Brook-Taylor-Strasse 2, 12489 Berlin, Germany

Keywords:
C(sp^2)-based substrates; graphene; Janus tecton; liquid–solid interface; scanning tunnelling microscopy; supramolecular self-assembly

Beilstein J. Nanotechnol. **2015,** *6,* 632–639.
doi:10.3762/bjnano.6.64

Received: 30 August 2014
Accepted: 10 February 2015
Published: 03 March 2015

This article is part of the Thematic Series "Molecular materials – towards quantum properties".

Guest Editor: M. Ruben

Abstract

Two-dimensional (2D), supramolecular self-assembly at surfaces is now well-mastered with several existing examples. However, one remaining challenge to enable future applications in nanoscience is to provide potential functionalities to the physisorbed adlayer. This work reviews a recently developed strategy that addresses this key issue by taking advantage of a new concept, Janus tecton materials. This is a versatile, molecular platform based on the design of three-dimensional (3D) building blocks consisting of two faces linked by a cyclophane-type pillar. One face is designed to steer 2D self-assembly onto C(sp^2)-carbon-based flat surfaces, the other allowing for the desired functionality above the substrate with a well-controlled lateral order. In this way, it is possible to simultaneously obtain a regular, non-covalent paving as well as supramolecular functionalization of graphene, thus opening interesting perspectives for nanoscience applications.

Review

Introduction

Graphene is of significant interest for next generation electronics [1] particularly due to its electronic properties [2,3]. Thus, many research programs have been focused on the development of numerous approaches for synthesizing/transferring graphene onto surfaces during the last decade [4]. The next step towards device integration requires improved modification and functionalization of the bare graphene sheet [5].

This can be achieved either by covalent or non-covalent approaches [6]. In the former strategy, the covalent chemistry of pristine graphene requires chemical modification and the transformation of sp^2 hybridized carbon atoms into sp^3 hybridized. As a consequence, this disruption of the C-sp^2 leads to the alteration of the characteristic electronic properties of graphene. For this reason, the non-covalent functionalization of graphene is expected to be more interesting, offering the opportunity to attach any functionality while simultaneously maintaining the integrity of the sp^2-hybridized carbon network (i.e., not disturbing its electronic substrate properties) [6]. This aspect is critical as far as electronic devices are concerned. It is known that even low-density sp^3 grafting strongly affects the delocalization of electrons within the graphene layer, making it incompatible for applications such as sensors [7]. Finally, an adsorbed molecular lattice can be applied to impose a super-period in the graphene atomic lattice. This new method allows the band and sub-band structure to be finely tuned for innovative two-dimensional (2D) semiconductor junctions [8].

However, the controlled positioning and organization of functional molecules into self-assembled monolayers at surfaces represent a major challenge for potential applications in various fields of nanotechnology [9,10]. Among the various manufacturing routes, bottom-up approaches [11] are particularly promising. They exploit supramolecular chemistry on surfaces to generate specific 2D structures and patterns at the nanometer scale through the self-assembly of building blocks, also called tectons [12]. These tectons are mainly planar π-conjugated molecules as they tend to bond to substrates in a flat-laying geometry. This allows the tectons to approach each other more easily and to engage in non-covalent interactions such as hydrogen bonding [13-15], metal–ligand coordination bonding [16,17] or even van der Waals interactions [18,19]. Thus, surface-confined supramolecular chemistry on surfaces appears to be the method of choice for the simple production of ordered arrays of molecules for the realization of complex functional surfaces. In other words, the exploration of both non-covalent and functionalized molecular self-assemblies on graphene, although a newly emerging approach, is a very promising strategy [20-24]. Moreover, the same principles reported for molecular in-plane-confined self-assembly on substrates (such as HOPG) can be directly transferred to graphene substrates, as was recently demonstrated for a few molecules. There are several examples regarding the formation of well-ordered 2D molecular adlayers self-assembled via hydrogen bonding [21] or other weak interactions on graphene [20], where most of these works were performed by evaporating small molecules onto graphene under ultra-high vacuum (UHV) conditions.

In this context, we recently developed a successful new strategy taking place at the liquid–solid interface at room temperature (RT) for the precise nanometer-scale 2D decoration of flat sp^2-hybridized carbon supports (such as HOPG and graphene) with periodic arrays of functional 3D building blocks, known as Janus tectons [25]. Here, we summarize this general, versatile, and convenient approach for simultaneously (i) generating surface-based, supramolecular, periodic architectures on C(sp^2)-based substrates, and (ii) independently exposing off-plane functionalities with controlled lateral order on demand.

Mastering the surface-confined self-assembly of 2D tectons on C(sp^2)-based substrates

In the first stage, a strategy to obtain "on demand", non-covalent self-assemblies with predetermined 2D periodic topologies on C(sp^2)-based substrates was proposed [26]. Indeed, the construction of predictable and well-defined assemblies remains difficult to achieve, where the resulting topologies are often explained a posteriori based on molecule symmetry, molecule–substrate interactions and molecule–molecule interactions [19]. As a consequence, the "molecular clip concept" was introduced as a tool for surface specific supramolecular bonding on C(sp^2)-based substrates and allowed for the first realization of a predetermined. "on demand" series of 0D, 1D or 2D topologies, based on a single rigid molecular core on HOPG. These achievements are based on the rational design of a novel functional molecular group, which turns into a non-covalent clip-like bond activated by graphite (Figure 1).

Among the interactions available for controlling supramolecular chemistry on surfaces, the interdigitation of alkyl chains was chosen because graphite surfaces such as HOPG exhibit a high affinity for *n*-alkane chains which form close-packed 2D lamellae described by the Groszek model [27]. This is due to the close match between the intra- and inter-chain distances and the graphite lattice parameters. More precisely, a new functional group, also called a "molecular clip", was designed in order to mimic the adsorption of *n*-alkane chains on HOPG. This molecular unit presents two alkyl chains linked by a π-conjugated bridge. Since the distance between the two alkyl

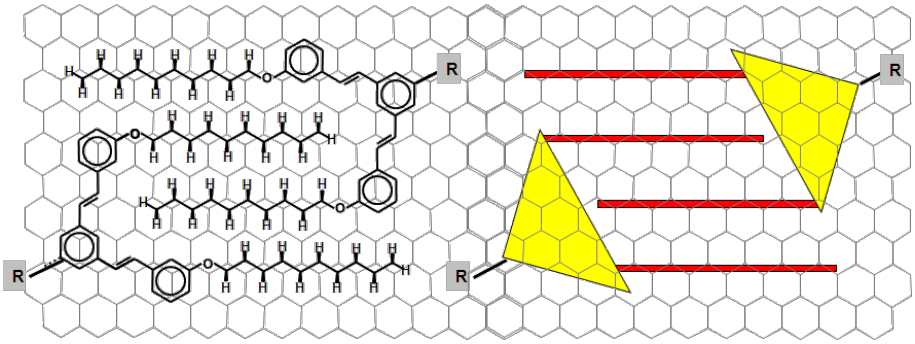

Figure 1: Molecular structure and schematic representation of the "molecular clip" illustrating its specific molecular bonding onto HOPG and showing the rigorous preservation of the Groszek structure [27] for the *n*-alkyl chains. Figure adapted with permission from [26], copyright 2007 Wiley-VCH Verlag GmbH & Co.

chains is twice the interchain distance in a well-organized *n*-alkane lamella, this unit acts as a supramolecular, functional linking group able to form strong, surface-assisted, intermolecular "clips" by interdigitation of the alkyl chains of two functional groups leading to the close-packing structure. Then, with this tool in hand, a fully deterministic strategy was developed where mono-, bi- and tri-multibranched functional building blocks (I–III) (based on a tristilbene rigid core bearing 1,2, and 3 peripheral molecular clips) have been designed, synthesized, and self-assembled on HOPG (Figure 2).

The surface-confined molecular self-assemblies were characterized by scanning tunneling microscopy (STM) at the liquid–solid interface. As expected, they form non-covalent, surface self-assembled dimers, supramolecular linear polymers, and 2D networks. The versatility of the design was then demonstrated by synthesizing bifunctional molecules bearing two functional "clips" that end-cap a central moiety consisting of, for example, a benzene ring (IV) (Figure 3a). As shown in Figure 3b, compound IV also gives stable monolayers on HOPG. In addition, the self-assembly yields large, highly ordered domains, for which the lattice parameters can be accurately measured (Figure 3c), resulting in average lattice parameter values of $a = 3.86 \pm 0.15$ nm, $b = 2.11 \pm 0.08$ nm, and $\alpha = 65 \pm 1°$.

These results demonstrate that we are now able to control the supramolecular self-assembly on HOPG. First, a new tool acting as a functional moiety for surface-specific supramolecular bonding has been designed by combining and controlling molecule–substrate epitaxial adsorption and intermolecular packing interactions. Second, the "molecular clip" concept validity was demonstrated through the good match between the various expected and experimental topologies resulting from the supramolecular self-assembly at the liquid–HOPG interface of designed building blocks.

3D tectons for the controlled placement of functional molecules on C(sp^2)-based substrates

In the second stage, the design of 3D building blocks was pursued [29]. This strategy is motivated by the need for functional surfaces for demanding forthcoming applications in nanotechnology. To address this issue, the realization of

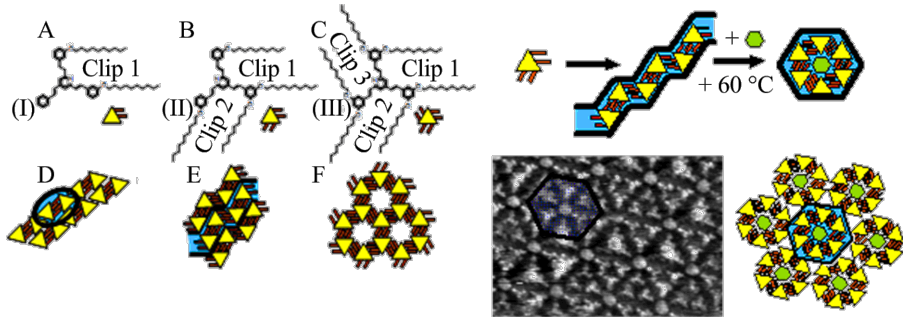

Figure 2: "On demand" realization of dimer-, polymer- or network-like topologies from a given rigid core and clips placed at different locations. Molecular structures of molecules I, II, and III (A–C), along with the anticipated self-assembly (D–F). Figure adapted with permission from [26], copyright 2007 Wiley-VCH Verlag GmbH & Co.

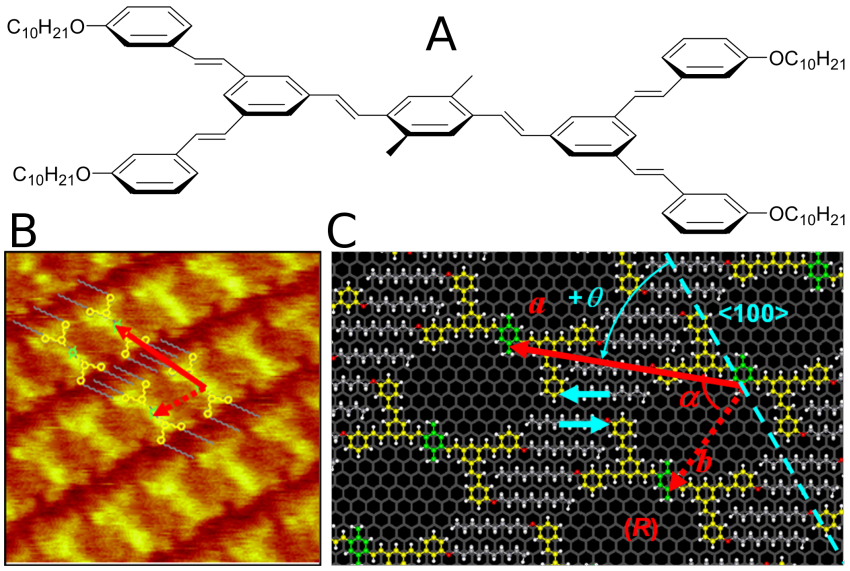

Figure 3: Compound IV: (A) molecular structure and (B) self-assembly of IV demonstrated by a high-resolution STM image of a monolayer domain of (IV) formed at the interface between graphite HOPG and a highly diluted (≈10^{-4} mol·L^{-1}) solution in phenyloctane. The sample bias was ≈−1.55 V and the tunnel current was ≈55 pA. The scan size and *z*-scale were ≈12.5 nm and ≈2.0 Å, respectively. The to-scale model of the molecular assembly is superimposed. (C) Molecular scheme of one unit cell of the monolayer adsorbed on HOPG (grey honeycomb background) of IV. Grey: alkyl chains; Yellow: conjugated cores; Green: multiple cyclophane levels. The unit cell is represented using red arrows: the solid arrow represents the intrachain period and the dotted arrow represents an interchain period. The blue line represents one <100> axis of HOPG. Figure adapted with permission from [28], copyright 2008 Wiley-VCH Verlag GmbH & Co.

controlled functional molecular assemblies under the surfaces is a key point. To achieve such an objective requires the creation of out-of-plane functions and the full exploitation of the area above the substrate, in order to obtain an exact placement of functional objects in the third dimension above (perpendicular to) the surface. Most molecular recognition processes at surfaces require 3D receptors, and accessing the third dimension is also a mandatory step for nano-optics/electronics. Indeed the close proximity between the active conjugated system and a conducting substrate results in the rapid quenching of any electronic excitations. Thus, it is of prime importance to provide a strategy to decouple active molecular units from conducting C(sp^2)-based substrates. In this context, we proposed for the first time a novel and highly versatile concept, the Janus-like 3D tecton concept. This building block consists of two different faces (A and B, like in all the Janus species) and a spacer linking them. Face A was designed to act as a pedestal capable of steering a 2D self-assembly onto the substrate, while B is a functional entity (e.g., a chromophore). The spacer acts as a pillar ensuring the decoupling of the B face from the substrate. Moreover, if the Janus tecton is laying on the substrate via the A face, the formation of a well-organized, in-plane monolayer covering the surface is expected as well as the steered positioning of the B face out of the plane. This concept was validated by designing and synthesizing the 3D tecton reported in Figure 4a. The pillar is a 3.3 Å [3.3]dithiaparacyclophane unit. The lower deck of this two-story linker is end-capped with two

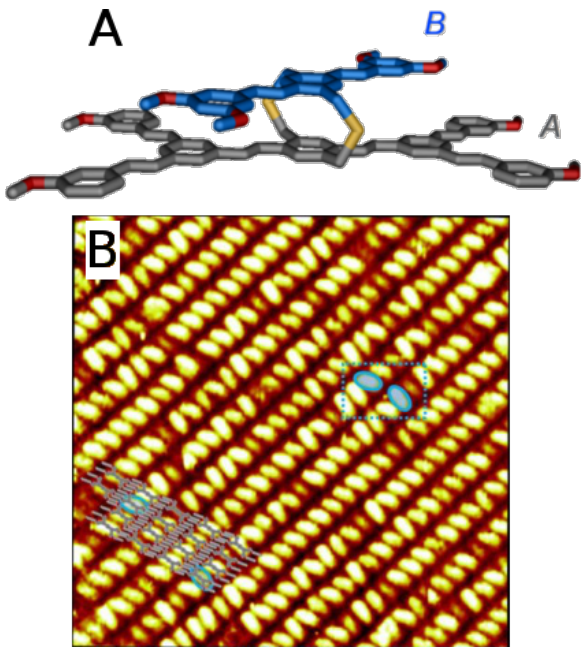

Figure 4: 3D Janus tecton: schematic structure of the two-faced building block laying on the substrate (alkyl chains are omitted for clarity), and large-scale STM image (49.3 x 49.3 nm^2) of the self-assembly at the HOPG–phenyloctane interface. The scaled model of the molecular assembly is superimposed on the STM picture (only lower levels A are represented for clarity). Figure adapted with permission from [29], copyright 2011 Wiley-VCH Verlag GmbH & Co.

molecular clips in order to form the pedestal (A face), while a functional molecule, namely a distyrylbenzene fluorophore (highlighted in blue), forms the upper level (B face). STM studies at the liquid–HOPG interface demonstrated that the 2D well-defined nanostructured platform made of face A on the surface allowed controlled organization of the chromophores (faces B), leading to a regular array of functional units raised from the substrate (Figure 4b).

With these last results, it was demonstrated that (i) the multi-story molecules stack perpendicular to the substrate paving HOPG with long-range ordering, and (ii) the "floor" does not disturb the self-assembly in supramolecular, linear polymeric chains, even at large scales. Thus, this approach appears to be a breakthrough given the ability to control the 3-axis positioning (x,y,z) of a chromophore above a substrate. Moreover, due to its substantial, inherent tunability, this strategy opens up a promising novel route toward functional molecular nanostructures and new perspectives towards active surfaces and interfaces on C(sp^2)-based substrates.

3D tectons for non-covalent functionalization of graphene by supramolecular self-assembly

In the third stage, it was recently demonstrated that the Janus tecton concept is a versatile platform that can be used towards the non-covalent functionalization of graphene [25]. Before presenting the details of this strategy, it must be noted that the most commonly used non-covalent approach for graphene functionalization involves binding of pyrene-substituted species by π–π interaction [30-32], however, without formation of a well-ordered adlayer. Well-organized adlayers have only recently been obtained by transferring HOPG, molecular, in-plane confined, self-assembly studies to graphene substrates. However, to date, the majority of the investigations deal with only a few of molecules: 3,4,9,10-perylenetetracarboxylic dianhydride (PTCDA), phthalocyanine (and its metal coordination complexes), and C60 fullerenes [20]. Moreover, to our knowledge, no route towards 3D tecton surface-confined self-assembly, which adds functionality to graphene substrates, has been previously described and or even explored. In this context, we took advantage of the tremendous ability of the Janus tectons to form periodic, functional adlayers on HOPG, used as a versatile new tool for a similar non-covalent functionalization of graphene. To ensure the versatility compared to our previous work, the synthetic sequence as well as the pillar design were revisited and rationalized. In fact, we developed a synthetic convergent strategy (Figure 5) which consists of first synthesizing a series of intermediate 3D building blocks (Janus precursors, JAP) bearing small terminal chemical groups at the top of the pillar (a dithia[3.3]metaparacyclophane derivative).

In a first attempt to validate the strategy, the terminal chemical groups were –Br, –CN, –CHO, and –COOH. Second, after appropriate post-functionalization, the Janus precursors formed the target Janus tectons (JA), exposing as an upper face different functional moieties such as triazine-4,5-diamine, 2,6-bis(2-pyridyl)pyridine and ferrocene units.

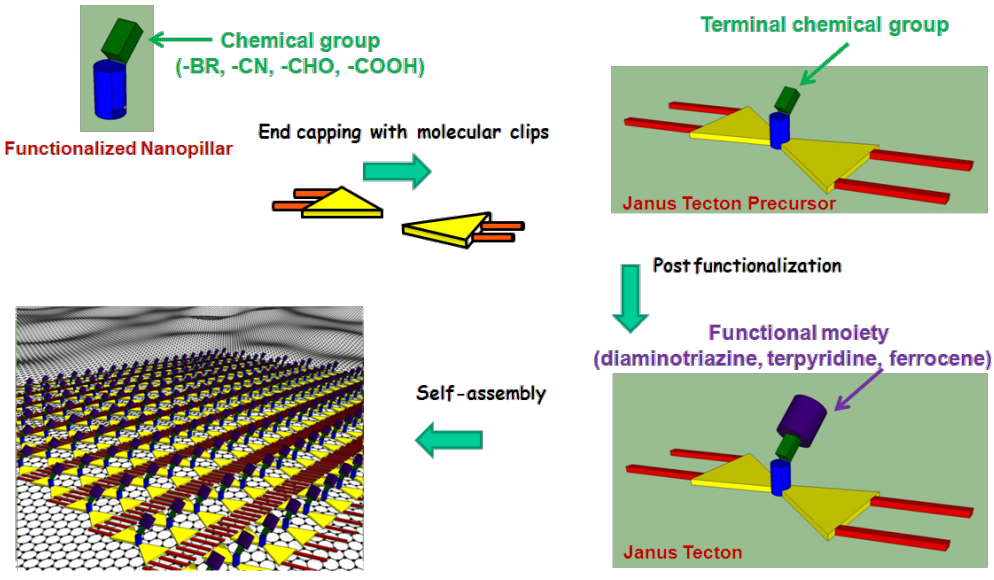

Figure 5: Synthetic strategy and expected organization on C(sp^2)-carbon-based supports of the self-assembled Janus tectons, exposing a wide range of external interfacial compositions.

The self-assembly properties of the JAPs and JAs were investigated by STM at the liquid–HOPG interface, at room temperature (Figure 6). First, it is obvious that all the probed Janus building blocks spontaneously self-assemble into 2D networks on HOPG. More surprisingly, they form periodic lattices with the same parameters within the typical experimental accuracy of ±5% for the distances and 2° for the angles (a = 3.84 nm, b = 2.08 nm and α = 64°) regardless of the building block. These values are compatible with those of the lattice formed by the neat ground floor [32]. Then, it was inferred that the same process drives the self-assembly on the substrate regardless of the tecton. An explanation is that the ground level of functionalized 3D Janus tectons of any shape, size or function in JAP and JA tectons, act to steer the 2D self-assembly. This is due to interactions with both the HOPG and with the neighboring adsorbed molecules, as confirmed by molecular mechanics calculations [25]. Both the experimental and theoretical lattice values of JA evidenced that the presence of relatively large entities on the upper level which did not perturb the self-assembly. In addition, they further confirmed that the self-assembly is stabilized by adsorption of alkyl chains in registry with HOPG and by their maximized close-packing interactions through interdigitation. The comparison of the cross-sectional area of the pedestal ($a \cdot b \cdot \sin\alpha$ = 7.18 nm^2) with the calculated cross-sectional areas occupied by each upper unit (to a maximum of 2.02 nm^2 for the largest upper level, terpyridine unit) can partially explain these features. All of the upper units are size-compatible with the huge footprint value.

Finally, the self-assembly of the Janus tectons onto a graphene monolayer, grown by chemical vapor deposition onto a polycrystalline foil, was investigated. As evidenced by a typical STM image (Figure 7) recorded at the liquid–graphene inter-

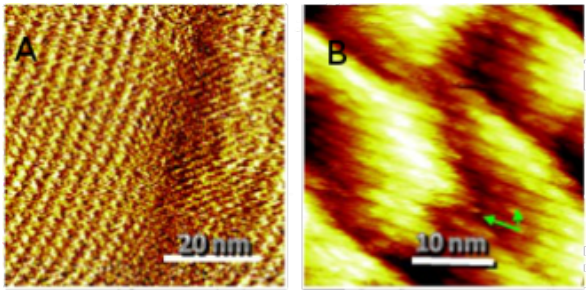

Figure 7: Self-assembly on graphene. Drift-corrected STM images obtained in air on a monolayer graphene substrate grown by chemical vapor deposition on a polycrystalline copper foil at the interface between this substrate and a 10^{-4} M solution of Janus tectons in phenyloctane. (A) 58 × 58 nm, set point I_T = 20 pA, sample bias V_B = −950 mV, (B) 34 × 34 nm, I_T = 13 pA, V_B = −950 mV. A unit cell corresponding to the lattice formed on HOPG (a = 3.84 nm, b = 2.08 nm, and α = 64°) is highlighted in (B) by green arrows. Figure adapted with permission from [25], copyright 2014 Wiley-VCH Verlag GmbH & Co.

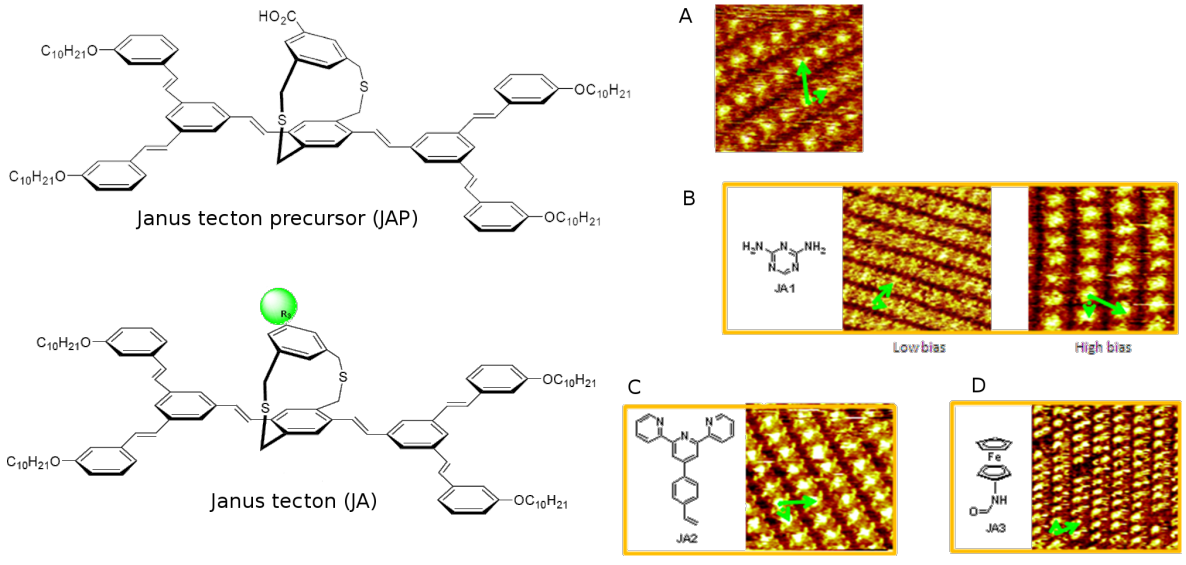

Figure 6: Self-assembly of a Janus tecton precursor (JAP) and the Janus tectons (JA). Drift-corrected STM images obtained at the interface between HOPG and a 10^{-4} M solution in phenyloctane of (A) JAP, 13 × 13 nm, set point I_T = 35 pA, sample bias V_B = −1200 mV, (B) JA functionalized with triazine-4,5-diamine, low bias: 22 × 22 nm, I_T = 8 pA, V_B = −950 mV and high bias: 15 × 15 nm, I_T = 14 pA, V_B = −1350 mV, (C) JA functionalized with terpyridine, 16 × 16 nm, I_T = 25 pA, V_B = −1500 mV, and (D) JA functionalized with ferrocene, 25 × 25 nm, I_T = 20 pA, V_B = −1330 mV. One of the unit cells corresponding to the lattice formed by the non-functionalized pedestal, a = 3.84 nm, b = 2.08 nm and α = 64°, is highlighted in each image (green arrows) to illustrate the agreement between all Janus tecton lattices. Figure adapted with permission from [25], copyright 2014 Wiley-VCH Verlag GmbH & Co.

face at room temperature, a self-assembled monolayer is observed. By using the same procedure as in the case of a HOPG substrate, the lattice parameters of the network have been estimated. The main result is that they are similar to those measured in the case of the HOPG substrate.

These results demonstrate that for the first time a general platform for the non-covalent functionalization of flat sp^2-carbon-based substrates (including graphene) has been investigated. In contrast to other studies performed by evaporating low molecular weight molecules under UHV conditions, in our approach, the self-assembly is achieved at the liquid–solid interface, additionally allowing the physisorption of higher molecular weight molecules.

Conclusion

Using the molecular clip concept as a tool for supramolecular bonding on C(sp^2)-based substrates, the Janus tecton concept offers a versatile platform towards the non-covalent functionalization of graphene. The reported strategy is expected to be applicable for the generation of self-assembly systems exhibiting on demand functionalization, expanding the application possibilities of this functionalization method. Moreover, working at the liquid–solid interface makes this strategy easy to implement and should also provide the opportunity to control the self-assembly by tuning the molecule–solvent and solvent–substrate interactions. Finally, the successful self-assembly on graphene, together with the possibility to transfer the graphene monolayer onto various substrates, should open up new opportunities in nanoscience.

Acknowledgements

We thank the French Research National Agency (ANR) (NOMAD project ANR-08-NAN O-013-02; NANOCRISNET project ANR-11 BS-1001801), the Ministère de la Recherche et de l'Enseignement Supérieur (MESR), Ville de Paris (Research in Paris Program), AOARD (Grant FA2386-12-1-4011), and the EU Graphene flagship for financial support.

References

1. Geim, A. K. *Science* **2009,** *324,* 1530–1534. doi:10.1126/science.1158877
2. Bolotin, K. I.; Sikes, K. J.; Jiang, Z.; Klima, M.; Fudenberg, G.; Hone, J.; Kim, P.; Stormer, H. L. *Solid State Commun.* **2008,** *146,* 351–355. doi:10.1016/j.ssc.2008.02.024
3. Du, X.; Skachko, I.; Barker, A.; Andrei, E. Y. *Nat. Nanotechnol.* **2008,** *3,* 491–495. doi:10.1038/nnano.2008.199
4. Batzill, M. *Surf. Sci. Rep.* **2012,** *67,* 83–115. doi:10.1016/j.surfrep.2011.12.001
5. Wang, X.; Li, X.; Zhang, L.; Yoon, Y.; Weber, P. K.; Wang, H.; Guo, J.; Dai, H. *Science* **2009,** *324,* 768–771. doi:10.1126/science.1170335
6. Georgakilas, V.; Otyepka, M.; Bourlinos, A. B.; Chandra, V.; Kim, N.; Kemp, K. C.; Hobza, P.; Zboril, R.; Kim, K. S. *Chem. Rev.* **2012,** *112,* 6156–6214. doi:10.1021/cr3000412
7. Fan, X.-Y.; Nouchi, R.; Yin, L.-C.; Tanigaki, K. *Nanotechnology* **2010,** *21,* 475208. doi:10.1088/0957-4484/21/47/475208
8. Järvinen, P.; Hämäläinen, S. K.; Banerjee, K.; Häkkinen, P.; Ijäs, M.; Harju, A.; Liljeroth, P. *Nano Lett.* **2013,** *13,* 3199–3204. doi:10.1021/nl401265f
9. Joachim, C.; Gimzewski, J. K.; Aviram, A. *Nature* **2000,** *408,* 541–548. doi:10.1038/35046000
10. Barth, J. V.; Costantini, G.; Kern, K. *Nature* **2005,** *437,* 671–679. doi:10.1038/nature04166
11. Barth, J. V. *Annu. Rev. Phys. Chem.* **2007,** *58,* 375–407. doi:10.1146/annurev.physchem.56.092503.141259
12. Rosei, F.; Schunack, M.; Naitoh, Y.; Jiang, P.; Gourdon, A.; Laegsgaard, E.; Stensgaard, I.; Joachim, C.; Besenbacher, F. *Prog. Surf. Sci.* **2003,** *71,* 95–146. doi:10.1016/S0079-6816(03)00004-2
13. Theobald, J. A.; Oxtoby, N. S.; Phillips, M. A.; Champness, N. R.; Beton, P. H. *Nature* **2003,** *424,* 1029–1031. doi:10.1038/nature01915
14. Pawin, G.; Wong, K. L.; Kwon, K.-Y.; Bartels, L. *Science* **2006,** *313,* 961–962. doi:10.1126/science.1129309
15. Nath, K. G.; Ivasenko, O.; Miwa, J. A.; Dang, H.; Wuest, J. D.; Nanci, A.; Perepichka, D. F.; Rosei, F. *J. Am. Chem. Soc.* **2006,** *128,* 4212–4213. doi:10.1021/ja0602896
16. Langner, A.; Tait, S. L.; Lin, N.; Rajadurai, C.; Ruben, M.; Kern, K. *Proc. Natl. Acad. Sci. U. S. A.* **2007,** *104,* 17927–17930. doi:10.1073/pnas.0704882104
17. Surin, M.; Samori, P.; Jouaiti, A.; Kyritsakas, N.; Hosseini, M. W. *Angew. Chem., Int. Ed.* **2006,** *46,* 245–249. doi:10.1002/anie.200603558
18. Samori, P.; Fechtenkötter, A.; Reuther, E.; Watson, M. D.; Severin, N.; Müllen, K.; Rabe, J. P. *Adv. Mater.* **2006,** *18,* 1317–1321. doi:10.1002/adma.200502391
19. Mali, K. S.; Adisoejoso, J.; Ghijsens, E.; De Cat, I.; De Feyter, S. *Acc. Chem. Res.* **2012,** *45,* 1309–1320. doi:10.1021/ar200342u
20. MacLeod, J. M.; Rosei, F. *Small* **2014,** *10,* 1038–1049. doi:10.1002/smll.201301982
21. Wang, Q. H.; Hersam, M. C. *Nat. Chem.* **2009,** *1,* 206–211. doi:10.1038/nchem.212
22. Yang, K.; Xiao, W. D.; Jiang, Y. H.; Zhang, H. G.; Liu, L. W.; Mao, J. H.; Zhou, H. T.; Du, S. X.; Gao, H.-J. *J. Phys. Chem. C* **2012,** *116,* 14052–14056. doi:10.1021/jp304068a
23. Hämäläinen, S. K.; Stepanova, M.; Drost, R.; Liljeroth, P.; Lahtinen, J.; Sainio, J. *J. Phys. Chem. C* **2012,** *116,* 20433–20437. doi:10.1021/jp306439h
24. Yang, H.; Mayne, A. J.; Comtet, G.; Dujardin, G.; Kuk, Y.; Sonnet, P.; Stauffer, L.; Nagarajan, S.; Gourdon, A. *Phys. Chem. Chem. Phys.* **2013,** *15,* 4939–4946. doi:10.1039/c3cp42591f
25. Du, P.; Jaouen, M.; Bocheux, A.; Bourgogne, C.; Han, Z.; Bouchiat, V.; Kreher, D.; Mathevet, F.; Fiorini-Debuisshert, C.; Charra, F.; Attias, A.-J. *Angew. Chem., Int. Ed.* **2014,** *53,* 10060–10066. doi:10.1002/anie.201403572
26. Bléger, D.; Kreher, D.; Mathevet, F.; Attias, A.-J.; Schull, G.; Huard, A.; Douillard, L.; Fiorini-Debuischert, C.; Charra, F. *Angew. Chem., Int. Ed.* **2007,** *46,* 7404–7407. doi:10.1002/anie.200702376
27. Groszek, A. J. *Proc. R. Soc. London, Ser. A* **1970,** *314,* 473. doi:10.1098/rspa.1970.0019

28. Bléger, D.; Kreher, D.; Mathevet, F.; Attias, A.-J.; Arfaoui, I.; Metgé, G.; Douillard, L.; Fiorini-Debuisschert, C.; Charra, F. *Angew. Chem., Int. Ed.* **2008,** *120,* 8540–8543. doi:10.1002/ange.200801335
29. Bléger, D.; Mathevet, F.; Kreher, D.; Attias, A.-J.; Bocheux, A.; Latil, S.; Douillard, L.; Fiorini-Debuisschert, C.; Charra, F. *Angew. Chem., Int. Ed.* **2011,** *50,* 6562–6566. doi:10.1002/anie.201008212
30. Urdampilleta, M.; Klyatskaya, S.; Cleuziou, J.-P.; Ruben, M.; Wernsdorfer, W. *Nat. Mater.* **2011,** *10,* 502–506. doi:10.1038/nmat3050
31. Mann, J. A.; Rodríguez-López, J.; Abruna, H. D.; Dichtel, W. R. *J. Am. Chem. Soc.* **2011,** *133,* 17614–17617. doi:10.1021/ja208239v
32. Qu, S.; Li, M.; Xie, L.; Huang, X.; Yang, J.; Wag, N.; Yang, S. *ACS Nano* **2013,** *7,* 4070–4081. doi:10.1021/nn4001963

License and Terms

BEILSTEIN JOURNAL OF NANOTECHNOLOGY

Electroburning of few-layer graphene flakes, epitaxial graphene, and turbostratic graphene discs in air and under vacuum

Andrea Candini[*1], Nils Richter[2,3], Domenica Convertino[4], Camilla Coletti[4], Franck Balestro[5,6], Wolfgang Wernsdorfer[5], Mathias Kläui[2,3] and Marco Affronte[1,7]

Full Research Paper

Open Access

Address:
[1]Centro S3, Istituto Nanoscienze – CNR, Via Campi 213/a, 41125 Modena, Italy, [2]Johannes Gutenberg Universität-Mainz, Institut für Physik, Staudinger Weg 7, 55128 Mainz, Germany, [3]Graduate School of Excellence Materials Science in Mainz (MAINZ), Staudinger Weg 9, 55128 Mainz, Germany, [4]Center for Nanotechnology Innovation @ NEST, Istituto Italiano di Tecnologia, Piazza San Silvestro 12, 56127 Pisa, Italy, [5]Institut Néel, CNRS and Université Joseph Fourier, B.P. 166, 38042 Grenoble Cedex 09, France, [6]Institut Universitaire de France, 103 Boulevard Saint-Michel, 75005 Paris, France and [7]Dipartimento di scienze Fisiche Informatiche e Matematiche, Università di Modena e Reggio Emilia, Via Campi 213/a, 41125 Modena, Italy

Email:
Andrea Candini[*] - andrea.candini@nano.cnr.it

* Corresponding author

Keywords:
graphene; graphene based electrodes; molecular electronics; molecular spintronics

Beilstein J. Nanotechnol. **2015,** *6,* 711–719.
doi:10.3762/bjnano.6.72

Received: 03 October 2014
Accepted: 09 February 2015
Published: 11 March 2015

This article is part of the Thematic Series "Molecular materials – towards quantum properties".

Guest Editor: M. Ruben

Abstract

Graphene-based electrodes are very promising for molecular electronics and spintronics. Here we report a systematic characterization of the electroburning (EB) process, leading to the formation of nanometer-spaced gaps, on different types of few-layer graphene (namely mechanically exfoliated graphene on SiO_2, graphene epitaxially grown on the C-face of SiC and turbostratic graphene discs deposited on SiO_2) under air and vacuum conditions. The EB process is found to depend on both the graphene type and on the ambient conditions. For the mechanically exfoliated graphene, performing EB under vacuum leads to a higher yield of nanometer-gap formation than working in air. Conversely, for graphene on SiC the EB process is not successful under vacuum. Finally, the EB is possible with turbostratic graphene discs only after the creation of a constriction in the sample using lithographic patterning.

Introduction

The vision of molecular electronics is the exploitation of single molecules as the active units in complex devices offering novel functionalities beyond the present technology [1-3]. To achieve this goal, several technological challenges need to be overcome, in particular how to embed nano-scale objects such as a single molecule in electronic circuits in a reliable way suitable for the mass production of devices [4]. Besides scanning probe techniques [5], to date the most popular approaches are mechanically controllable break junctions [6] and electromigrated junctions [7], with the use of gold as the preferred material for electrodes, due to its noble metal character and (relatively) easy handling. The use of gold, however, brings several well known disadvantages: The mobility of the atoms limits the stability of the junctions and their use for room temperature operations [8,9]. In a three-terminals geometry, the relatively thick electrodes lead to a screening of the gate potential; the atomistic configuration of the metal–molecule–metal junction has a large number of parameters that determine the transport properties which cannot be controlled experimentally, yet [4].

Recently, the use of graphene as electrode material for molecular electronics has been proposed [1,10]. With respect to metallic contacts, graphene offers a planar geometry with a thickness comparable to the molecular size and the strong sp^2 carbon bonds assure a high mechanical stability even above room temperature. Finally, the possibility to exploit specific functionalizations to attach the molecular units to the graphene electrodes through carbon bonds and/or π-stacking seems to be a promising route to develop well-defined and robust junction configurations. In addition to these advantages, several theoretical papers have investigated the possibility to use graphene as an electrode to contact individual molecules [11-16], predicting interesting specific features such as quantum coherent transport [11], edge effects [13], and suppression of conductance fluctuations [14].

Recent works have successfully made use of graphene for the realization of electrodes in molecular devices [10,17]. Specifically, parallel multi-junctions devices have been fabricated in chemical vapor deposition (CVD) graphene by electron beam lithography and plasma etching [17-19]. In order to address individual molecules the electroburning (EB) technique has been employed on exfoliated few-layer graphene on a substrate, showing electrostatic gating in molecular units at room temperature [10]. More recently, it has been shown how the yield of fabrication of nanometer-sized gaps can be increased from about 50% [20] to more than 95% by performing the EB process under vacuum [21,22]. While this last result is certainly very promising, it has been demonstrated only for single-layer graphene grown by CVD and then transferred on SiO_2. Therefore it is important to test it also on other types of graphene. In particular, since many envisaged applications require the use of a gate electrode to tune the molecular junctions properties, it seems appealing the use of few-layer graphene, which is still thin but much less gate-dependent than the single layer [10,20].

In this work we compare the EB process in air and in vacuum in few-layer graphene flakes exfoliated on SiO_2 substrate and we show that the yield of nanometer-gap formation can be increased significantly when working at a reduced pressure. In addition, we report, for the first time, the EB process (in air and under vacuum) also on other types of few-layer graphene, which are better suited for large scale integration, namely multilayer graphene grown on the C-face of SiC [23] and thin discs of turbostratically stacked graphene [24,25].

Results

Mechanically exfoliated few-layer graphene

We first consider the case of few-layer graphene flakes obtained by the mechanical exfoliation technique (see Experimental for more details). A typical flake is shown in the inset of Figure 1a. Several electrical contacts are fabricated on the same sample, leading to a certain number of nearly identical graphene junctions (same layer thickness, roughly the same geometrical parameters). For each flake we processed approximately half of the junctions under ambient conditions (room temperature and in air) and the other half under vacuum (pressure below 10^{-4} mbar) so that the final comparison between the results in air and under vacuum is made independent on the geometrical factors. In total, we measured 23 graphene flakes of thickness of 1–20 layers, corresponding to 115 junctions.

To open a nanometer-size gap in the graphene devices, we polarized the junctions with a single voltage ramp with a fast feedback loop in order to stop the current immediately after the opening of the junction. We used the same method previously employed for the electromigration of gold nanowires [26]. A typical example of the process is visible in Figure 1a. Above a certain voltage value, the I–V curves become strongly nonlinear, probably related to the removal of contaminants induced by the current annealing [10,20,21,27]. Increasing the voltage further, the true EB process develops. At high temperatures, induced by the Joule heating, the carbon atoms react with oxygen until the device breaks and an abrupt increase of the resistance is observed [10]. When the measured resistance overcomes a fixed value corresponding to the complete formation of an open gap in the device, a feedback control of our electronics restores the voltage to zero very rapidly (<100 μs). The complete process takes approximately 10 to 20 s.

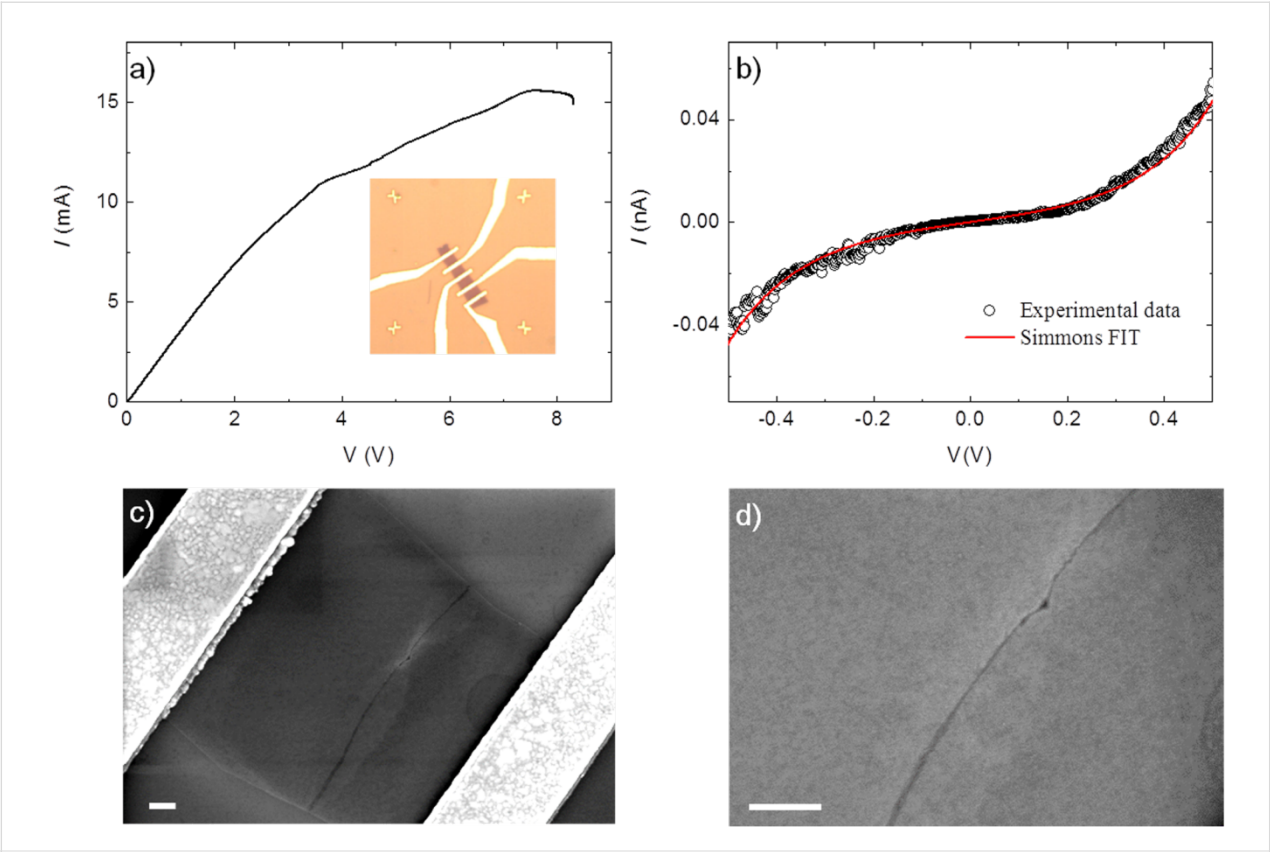

Figure 1: a) *I–V* curve recorded for a typical electroburning (EB) process. Inset: optical image of one of the few-layer graphene flakes used (the distance between the crosses at the corners is 45 μm); b) example of an *I–V* measurement for a device showing a sizeable tunneling current after the EB process. The black circle are the experimental data and the red line is the fitting according to the Simmons model by using the following parameters: gap size d = 1.83 nm; junction area A = 5 nm^2; barrier height Φ = 0.6 eV; c) and d) corresponding SEM images showing the opening of a gap that is a few nanometers wide (scale bars: 300 nm).

After the EB process, the device is characterized by an *I–V* measurement keeping the bias voltage below ±1.5 V to avoid any modification of the gap [10,28]. An example of a device displaying a sizeable tunneling current in this range is given in Figure 1b. Figure 1c and Figure 1d show the corresponding scanning electron microscope (SEM) images for the device after the EB process. The opening of the gap, which can be as small as few nanometers, is visible. The image indicates that the reaction starts at the edges of the central part of the device. Indeed, the gold contacts act as a thermal reservoir dissipating the heat and the central part is therefore the hottest part of the device. In addition, the edges of the flake, which are characterized by nonsaturated carbon bonds, are likely the most reactive point to initiate the process.

In order to characterize the gap size in more details, we fit the *I–V* curves according to the Simmons model [29] (see Supporting Information File 1 for more details), using the gap width d, the junction area A and the height of the tunnel barrier Φ as the fitting parameters. For the fit shown in Figure 2b we used d = 1.83 nm, A = 5 nm^2, Φ = 0.6 eV. It is known that the value of d is a quite robust fitting parameter, while the other two are not, since good fits are still possible even with very different values. Indeed, we can fit our data with almost the same accuracy by using a very broad range of values for A and Φ (see the Supporting Information File 1 for some examples) but the optimal value for d is always between 1.5 nm and 2.5 nm. For all of our measured devices for which we observed a tunneling current at low bias voltages (also for the ones made of different type of graphene, see following sections) the values for d are in the range from 0.5 nm to 3 nm. This narrow distribution, which is expected since in the model the current depends exponentially on the width of the gap, is a strong indication that we can obtain electrodes with distances in the true nanometer range.

In the following, we discuss the yield of this EB process, with particular attention on the differences encountered between air and vacuum working conditions. In total, 58 junctions were processed in air and 57 under vacuum and they have been divided in three categories depending on the *I–V* characterization after the EB process. The first class (A) is composed by the

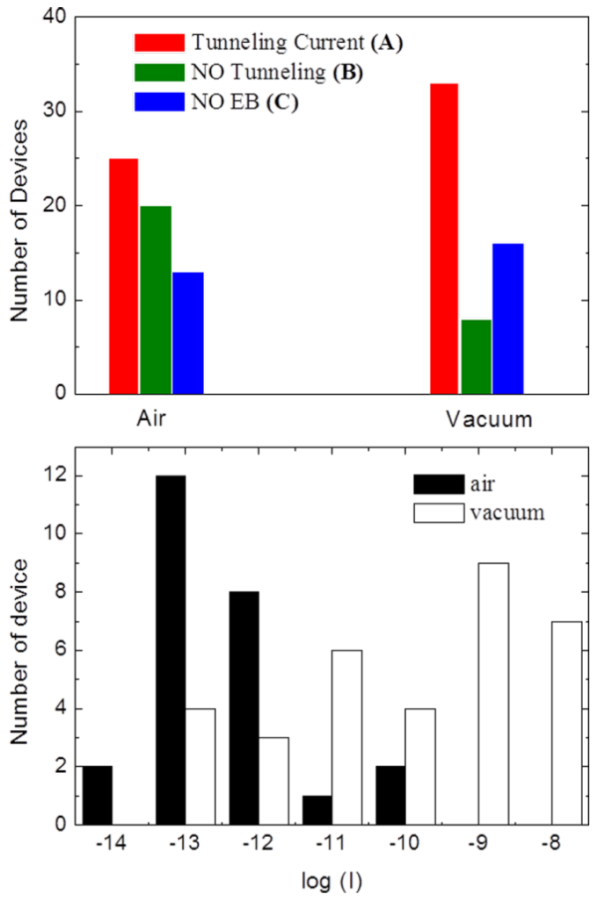

Figure 2: top) Number of measured devices displaying the following behavior: A) sizeable tunneling current ($I > 10^{-13}$A @ 1.5 V) after the EB process (red); B) no tunneling current after EB (green); C) no EB for the maximum currents and/or voltages available. Results related to both procedures, in air and under vacuum, are presented. Bottom) Logarithm of the current (in amperes) measured at $V = 0.5$ V for the devices of group A: the measured current is significantly different if the EB process is carried out in air (black histograms) or under vacuum (white histograms).

devices showing a sizeable tunneling current ($I > 10^{-13}$ A) within the range of ±1.5 V. In these devices, the EB process created a gap with sizes of a few nanometers. In the second group (B) we consider junctions that underwent an EB process but no tunneling current is observed in our measurement range. These are "open" devices, with a gap larger than about 10 nm, which can be still useful for contacting long molecules or nanoparticles. Finally, the last group (C) comprises those devices that did not break under the maximum voltage/current we applied. The results of these studies are summarized in the upper panel of Figure 2.

Considering the junctions processed in air, 25 of them (ca. 43%) exhibited a tunneling current after the EB, in 20 (ca. 35%) no detectable current was measured and finally 13 (ca. 22%) did not break during the process. Such a yield is comparable with what has been found by Burzurì et al. [20], but with a different electroburning procedure (i.e., feedback controlled). Moving to the devices electroburned under vacuum, in 33 junctions (ca. 58%) we measured a sizeable tunneling current after the process, while only in eight (ca. 14%) we did not find any measurable current. Finally for 16 (ca. 28%) of them, the EB process was not possible under our experimental conditions. The difference in yield between the process in air and under vacuum is evident.

Interestingly, the tunneling currents measured after the EB process generally display a much higher value when the process is carried out under vacuum than in air, as shown in the bottom panel of Figure 2, in which we plot the current measured at $V = 0.5$ V in different devices. We stress that the I–V tests after the EB process were repeated also under different conditions (air or vacuum) and we did not find a significant dependence on the measurement conditions (only the conditions of the EB process are relevant). Since the tunneling current is inversely proportional to the size of the gap, we conclude that under vacuum conditions the EB is more controllable, leading to higher yield of success and generally smaller gap sizes.

It is also worthy of note that the number of devices that were not burned is almost the same for air and vacuum conditions. We noted that very thick or very large flakes led to devices displaying very small two-probes resistance (≤200 Ω), which did not undergo the EB process for our maximum applied voltage (10 V) and/or led to the saturation of our current-meter (30 mA). Indeed, the largest part of the devices falling in the category C of Figure 2 is made by junctions belonging to the same thick or large flakes.

If we consider only the flakes that were effectively electroburned, i.e., neglecting devices falling in category C, the difference in yield between the EB process in air and in vacuum is even more evident: the rate of success (junctions displaying tunneling current after EB) is 55% in air and 80% in vacuum. In addition, the gaps obtained by the vacuum process generally display much larger currents implying a smaller size of the gap itself. Similarly, an improved yield in the fabrication of nanometer-sized gaps in graphene junctions by changing the environment conditions from air to vacuum was also reported by Nef et al. [21] who, however, considered only graphene monolayer devices.

In order to analyze further the dependence of the EB process on the environment conditions, in Figure 3 we show the current I_{break} (upper panel) and the voltage V_{break} (lower panel) at which the EB process occurs as a function of the initial resis-

tance of the junctions for both the working conditions (air and vacuum).

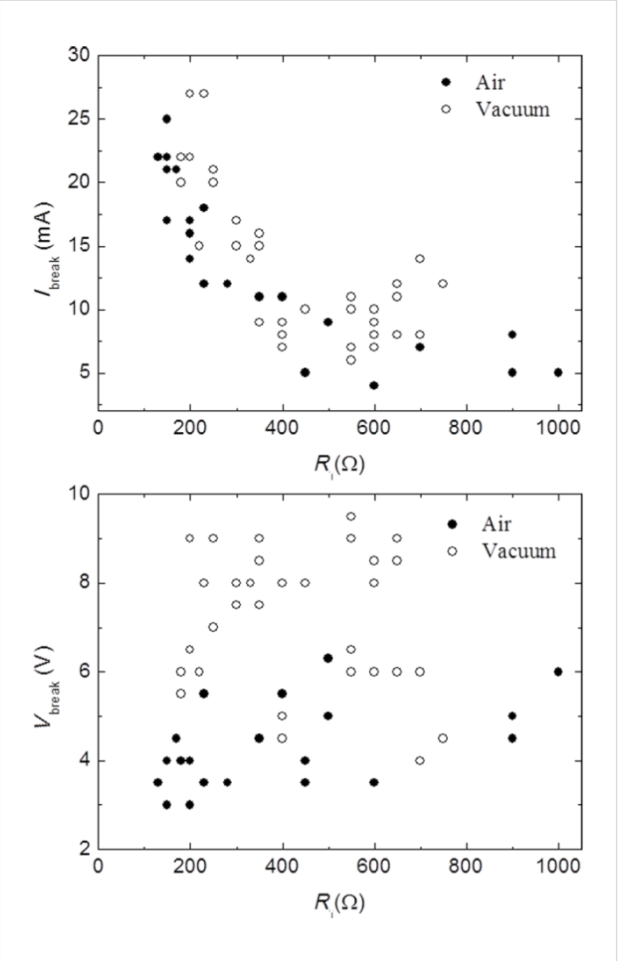

Figure 3: (top) I_{break} current at which the EB process was observed in air (filled dots) and under vacuum (open circles) as a function of the initial resistance of the device. (bottom) Corresponding V_{break}.

We found that the current is generally similar in the two cases (air or vacuum) and it always scales with the initial resistance. On the other hand, the voltage at which the device rupture is found does not show a clear dependence on R_i while it is clearly higher when the process is performed under vacuum. The dependence of I_{break} on R_i, which is primarily determined by the number of layers of the flakes (inversely proportional), suggests that the EB occurs at a constant current density (which only depends on the geometry of the device), regardless of the environment conditions, and in agreement with previous works [10]. On the other hand, the higher voltage values (at a given current) found when working under vacuum indicate a higher resistance for the devices at the breaking point. This can be related to a different efficiency of the removal of contamination induced by the current annealing in vacuum with respect to air [27]. We will return to this point in the Discussion section.

Epitaxial graphene on the C-face of SiC

The EB procedure has been repeated also on two-terminal junctions made of graphene epitaxially grown on the C-face of SiC through thermal decomposition in an argon atmosphere [30]. Here the graphene layers are found to grow in a turbostratic fashion, in which each layer is rotated by a certain angle with respect to both adjacent layers. This can be regarded as a large-area few-layer graphene (we found an average of ten layers from Raman measurements, see Experimental section and the Supporting Information File 1 for more details on the sample growth and characterization), which should display a smaller gate dependence with respect to single layer graphene. In total, we processed twelve junctions in air and nine under vacuum. When working under ambient conditions, all the junctions underwent the EB process and an example of the *I*–*V* curve is shown in Figure 4c. In particular, a SEM inspection after the process revealed that the rupture is always in the graphene junction (see the devices on the left in Figure 4a and Figure 4b). After EB, seven junctions displayed a sizeable tunneling current similar to what is shown in Figure 4d. A completely different scenario is found for all the devices processed under vacuum conditions: We did not found any signature of rupture up to very high voltages (V_{break} > 40 V for vacuum processed devices, while it is in the range 10–15 V when working in air) and no detectable currents were ever measured after the EB process. Interestingly, the SEM images revealed that the rupture is always at the metal contacts and not in the graphene devices (junctions on the right in Figure 4a).

Turbostratic graphene discs

We also tested the EB process in multilayered graphene microstructures, employing thin discs of turbostratically stacked graphene (TG, see Experimental for details on the preparation). These discs are comprise up to 100 graphene layers exhibiting a rather large charge carrier mobility in the range of 10^5 $cm^2/V{\cdot}s$ which typically leads to a resistivity of around 3.5 Ω·μm in untreated discs [24]. They can be easily deposited on a substrate (SiO_2 in our case) in large quantities (hundreds of discs with a diameter of about 1–2 μm in a single deposition).

In a first attempt, simple pairs of source–drain electrodes have been defined on the discs by electron beam lithography. More than 10 discs have been contacted and underwent the EB process in air. In all of these experiments the EB took place at the contact areas as exemplary shown in Figure 5a and it was not possible to reach sufficiently high current densities to initiate any EB process. Instead, more power was dissipated where the resistance was higher due to the additional contact resistances. This turned out to occur most likely close to damaged electrodes. In all of these devices, no current is measured after the EB process. In order to overcome this

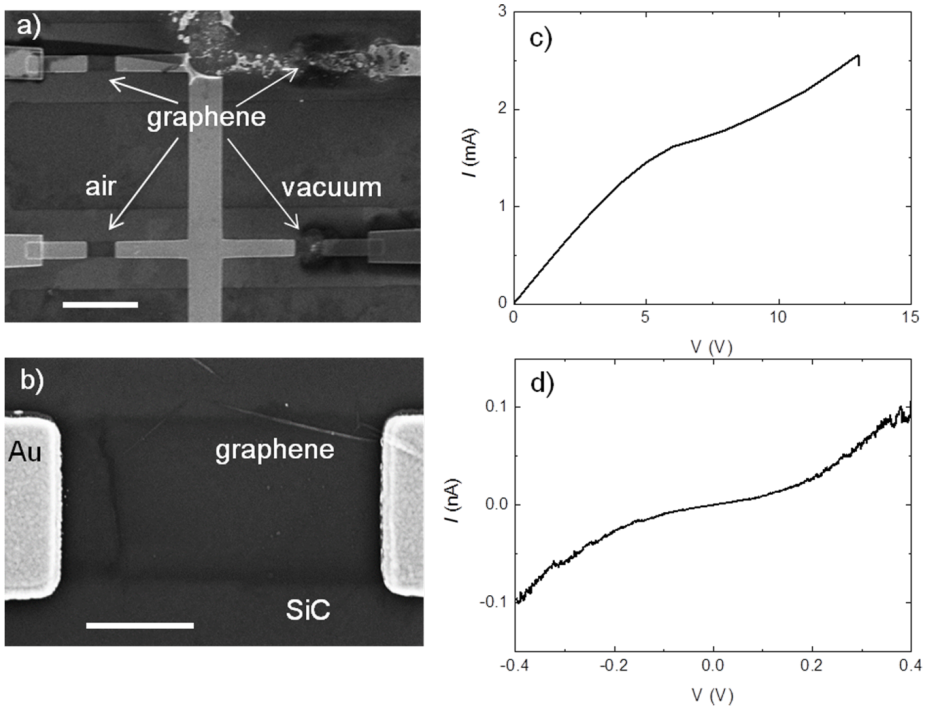

Figure 4: a) SEM image of epitaxial graphene devices after the EB process in air (left) and under vacuum (right). The scale bar is 5 µm. b) Magnification of the open gap in an air-processed device. Scale bar is 1 µm. c) *I*–*V* curve recorded for a typical electroburning (EB) process in air. d) Example of an *I*–*V* measurement after the EB process in air (no current is measured in the *I*–*V* when the EB process is performed under vacuum).

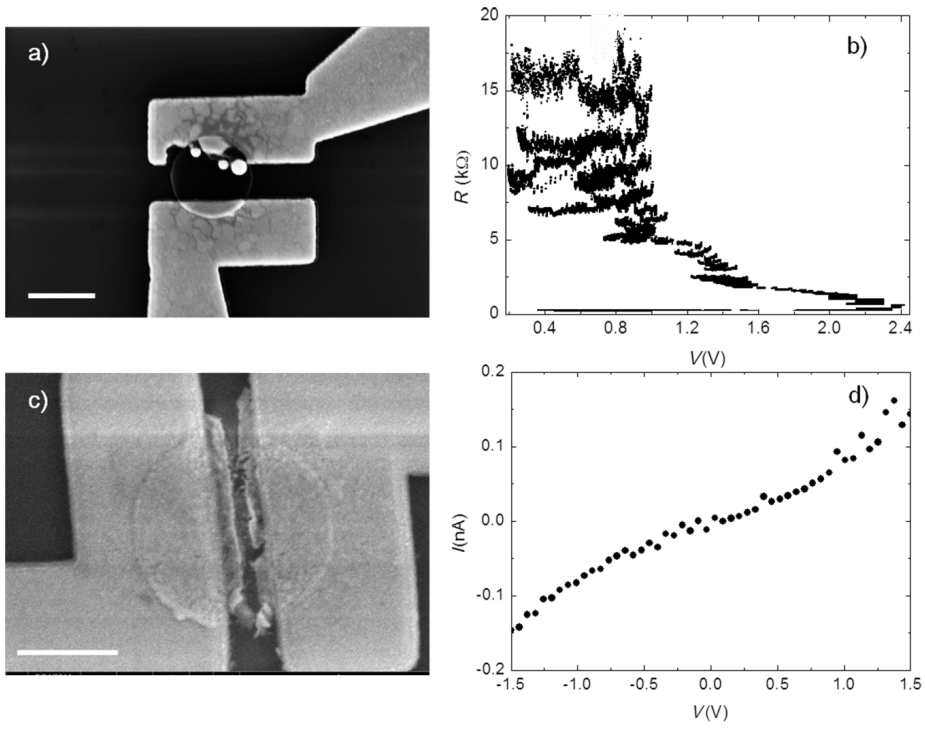

Figure 5: a) SEM image of a non-patterned disc after the EB process. During EB the area around the graphene–metal contact gets heavily damaged due to high power dissipation at these spots. b) EB cycle for a patterned TG disc (see text) showing the transition from low-ohmic (≈200 Ω) to high-ohmic (≈20 kΩ) behavior, which indicates the opening of a gap. c) Corresponding SEM image showing intact metal contacts while a breaking is visible in the disc. d) *I*–*V*-characteristic of electroburned TG device. A tunneling current is visible, demonstrating the presence of an open gap in the range of a few nanometers only. The scale bar is always 1 µm.

problem and to obtain a high current density in the interior of the discs, we pre-patterned them before making the electrical contacts, thus defining a constriction inside the discs (see Experimental for details on the lithography procedure). The narrowest spot now gives the largest current density when a bias is applied. Indeed, we find that the EB process in those devices is well-controlled up to resistances of around 16 kΩ before it opens up a gap and the resistance eventually jumps to higher values showing that one can obtain controlled contact dimensions. Figure 5b shows how the resistance evolves over several EB cycles. A cycle is defined as the increase of bias voltage until either a target voltage is reached or the resistance increases by a certain percentage and then starting again from a voltage level that corresponds to a defined fraction of dissipated power in the device. The resulting gap at the desired position close to the disc center rather than at the contacts is shown in Figure 5c. We measured four patterned discs and all of them showed a similar behavior. Measuring the *I*–*V*-characteristics of such an electroburned device can verify the actual presence of a gap. Typically a bias voltage of 1 V results in a current of 80 pA, as exemplified in Figure 5d showing a typical tunneling current through the gap in the disc.

Discussion

We now compare the different behaviors encountered in the three types of graphene analyzed. Concerning the exfoliated few-layer graphene flakes, we found that performing the EB in vacuum leads to a higher yield of nanometer-gap fabrication. At the same time the EB process happens at higher voltages under vacuum than in air, the current being almost identical under the two conditions. This means that the dissipated electrical power and the local temperature of the devices are similar or even slightly higher in the case of vacuum. Since a higher local temperature is usually considered to be detrimental for a controlled gap formation, we conclude that the environment pressure must be the key parameter to optimize the EB process of few-layer graphene on SiO_2 and achieve a better control on the gap formation.

Graphene grown on the C-face of SiC exhibits a similar behavior under ambient conditions, while under vacuum the oxygen–carbon reaction does not even initiate. This difference must be related to the different stacking feature (turbostratic vs graphite-like) of the graphene itself and/or to the different characteristics of the graphene/substrate systems (exfoliated graphene/SiO_2 vs graphene/SiC).

Focusing on these parameters, it is interesting to consider the case of turbostratic microdiscs, which have a morphology similar to that of graphene on SiC but are deposited on the same substrate as the exfoliated graphene. Here, we found that the EB process leads to a breaking of the graphene devices only after the patterning of a constriction. This hardness with respect to exfoliated graphene suggests that the different morphology of the edges also plays a role to initiate the burning. Indeed, the presence of nonsaturated carbon bonds makes the edges the most reactive part of the device. Edges cleaved during the exfoliation (exfoliated graphene), edges created during the oxygen plasma (graphene on SiC and turbostratic discs after the patterning), and edges of the untreated microdiscs [25] do have different configurations and therefore a different propensity to ignition. Moreover, we expect a higher presence of impurities when using exfoliated graphene on SiO_2 (which is known to be more reactive than SiC). Such impurities may be working as catalysts, initiating the EB process of graphene even under a reduced oxygen atmosphere.

Conclusion

We presented a systematic study of the electroburning (EB) process in few-layer graphene devices for different graphene types. We focused our attention on exfoliated graphene, graphene epitaxially grown on the C-face of SiC and turbostratic graphene microdiscs comparing the results obtained when working in air and under vacuum. We showed how the process strongly depends on the specific type of graphene and on the environment pressure in the chamber. For mechanically exfoliated graphene, the vacuum process leads to the formation of nanometer-sized gaps with a higher yield and generally smaller sizes. On the other hand, for graphene on the C-face of SiC, the EB process creates a gap in the graphene devices when it is performed in air, while under vacuum conditions it simply leads to the blow-up of the metal contacts. As-deposited turbostratic graphene discs are found to be extremely resilient against the EB process: The opening of a gap in the device is possible only after creating a hot spot in the discs, as demonstrated in our work after the patterning of a constriction.

Our work suggests that the oxygen pressure is a key factor in the EB process but also other factors such as the type of graphene stacking, the morphology of the edges and the specific graphene/substrate system play an important role. Further studies will focus on tuning the partial oxygen pressure during the electroburning to determine the optimal working conditions for the different types of device. We believe that these results will contribute to the realization of reliable graphene based electrodes for molecular electronics and spintronics.

Experimental

Few-layer graphene flakes were deposited by the standard "scotch tape" mechanical exfoliation method from natural graphite pieces on top of a p-doped silicon wafer coated with 300 nm of oxide. Flakes of suitable thickness (1 to approx.

20 layers) were located with an optical microscope on the basis of their contrast with the substrate. In some cases, the effective number of layers is also checked by micro-Raman spectroscopy, see Supporting Information File 1 for some examples. Metal contacts (10 nm Cr/100 nm Au) on the graphene sheets have been obtained by electron beam lithography (EBL), thermal evaporation and lift-off in acetone.

Turbostratic graphene was obtained on on-axis SiC(000−1) semi-insulating wafer dice. First, the SiC dice were hydrogen-etched in order to obtain atomically flat surfaces [31]. This process was carried out in a resistively heated cold-wall reactor (high-temperature Aixtron BM) at a temperature of 1350 °C, a pressure of 450 mbar, for 10 min. Subsequently, graphene was obtained in the same reactor through thermal decomposition of SiC [30] under an argon atmosphere, heating at 1420 °C for 90 min. Attenuation of the SiC signal in Raman spectroscopy was used to estimate the number of grown layers, which were found to be about ten. Also, combined Raman and atomic force microscopy (AFM) indicated a good homogeneity and quality of the grown graphene. More details are given in the Supporting Information File 1.

To assure good ohmic contacts, the first fabrication step was the thermal deposition of 3 nm Cr/30 nm Au as the initial metal contacts. Successively, graphene was patterned in the desired device geometry (two-probe device, the graphene channel is roughly 1 × 3 μm) by electron beam lithography and oxygen plasma etching (30 s in a Diener Femto plasma system at maximum power). Finally, the remaining metal parts (the bonding pads and the connections from the contacts to the pads) were obtained by the evaporation of 10 nm Cr/100 nm Au and lift-off.

For mechanically exfoliated and epitaxial graphene the electroburning process was performed by applying an increasing voltage ramp (20 mV/s) while continuously measuring the conductance of a junction. The burning of carbon atoms initiated the formation of a gap and increased the resistance. Once the resistance overcome the chosen value of 200,000 Ω, the voltage was immediately reset to zero (<100 μs). The process was performed at room temperature either in air or under vacuum (<10^{-4} mbar). After the electroburning process, *I*–*V* measurements were taken with an AdWin-Pro system (16 bit output and input) using a FEMTO pre-amplifier.

Turbostratic multilayer graphene discs were grown in large quantities by the pyrolysis of hydrocarbons in a plasma torch process. The graphitic discs were dispersed in 1-methyl-2-pyrrolidinone by using bath sonication followed by centrifugation allowing for the separation of the discs from each other and from other types of microstructure [25]. The material was then dried in the form of powders, which were then deposited on a p-doped silicon wafer coated with 300 nm of oxide by an adhesive tape. After rinsing with acetone and isopropanol, hundreds of discs were left on the surface. Typical Raman spectra of the as-deposited discs are shown in the Supporting Information File 1. The discs were located by an optical microscope and then patterned in the hour-glass geometry by oxygen plasma (2–3 min depending on the discs thickness, for such a long etching time we had to use a 800 nm thick PMMA layer) and finally electrically contacted with thermally evaporated 10 nm Cr/100 nm Au by electron beam lithography and lift-off. After the PMMA development and immediately before the metal evaporation, a short (<10 s) plasma step was performed to assure good ohmic contacts on the discs. Electroburning and *I*–*V* tests were made under ambient conditions by using a Keithley voltage source and femtoamperometer in the two-probe configuration.

Supporting Information

See Supporting Information for the Raman spectra of the different graphene materials (exfoliated, graphene on the C-face of SiC, turbostratic micro-discs deposited on SiO_2); the AFM characterization of the graphene grown on SiC; additional details about the fitting procedure of the non linear *I*–*V* curves according to the Simmons model.

Supporting Information File 1

Titel: Material characterization.
[http://www.beilstein-journals.org/bjnano/content/supplementary/2190-4286-6-72-S1.pdf]

Acknowledgements

This work has been partially supported by European Community through the FET-Proactive Project “MoQuaS”, contract N.610449, by the Italian Ministry for Research (MIUR) through the FIR grant RBFR13YKWX and the German Research Foundation (DFG Priority Program SPP 1459 Graphene). We thank Y. Hernandez for help with the preparation of the turbostratic graphene samples.

References

1. Aradhya, S. V.; Venkataraman, L. *Nat. Nanotechnol.* **2013,** *8,* 399–410. doi:10.1038/nnano.2013.91
2. Sun, L.; Diaz-Fernandez, Y. A.; Gschneidtner, T. A.; Westerlund, F.; Lara-Avila, S.; Moth-Poulsen, K. *Chem. Soc. Rev.* **2014,** *43,* 7378–7411. doi:10.1039/C4CS00143E
3. Bogani, L.; Wernsdorfer, W. *Nat. Mater.* **2008,** *7,* 179–186. doi:10.1038/nmat2133

4. Lörtscher, E. *Nat. Nanotechnol.* **2013,** *8,* 381–384. doi:10.1038/nnano.2013.105
5. Bumm, L. A.; Arnold, J. J.; Cygan, M. T.; Dunbar, T. D.; Burgin, T. P.; Jones, L., II; Allara, D. L.; Tour, J. M.; Weiss, P. S. *Science* **1996,** *271,* 1705–1707. doi:10.1126/science.271.5256.1705
6. Reed, M. A.; Zhou, C.; Muller, C. J.; Burgin, T. P.; Tour, J. M. *Science* **1997,** *278,* 252–254. doi:10.1126/science.278.5336.252
7. Park, H.; Lim, A. K. L.; Alivisatos, A. P.; Park, J.; McEuen, P. L. *Appl. Phys. Lett.* **1999,** *75,* 301–303. doi:10.1063/1.124354
8. Moth-Poulsen, K.; Bjørnholm, T. *Nat. Nanotechnol.* **2009,** *4,* 551–556. doi:10.1038/nnano.2009.176
9. Ratner, M. *Nat. Nanotechnol.* **2013,** *8,* 378–381. doi:10.1038/nnano.2013.110
10. Prins, F.; Barreiro, A.; Ruitenberg, J. W.; Seldenthuis, J. S.; Aliaga-Alcalde, N.; Vandersypen, L. M. K.; van der Zant, H. S. J. *Nano Lett.* **2011,** *11,* 4607–4611. doi:10.1021/nl202065x
11. Bergvall, A.; Berland, K.; Hyldgaard, P.; Kubatkin, S.; Löfwander, T. *Phys. Rev. B* **2011,** *84,* 155451. doi:10.1103/PhysRevB.84.155451
12. García-Suárez, V. M.; Ferradás, R.; Carrascal, D.; Ferrer, J. *Phys. Rev. B* **2013,** *87,* 235425. doi:10.1103/PhysRevB.87.235425
13. Ryndyk, D. A.; Bundesmann, J.; Liu, M.-H.; Richter, K. *Phys. Rev. B* **2012,** *86,* 195425. doi:10.1103/PhysRevB.86.195425
14. Péterfalvi, C. G.; Lambert, C. J. *Phys. Rev. B* **2012,** *86,* 085443. doi:10.1103/PhysRevB.86.085443
15. Prasongkit, J.; Grigoriev, A.; Pathak, B.; Ahuja, R.; Scheicher, R. H. *J. Phys. Chem. C* **2013,** *117,* 15421–15428. doi:10.1021/jp4048743
16. Pshenichnyuk, I. A.; Coto, P. B.; Leitherer, S.; Thoss, M. *J. Phys. Chem. Lett.* **2013,** *4,* 809–814. doi:10.1021/jz400025q
17. Cao, Y.; Dong, S.; Liu, S.; He, L.; Gan, L.; Yu, X.; Steigerwald, M. L.; Wu, X.; Liu, Z.; Guo, X. *Angew. Chem., Int. Ed.* **2012,** *51,* 12228–12232. doi:10.1002/anie.201205607
18. Jia, C.; Wang, J.; Yao, C.; Cao, Y.; Zhong, Y.; Liu, Z.; Liu, Z.; Guo, X. *Angew. Chem., Int. Ed.* **2013,** *52,* 8666–8670. doi:10.1002/anie.201304301
19. Cao, Y.; Dong, S.; Liu, S.; Liu, Z.; Guo, X. *Angew. Chem., Int. Ed.* **2013,** *52,* 3906–3910. doi:10.1002/anie.201208210
20. Burzurí, E.; Prins, F.; van der Zant, H. S. J. *Graphene* **2012,** *1,* 26–29. doi:10.4236/graphene.2012.12004
21. Nef, C.; Pósa, L.; Makk, P.; Fu, W.; Halbritter, A.; Schönenberger, C.; Michel, C. *Nanoscale* **2014,** *6,* 7249–7254. doi:10.1039/c4nr01838a
22. Lau, C. S.; Mol, J. A.; Warner, J. H.; Briggs, G. A. D. *Phys. Chem. Chem. Phys.* **2014,** *16,* 20398–20401. doi:10.1039/C4CP03257H
23. Orlita, M.; Faugeras, C.; Plochocka, P.; Neugebauer, P.; Martinez, G.; Maude, D. K.; Barra, A.-L.; Sprinkle, M.; Berger, C.; de Heer, W. A.; Potemski, M. *Phys. Rev. Lett.* **2008,** *101,* 267601. doi:10.1103/PhysRevLett.101.267601
24. Krishnan, A.; Dujardin, E.; Treacy, M. M. J.; Hugdahl, J.; Lynum, S.; Ebbesen, T. W. *Nature* **1997,** *388,* 451–454. doi:10.1038/41284
25. Hernandez, Y. R.; Schweitzer, S.; Kim, J.-S.; Kumar Patra, A.; Englert, J.; Lieberwirth, I.; Liscio, A.; Palermo, V.; Feng, X.; Hirsch, A.; Kläui, M.; Müllen, K. *arXiv* **2013,** No. 1301.6087.
26. Thiele, S.; Balestro, F.; Ballou, R.; Klyatskaya, S.; Ruben, M.; Wernsdorfer, W. *Science* **2014,** *344,* 1135–1138. doi:10.1126/science.1249802
27. Moser, J.; Bachtold, A. *Appl. Phys. Lett.* **2009,** *95,* 173506. doi:10.1063/1.3243690
28. Standley, B.; Bao, W. Z.; Zhang, H.; Bruck, J.; Lau, C. N.; Bockrath, M. *Nano Lett.* **2008,** *8,* 3345–3349. doi:10.1021/nl801774a
29. Simmons, J. G. *J. Appl. Phys.* **1963,** *34,* 1793. doi:10.1063/1.1702682
30. Starke, U.; Forti, S.; Emtsev, K. V.; Coletti, C. *MRS Bull.* **2012,** *37,* 1177–1186. doi:10.1557/mrs.2012.272
31. Frewin, C. L.; Coletti, C.; Riedl, C.; Starke, U.; Saddow, S. E. *Mater. Sci. Forum* **2009,** *615–617,* 589–592. doi:10.4028/www.scientific.net/MSF.615-617.589

License and Terms

BEILSTEIN JOURNAL OF NANOTECHNOLOGY

Graphene quantum interference photodetector

Mahbub Alam*[1,2] and Paul L. Voss[1,2]

Full Research Paper

Open Access

Address:
[1]Georgia Institute of Technology, School of Electrical and Computer Engineering, Atlanta, Georgia 30324-0250, USA and [2]UMI 2958 Georgia Tech-CNRS, Georgia Tech Lorraine, 2–3 Rue Marconi, 57070 Metz, France

Email:
Mahbub Alam* - malam@georgiatech-metz.fr

* Corresponding author

Keywords:
decoherence; graphene nanoribbon; phase coherence; photodetector; quantum interference; resonant tunneling

Beilstein J. Nanotechnol. **2015,** *6,* 726–735.
doi:10.3762/bjnano.6.74

Received: 12 July 2014
Accepted: 09 February 2015
Published: 12 March 2015

This article is part of the Thematic Series "Molecular materials – towards quantum properties".

Guest Editor: M. Ruben

Abstract

In this work, a graphene quantum interference (QI) photodetector was simulated in two regimes of operation. The structure consists of a graphene nanoribbon, Mach–Zehnder interferometer (MZI), which exhibits a strongly resonant transmission of electrons of specific energies. In the first regime of operation (that of a linear photodetector), low intensity light couples two resonant energy levels, resulting in scattering and differential transmission of current with an external quantum efficiency of up to 5.2%. In the second regime of operation, full current switching is caused by the phase decoherence of the current due to a strong photon flux in one or both of the interferometer arms in the same MZI structure. Graphene QI photodetectors have several distinct advantages: they are of very small size, they do not require p- and n-doped regions, and they exhibit a high external quantum efficiency.

Introduction

Graphene, a single layer of carbon atoms arranged in a honeycomb lattice structure, has attracted much attention from researchers because of its exceptional electronic, mechanical and optical properties such as high electrical mobility, high thermal conductivity, high mechanical strength, linear energy dispersion around the Dirac point and strong light absorption from near-infrared to visible wavelengths [1-3]. Graphene also exhibits ballistic electron transport over unusually long lengths [4-8]. Researchers have recently measured a momentum relaxation length of 10 μm in graphene nano-ribbons at room temperature [4]. Up to this length, resistance is independent of length and Ohm's law does not describe transport [9]. They have also demonstrated a phase-coherence length of 100 nm at room temperature, that is, up to this length the electrons keep their phase-coherent wave nature and interference phenomena can be observed [6,9]. With semiconductor device size approaching its limits, a potential path forward could be new device structures that use the wave property of electrons. One device structure that has attracted attention is the resonant tunneling diode, whose operation is based on quantum interference [10]. In graphene nanoribbons, a Mach–Zehnder interferometer (MZI) structure can be devised which gives the same transmittance pattern as that of a resonant tunneling diode for incoming electrons [11-14]. Photon-assisted tunneling through

double quantum walls by spatial Rabi oscillation has also been studied [15,16]. In this paper we investigate the optoelectronic properties of this MZI structure formed by graphene nanoribbons and a possible application of this structure as photodetector. In a MZI structure, an electron in the ground, transverse mode goes through the device with a transmittance of one (T = 1) due to constructive interference at energies corresponding to longitudinal resonant modes. At these resonant energies, the electrons have a high density of states. In this paper we investigate for the first time the interaction of light in a graphene nanoribbon MZI structure and specifically we study the coupling of light between longitudinal resonant modes for both zigzag and armchair structures.

Graphene photodetectors have been studied in detail [2,3,17-19]. The primary distinguishing features of graphene photodetectors are: photodetection over a wide spectral range from infrared to ultraviolet wavelengths, a transit-time-limited bandwidth of approximately 1.5 THz and a high internal quantum efficiency of 15–30% [2,3,19]. The photocurrent generation mechanisms in graphene photodetectors include the photovoltaic effect, photothermoelectric effect, bolometric effect and phonon drag effect [3]. In the photovoltaic effect, the built-in electric field generated in the junction of p- and n-type graphene is utilized for separation of photogenerated electrons and holes. Photocurrent generation without a p–n junction and bias has also been demonstrated by utilizing the built-in electric field at the metal–graphene interface [20].

In this paper, we present the simulation results of two different approaches for an all-graphene (leads and device) nanoribbon photodetector with applied bias in a MZI structure. In the first part, we analyze the efficiency of the coupling of light between two resonant peaks of the MZI structure in a graphene nanoribbon. Each absorbed photon produces an electron and all of the photogenerated electrons are collected at the leads. This occurs because we are considering an all-graphene (both lead and device) structure, the calculated lifetime of the electron from photoexcitation is greater than the calculated transit time of the electron through the device and the device length is less than the mean free path of the electron. Half of the electrons collected at the leads contribute to the net current, resulting in an internal quantum efficiency of 50%. With proper bias and a high-pass frequency filter, this structure could be used to detect time-varying optical input with subwavelength resolution. In the second part, we analyze the total current switching caused by the phase decoherence of electrons by placing a strong photon flux in one or both of the interferometer arms.

This structure has the advantages that it does not require a p–n junction, it can operate at subwavelength resolution, its dimensions are very small, and that the photodetector has a high internal quantum efficiency of 50% and external quantum efficiency of up to 5.2%. By varying the device dimensions or using different resonant peaks, this structure can be used to detect light of various photon energies.

Device geometry

The device has a symmetric Mach–Zehnder-type interferometer structure as shown in Figure 1 and Figure 2. The device can be made of either armchair- or zigzag-type graphene nanoribbon.

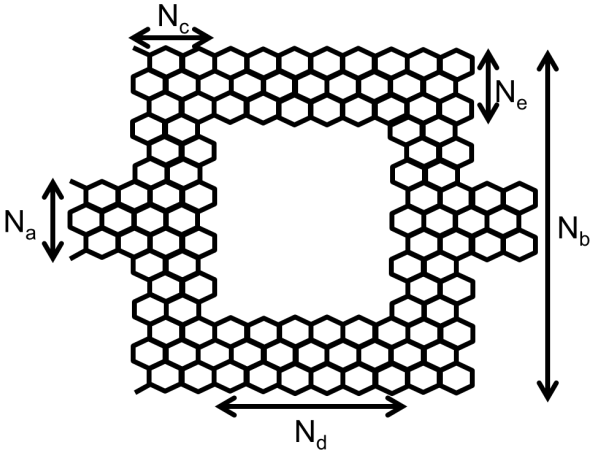

Figure 1: Graphene nanoribbon MZI structure (zigzag type).

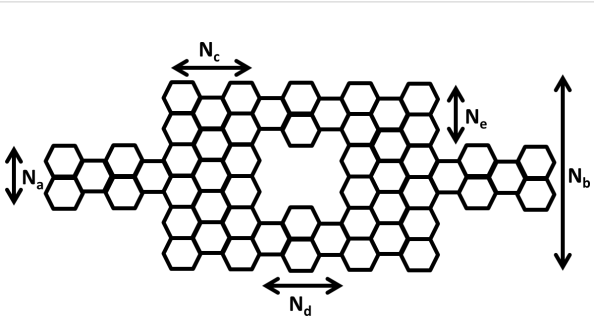

Figure 2: Graphene nanoribbon MZI structure (armchair type).

This paper presents simulation results for both zigzag- and armchair-type nanoribbon structures. For the simulation of the zigzag-type we used N_a = 1.136 nm (12 atoms), N_b = 5.396 nm (52 atoms), N_c = 0.986 nm (10 atoms), N_d = 1.968 nm (18 atoms) and N_e = 1.136 nm (12 atoms). For the armchair-type, N_a = 0.738 nm (7 atoms), N_b = 2.214 nm (19 atoms), N_c = 0.71 nm (8 atoms), N_d = 4.97 nm (48 atoms) and N_e = 0.738 nm (7 atoms) were used. The lattice constant was set at 0.142 nm.

Mathematical model

A non-equilibrium Green's function (NEGF) formalism was used to calculate the current through the device [9,21-23]. Here, the Green's function, G^R, is the impulse response of the device and non-equilibrium implies that some voltage is applied for the current to flow. The Green's function of the device, G^R, is calculated from the Hamiltonian, H_C, of the device and the self-energies, Σ_{l1}, Σ_{l2} and Σ_{photon} (leads and photon) of the interaction. All calculations are performed in the energy domain and the position basis:

$$\left[EI - H_C - \Sigma_{l1} - \Sigma_{l2} - \Sigma_{\text{photon}}\right]G^R = I \tag{1}$$

We have used a nearest neighbor, tight binding model to calculate the Hamiltonian, H_C, of the device [11-13,24-29]. If the transfer energy, t, is greater than the energy range of interest, then the tight binding model (the discrete lattice representation) gives fairly accurate results [23,30]. In the second quantized form, the nearest neighbor, tight binding model has the following form:

$$\hat{H}_C = \sum_i \varepsilon_i \hat{c}_i^\dagger \hat{c}_i + \sum_{(i,j)} t_{i,j} \hat{c}_i^\dagger \hat{c}_j \tag{2}$$

where ε_i (= 0) is the on-site energy, $t_{i,j} = -t$ (t = 2.7 eV) is the transfer energy of the nearest neighbor sites and $\hat{c}_i^\dagger$ and $\hat{c}_j$ are the creation and annihilation operators of the π electron at sites i and j, respectively.

The electron correlation function, G^n, and the hole correlation function, G^p, (equivalent to density matrices) are calculated from the Green's function of the device and the scattering functions Σ^{in} and Σ^{out} as

$$G^n = G^R \Sigma^{\text{in}} G^A \tag{3}$$

$$G^p = G^R \Sigma^{\text{out}} G^A \tag{4}$$

The scattering functions (Σ^{in} and Σ^{out}) describe the rate at which electrons are scattered in and out for a certain energy level. This can be scattering into the device or out of the device at a certain energy (Σ_{l1}^{in}, Σ_{l2}^{in}, Σ_{l1}^{out} and Σ_{l2}^{out}) or scattering from one energy to another energy due to some interaction ($\Sigma_{\text{photon}}^{\text{in}}$ and $\Sigma_{\text{photon}}^{\text{out}}$). We assume a Fermi–Dirac distribution in the leads (f_1 and f_2). The Γ_l functions are scattering rates provided that there are electrons and free states available and the Σ_l functions are scattering rates which consider the availability of electrons and free states through Fermi–Dirac distribution and Pauli exclusion principle.

The scattering functions are calculated in the following way:

$$\Sigma^{\text{in}} = \Sigma_{l1}^{\text{in}} + \Sigma_{l2}^{\text{in}} + \Sigma_{\text{photon}}^{\text{in}} \tag{5}$$

$$\Sigma^{\text{out}} = \Sigma_{l1}^{\text{out}} + \Sigma_{l2}^{\text{out}} + \Sigma_{\text{photon}}^{\text{out}} \tag{6}$$

$$\Gamma_{l1} = i\left[\Sigma_{l1} - \Sigma_{l1}^\dagger\right] \tag{7}$$

$$\Gamma_{l2} = i\left[\Sigma_{l2} - \Sigma_{l2}^\dagger\right] \tag{8}$$

$$\Sigma_{l1}^{\text{in}} = f_1\Gamma_{l1}; \Sigma_{l1}^{\text{out}} = \left(1 - f_1\right)\Gamma_{l1} \tag{9}$$

$$\Sigma_{l2}^{\text{in}} = f_2\Gamma_{l2}; \Sigma_{l2}^{\text{out}} = \left(1 - f_2\right)\Gamma_{l2} \tag{10}$$

The transmittance, T, through the device can be calculated as

$$T = \text{tr}\left[\Gamma_{l1} G^R \Gamma_{l2} G^A\right] \tag{11}$$

The effect of light illumination is incorporated in the calculation by the the inclusion of the Σ_{photon} term in the calculation of Green's function as shown in Equation 1. The electron–photon interaction is calculated by the lowest order perturbation theory and self-consistent Born approximation [25,29,31-33]. The term lowest order implies that only single photon (linear) processes are included and the term self-consistent Born approximation implies that iteration is necessary until a self-consistent electron density in the ground and excited states is reached. The electron–photon interaction has the form $H_{\text{elec–photon}} = (e/m_0)A \cdot P$, where A is the vector potential and P is the momentum operator. If the vector potential, A, is expressed in the second quantized form, the electron–photon interaction in the position basis (after some manipulation) assumes the following form [31]:

$$H_{\text{elec–photon}} = \sum_{lm} M_{lm}\left[\hat{b}e^{-i\omega t} + \hat{b}^\dagger e^{i\omega t}\right]\hat{c}_l^\dagger \hat{c}_m \tag{12}$$

where

$$M_{lm} = \left(z_m - z_l\right)\frac{ie}{\hbar}\sqrt{\frac{\hbar I_\omega}{2N\omega\varepsilon c}}\left\langle l\middle|\hat{H}_c\middle|m\right\rangle \tag{13}$$

and

$$I_w = \frac{Nc}{V\sqrt{\mu_r \varepsilon_r}} \tag{14}$$

where l and m are site basis states. z_m and z_l are the positions of sites m and l, respectively. $\hat{b}$ and $\hat{b}^\dagger$ are the bosonic annihilation and creation operators, respectively. I_w is the photon flux in units of photons/m^2/s, N is the number of photons in a control volume of V, c is the speed of light, ε_r is the relative permittivity, μ_r is the relative permeability and ε is the absolute permittivity.

The photon scattering functions, $\Sigma^{\text{in}}_{\text{photon}}$ and $\Sigma^{\text{out}}_{\text{photon}}$, are calculated assuming monochromatic light and two energy levels for excitation.

$$\Sigma^{\text{in}}_{\text{photon}} = \sum_{pq} M_{lp} M_{qm} \left[N G^n_{pq}(E - \hbar w) + (N+1) G^n_{pq}(E + \hbar w) \right] \tag{15}$$

$$\Sigma^{\text{out}}_{\text{photon}} = \sum_{pq} M_{lp} M_{qm} \left[N G^p_{pq}(E + \hbar w) + (N+1) G^p_{pq}(E - \hbar w) \right] \tag{16}$$

$$\Sigma_{\text{photon}} \simeq i \left[\Sigma^{\text{in}}_{\text{photon}} + \Sigma^{\text{out}}_{\text{photon}} \right] / (-2) \tag{17}$$

Both the acoustic phonon and optical phonon scattering have been neglected here because we are assuming phase coherent, ballistic transport and the mean free path for electrons is greater than the device length [25].

Knowing the electron and hole density functions (G^n and G^p) and the rate at which electrons are scattered in and out of the device (Σ^{in}_{l1} and Σ^{out}_{l1}), the energy resolved current (current per unit energy) is given by

$$I_{en}(E) = \text{tr}\left(\frac{q}{\pi\hbar} \left(\Sigma^{\text{in}}_{l1} G^p - \Sigma^{\text{out}}_{l1} G^n \right) \right) \tag{18}$$

The total current is found by integrating the energy-resolved current over the energy range of the applied bias:

$$I_{\text{total}} = \int I_{en}(E)\, dE \tag{19}$$

The total incoming scattering and outgoing scattering (Σ^{in} and Σ^{out}) consists of incoming scattering from the leads and the photon (Σ^{in}_{l1}, Σ^{in}_{l2} and $\Sigma^{\text{in}}_{\text{photon}}$) and outgoing scattering from the leads and the photon (Σ^{out}_{l1}, Σ^{out}_{l2} and $\Sigma^{\text{out}}_{\text{photon}}$) as shown in Equation 5 and Equation 6. If we want to calculate only the photoexcited portion of the electron and hole density matrices, then we consider the scattering due only to photons ($\Sigma^{\text{in}}_{\text{photon}}$ and $\Sigma^{\text{out}}_{\text{photon}}$) given by:

$$G^{\text{ph}}_n = G^R \Sigma^{\text{in}}_{\text{photon}} G^A \tag{20}$$

$$G^{\text{ph}}_p = G^R \Sigma^{\text{out}}_{\text{photon}} G^A \tag{21}$$

The energy-resolved photoexcited current is given by

$$I^{\text{ph}}_{en}(E) = \text{tr}\left(\frac{q}{\pi\hbar} \left(\Sigma^{\text{in}}_{l1} G^{\text{ph}}_p - \Sigma^{\text{out}}_{l1} G^{\text{ph}}_n \right) \right) \tag{22}$$

In this report, a Poisson solver was not used to account for the interaction of electrons present in the device. Since our applied voltage is quite low (0.1 eV) and there is no gate modulation in the device, the results obtained will still hold with good accuracy.

It should be mentioned here that we have used the tight binding model for both the armchair and zigzag structures. Zigzag edges of graphene nanoribbons have been shown to be magnetic [34-36]. Some reports used the tight binding model without magnetism in NEGF formalism for zigzag MZI structures [12,13] as well as other zigzag nanoribbon structures [37]. The device operation developed herein is not spin-dependent. We have not included the effect of magnetism in our tight binding Hamiltonian. However, an armchair nanoribbon does not have edge magnetism. Thus the tight binding Hamiltonian without magnetism can be used for an armchair nanoribbon without loss of accuracy. Our device operation is also valid for an armchair MZI structure although inclusion of the effect of magnetism is planned for our future studies of the zigzag MZI structure.

Results and Discussion

The MZI structure in a graphene nanoribbon behaves like a resonant tunneling structure, meaning that at some energy, electrons pass through the structure as if there were no barriers. At this energy, the transmittance is one ($T = 1$) and constructive interference occurs. The energy at which this occurs is called the resonant energy level. There can be a 1st resonant level, a 2nd resonant level, etc. In contrast, at other energies, the electrons cannot pass through the device at all. At these energies the transmittance is zero ($T = 0$) and destructive interference occurs. These regions are called the valley regions. The modes described so far are the longitudinal resonant modes for the first transverse mode. At a higher energy and higher transverse

modes, longitudinal resonant modes can also occur. The transmittance pattern for the zigzag structure is shown in Figure 3a and the transmittance pattern for armchair structure is shown in Figure 3b.

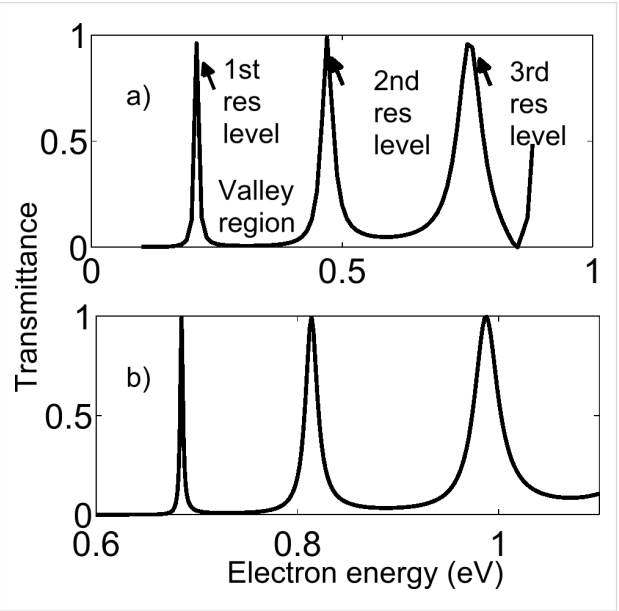

Figure 3: Transmittance versus change in electron energy for graphene nanoribbon MZI structure (a) zigzag type (b) armchair type.

As the length of the middle arm, N_d, increases, the longitudinal resonant peaks become sharper and the peaks become closer in energy. As the width of the nanoribbon, N_a, increases, the higher transverse modes become closer in energy and the energy space available for longitudinal resonant modes to occur within a transverse mode decreases. Also, as the width N_a increases, the longitudinal resonant peaks become sharper in energy. From our simulation results we see that by changing the device dimensions, we can detect photons of energy of 0.1 eV to 1 eV.

In the next section, we consider the response of the structure after light illumination. The two schemes for interaction with light are described below.

Scheme 1: Coupling light between resonant peaks

By illuminating on both the interferometer arms as is shown in Figure 4, this structure can be operated as a photodetector. Upon illumination, electrons in the low-energy level (1st resonant level) absorb the light and get transferred to the high-energy level (2nd resonant level) and are emitted from the device without any other kind of interaction. The calculated lifetime of the electron from photoexcitation is greater than the calculated transit time of the electron through the device. Since we are assuming that the device length is less than the mean free path of the electron, we are neglecting all phonon interactions here. The photocurrent flows through the leads because one of the leads (drain) cannot supply the electrons to fill up the holes in the device (because the Fermi level in the drain is lower than the Fermi level in the source due to the applied bias). All of the photogenerated electrons are collected in the leads. Half of these electrons contribute to the net photocurrent, resulting in an internal quantum efficiency of 50% for the device.

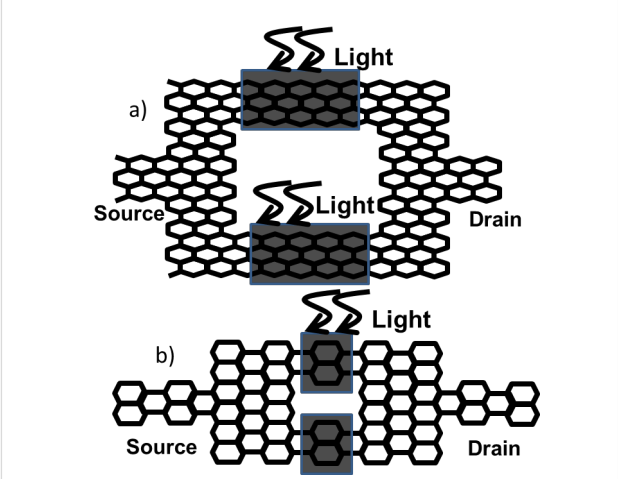

Figure 4: Device structure for light detection by coupling light between two resonant peaks. (top) zigzag structure (bottom) armchair structure.

The results of the interaction of light with the zigzag and armchair structures are shown in Figure 5 and Figure 6, respectively. For this simulation, the parameters used for the zigzag structure were an applied voltage of 0.1 eV, photon energy of 0.26 eV and a photon flux of 10^{25} photon/m^2/s (4.16×10^6 W/m^2). The parameters used for armchair structure were an applied voltage of 0.1 eV, photon energy of 0.13 eV and a photon flux of 10^{25} photon/m^2/s (2.08×10^6 W/m^2). For both the zigzag and armchair structures, the polarization of the applied electromagnetic field was along the length of the device. The full length of the middle, horizontal arms (216 ($12 \times 9 \times 2$) atoms for the zigzag structure and 336 ($14 \times 12 \times 2$) atoms for the armchair structure) was illuminated for this result. In the vertical arms, the absorption is two orders of magnitude less than the horizontal arms, so this result is equivalent to illuminating the entire structure. The voltage was applied in such a way that the first resonant level is within the applied voltage range. In top graphs of Figure 5 and Figure 6, we see that when there is no light, current flows in the low-energy level (1st resonant) but there is no current in the high-energy level (2nd resonant). Upon illumination, current flows in the high-energy level (2nd resonant) as shown in bottom part of Figure 5 and Figure 6. The currents shown in Figure 5 and

Figure 6 are energy-resolved current, that is, the current per unit energy. A negative current indicates that electrons are entering the device.

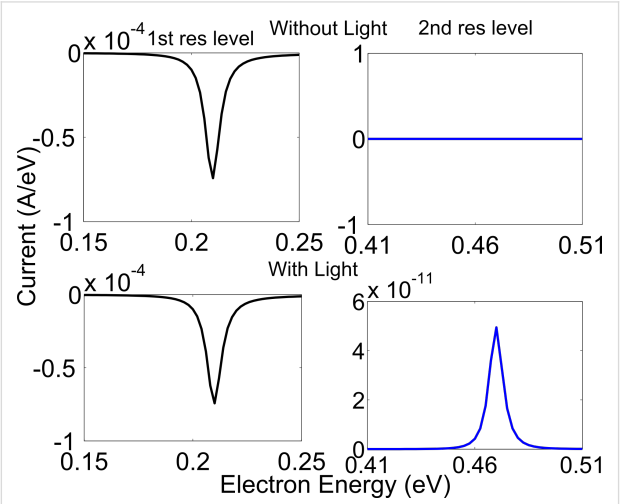

Figure 5: (zigzag structure) Current density versus electron energy for light detection by coupling light between two resonant peaks (top) without light (bottom) with light.

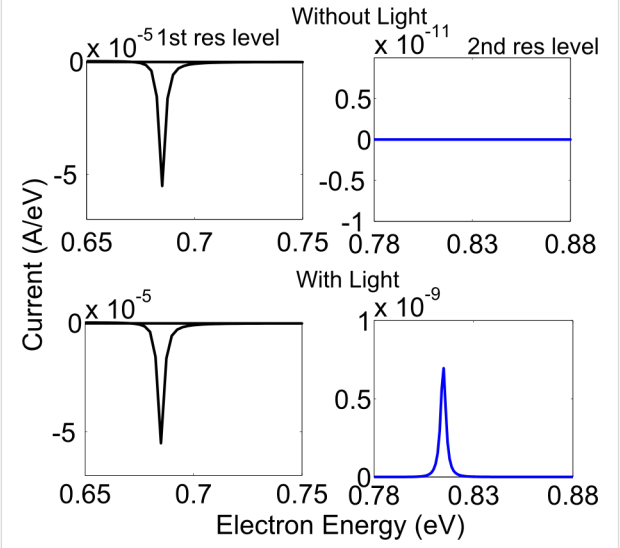

Figure 6: (armchair structure) Current density versus electron energy for light detection by coupling light between two resonant peaks (top) without light (bottom) with light.

The photocurrent does not increase linearly with the number of atoms illuminated in the middle arm. The variation of the peak photocurrent with the number of blocks illuminated is shown in Figure 7. Each block contains 12 atoms in the zigzag structure and 14 atoms in the armchair structure. Initially, the peak photocurrent increases quadratically with the number of blocks illuminated and then the current saturates. This particular variation of current comes from the particular wave shape of the electron in position basis in the ground and excited states and Fermi's golden rule, which is inherently contained in the NEGF formalism. The photocurrent is higher in the armchair structure compared with the zigzag structure. This is because in a zigzag structure, some neighboring atoms lie vertically and thus do not intercept the electric field because the polarization is in the horizontal direction. Also, the number of illuminated atoms (336) is greater in the armchair structure than for the number of illuminated atoms (216) in the zigzag structure.

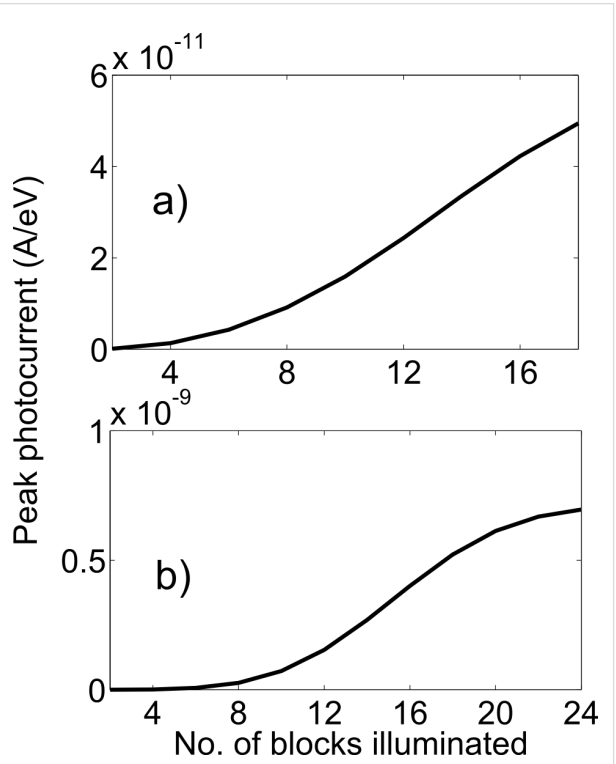

Figure 7: Variation of peak photocurrent with number of blocks illuminated. (a) zigzag structure, (b) armchair structure.

It should be mentioned here that without excitation light, the bias current through the device is in the range of 10^{-5} A/eV and with light the photocurrent is in the range of 10^{-11} A/eV. Thus, some kind of differential measurement is needed to detect the current in the leads. Alternatively, a high-pass frequency filter can be used at the output of the device for the detection in the variation of light.

With the appropriate bias, the device can also be used to detect the photon energy corresponding to the energy difference of any two resonant levels. The peak photocurrent variations with different photon energies are shown in Figure 8a and Figure 8b corresponding to zigzag and armchair structures, respectively. 144 (12 × 6 × 2) and 140 (14 × 5 × 2) atoms of zigzag and

armchair structures, respectively, in the middle arm were illuminated for this result. 0.26 eV and 0.55 eV are the energy differences of 1st and 2nd resonant levels and 1st and 3rd resonant levels in the zigzag structure. 0.13 eV and 0.3 eV are the energy differences of 1st and 2nd resonant levels and 1st and 3rd resonant levels in the armchair structure.

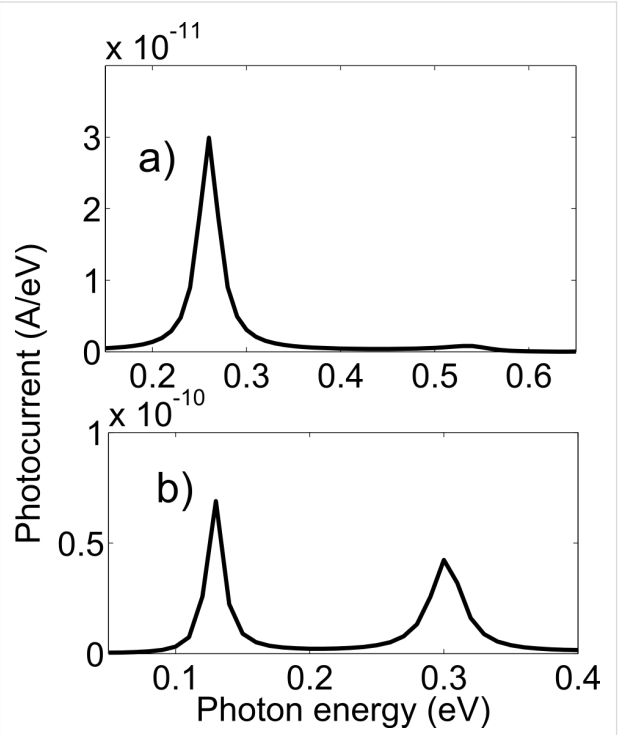

Figure 8: Variation of the peak photocurrent with photon energy. (a) Zigzag structure, (b) armchair structure.

If we integrate the energy-resolved photocurrent, we can calculate the total photocurrent through the device. For the integration, we have used Fermi–Dirac statistics at 300 K in the leads. Given the photocurrent, the external quantum efficiency of the device can be calculated as

$$\text{quantum efficiency} = \frac{\text{photocurrent}/q}{\text{no. of photons in the illuminated area}}$$

For the zigzag structure, the external quantum efficiency reaches a maximum of 1.6% at a photon energy of 0.26 eV and for the armchair structure, the external quantum efficiency shows a peak of 5.2% at a photon energy of 0.13 eV, as shown in Figure 9a and Figure 10a. The photon energies 0.26 eV and 0.13 eV are the energy differences between the first two resonant levels in the zigzag and armchair structures, respectively. The quantum efficiencies are highest at 0.26 eV and 0.13 eV because the density of states is higher near the resonant energy levels. The external quantum efficiency remains constant with a photon flux of up to approximately 10^{31} photon/m^2/s. The variation of the peak photocurrent with photon flux is shown in Figure 9b and Figure 10b.

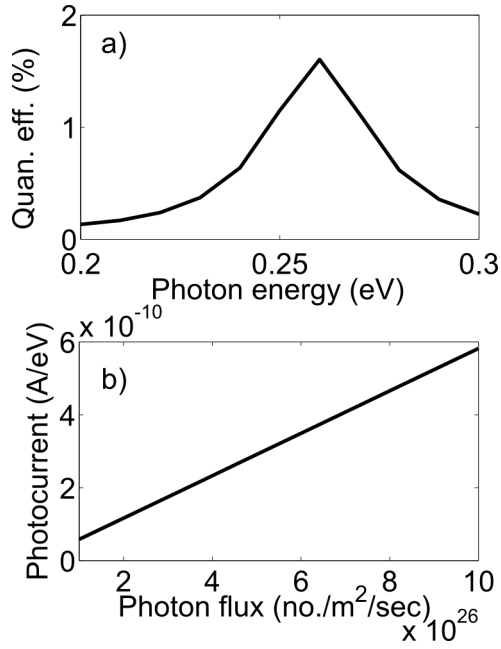

Figure 9: (a) The variation of the external quantum efficiency with photon energy. (b) Linear trend of peak photocurrent with photon flux (zigzag device).

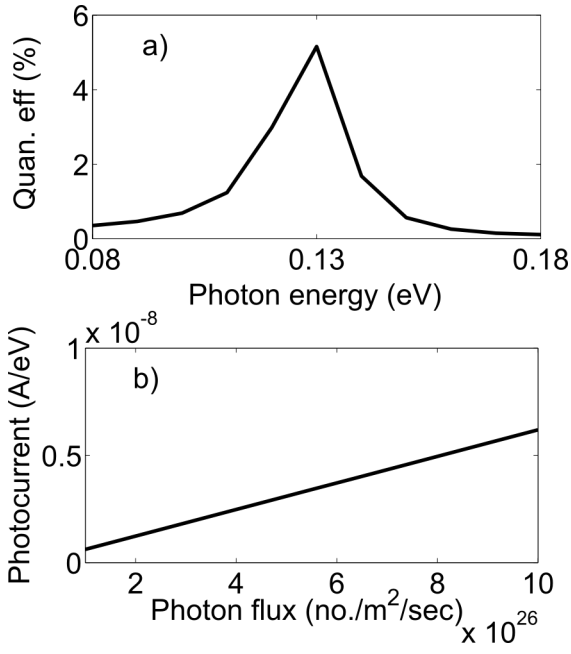

Figure 10: (a) Variation of the external quantum efficiency with photon energy. (b) Linear trend of the peak photocurrent with photon flux (armchair device).

We should mention here that the internal quantum efficiency for this device is 50%. In the literature, the reported value of experimentally determined internal quantum efficiency is 15–30% [19]. In the experimental result, the electron–hole pairs are separated by the built-in potential of the metal–semiconductor junction. The experimental internal quantum efficiency is lower because of electron–hole recombination from phonon scattering and scattering at the metal–semiconductor interface. The model presented herein does not allow for electron–hole recombination. The external quantum efficiency was 5.2% for the armchair structure and 1.6% for the zigzag structure. The photon absorption rate was 10.4% for the armchair structure and 3.2% for the zigzag structure. This is higher than the 2.3% absorption rate of bulk graphene due to two reasons. First, fully coherent transport of electrons occurs in the device, and second, the particular wave shapes of the electron in the 1st longitudinal resonant state and 2nd longitudinal resonant state within the first transverse mode in MZI structure contribute to the high absorption rate.

Experimentally, ballistic transport has been shown in graphene nanoribbons and MZI interferometer structures have been made in the graphene nanoribbons with a width of 40 nm [4]. The results presented here illustrate a MZI structure with a graphene nanoribbon width of 1 nm. The basic physics remains intact for devices of larger width and the device sizes will become smaller in future.

Scheme 2: Decoherence with strong photon flux

One arm illuminated

In the previous section, it was shown that the photocurrent is quite low in comparison with the bias current through the device. In order to switch the total current a strong photon flux is needed. When the self energy (broadening) due to the incident light is comparable with the self energy (broadening) due to the contacts (i.e., when the lifetime of the electron from photoexcitation in the 1st and 2nd resonant levels is comparable with the transit time of the electron through the device), the incident light can cause phase decoherence for the majority of the propagating electrons. The lifetime of the electron, τ, is related to the self energy, Σ, by the following formula:

$$\tau = \frac{\hbar}{2Im(\Sigma)} \tag{23}$$

The results of the simulation with one of the MZI arms illuminated are shown in Figure 11 and Figure 12 and for zigzag and armchair structures, respectively. The parameters used for the zigzag structure were an applied voltage of 0.2 eV, a photon energy of 0.26 eV and a photon flux of 10^{35} photon/m^2/s (4.16×10^{16} W/m^2). The parameters for the armchair structures were an applied voltage of 0.1 eV, a photon energy of 0.13 eV and a photon flux of 10^{35} photon/m^2/s (2.08×10^{16} W/m^2). In Figure 11 and Figure 12, the simulation results for a large energy range are shown. For a practical device, the device will either be biased around the resonant level, where we want to reduce the current or around the valley region where we want to increase the current. With one arm illuminated, for the zigzag structure, as is shown in middle part of Figure 11, the transmittance in the peak region remains almost constant, but the peak position shifts by 0.002 eV, while the current in the peak region remains almost same, but the peak position shifts by 0.002 eV and the current in the valley region increases by 10 times. For the armchair structure, as is shown in middle part of Figure 12, the transmittance in the peak region decreases by 7 times and the peak position shifts by 0.006 eV, the current in the peak region remains almost same, but the peak position shifts by 0.006 eV and the current in the valley region increases by 10 times. With one arm illuminated, the coherent transmittance around the resonant level remains same for the zigzag structure

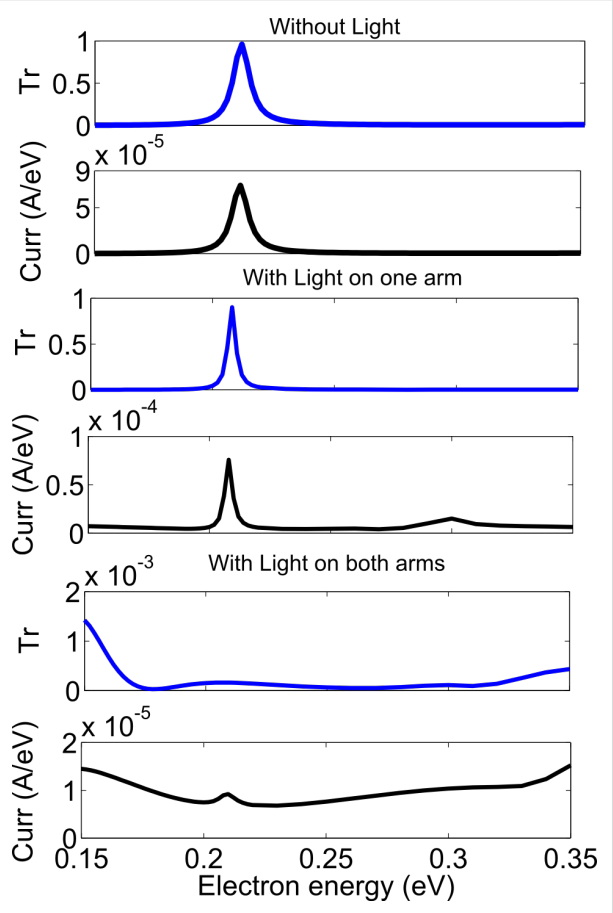

Figure 11: Transmittance and current density vs electron energy for strong photon flux (zigzag structure).

but decreases by 7 times for the armchair structure. This is assumed to be because though the electrons lose their wave nature in one arm, yet resonant tunneling can still occur through the other arm. The destructive interference in the valley region is lifted due to the loss of coherent transport in one arm and thus incoherent current flows there.

Both arms illuminated

In order to reduce the current in the resonant energy level, both arms must be illuminated. When both arms are illuminated, scattering is induced in both arms, and the electrons lose their wave nature in both the arms, which effectively destroys the constructive interference. As stated before, the destructive interference in the valley region is also lifted. For the zigzag structure, as shown in the bottom part of Figure 11, the coherent transmittance in the peak region is reduced by a factor of 1000, the current in the peak region is reduced by a factor of 5, and the current in the valley region increases by a factor of 10 as compared to the values of these parameters (transmittance, peak current and valley current) without excitation light. For the armchair structure, as shown in the bottom part of Figure 12, the coherent transmittance in the peak region is reduced by a factor of 1000, the current in the peak region is reduced by a factor of 4, and the current in the valley region increases by a factor of 30 as compared to the values of these parameters (transmittance, peak current and valley current) without excitation light.

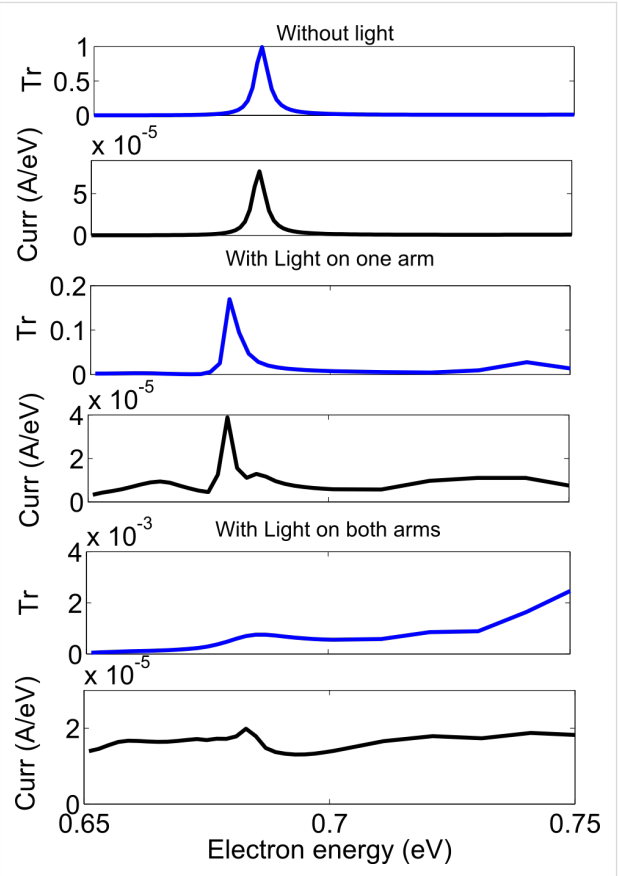

Figure 12: Transmittance and current density versus electron energy for a strong photon flux (armchair structure).

Conclusion

We have proposed a graphene photodetector that makes use of quantum interference. We have shown that such a device can be operated as a linear photodetector that is most sensitive when the excitation light can couple two of the resonant energy levels in the graphene nanoribbon MZI structure. At this photon energy, the calculated external quantum efficiency was approximately 1.6% for the zigzag structure and 5.2% for the armchair structure. It is also possible to switch the total current in the device by causing a phase decoherence of electrons with a very strong photon flux. In this regime, the electrons lose their phase coherent, wave property and the ability to exhibit interference. This study is a step forward in analyzing the physics and potential performance of coherent electronic and optoelectronic devices.

Acknowledgements

We acknowledge the CNRS grant.

References

1. Novoselov, K. S.; Fal'ko, V. I.; Colombo, L.; Gellert, P. R.; Schwab, M. G.; Kim, K. *Nature* **2012,** *490,* 192–200. doi:10.1038/nature11458
2. Xia, F.; Yan, H.; Avouris, P. *Proc. IEEE* **2013,** *101,* 1717–1731. doi:10.1109/JPROC.2013.2250892
3. Avouris, P.; Freitag, M. *IEEE J. Sel. Top. Quantum Electron.* **2014,** *20,* 6000112. doi:10.1109/JSTQE.2013.2272315
4. Baringhaus, J.; Ruan, M.; Edler, F.; Tejeda, A.; Sicot, M.; Taleb-Ibrahimi, A.; Li, A.-P.; Jiang, Z.; Conrad, E. H.; Berger, C.; Tegenkamp, C.; de Heer, W. A. *Nature* **2014,** *506,* 349–354. doi:10.1038/nature12952
5. Miao, F.; Wijeratne, S.; Zhang, Y.; Coskun, U. C.; Bao, W.; Lau, C. N. *Science* **2007,** *317,* 1530–1533. doi:10.1126/science.1144359
6. Berger, C.; Song, Z.; Li, X.; Wu, X.; Brown, N.; Naud, C.; Mayou, D.; Li, T.; Hass, J.; Marchenkov, A. N.; Conrad, E. H.; First, P. N.; de Heer, W. A. *Science* **2006,** *312,* 1191–1196. doi:10.1126/science.1125925
7. Heersche, H. B.; Jarillo-Herrero, P.; Oostinga, J. B.; Vandersypen, L. M. K.; Morpurgo, A. F. *Eur. Phys. J. Special Topics* **2007,** *148,* 27–37. doi:10.1140/epjst/e2007-00223-7
8. Du, X.; Skachko, I.; Barker, A.; Andrei, E. Y. *Nat. Immunol.* **2008,** *3,* 491–495. doi:10.1038/nnano.2008.199
9. Datta, S. *Lessons from Nanoelectronics - A New Perspective on Transport,* 1st ed.; World Scientific: USA, 2012.
10. Britnell, L.; Gorbachev, R. V.; Geim, A. K.; Ponomarenko, L. A.; Mishchenko, A.; Greenaway, M. T.; Fromhold, T. M.; Novoselov, K. S.; Eaves, L. *Nat. Commun.* **2013,** *4,* 1794. doi:10.1038/ncomms2817
11. Munárriz, J.; Domínguez-Adame, F.; Malyshev, A. V. *Nanotechnology* **2011,** *22,* 365201. doi:10.1088/0957-4484/22/36/365201

12. Wu, Z.; Zhang, Z. Z.; Chang, K.; Peeters, F. M. *Nanotechnology* **2010,** *21,* 185201. doi:10.1088/0957-4484/21/18/185201
13. Zhang, Z. Z.; Chang, K.; Chan, K. S. *Appl. Phys. Lett.* **2008,** *93,* 062106. doi:10.1063/1.2970957
14. Stafford, C. A.; Cardamone, D. M.; Mazumdar, S. *Nanotechnology* **2007,** *18,* 424014. doi:10.1088/0957-4484/18/42/424014
15. Stoof, T.; Nazarov, Y. *Phys. Rev. B* **1996,** *53,* 1050–1053. doi:10.1103/PhysRevB.53.1050
16. Stafford, C.; Wingreen, N. *Phys. Rev. Lett.* **1996,** *76,* 1916–1919. doi:10.1103/PhysRevLett.76.1916
17. Bonaccorso, F.; Sun, Z.; Hasan, T.; Ferrari, A. C. *Nat. Photonics* **2010,** *4,* 611–622. doi:10.1038/nphoton.2010.186
18. Urich, A.; Unterrainer, K.; Mueller, T. *Nano Lett.* **2011,** *11,* 2804–2808. doi:10.1021/nl2011388
19. Mueller, T.; Xia, F.; Avouris, P. *Nat. Photonics* **2010,** *4,* 297–301. doi:10.1038/nphoton.2010.40
20. Xia, F.; Mueller, T.; Lin, Y.-M.; Valdes-Garcia, A.; Avouris, P. *Nat. Nanotechnol.* **2009,** *4,* 839–843. doi:10.1038/nnano.2009.292
21. Datta, S. *Quantum Transport: Atom to Transistor,* 1st ed.; Cambridge University Press: UK, 2005.
22. Datta, S. *Electronic Transport in Mesoscopic Systems,* 5th ed.; Cambridge University Press: UK, 2003.
23. Datta, S. *Superlattices Microstruct.* **2000,** *28,* 253–278. doi:10.1006/spmi.2000.0920
24. Stewart, D.; Léonard, F. *Phys. Rev. Lett.* **2004,** *93,* 107401. doi:10.1103/PhysRevLett.93.107401
25. Guo, J.; Alam, M. A.; Yoon, Y. *Appl. Phys. Lett.* **2006,** *88,* 133111. doi:10.1063/1.2189827
26. Wohlthat, S.; Reimers, J. R.; Hush, N. S. *Phys. Rev. B* **2010,** *81,* 195125. doi:10.1103/PhysRevB.81.195125
27. Castro Neto, A. H.; Guinea, F.; Peres, N. M. R.; Novoselov, K. S.; Geim, A. K. *Rev. Mod. Phys.* **2009,** *81,* 109–162. doi:10.1103/RevModPhys.81.109
28. Mohammadpour, H.; Asgari, A. *Physica E* **2011,** *43,* 1708–1711. doi:10.1016/j.physe.2011.05.027
29. Ostovari, F.; Moravvej-Farshi, M. K. *Appl. Surf. Sci.* **2014,** *318,* 108–112. doi:10.1016/j.apsusc.2014.01.117
30. Marconcini, P.; Cresti, A.; Triozon, F.; Fiori, G.; Biel, B.; Niquet, Y.-M.; Macucci, M.; Roche, S. *ACS Nano* **2012,** *6,* 7942–7947. doi:10.1021/nn3024046
31. Henrickson, L. E. *J. Appl. Phys.* **2002,** *91,* 6273. doi:10.1063/1.1473677
32. Guo, J. *J. Appl. Phys.* **2005,** *98,* 063519. doi:10.1063/1.2060942
33. Gao, Q.; Guo, J. *J. Appl. Phys.* **2012,** *112,* 084316. doi:10.1063/1.4759369
34. Son, Y.-W.; Cohen, M. L.; Louie, S. G. *Nature* **2006,** *444,* 347–349. doi:10.1038/nature05180
35. Wang, Z. F.; Liu, F. *Appl. Phys. Lett.* **2011,** *99,* 042110. doi:10.1063/1.3619817
36. Tao, C.; Jiao, L.; Yazyev, O. V.; Chen, Y.-C.; Feng, J.; Zhang, X.; Capaz, R. B.; Tour, J. M.; Zettl, A.; Louie, S. G.; Dai, H.; Crommie, M. F. *Nat. Phys.* **2011,** *7,* 616–620. doi:10.1038/nphys1991
37. Ahsan, S.; Masum Habib, K. M.; Neupane, M. R.; Lake, R. K. *J. Appl. Phys.* **2013,** *114,* 183711. doi:10.1063/1.4830019

License and Terms